Novel catalyst materials for the cathode side of MEAs suitable for transportation applications				
G.A. 303492				05.07.2016
Deliverable **D3.8**	WP3	**Preparation and structural characterization of new catalysts and modified catalyst support materials**		
Deliverable: Publications				
Description of Deliverable: Publications regarding new synthesis techniques and advanced support materials				
PM for D3.8: 4	Nature: O	Dissemination Level: PU	Delivery Date: 31.12.2014	Lead Beneficiary: UP-IC2MP

Objectives of Work

- Fabrication of well-defined bimetallic Pt(Pd)M_x NPs with good control of material composition and morphological parameters, such as particle size and dispersion, and their characterization by Surface Science tools and TEM. Also core-shell and skin-like Pt monolayer (ML) NPs will be prepared and characterized;
- Preparation of innovative support materials to increase catalyst stability and reduce mass loading of catalysts. Two different routes will be explored: (a) Ar and N ion implantation of carbon support; (b) mixed electron- and cation conducting transition metal oxides (e.g. V, Ti, Mo, Ru, and Mn), synthesized as highly porous materials with a high surface area;

Relevant Sections from the Description of Work

"Task 3.2: *Synthesis of NPs of Pt_3Y and Pt_3Sc with defined size and size distribution (month 1-12) (TUM, DTU, UP-IC2MP)*
NPs of PtM_x NPs (M=Y, Sc) will be prepared and deposited on a carbon based support by exploiting several different methods already detailed. These materials then will be tested in WP4. "

"Task 3.3: *Synthesis of NPs from other binary alloys and Pt skin alloys based on new theoretical predictions (month 6-24) (TUM, DTU, UP-IC2MP, CUT)*
Nanoparticles of PtM_x and PdM_x suggested by the DFT derived predictions from WP2 will be prepared, and deposited both on standard carbon supports as well as advanced support materials for further testing in WP4. Selected NPs will be deposited onto substrates for study with INPS."

"Task 3.5: *Advanced carbon supports modified by ion implantation (month 1-24) (UniPd, TUM)*
In order to enhance the stability of the NP arrays, the effect of ion implantation of the support will be studied. Three different cases will be studied: (i) undoped HOPG surface prepared by cleaving; (ii) N-doped HOPG and (III) Ar-doped HOPG. The HOPG doping will be carried out via N and Ar ion implantation. Comparing structural and chemical modifications of HOPG surfaces after Ar and N ion implantation as a function of dosage enables separation of physical and chemical factors and is further used to assist in elucidating the specific roles of the surface nitrogen and oxygen functionalities as well as surface defects on: (i) nucleation and growth of metal NPs; (ii) metal/support binding; and (iii) metal

NP electronic structure modification. If the results will go along the expectative, during the latest part of the task methods for doping standard carbon supports will be explored. "

"Task 3.6: *Advanced composite supports based on porous oxides. (month 1-36) (UP-IC2MP)*
High surface-area support materials with defective or charged surfaces are needed to facilitate ion- and/or electron-transfer reactions. In this line, mixed electron- and cation conducting transition metal oxides of Vanadium, Molybdenum, Ruthenium, and Manganese, synthesized as highly porous materials with a high surface area have been reviewed. We expect that a controlled synthesis of mixed conductivity oxides (TiO_2, RuO_2) in a network, such as carbon, will provide the necessary chemical stability against corrosion of the latter at potentials positive or near the open circuit potential of the Oxygen reduction reaction on cathodes based on $Pt(Pd)M_x$. The ionic conductivity as well as the electronic conductivity will be the critical parameters to optimize in the composite materials."

Description of Work Done / Results

The work done has been described in recent progress reports, in D3.4 and D3.5, and was more detailed in D3.7. For this deliverable, the papers published so far on synthesis of improved catalysts (apart from the DTU work on mass-selected nanoparticles, which is part of D4.3) and on advanced support materials are listed below. The papers are added to this deliverable, but they are not open access.

Publications

Publications regarding synthesis of catalysts
Y. Luo, A. Habrioux, L. Calvillo, G. Granozzi, N. Alonso-Vante, *Yttrium Oxide/Gadolinium Oxide-Modified Platinum Nanoparticles as Cathodes for the Oxygen Reduction Reaction*, Chemphyschem : a European journal of chemical physics and physical chemistry, 15 (2014) 2136–2144.

Y. Luo, J.M. Mora-Hernández, L.A. Estudillo-Wong, E.M. Arce-Estrada, N. Alonso-Vante, *Nanostructured palladium tailored via carbonyl chemical route towards oxygen reduction reaction*, Electrochimica Acta, 173 (2015) 771-778.

Publications regarding advanced support materials
S. Mokrane-Soualah, A.S. Gago, A. Habrioux, N. Alonso-Vante, *Mixed-oxide* $Ti_{1-x}W_xO_2$ *as support for (photo)-electrochemical processes*, Applied Catalysis B: Environmental, 147 (2014) 756-763.

J. Ma, A. Habrioux, Y. Luo, G. Ramos Sanchez, L. Calvillo, G. Granozzi, P.B. Balbuena, N. Alonso-Vante, *Electronic Interaction between Platinum Nanoparticles and Nitrogen-doped Reduced Graphene Oxide: Effect on the Oxygen Reduction Reaction*, Journal of Materials Chemistry A, 3 (2015) 11891-11904.

Y. Luo, N. Alonso-Vante, *The Effect of Support on Advanced Pt-based Cathodes towards the Oxygen Reduction Reaction. State of the Art*, Electrochimica Acta, 179 (2015) 108-118.

W. Ju, M. Favaro, C. Durante, L. Perini, S. Agnoli, O. Schneider, U. Stimming, G. Granozzi, Pd Nanoparticles deposited on nitrogen-doped HOPG: New Insights into the Pd-catalyzed Oxygen Reduction Reaction, Electrochim. Acta, 141 (2014) 89-101.

L. Perini, C. Durante, M. Favaro, S. Agnoli, G. Granozzi, A. Gennaro, Electrocatalysis at palladium nanoparticles: Effect of the support nitrogen doping on the catalytic activation of carbon-halogen bond, Applied Catalysis B: Environmental, 144 (2014) 300-307.

M. Favaro, G.A. Rizzi, S. Nappini, E. Magnano, F. Bondino, S. Agnoli, G. Granozzi, *A synchrotron-based spectroscopic study of the electronic structure of N-doped HOPG and PdY/N-doped HOPG*, Surface Science, 646 (2016) 132-139.

L. Perini, C. Durante, M. Favaro, V. Perazzolo, S. Agnoli, O. Schneider, G. Granozzi, A. Gennaro, *Metal-Support Interaction in Platinum and Palladium Nanoparticles Loaded on Nitrogen Doped Mesoporous Carbon for Oxygen Reduction Reaction*, ACS Applied Materials & Interfaces, 7 (2015) 1170-1179.

ChemPubSoc
Europe

DOI: 10.1002/cphc.201400042

Yttrium Oxide/Gadolinium Oxide-Modified Platinum Nanoparticles as Cathodes for the Oxygen Reduction Reaction

Yun Luo,[a] Aurélien Habrioux,[a] Laura Calvillo,[b] Gaetano Granozzi,[b] and Nicolas Alonso-Vante*[a]

Rare-earth-element (Y, Gd) modified Pt nanoparticles (NPs) supported on a carbon substrate (Vulcan XC-72) are synthesized via a water-in-oil chemical route. In both cases, X-ray diffraction (XRD) measurements show the non-formation of an alloyed material. Photoemission spectroscopy (XPS) results reveal that Y and Gd are oxidized. Additionally, no evidence of an electronic modification of Pt can be brought to light. Transmission electron microscopy (TEM) studies indicate that Pt-Y_2O_3 and Pt-Gd_2O_3 particles are well dispersed on the substrate—and that their average particle sizes are smaller than the Pt-NP sizes. The catalytic activity of the Pt-Y_2O_3/C and Pt-Gd_2O_3/C catalysts towards the oxygen reduction reaction (ORR) is studied in a 0.5 M H_2SO_4 electrolyte. The surface and mass specific activities of the Pt-Y_2O_3/C catalyst towards the ORR at 0.9 V (vs. the reversible hydrogen electrode, RHE) are $(54.3 \pm 1.2)\ \mu A\,cm^{-2}{}_{Pt}$ and MA $= (23.1 \pm 0.5)\ mA\,mg^{-1}{}_{Pt}$, respectively. These values are 1.3-, and 1.6-fold higher than the values obtained with a Pt/C catalyst. Although the as-prepared Pt-Gd_2O_3/C catalyst has a lower catalytic activity for the ORR compared to Pt/C, the heat-treated sample shows a surface specific activity of about $(53.0 \pm 0.7)\ \mu A\,cm^{-2}{}_{Pt}$, and a mass specific activity (MA) of about $(18.2 \pm 0.5)\ mA\,mg^{-1}{}_{Pt}$ at 0.9 V (vs. RHE). The enhancement of the ORR kinetics on the Pt-Y_2O_3/C and heat-treated Pt-Gd_2O_3/C catalysts could be associated with the formation of platinum NPs presenting modified surface properties.

1. Introduction

Proton exchange membrane fuel cells (PEMFC) are one of the most promising candidates to be applied in mobile, stationary, and portable energy devices because of the green and highly efficient energy conversion,[1,2] though their performance needs to be improved. The oxygen reduction reaction (ORR) at the cathode of PEMFCs is still a great challenge for improving the efficiency of PEMFCs, since this electrochemical reduction process largely depends on the electrocatalytic activity of the catalysts used. Therefore, in the last decades, many efforts have concentrated on developing novel materials, including catalysts based on non-noble metals and materials containing earth-crust-abundant elements,[3] for instance, $CoSe_2$/C and Fe-N/C complexes.[4,5] Some catalysts exhibit a similar ORR activity and/or a better stability compared to commercial Pt/C catalysts. However, their performance in PEMFC should be improved and studied further in detail. Pt-based catalysts are widely used and studied for ORR. However, the application of Pt-based catalyst in PEMFC faces many challenges, namely, the cost, performance and durability.[6] Therefore, many efforts have been done to alloy 3d transition metals with Pt. This kind of catalysts becomes a hot issue in this domain for the following reasons: 1) the amount of Pt could be reduced in the catalyst; 2) the catalytic behavior of Pt could be modified based on the "ligand effect" and "geometric effect".[7] In terms of the ligand effect, the formation of hetero-atoms bonds between the 3d transition metal and Pt atoms could affect the electronic structure of Pt surface. The geometric effect in Pt-M (M = 3d transition metals) catalyst alters the Pt-Pt surface inter-atomic distance, resulting in change in orbital overlap and finally leading to different Pt electronic structure. Hence, the catalytic activity of Pt in this kind of catalysts could be improved.

Recently, it was reported that bimetallic nanoparticles (NPs) supported onto different substrates show a high ORR kinetics and stability, such as Pt_xM_y (M = Ni, Co, Ti, Cu, W, Pd, Ag, Au, Rh, Zn, Sn, Fe and Cr).[8–18] However, few works have been devoted to studying Pt catalysts involving rare-earth elements, such as, yttrium, scandium, and gadolinium.[19–23] Regardless of a two- or a four-electron charge-transfer pathway in the ORR process, the OOH is adsorbed on the catalyst surface prior to splitting the O–O bond.[24] After breaking the O–O bond, O and OH are formed on the surface. Hence the catalyst should be able to release these species to form H_2O. According to the calculation results via density functional theory (DFT) in 2009, Nørskov et al. firstly reported that bulk alloyed Pt_3Y is one of the most stable face-centered cubic (fcc) alloys, since each of two metals in the Pt-Y d-bond contributes half of nine d-electrons for Pt.[19] This indicates that the bonding states are filled, while the anti-bonding states are empty in such a system.[25,26]

---

[a] Dr. Y. Luo, Dr. A. Habrioux, Prof. N. Alonso-Vante
IC2MP, UMR-CNRS 7285, University of Poitiers
4 rue Michel Brunet, 86022 Poitiers (France)
E-mail: nicolas.alonso.vante@univ-poitiers.fr

[b] Dr. L. Calvillo, Prof. G. Granozzi
Dipartimento di Scienze Chimiche, Università di Padova
Consorzio INSTM and Unità di Ricerca INFM-CNR
35131 Padova (Italy)

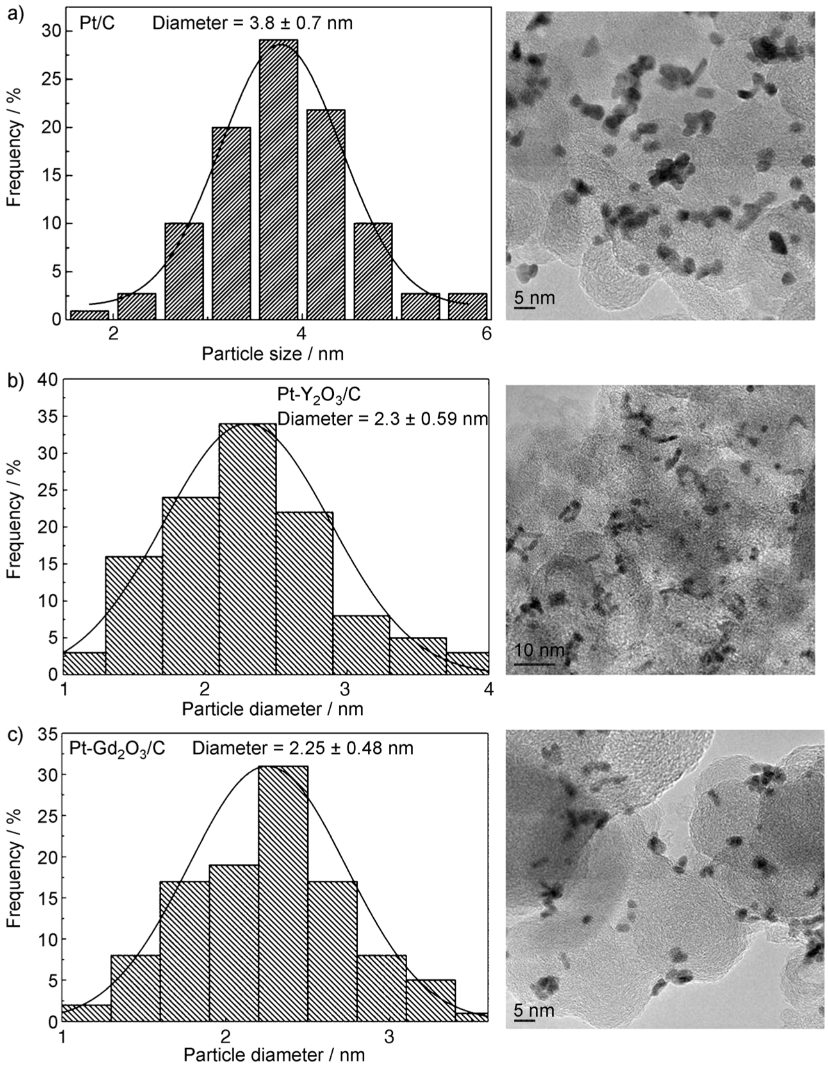

Figure 1. TEM images and histograms of the particle-size distribution deduced from the TEM images for: a) Pt/C, b) Pt-Y_2O_3/C, and c) Pt-Gd_2O_3/C catalysts.

The experimental results of the bulk alloyed platinum-rare-earth materials show an extraordinarily high ORR activity and stability among the binary metallic catalysts,[19,22,23] inspiring us to synthesize cathodic nanocatalysts containing rare-earth elements for ORR. As described in the literature,[19,22,23] the metallic alloys are prepared by physical metallurgical methods, which are high-cost and hardly to be realized in a chemical laboratory. Besides, the catalytic reaction on the surface of the metallic electrode could be easily interfered by many factors. By contrast, the bi-metallic nanoparticle might be a better candidate in case of synthesis, application and commercialization. Bimetallic NPs containing Pt and Y, prepared via co-reduction method, were reported,[20,21] but the ORR activity of these materials was low. Moreover, it is difficult to predict the product of the synthesis, since the reduction potential of rare-earth elements is around −2 V (vs. the normal hydrogen electrode, NHE). Therefore, in the present work, a chemical route to prepare the Pt-M (M = Gd, Y) nanomaterials supported onto carbon substrate is presented. Herein, we report on the synthesis, characterization and ORR activity of Pt-M (M = Gd, Y) NPs via water-in-oil chemical route. To adapt the experimental conditions of low-temperature PEMFC,[27] the as-prepared catalysts were compared to heat-treated samples at 100 °C and the ORR activity investigated. The effect of yttrium or gadolinium oxide on surface properties of platinum NPs as well as its implication on ORR kinetics is discussed.

2. Results and Discussion

2.1. Structural and Surface Characterization of Pt-M_2O_3/C (M = Gd and Y) Catalysts

The metal loading in these three catalysts was confirmed by thermogravimetric analysis (TGA), giving 21.5, 20.7, and 22 wt% for Pt/C, Pt-Y_2O_3/C, and Pt-Gd_2O_3/C, respectively. The stoichiometric composition of Pt-M_2O_3/C (M = Gd and Y) catalysts, determined by inductively coupled plasma, was, respectively, $Pt_{2.3}Y_1$/C and $Pt_{1.8}Gd_1$/C. This indicates that all the catalysts have a similar metal-loading, with a Pt:M ratio close to 2:1.

The Pt-based catalysts were firstly analyzed by transmission electron microscopy (TEM). TEM images of Pt-Y_2O_3/C, Pt-Gd_2O_3/C, and Pt/C catalysts synthesized by the water-in-oil microemulsion technique are shown in Figures 1 (a)–(c). It can be observed that this synthesis method leads to a homogeneous dispersion of the metal NPs onto the carbon matrix, although some agglomerates are formed. The mean average particle sizes are around (3.80 ± 0.70), (2.30 ± 0.59), and (2.25 ± 0.48) nm for the Pt/C, Pt-Y_2O_3, and Pt- Gd_2O_3 samples, respectively.

Figure 2 (a) shows the X-ray diffraction (XRD) corrected pattern of the different catalysts as well as the fitted profile. It is clear that all catalysts have the five typical diffraction peaks characteristic of the face-centered cubic (fcc) Pt cell: (111), (200), (220), (222) and (311) plane without the presence of a secondary phase, suggesting that the crystal structure for all catalysts is fcc Pt NPs. The fit with five pseudo-Voigt functions

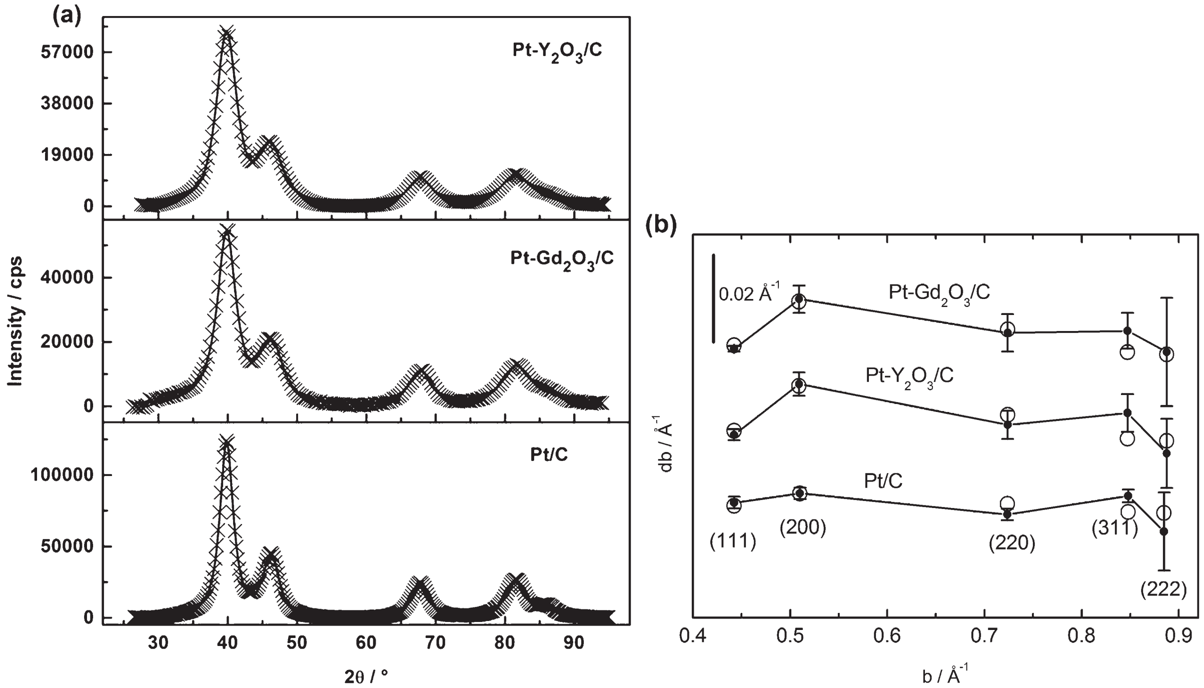

Figure 2. a) X-ray patterns of the as-prepared catalysts. Background contributions of the supporting carbon materials (Vulcan XC-72) were removed. The solid lines are profile fittings to pseudo-Voigt functions and the dots are experimental points. b) Williamson–Hall plot of the integral line width based on the fitting parameters for the first five Bragg peaks (●). The curves are offset for a better visualization. The open circles (○) relate to the simulated data. Calculated standard deviations are also given.

gives two important parameters: the peak position and the integral line width. X-ray pattern registered for Vulcan XC-72 was used to calibrate and subtract all the background contributions. From Figure 2 (a), it can be clearly seen that the presence of Y and Gd leads to an increase of the integral width of the different diffraction peaks but does not modify the peak positions respect to those for the Pt/C sample. Information concerning the microstructure of the different samples can be extracted from the fitted patterns presented in Figure 2 (a) by using line broadening analysis and Williamson-Hall plot.[28] For each diffraction peak, the integral width of the Lorentzian and Gaussian components of the pseudo-Voigt function used for the fit are first determined according to the empirical formulas given by De Keijser et al.[29] After correcting the instrumental broadening using a LaB_6 standard powder, the integral width (β_f) of the function corresponding to a diffraction peak was calculated.[30] The values of $db = \beta_f \cos(\theta)/\lambda$ were plotted against $b = 2\sin(\theta)/\lambda$, where θ is the Bragg angle and λ the wavelength in angstroms. Results are shown in Figure 2 (b). From this figure, it can be seen that the *db* parameter shows an unusual variation with increasing *b* value in particular for Pt-Y_2O_3/C and Pt-Gd_2O_3/C samples. There are large variations of the *db* value that are not expected for simple size broadening. Additionally, the isotropic stress would produce compressions or dilatations with no variations for the different lattice directions thus predicting a linear variation of *db* with *b*. However, it has been shown that stacking faults can also be responsible for an additional line broadening depending on Miller indexes. In such a case, three different contributions to the integral line width broadening (size broadening, stacking fault broadening and microstrain broadening) must be taken into account according to Equation (1)[31]:

$$db = \frac{1}{L_v} + \frac{\alpha V_{hkl}}{a} + 2\,\varepsilon b \tag{1}$$

where L_v is the mean crystalline size, V_{hkl} is a constant depending on the miller indexes *h*, *k* and *l* ($V_{111} = 0.43$; $V_{200} = 1$; $V_{220} = 0.71$; $V_{311} = 0.45$ and $V_{222} = 0.43$), a is the lattice parameter, α is the stacking fault probability, and ε is the micro strain. As a result of the best fit (open circles in Figure 2 (b)), the values of L_v, α, and ε are obtained and summarized in Table 1.

Table 1. Structural parameters of the obtained Pt/C, Pt-Y_2O_3/C, and Pt-Gd_2O_3/C catalysts, calculated from the XRD and TEM data.

Sample	$a^{[a]}$ [nm]	$L_v^{[a]}$ [nm]	$\alpha^{[a]}$ [%]	$\varepsilon^{[a]}$ [%]	$d^{[b]}$ [nm]
Pt/C	0.3915	2.82	2.2	0.19	3.80 ± 0.70
Pt-Y_2O_3/C	0.3909	2.08	7.5	0.27	2.30 ± 0.59
Pt-Gd_2O_3/C	0.3907	2.08	7.3	0.24	2.25 ± 0.48

[a] Calculated from the XRD data. [b] Calculated from the TEM data.

In addition, it seems that platinum-based NPs exhibit a contraction effect, which could be associated with surface tensions compressing the nanoclusters. The magnitude of this phenomenon is stronger as the surface-to-volume ratio increases. Such effects have already been described by Wasserman and Vermaak.[32] It seems that the lattice contraction is slightly more pronounced for Pt-Y_2O_3/C and Pt-Gd_2O_3/C nanomaterials. This could be related with the observed decrease in L_v value for Pt-Y_2O_3 and Pt-Gd_2O_3 samples. From Table 1, it can actually be stated that the size of coherently diffracting domains decreases by adding Gd or Y in the nominal composition of the material. This is fairly in agreement with TEM data. One can note that both stacking fault probabilities and internal mean strains are more important for Pt-Y_2O_3 and Pt-Gd_2O_3 materials in comparison with Pt. The presence of an anisotropic stress field related to interfacial strains with a supporting (hydr)oxide[33] may be responsible for differences observed between calculated and experimental data extracted from the (311) Bragg peak for Pt-Y_2O_3/C and Pt-Gd_2O_3/C samples.

X-ray photoelectron spectroscopy (XPS) measurements were carried out to study the chemical and electronic states of Pt and the rare-earth metals, as well as the "surface" composition of the samples. Figure 3 shows the Pt 4f, Y 3d, and Gd 4d XPS spectra for the Pt/C and Pt-oxide/C samples. The Pt 4f XPS spectra were deconvoluted with two different Pt oxidation states (Pt^0 and Pt^{2+}) to identify the predominant oxidation state of Pt (Table 2). Pt^0 is the predominant oxidation state in all the samples (around 67–69%). However, all samples present a significant amount of Pt^{2+} oxidized species, mainly (31–33%). This can be traced back to the presence of an ultrathin layer of Pt oxide in all the samples that can be attributed to air exposure. The Pt binding energies are well in tune with literature reference data.[34] The addition of the rare-earth metals to Pt did not caused any shift in the binding energy of the Pt core level, compared to those for Pt/C, indicating that the addition of Y and Gd did not significantly modified the electronic environment of Pt. There is only a minor broadening of the Pt 4f peaks (FWHM = 1.9 eV for Pt/C and 2.0 eV for the Pt-M_2O_3/C samples).

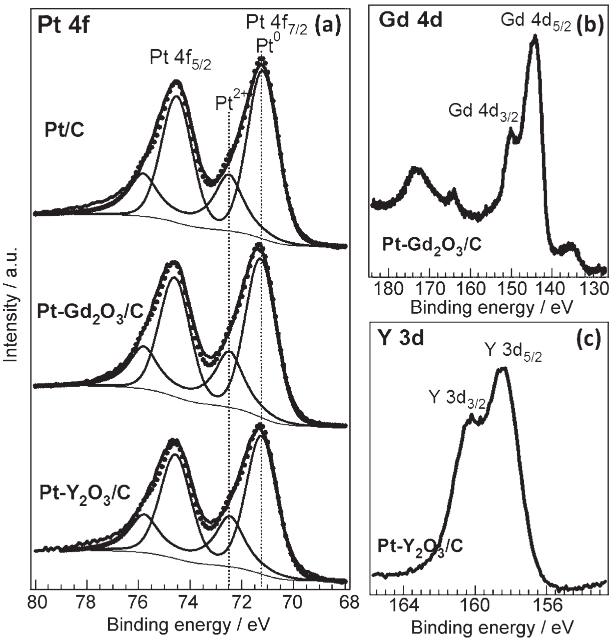

Figure 3. a) Pt 4f XPS spectra and deconvolution of the different Pt oxidation states for the Pt/C, Pt-Gd_2O_3/C, and Pt-Y_2O_3/C samples. b) Gd 4d XPS spectra for the Pt-Gd_2O_3/C sample. (c) Y 3d XPS spectra for the Pt-Y_2O_3/C sample. Measurements acquired using a $Mg_{K\alpha}$ X-ray source.

Table 2. Pt $4f_{7/2}$ binding energies [eV], oxidation state of Pt, and atomic Pt:M ratio in the Pt/C and Pt-M/C catalysts, obtained from the XPS data.

	Pt/C	Pt-Y_2O_3/C	Pt-Gd_2O_3/C
Pt^0	71.18 (69%)	71.23 (67%)	71.26 (68%)
Pt^{2+}	72.43 (31%)	72.4 (33%)	72.48 (32%)
atomic Pt:M ratio	–	39:61	50:50

In the Pt-Y_2O_3/C sample, the Y $3d_{5/2}$ peak (an unresolved doublet) is located at 158.4 eV, which can be attributed to a strongly oxidized Y_2O_3 layer,[35] whereas there is no peak attributable to metallic Y (expected at ca. 156 eV). The same result was found for the Pt-Gd_2O_3/C sample: the strong main peak at 143.7 eV in the Gd 4d XPS spectra is a signature of the presence of Gd_2O_3 and no metallic Gd was observed.[36] In this case, the XPS spectra show the common rather complex peak shape due to the multielectronic effects (shake-up peaks). The absence of peaks due to metallic Y and Gd indicates that the rare earth metals are covered by an oxide layer of at least 0.6–1 nm (taking into consideration the attenuation length of the oxides). These data, together with the fact that the Pt environment is not modified by the addition of the rare earth metal, suggests that Pt is not alloyed to Y or Gd, in good agreement with the XRD data.

According to inductively coupled plasma (ICP) results, the stoichiometric composition of the Pt-M_2O_3/C (M = Gd, Y) catalysts is, respectively, $Pt_{2.3}Y_1$ and $Pt_{1.8}Gd_1$. Comparing the Pt:M atomic ratios estimated by ICP and XPS (Table 2), it can be deduced that when probing the surface, there is an enrichment of the Gd and Y metals. These data would be incompatible with a model where independent Pt and MO_x rare-earth NPs of similar size are coexistent. Therefore, the most probable hypothesis would be compatible with the difference in the Pt:M atomic ratios deduced from XPS and XRD: hierarchically segregated binary Pt-M_2O_3 NPs (i.e. larger Pt NPs decorated with smaller MO_x ones).

2.2. Electrochemical Characterization of Pt-M_2O_3/C (M = Gd, Y) Catalysts

Before evaluating the ORR activity of Pt-M_2O_3/C (M = Gd, Y) catalysts, the working electrode (WE) surface was electrochemically cleaned by cyclic voltammograms (CVs) for 20 cycles at 50 mV s^{-1} under 25 °C in the N_2 saturated electrolyte between 0.1 and 1.2 V (vs. the reversible hydrogen electrode, RHE). The CV curves for the Pt/C and Pt-M_2O_3/C (M = Gd, Y) catalysts are shown in Figure 4. It is clear that the shape of the CV curves of the as-prepared Pt/C and Pt-M_2O_3/C (M = Gd, Y) are basically the same with well-defined peaks associated to hydrogen adsorption and desorption in the H_{upd} (underpotential deposition) region. The Pt active surface calculated from the H_{upd} surface for Pt/C, Pt-Gd_2O_3/C and Pt-Y_2O_3/C was 1.12, 1.31, and 1.24 cm^2, respectively. Three hydrogen desorption/adsorption

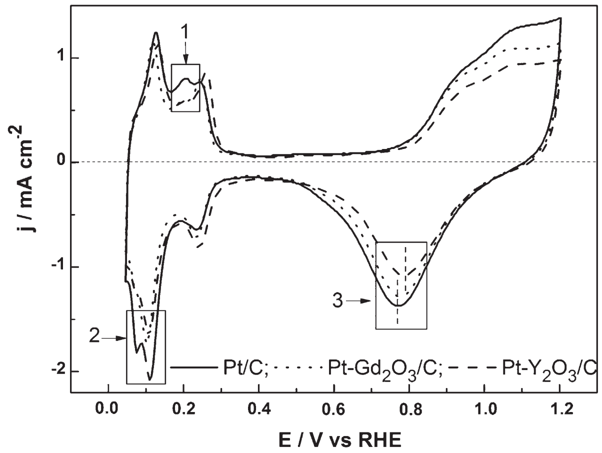

Figure 4. CVs of the Pt/C and Pt-M$_2$O$_3$/C (M = Gd, Y) catalysts at a scan rate of 50 mV s^{-1} at 25 °C in N$_2$-saturated 0.5 M H$_2$SO$_4$. The current density is normalized to the geometric surface of the electrode.

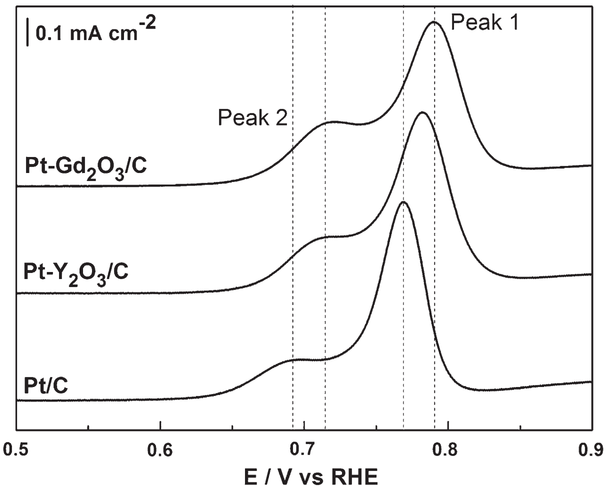

Figure 5. Voltammograms obtained for the Pt/C and Pt-M$_2$O$_3$/C (M = Gd, Y) catalysts at a scan rate of 5 mV s^{-1} in an N$_2$-saturated 0.5 M H$_2$SO$_4$ solution. The current density is normalized to the geometric surface of the electrode.

peaks located in the H$_{\mathrm{upd}}$ region can be observed for all the catalysts. However, those belonging to Pt/C are sharper as compared to the peaks for the Pt-M$_2$O$_3$/C (M = Gd, Y) samples (framework 1 and 2 in Figure 4). Additionally, it seems that the intensity of the hydrogen desorption peaks is affected by the presence of rare-earth elements. This testifies that the balance between the facets composing the surface of NPs is modified. A significant increase in the intensity of the desorption peak centered at ca. 0.255 V vs. RHE can be notably observed with Pt-Y$_2$O$_3$/C and Pt-Gd$_2$O$_3$/C catalysts. In agreement with the literature,[37] thus assessing that an increase of (100) sites is observed. Additionally, a decrease in the intensity of the hydrogen desorption peak centered at ca. 0.2 V (vs. RHE) can be observed for Pt-Y$_2$O$_3$/C and Pt-Gd$_2$O$_3$/C samples. This peak is commonly associated with the presence of defective (110) planes.[38] All the catalysts show a similar double-layer behavior. Besides, oxide reduction peak on the Pt-Y$_2$O$_3$/C can be observed at more positive potentials than those for Pt/C and Pt-Gd$_2$O$_3$/C (framework 3 in Figure 4), implying that the adsorption of OH on Pt site takes place at higher potential on the Pt-Y$_2$O$_3$/C catalyst. This might be beneficial for the O$_2$ adsorption at lower overpotential and may lead to an enhancement of ORR kinetics.[39,40]

CO was electrochemically adsorbed at 0.1 V (vs. RHE) on all samples. CO stripping was carried out and the results for Pt/C and Pt-M$_2$O$_3$/C (M = Gd, Y) are shown in Figure 5. For all catalysts, the CO oxidation displayed two peaks, denoted as peaks 1 and 2. In fact, this multi-peak CO stripping has been reported for Pt(100), Pt(111), and Pt(poly) electrodes as well as for Pt-based NPs on a carbon substrate.[41–46] Such a multiplicity of peaks can be related to dosing potential, particle size, NPs agglomeration, surface structure effects, and substrate effects.[47,48] In this case, the main reason for such a phenomenon can be related to CO oxidation on different surface Pt sites. It was reported that the formation of pre-peaks and multi-peaks in CO stripping is largely associated with the surface structure of Pt NPs.[44–46] The Pt NPs without faceting give a single CO oxidative peak. However, Pt NPs with enhanced faceting oxidize CO on different Pt sites, thus leading to multiple oxidation peaks.[37,49] According to the literature,[46] peak 1 is related to CO oxidation on (100) preferentially oriented domains whereas peak 2 is associated with the reaction on (111) sites. The addition of Y and Gd leads to changes in the intensity ratio of the two CO oxidation peaks. This implies that the balance between the facets in the NPs synthesized in this work is broken. This is fairly in agreement with conclusions drawn from voltammograms recorded in supporting electrolyte. The Pt active surface, calculated from the CO-oxidation peak area, is 1.25, 1.38 and 1.35 cm^2 for the as-prepared Pt/C, Pt-Y$_2$O$_3$/C and Pt-Gd$_2$O$_3$/C catalysts, respectively. It can also be observed that the CO-oxidation peaks for Pt-M$_2$O$_3$/C (M = Gd, Y) are slightly larger in half-wave width respect to that for Pt/C. The presence of Y or Gd leads to a slight broadening of CO oxidation peaks. This relates slight changes in adsorption energy levels of CO on Pt and can be associated with the presence of yttrium or gadolinium oxide weakly interacting with Pt sites. Additionally, the slight shift of CO oxidation peaks towards higher potentials observed with Pt-Y$_2$O$_3$/C and Pt-Gd$_2$O$_3$/C catalysts may be related to the different size of platinum NPs[50] and is in fair agreement with the TEM data.

The ORR activity of these catalysts was investigated by the rotating disk electrode (RDE) technique using rotating rates of 400, 900, 1600, and 2500 rpm at a scan rate of 5 mV s^{-1} from 1.0 to 0.2 V (vs. RHE) in the O$_2$-saturated electrolyte, as shown in Figure 6. In the Tafel plot (see inset), the ORR activity of these catalysts shows the following order: Pt-Y$_2$O$_3$/C > Pt/C > Pt-Gd$_2$O$_3$/C. This sequence corresponds to the onset potential of the oxide reduction peak observed in the CVs (see Figure 4.) For the as-prepared samples, the half-wave potentials are: 0.86, 0.84, and 0.83 V (vs. RHE) for Pt-Y$_2$O$_3$/C, Pt/C, and Pt-Gd$_2$O$_3$/C, respectively. The kinetic current (j_k) was calculated using the Koutecky–Levich (K–L) equation [Eq. (2)]:[51]

$$\frac{1}{j} = \frac{1}{j_{\mathrm{k}}} + \frac{1}{j_{\mathrm{d}}} = \frac{1}{j_{\mathrm{k}}+} + \frac{1}{BC^{\circ}\omega^{1/2}} \qquad (2)$$

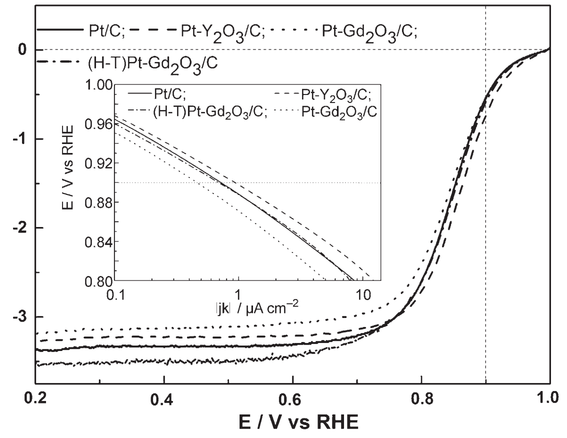

Figure 6. Linear-sweep voltammograms recorded in an O_2-saturated 0.5 M H_2SO_4 electrolyte at a rotating speed of 900 rpm at room temperature. Scan rate: 5 $mV\,s^{-1}$. Inset: Tafel plots extracted from the data of the linear sweep. The current density is normalized to the geometric surface of the electrode.

Table 3. Electrochemically active surface area (ESA), surface specific activity (SA), mass specific activity (MA) (at 0.9 V vs. RHE), and number of electrons transferred per O_2 molecule for all the catalysts.[a]

Sample	ESA $[m^2\,g^{-1}{}_{Pt}]$	SA $[\mu A\,cm^{-2}{}_{Pt}]$	MA $[mA\,mg^{-1}{}_{Pt}]$	*n*
Pt/C	35.5	41.1 ± 0.6	14.4 ± 1.2	3.91
Pt-Y_2O_3/C	48.6	54.3 ± 1.2	23.1 ± 0.5	3.85
Pt-Gd_2O_3/C	52.7	34.3 ± 3.7	13.4 ± 3.2	3.71
(H-T)[b] Pt-Gd_2O_3/C	31.4	53.0 ± 0.7	18.2 ± 0.5	3.99

[a] The Pt active surface was calculated from CO stripping measurements while the Pt mass was evaluated from the ICP data. [b] H-T: heat-treated.

where j_k and j_d refer to the kinetic and diffusion current densities. For $B = 0.62\,nFD^{2/3}\,\nu^{-1/6}$, *n* is the number of electrons, *F* is Faraday's constant, *D* is the diffusion coefficient of O_2 in 0.5 M H_2SO_4 ($1.8 \times 10^{-5}\,cm^2\,s^{-1}$), and ν is the kinematic viscosity ($0.010\,cm^2\,s^{-1}$). C^0 is the concentration of molecular oxygen ($1.13 \times 10^{-6}\,mol\,cm^{-3}$),[52] ω the RDE rotating speed. The number of electrons transferred for the as-prepared catalysts varies from 3.71 to 3.91 (cf. Table 3) for the obtained catalysts in this work. The use of as-prepared Pt-Gd_2O_3/C catalysts leads to a small number of electrons transferred per O_2 molecule (i.e. 3.71). This could be associated with a change in the adsorption mode of O_2 molecule at platinum sites leading to an increased formation of hydrogen peroxide during the reduction process.[53] This can be explained by a geometric effect of gadolinium oxide on platinum. After heat treatment of Pt-Gd_2O_3/C at 100 °C under a H_2/N_2 atmosphere, noted as (H-T) Pt-Gd_2O_3/C, one can note that the number of electrons transferred per O_2 molecule increases up to 3.99. The heat treatment is responsible for modifying the surface structure of NPs thus modifying the geometric effect.

The Tafel plots (inset in Figure 6) indicate that the reaction pathway and the rate-determining steps are similar for all the catalysts studied in this work, since there is actually no relevant variation in the Tafel slope which is about 84, 79, 82, and 85 $mV\,dec^{-1}$ for Pt/C, Pt-Y_2O_3/C, (H-T) Pt-Gd_2O_3/C, and Pt-Gd_2O_3/C, respectively. The electrochemically active surface area (ESA) determined for all the catalysts is listed in Table 3. These values are fairly in agreement with the TEM data.

The specific activities (SAs) and mass activities (MAs) of all the catalysts, determined at 0.9 V (vs. RHE) on an RDE at 900 rpm, are shown in Figure 7 (a) and Table 3. It is evident that Pt-Y_2O_3/C has the highest SA (ca. $54.3 \pm 1.2\,\mu A\,cm^{-2}{}_{Pt}$) and MA (ca. $23 \pm 0.5\,mA\,mg^{-1}{}_{Pt}$) among the as-prepared catalysts. When the SA and MA were normalized by the values of the as-prepared Pt/C catalyst, as shown in Figure 7 (b), it demonstrates that the SA and MA of ORR in case of as-synthesized Pt-Y_2O_3/C powder are respectively 1.3-, and 1.6-fold higher than the Pt/C catalyst. However, the as-prepared Pt-Gd_2O_3/C catalyst shows lower ORR catalytic activity than the as-prepared Pt/C catalyst, demonstrating both the positive and negative effect of the rare earth metal atoms. In fact, although Y and Gd atoms belong to the rare earth elements, their physi-

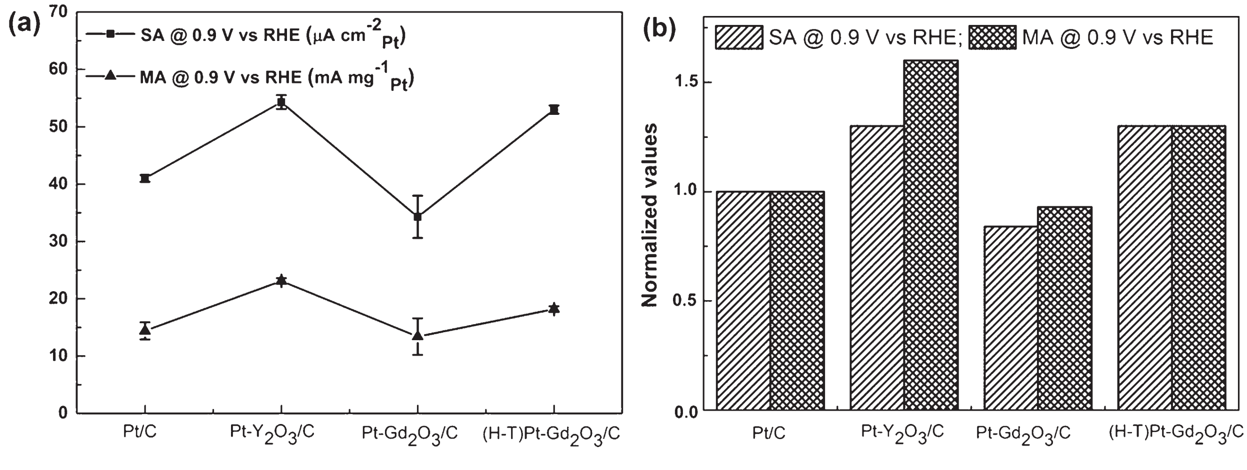

Figure 7. SA ($\mu A\,cm^{-2}{}_{Pt}$) and MA ($mA\,mg^{-1}{}_{Pt}$) (a) and normalized SA and MA (b) for all the catalysts. The results are calculated from the linear-sweep data at 900 rpm and 0.9 V (vs RHE). The real Pt surface area is calculated from the CO oxidation peak surface during CO stripping, and the Pt mass is evaluated from the ICP results.

cal-chemical properties might differ from each other. Thus, it is possible to assume that platinum atoms on Pt-Y_2O_3/C are different from those of Pt-Gd_2O_3/C, and thus leading to different catalytic behavior. To evaluate the catalytic activity at the experimental temperature (80–100 °C) of low-temperature PEMFCs,[27] the obtained catalysts were heat-treated at 100 °C under N_2/H_2 for 2 h. After such a heat treatment, the catalytic activity of the Pt/C and Pt-Y_2O_3/C catalysts remained basically unchanged. Nevertheless, as shown in Figures 7 (a),(b), the SA and MA of Pt-Gd_2O_3/C were about $52.6 \pm 0.7\ \mu A\,cm^{-2}{}_{Pt}$ and about $18.2 \pm 0.5\ mA\,mg^{-1}{}_{Pt}$, respectively, enhanced 1.3-fold with respect to the as-prepared Pt/C catalysts. Moreover, after the treatment, the half-wave potentials for Pt/C and Pt-Y_2O_3/C remained unchanged while that for Pt-Gd_2O_3/C was shifted to 0.85 V. This implies that the surface diffusion of Gd on Pt-Gd_2O_3/C sample might be temperature dependent.[54] Recently, McGinn and co-worker reported the synthesis and catalytic activity of Pt-Y_2O_3 NPs supported onto Vulcan XC-72R substrate for ORR.[20] Such a Pt-Y_2O_3/C catalyst was prepared by classical co-reduction chemical route and was applied as catalyst for ORR in the similar condition used in this work. However, the ORR catalytic activity at 0.75 V (vs. RHE) on their catalyst (ca. $ESA = 51.6\ m^2\,g^{-1}{}_{Pt}$, $SA = 411\ \mu A\,cm^{-2}{}_{Pt}$, $MA = 212\ mA\,mg^{-1}{}_{Pt}$) was lower as compared to the ORR activity obtained on our catalysts. This means that the obtained Pt-Y_2O_3/C catalysts via W/O are advantageous over those reported. It should also be noted that the Pt-M_2O_3 (M = Gd, Y) NPs as-prepared in both works are not evidently alloyed, showing that the direct chemical reduction route is not so efficient to change the oxidation state of Y^{3+} to Y^0. Besides, Nishanth et al.[21] also reported the ORR activity of carbon supported (Vulcan XC-72R) Pt-$Y(OH)_3$ NPs prepared via co-reduction route. However, the particle size, electronic structure of Pt skin, surface specific and mass activity for ORR for such a catalyst were not further reported.

According to XPS and XRD data, the formation of platinum NPs decorated with highly oxidized Y or Gd clusters is responsible for modifying the adsorption energy of OH on Pt sites. This is beneficial for O_2 adsorption at lower overpotentials, thus explaining the enhanced ORR kinetics. This change in OH adsorption energy may be related to surface structural changes affecting the platinum NPs in the presence of Gd or Y oxide.

3. Conclusions

Pt-M_2O_3 (M = Gd, Y) NPs on a carbon substrate (Vulcan XC-72) were synthesized via the water-in-oil chemical route and then investigated for use in the ORR. ICP and TGA studies revealed the stoichiometric composition and metal loading of the catalysts on the substrate. The microstructure of the Pt-M_2O_3 (M = Gd, Y) catalysts was investigated by XRD, TEM and XPS. The as-prepared Pt-Y_2O_3/C catalyst showed a high activity towards the ORR ($SA = 54.3 \pm 1.2\ \mu A\,cm^{-2}{}_{Pt}$ and $MA = 23.1 \pm 0.5\ mA\,mg^{-1}{}_{Pt}$ at 0.9 V vs. RHE), whereas the ORR activity of the Pt-Gd_2O_3/C catalyst was lower than that of the Pt/C catalyst. After heat-treatment at 100 °C under a H_2/N_2 atmosphere, the SA and MA values on the Pt-Y_2O_3/C catalyst (at 0.9 V vs. RHE) remained almost unchanged, whereas those on the Pt-Gd_2O_3/C catalyst were enhanced to $SA = 53.0 \pm 0.7\ \mu A\ cm^{-2}{}_{Pt}$ and $MA = 18.2 \pm 0.5\ mA\,mg^{-1}{}_{Pt}$ (at 0.9 V vs. RHE). Therefore, both Pt-Y_2O_3/C and Pt-Gd_2O_3/C could be promising cathode catalysts in PEMFCs. The enhancement of the ORR activity on Pt-M_2O_3/C (M = Gd, Y) can be attributed to the formation of platinum NPs decorated with highly oxidized Y or Gd clusters, which are responsible for modifying the adsorption energy of OH at the Pt sites, leading to an enhanced ORR kinetics. This modification can be related to surface structural changes of platinum NPs generated by the presence of Y or Gd oxides. Consequently, the geometric effects of Y or Gd oxide on platinum NPs, as well as their implications on the ORR kinetics, have been demonstrated in this study and may pave the way towards novel substrate design.

Experimental Section

Synthesis of Pt/C and Pt-M_2O_3/C (M = Gd, Y) Catalysts by the Water-in-Oil Route

NPs were synthesized by realizing two water-in-oil microemulsions. The two microemulsions contained 5.60 mL of $Brij_{30}$ (provided by Sigma–Aldrich) as emulsifier, 1 mL ultrapure water (Milli-Q, Millipore), and 27.35 mL n-heptan (by Sigma–Aldrich) as the oil phase. In the aqueous phase of the first microemulsion, reliable amounts of yttrium trichloride (99.9 %, ACS reagent), gadolinium trichloride (99.9 %, ACS reagent) and sodium hexa-chloroplatinate (99.9 %, ACS reagent), purchased from Alfa Aesar, were dissolved. For the synthesis of the Pt-Y_2O_3 material, 9.8 mg of YCl_3 and 84.3 mg of Na_2PtCl_6 were used. For the synthesis of the Pt-Gd_2O_3 nanomaterials, 15.8 mg of $GdCl_3$ and 78.7 mg of Na_2PtCl_6 were used. 114 mg of reducing agent ($NaBH_4$, 99 % by Acros Organics) were dissolved in the aqueous phase of the second micro-emulsion. The mixture of the two micro-emulsions led to the formation of NPs. Finally, Vulcan XC-72 (Cabot), preliminary heat-treated at 400 °C under a nitrogen atmosphere for 2 h, was added to the solution and dispersed under magnetic stirring for 2 h. The final mass metal loading of the catalysts was 20 wt %. The supported catalysts were separated, washed several times with acetone and ultrapure water to eliminate excess of surfactant molecules, and finally dried overnight in an oven at 60 °C. The heat-treated samples were obtained under H_2/N_2 (5 % H_2 in N_2, Air Liquide) at 100 °C for 2 h.

Physical Characterization of the Pt/C and Pt-M_2O_3/C (M = Gd, Y) Catalysts

XRD measurements of the catalyst powders were carried out on an EMPYREAN PANALYTICAL X-ray diffractometer using $Cu_{K\alpha}$ radiation ($\lambda = 0.15406$ nm). The XRD spectra were obtained at high resolution using the step-scanning mode, a narrow receiving slit (1/16°), and a counting time of 240 s per 0.05°. Scans were recorded in the range of 20°–95°. The phase was identified by referring to the Joint Committee on Powder Diffraction Standards International Center for Diffraction Data (JCPDS-ICDD) database. Diffraction peaks were simulated using the Fytik free software. Simulations were performed according to a previously reported procedure.[31]

The nanoparticle size of the Pt/C and Pt-M_2O_3/C (M = Gd, Y) catalysts was evaluated by TEM on a JEOL microscope (JEM-2001). The samples were dispersed in ethanol, then a drop of such a solution was placed on a copper grid covered by carbon film and the ethanol was evaporated. For all the catalysts, the diameter of particle in

TEM images was evaluated by the ImageJ software. Particle-size-distribution histograms were done by counting 300 particles in different TEM images.

The composition of the samples was evaluated by ICP and energy-dispersive X-ray (EDX), equipped within the TEM microscope. The metal loading for all the samples was investigated by TGA from 25 to 800 °C under air. The resist sample was maintained at 200 °C for 2 h to reduce the Pt and M (M = Y, Gd) oxides.

Photoemission data were acquired in a custom-designed ultrahigh vacuum (UHV) system equipped with a VG MK II Escalab electron analyzer, working at a base pressure of 10^{-10} mbar. Core-level photoemission spectra (Pt 4f, Y 3d and Ga 4d, pass energy 20 eV) were taken at room temperature in normal emission using a non monochromatized Mg anode. Powder samples were suspended in ethanol and drop-casted on a conductive carbon tape. After drying in air, the samples were introduced in the UHV system, outgassed for 1 h, and finally analyzed. There was no evidence for charging. Spectrometer energy calibration was carried out using a gold sample (Au 4f at 84 eV).

The stoichiometric composition of all the obtained catalysts was analyzed on an ICP-OES (Optima 2000 DV, PerkinElmer). The metal loadings of all the obtained catalysts were analyzed on a TGA instrument (SDT Q600, TA Instruments). The sample was heat-treated from 25 to 800 °C under air (Air Liquide) with a temperature increasing rate of 5 °C min^{-1} and maintained at 800 °C under N_2 (99.99 %, Air Liquide) for 1 h.

Electrode Preparation and Electrochemical Measurements

All the chemicals used in this work were of analytical grade (Alfa Aesar). The glassy carbon (GC) electrode (3 mm diameter) used as the working electrode (WE) was previously polished using alumina mixed with ultrapure water (MilliQ, Millipore). 10 mg catalyst was added into 0.25 mL of a Nafion solution (5 wt %, Aldrich) and 1.25 mL ultrapure water to obtain the ink. 3 μL ink was deposited onto the WE surface, which was dried under Ar (99.99 %, Air Liquide). The reproducibility of this method has been reported previously.[55,56] About 52 μg cm^{-2} of metal was loaded onto the WE surface. Electrochemical measurements were recorded on an Autolab Potentiostat/Galvanostat and performed in a standard three-electrode electrochemical cell. The RDE technique was applied to study the ORR activity. The counter electrode (CE) and reference electrode (RE) were, respectively, a GC plate and an RHE. A 0.5 м H_2SO_4 solution was used as the electrolyte. The WE surface was firstly electro-cleaned by cycling at 50 mV s^{-1} between 0.05 and 1.2 V (vs. RHE) until stable cyclic voltammograms (CVs) were obtained. The real Pt surface area was determined via CO stripping by absorbing CO (99.9 %, Air Liquide) at 0.1 V (vs. RHE) in a CO-saturated electrolyte for 10 min. Then, CVs at a scan rate of 5 mV s^{-1} were performed in an N_2-saturated medium (99.9 %, Air Liquide), from 0.05 to 1.2 V (vs. RHE). The ORR activity was measured by linear sweeps at 5 mV s^{-1} from 1.0 to 0.1 V (vs. RHE) in an O_2-saturated (99.9 %, Air Liquide) electrolyte.

Acknowledgements

This work was partially supported by the European Union's Seventh Framework Programme (FP7/2007–2013) for the Fuel Cell and Hydrogen Joint Technology Initiative under grant agreement nr. 303492 CathCat.

Keywords: cathode materials · oxygen reduction reaction · Pt-based nanoparticles · rare earths · water-in-oil synthesis

[1] H. A. Gasteiger, S. S. Kocha, B. Sompalli, F. T. Wagner, *Appl. Catal. B* **2005**, *56*, 9–35.
[2] C. K. Dyer, *J. Power Sources* **2002**, *106*, 31–34.
[3] J. Zhang, *PEM Fuel Cell Electrocatalysts and Catalyst Layer: Fundamentals and Applications*, Springer, London, **2008**.
[4] N. Alonso-Vante, *ChemPhysChem* **2010**, *11*, 2732–2744.
[5] C. W. B. Bezerra, L. Zhang, K. Lee, H. Liu, A. L. B. Marques, E. P. Marques, H. Wang, J. Zhang, *Electrochim. Acta* **2008**, *53*, 4937–4951.
[6] M. K. Debe, *Nature* **2012**, *486*, 43–51.
[7] W. Yu, M. D. Porosoff, J. G. Chen, *Chem. Rev.* **2012**, *112*, 5780–5817.
[8] J. Snyder, I. McCue, K. Livi, J. Erlebacher, *J. Am. Chem. Soc.* **2012**, *134*, 8633–8645.
[9] E. Favry, D. Wang, D. Fantauzzi, J. Anton, D. S. Su, T. Jacob, N. Alonso-Vante, *Phys. Chem. Chem. Phys.* **2011**, *13*, 9201–9208.
[10] J. Ma, A. Habrioux, T. Miyao, K. Kakinuma, J. Inukai, M. Watanabe, N. Alonso-Vante, *J. Mater. Chem. A* **2013**, *1*, 8798–8804.
[11] T. He, E. Kreidler, L. Xiong, E. Ding, *J. Power Sources* **2007**, *165*, 87–91.
[12] H. Ye, R. M. Crooks, *J. Am. Chem. Soc.* **2007**, *129*, 3627–3633.
[13] Y.-Y. Feng, J.-H. Ma, G.-R. Zhang, G. Liu, B.-Q. Xu, *Electrochem. Commun.* **2010**, *12*, 1191–1194.
[14] D. D. A. Habrioux, J. Rousseau, T. W. Napporn, K. Servat, L. Guétaz, A. Trokourey, K. B. Kokoh, *Electrocatalysis* **2010**, 1.
[15] V. Di Noto, E. Negro, *J. Power Sources* **2010**, *195*, 638–648.
[16] B.-J. Su, K.-W. Wang, T.-C. Cheng, C.-J. Tseng, *Mater. Chem. Phys.* **2012**, *135*, 395–400.
[17] J. Kim, Y. Lee, S. Sun, *J. Am. Chem. Soc.* **2010**, *132*, 4996–4997.
[18] H. Yang, W. Vogel, C. Lamy, N. Alonso-Vante, *J. Phys. Chem. B* **2004**, *108*, 11024–11034.
[19] J. Greeley, I. E. L. Stephens, A. S. Bondarenko, T. P. Johansson, H. A. Hansen, T. F. Jaramillo, J. Rossmeisl, I. Chorkendorff, J. K. Nørskov, *Nat. Chem.* **2009**, *1*, 552–556.
[20] M. K. Jeon, P. J. McGinn, *J. Power Sources* **2011**, *196*, 1127–1131.
[21] K. G. Nishanth, P. Sridhar, S. Pitchumani, *Electrochem. Commun.* **2011**, *13*, 1465–1468.
[22] S. J. Yoo, K.-S. Lee, S. J. Hwang, Y.-H. Cho, S.-K. Kim, J. W. Yun, Y.-E. Sung, T.-H. Lim, *Int. J. Hydrogen Energy* **2012**, *37*, 9758–9765.
[23] M. Escudero-Escribano, A. Verdaguer-Casadevall, P. Malacrida, U. Grønbjerg, B. P. Knudsen, A. K. Jepsen, J. Rossmeisl, I. E. L. Stephens, I. Chorkendorff, *J. Am. Chem. Soc.* **2012**, *134*, 16476–16479.
[24] J. K. Nørskov, J. Rossmeisl, A. Logadottir, L. Lindqvist, J. R. Kitchin, T. Bligaard, H. Jónsson, *J. Phys. Chem. B* **2004**, *108*, 17886–17892.
[25] G. H. Jóhannesson, T. Bligaard, A. V. Ruban, H. L. Skriver, K. W. Jacobsen, J. K. Nørskov, *Phys. Rev. Lett.* **2002**, *88*, 255506.
[26] A. V. Ruban, H. L. Skriver, J. K. Nørskov, *Phys. Rev. Lett.* **1998**, *80*, 1240–1243.
[27] Y. Shao, G. Yin, Z. Wang, Y. Gao, *J. Power Sources* **2007**, *167*, 235–242.
[28] G. K. Williamson, W. H. Hall, *Acta Metall.* **1953**, *1*, 22–31.
[29] T. de Keijser, E. J. Mittemeijer, H. C. F. Rozendaal, *J. Appl. Crystallogr.* **1983**, *16*, 309–316.
[30] T. H. de Keijser, J. I. Langford, E. J. Mittemeijer, A. B. P. Vogels, *J. Appl. Crystallogr.* **1982**, *15*, 308–314.
[31] A. Habrioux, W. Vogel, M. Guinel, L. Guetaz, K. Servat, B. Kokoh, N. Alonso-Vante, *Phys. Chem. Chem. Phys.* **2009**, *11*, 3573–3579.
[32] H. J. Wasserman, J. S. Vermaak, *Surf. Sci.* **1972**, *32*, 168–174.
[33] L. Timperman, A. Lewera, W. Vogel, N. Alonso-Vante, *Electrochem. Commun.* **2010**, *12*, 1772–1775.
[34] A. V. Naumkin, S. W. Gaarebstroom, C. J. Powell, *NIST Photoelectron Spectroscopy Database: NIST Standard Reference Database 20, Version 4.1*, U. S. Secretary of Commerce on behalf of the United States of America, **2012**.
[35] R. Reichl, K. H. Gaukler, *Appl. Surf. Sci.* **1986**, *26*, 196–210.
[36] D. D. Sarma, C. N. R. Rao, *J. Electron Spectrosc. Relat. Phenom.* **1980**, *20*, 25–45.
[37] J. Solla-Gullón, F. J. Vidal-Iglesias, E. Herrero, J. M. Feliu, A. Aldaz, *Electrochem. Commun.* **2006**, *8*, 189–194.

[38] G. A. Attard, J. E. Gillies, C. A. Harris, D. J. Jenkins, P. Johnston, M. A. Price, D. J. Watson, P. B. Wells, *Appl. Catal. A* **2001**, *222*, 393 – 405.

[39] S. S. S. Mukerjee, M. P. Soriaga, J. McBreen, *J. Electrochem. Soc.* **1995**, *142*, 14.

[40] C. W. Hills, M. S. Nashner, A. I. Frenkel, J. R. Shapley, R. G. Nuzzo, *Langmuir* **1999**, *15*, 690 – 700.

[41] A. López-Cudero, Á. Cuesta, C. Gutiérrez, *J. Electroanal. Chem.* **2006**, *586*, 204 – 216.

[42] A. López-Cudero, A. Cuesta, C. Gutiérrez, *J. Electroanal. Chem.* **2005**, *579*, 1 – 12.

[43] A. Cuesta, A. Couto, A. Rincón, M. C. Pérez, A. López-Cudero, C. Gutiérrez, *J. Electroanal. Chem.* **2006**, *586*, 184 – 195.

[44] J. Ma, A. Habrioux, N. Guignard, N. Alonso-Vante, *J. Phys. Chem. C* **2012**, *116*, 21788 – 21794.

[45] J. Ma, A. Habrioux, M. Pisarek, A. Lewera, N. Alonso-Vante, *Electrochem. Commun.* **2013**, *29*, 12 – 16.

[46] P. Urchaga, S. Baranton, C. Coutanceau, G. Jerkiewicz, *Langmuir* **2012**, *28*, 3658 – 3663.

[47] N. M. Marković, P. N. Ross, Jr., *Surf. Sci. Rep.* **2002**, *45*, 117 – 229.

[48] M. T. M. Koper, *Fuel Cell Catalysis: A Surface Science Approach*, Wiley, Hoboken, **2009**.

[49] N. P. Lebedeva, M. T. M. Koper, J. M. Feliu, R. A. van Santen, *J. Phys. Chem. B* **2002**, *106*, 12938 – 12947.

[50] F. Maillard, M. Eikerling, O. V. Cherstiouk, S. Schreier, E. Savinova, U. Stimming, *Faraday Discuss.* **2004**, *125*, 357 – 377.

[51] L. R. F. A. J. Bard, *Electrochemical Methods: Fundamentals and Applications*, Wiley, New York, **2001**.

[52] B. Y. J. Jiang, *J. Electroanal. Chem.* **2005**, *577*, 9.

[53] M. R. Tarasevich, A. Sadkowski, E. Yeager in *Oxygen Electrochemistry* (Eds.: B. Conway, J. M. Bockris, E. Yeager, S. M. Khan, R. White), Springer, New York, London, **1983**, pp. 301 – 398.

[54] V. G. L. K. Oura, A. Saranin, A. V. Zotov, M. Katayama, *Surface Science: An Introduction*, Springer, New York, **2003**.

[55] F. Maillard, M. Martin, F. Gloaguen, J. M. Léger, *Electrochim. Acta* **2002**, *47*, 3431 – 3440.

[56] H. Yang, N. Alonso-Vante, J.-M. Léger, C. Lamy, *J. Phys. Chem. B* **2004**, *108*, 1938 – 1947.

Received: January 17, 2014
Revised: March 10, 2014

Electrochimica Acta 173 (2015) 771–778

Contents lists available at ScienceDirect

Electrochimica Acta

journal homepage: www.elsevier.com/locate/electacta

Nanostructured palladium tailored *via* carbonyl chemical route towards oxygen reduction reaction

Y. Luo [a], J.M. Mora-Hernández [a,b], L.A. Estudillo-Wong [a], E.M. Arce-Estrada [b], N. Alonso-Vante [a,*]

[a] IC2MP, UMR-CNRS 7285, Université de Poitiers, 4 rue Michel Brunet, 86022 Poitiers, France
[b] IPN-ESIQIE-DIMM, Unidad Profesional Adolfo López Mateos 07738, México D.F, Mexico

ARTICLE INFO

Article history:
Received 17 April 2015
Received in revised form 18 May 2015
Accepted 23 May 2015
Available online 27 May 2015

Keywords:
ORR
Palladium
Morphology
Carbonyl chemical route
Nanostructures

ABSTRACT

Carbon supported palladium nanostructures were synthesized via the carbonyl chemical route. Compared with nanostructured platinum, prepared via carbonyl chemical route, Pd nanomaterials showed mass-loading morphology, whereas particle size and morphology of Pt nanostructures was constant. The oxygen reduction reaction (ORR) on nanostructured Pd, with different morphology in both acid and alkaline medium was investigated. A relationship, based on X-ray diffraction structural analysis pattern, transmission electron microscope, with the Pd morphological effect on ORR activity was identified.

1. Introduction

Among platinum group metals, palladium-based cathode catalysts for low-temperature fuel cell received lots of attention because of their catalytic performance towards the oxygen reduction reaction (ORR) [1–4]. However, the development of Pd-based catalysts is a great challenge, since the control of morphology for such nano-materials is still under investigation. The Pd-based nanomaterials prepared *via* a direct reduction of Pd salts usually produces agglomerations [5]. Strong binding surfactants, e.g. the trialkyphosphines, 1-alkanethiols, have been used to prevent agglomeration of nanostructured Pd NPs [6–9]. On one hand, the nanostructured Pd morphology can be tailored by using organic surfactants; on the other hand, these surfactants, strongly bonded to Pd NPs surface, are difficult to be removed, thus preventing the contact between the active catalytic sites with the species, hence reducing the catalytic activity. Therefore, many works focused on the synthesis of "clean" surface of Pd nanomaterials *via* various chemical routes [10–12]. In addition, it is well known that the morphology significantly impact the catalytic activity of Pd catalysts [13,14]. Abruña et al. reported, an enhanced ORR activity on Pd nanorods (NRs) with respect to NPs, prepared *via* the same procedure [14], indicating that ORR activity of Pd nanomaterials should be highly dependent on the morphology.

Herein, we report the synthesis of Pd nanomaterials via carbonyl chemical route. This latter was selected based on the following reasons. Previous works demonstrated that this method is powerful to control the size (ca. 2–5 nm) and morphology of Pt-based NPs without surface faceting (spherical NPs) [15,16]. The particle size and morphology are controlled via the formation of clusters di-anions $[Pt_3(CO)_6]_n^{2-}$ under CO atmosphere, which then decompose and release Pt NPs [15,16]. Likely, this carbonyl chemical route should also allow for the formation and decomposition of $[Pd_x(CO)_y]_n^{2-}$ clusters [17]. Methanol is used as solvent during the synthesis via the carbonyl chemical route. Pd NPs surface is free of surfactants and thus "clean". To best of our knowledge, no work done on the use of carbonyl route to tailor Pd-based nanomaterials supported on carbon substrate has been reported. Therefore, in order to develop a reliable synthetic method, a systematic study on the comparison of nanostructured Pt and Pd, tailored via carbonyl chemical route was necessary. As reported in this work, different Pd morphologies derived from the same synthetic procedure of carbonyl chemical route led us to study its effect on the ORR activity in acid (0.1 M $HClO_4$), and alkaline (0.1 M KOH) media, compared with the performance of a reference commercial Pd catalyst.

---

* Corresponding author. Tel.: +33 5 4945 3625; fax: +33 5 4945 3580.
E-mail address: Nicolas.Alonso.Vante@univ-poitiers.fr (N. Alonso-Vante).

http://dx.doi.org/10.1016/j.electacta.2015.05.140

2. Experimental

2.1. Synthesis of Pd nanomaterials via carbonyl chemical route

The nanosized Pd/C catalysts were prepared via a Pd-carbonyl chemical route. Briefly, K_2PdCl_6 (Alfa-Aesar, 99.9%) and the sodium acetate (Alfa-Aesar, 99.9%) were used as precursors. These precursors were dissolved in methanol (VMR, 99.9%), reacting with CO (99.99%, Air Liquide) in ice bath (ice-water mixture, ca. 2 °C) for 2 h. Thereafter, carbon substrate was added into the solution at room temperature under N_2 (99.99%, Air Liquide). 153.6 mg K_2PdCl_6 with 231.6 mg sodium acetate were dissolved in 25 mL CH_3OH in 50 mL two-neck flask, and flushed with N_2 for 20 min. Then, the system, in ice bath, was exchanged to CO atmosphere for 2 h under continuous stirring. The colour of the solution turned instantaneously from orange to black-brown during the reaction. The ice bath was removed, and for each synthesis 450, 200, 117 or 75 mg carbon (Vulcan XC-72) was added under N_2 atmosphere. The system was under N_2 for 12 h under continuous stirring at room temperature. The solvent was evaporated at 80 °C. The black powder was filtrated and rinsed by ultra-pure water (Milli-Q, Milipore) at least three times. Finally, the powder was dried at 60 °C under air overnight. The generated carbon (Vulcan XC-72) supported Pd with metal mass-loadings of *ca.* 11.5, 14.7, 27.1 and 38.5 wt% (*cf.* Table 2), are noted respectively as Pd/C-1, Pd/C-2, Pd/C-3 and Pd/C-4.

2.2. Physical characterizations

The Pd mass-loading of catalysts were determined by thermogravimetric analysis (TGA). The sample was heat-treated under air flux (Air Liquide) at a heating rate of 5 °C per minute, from 25 to 850 °C and kept at 850 °C for 30 min. The morphology of the nanomaterials was investigated by transmission electron microscopy (TEM) on a JEOL (JEM-2001) microscope. The particle size was estimated on 100 isolated particles using the free software "ImageJ". The powder X-ray diffraction (*p*XRD) was performed on an Empyrean Panalytical X-ray diffractometer using Cu-Kα radiation (λ = 0.15406 nm). The *p*XRD patterns were obtained, using high resolution, with step-scanning mode, slit at 1/16°, and counting time of 240 s/0.05° in the range of 20–95°. Using the Joint Committee on Powder Diffraction Standard International Centre for Diffraction Data (JCPD-ICDD), the structural phase in *p*XRD pattern was identified. Prior to analysis of *p*XRD patterns of Pd/C catalysts, XRD patterns for XC-72 was used to calibrate the background contribution of the supporting materials. The instrumental broadening was corrected by the standard pattern of LaB_6. The lattice parameter, a, of catalysts was estimated using Eqs. (1), and (2).

$$d_{hkl} = \frac{\lambda}{2\sin\theta} \tag{1}$$

Table 1
Mean particle size (d/nm) and morphology (Morph.) estimated from TEM images; crystallite size (D_v / nm) calculated via Scherrer's law based on pXRD patterns; dispersion for Pt/C catalysts prepared via carbonyl route with 10–40 wt % Pt mass loading. Data extracted from Ref. [21].

	Pt/C (10 wt.%)	Pt/C (20 wt.%)	Pt/C (30 wt.%)	Pt/C (40 wt.%)
d	2.0 ± 0.9	2.0 ± 1.0	2.0 ± 0.6	1.9 ± 0.7
D_v	3.9	2.5	3.3	3.3
Morph.	Spherical NPs	Spherical NPs	Spherical NPs	Spherical NPs

$$d_{hkl} = \frac{a}{\sqrt{h^2 + k^2 + l^2}} \tag{2}$$

Where λ = 0.154056 nm, θ diffraction angle in radians, hkl Miller indices, and d_{hkl} the interplanar distance.

In this work, a, was the average value of calculations of 5 typical diffraction peaks belonging to Pd and Pt face centred cubic (fcc). Strain effect (ε), stacking fault (α) and crystallite size (L_v) for Pd-based catalyst were estimated based on Williamson-Hall method, following the same calculation procedure *via* Eq. (3) in our previous works [18,19].

$$\frac{\beta\cos\theta}{\lambda} = \frac{k}{L_v} + \frac{K_{hkl}}{a}\alpha + \frac{4\sin\theta}{\lambda}\varepsilon \tag{3}$$

Where β is the full width at half-maximum (FWHM) of diffraction peak, λ = 0.154056 nm, θ diffraction angle in radians, *k* is the Scherrer Constant considering equal to 1, K(111) = 0.43, K(200) = 1, K(220) = 0.71, K(311) = 0.45 and K(222) = 0.43. Therefore, each diffraction peak was fitted with a Pearson VII function in order to obtain the diffraction peaks θ_p and β, equations (4)–(6).

$$I_C = \frac{I_p}{(1 + \kappa * \Delta 2\theta^2)^m} \tag{4}$$

$$\Delta 2\theta = 2\theta_i - 2\theta_p \tag{5}$$

$$\kappa = \frac{4(2^{\frac{1}{m}} - 1)}{\beta^2} \tag{6}$$

Where I_C is the calculated profile intensity of a data point *i* in equation (5),I_p is the peak height, $2\theta_p$is the peak position, and *m* is the exponential parameter in the function. The κ, θ_p, β and m were extracted by Leverberg-Marquardt algorithm implemented in Fityk (free software). The crystallite size (D_v) of all Pt-based catalysts was calculated *via* Scherrer's law (ignoring other effects, e.g., strains and stacking faults).

2.3. Electrochemical measurements

The catalysts were evaluated in 0.1 M $HClO_4$ and 0.1 M KOH solution at 25 °C. A standard three-electrode system was used for recording the electrochemical behaviour. The reference electrode was a reversible hydrogen electrode (RHE), and the counter electrode a piece of glassy carbon. The rotating disk electrode (RDE) with glassy carbon disk (3 mm dia.) was used as working electrode. The ink was prepared by mixing 5 mg catalysts, 40 μL Nafion (5 wt%) and 710 μL ultra-pure water (Milli-Q, Millipore), and ultrasonicated for 2 h. 3 μL ink was dropped at the surface of RDE. The cyclic voltammograms (CVs) were recorded at scan rate of 50 mV s^{-1} in N_2-saturated electrolyte, from 0.05 to 1.2 V vs. RHE. A stable CV cycle was recorded (20th cycle). For CO-stripping, the CO was electrochemically adsorbed on the electrode surface at 0.1 V *vs.* RHE for 10 min in the CO-saturated electrolyte, followed by 2 cycles of CV at 5 mV s^{-1} in N_2-saturated electrolyte. The polarization curve of oxygen reduction reaction was recorded *via* linear sweep voltammograms (LSVs) at a scan rate of 5 mV s^{-1} in O_2-saturated electrolyte, from 1.0 to 0.2 V *vs.* RHE, on RDE with rotating speed of 400, 900, 1600 and 2500 rpm (cf. Fig. S1 in supplementary content). The kinetic current was calculated with the Koutecky-Levich (K-L) Eq. (7) [20]:

$$\frac{1}{j}=\frac{1}{j_k}+\frac{1}{j_d}=\frac{1}{j_k}+\frac{1}{BC^0\omega^{1/2}} \quad (7)$$

Where j is the current density, j_k the kinetic current density, j_d the diffusion current density, C^0 the concentration of molecular oxygen, ω the angular rate of rotating disk electrode. A linear fitting of j^{-1} *vs.* $\omega^{-1/2}$ Eq. (7), j_d can be thus obtained from the slope and $\omega^{1/2}$. And j_k could be derived, using Eq. (5). n, the number of electrons, was calculated from the slope, given $B = 0.62nFD^{2/3}\nu^{-1/6}$, where F Faraday's constant, D the diffusion coefficient of O_2 and ν the kinematic viscosity. The active surface area (cm^2) was calculated by the coulometry of the hydrogen under potential deposition (H_{upd}) in 0.1 M $HClO_4$ and by the CO oxidation peak surface in 0.1 M KOH, using a charge of 210 and 420 $\mu C\,cm^{-2}$, respectively. The electrochemical surface area (ECSA), ORR specific activity (SA), and mass activity (MA) were defined in Eqs. (8)–(10).

$$\text{ECSA}=\frac{\text{Active surface}}{\text{Pd mass}} \quad (8)$$

$$\text{SA}=\frac{\text{Kinetic current}}{\text{Active surface}} \quad (9)$$

$$\text{MA}=\frac{\text{Kinetic current}}{\text{Pd mass}} \quad (10)$$

3. Results and discussion

The modified carbonyl chemical route for Pd/C-1, Pd/C-2, Pd/C-3 and Pd/C-4 with a corresponding Pd-mass-loadings (11.5, 14.7, 27.1 and 38.5 wt.%) *cf.* Table 2, is shown in Scheme 1. The heating bath (used for the synthesis of Pt-based catalysts) is replaced by a cooling bath to gently form the nanostructured Pd from $[Pd_x(CO)_y]_n^{2-}$ clusters. Using the carbonyl chemical route, previous works in our group showed that spherical morphology and similar particle size of Platinum were present on carbon (Vulcan XC-72) supports with a metal mass loading varying from 10 to 40 wt.%, Fig. 1A and Table 1 [16,21]. One can observe spherical platinum particles homogeneously dispersed onto carbon substrate with a similar particle size (d) by TEM. However, the crystallite size (D_v), varies from *ca.* 2.5 to 3.9 nm, hence slightly higher than d values. This might be due to some agglomeration of Pt NPs. It can be concluded that Pt NPs supported on carbon substrate, possess similar size and morphology with the loading from 10 to 40 wt.%.

TEM images for Pd/C-1, Pd/C-2, Pd/C-3 and Pd/C-4 samples are depicted in Fig. 1B-E. Unlike Pt-based nanomaterials, Pd samples show various morphologies, depending on the metal mass-loading. NPs in Pd/C-1 are highly agglomerated on carbon substrate (*cf.* Fig. 1B), and many particles with a diameter higher than 10 nm can be found (Fig. 1B). The mean particle size (d), based on 50 isolated particles from TEM images, is *ca.* 18 ± 6 nm. For Pd/C-2, large amount of Pd NWs can be observed, see Fig. 1C, forming a layer-like structure and well-dispersed on carbon substrate. Few agglomerated NPs can be also found in the sample (not shown here). The diameter of NWs is about *ca.* 13 ± 4 nm, and length varies from *ca.* 18 to 50 nm, based on the analysis of 30 isolated NWs. Pd NRs with length of *ca.* 6–8 nm and diameter of 2.8 ± 0.7 nm, seen in Fig. 1D, are dispersed on the supporting material in Pd/C-3 sample, mixed with small amount of Pd NPs (d = 2.6 ± 0.5 nm). In Pd/C-4, the NPs are almost all agglomerated (Fig. 1E), forming a network-like and porous structure (Fig. 1E) on carbon substrate. Compared with Pt-based catalysts, the morphology of nanostructured Pd *via* carbonyl route varies depending on the metal mass loading.

In order to obtain the detailed morphological information for Pd/C catalysts, further analyses on particle diameter (d) and length (L) are represented in Fig. 2. For Pd/C-1, although a large amount of NPs are agglomerated, the analysis based on isolated NPs showed that d/L is nearly 1 (1.0 ± 0.4), indicating spherical NPs. Analysing isolated NWs in Pd/C-2, the d/L ratio decreases to 0.5 ± 0.2 supporting the formation of NWs. It should be noted that, the length of isolated NWs is shorter with respect to those in the layer-like structure. One can observe from TEM images (Fig. 1C) that some NWs in the layer grow to more than 50 nm. As linked to each other, it is impossible to estimate the exact dimensions of NWs in the layer-like structure. Concerning Pd/C-3, this value is 0.6 ± 0.1, corresponding to the dimensions of NRs discussed before. For Pd/C-4, it is very difficult to calculate particle dimensions, since all NPs are agglomerated.

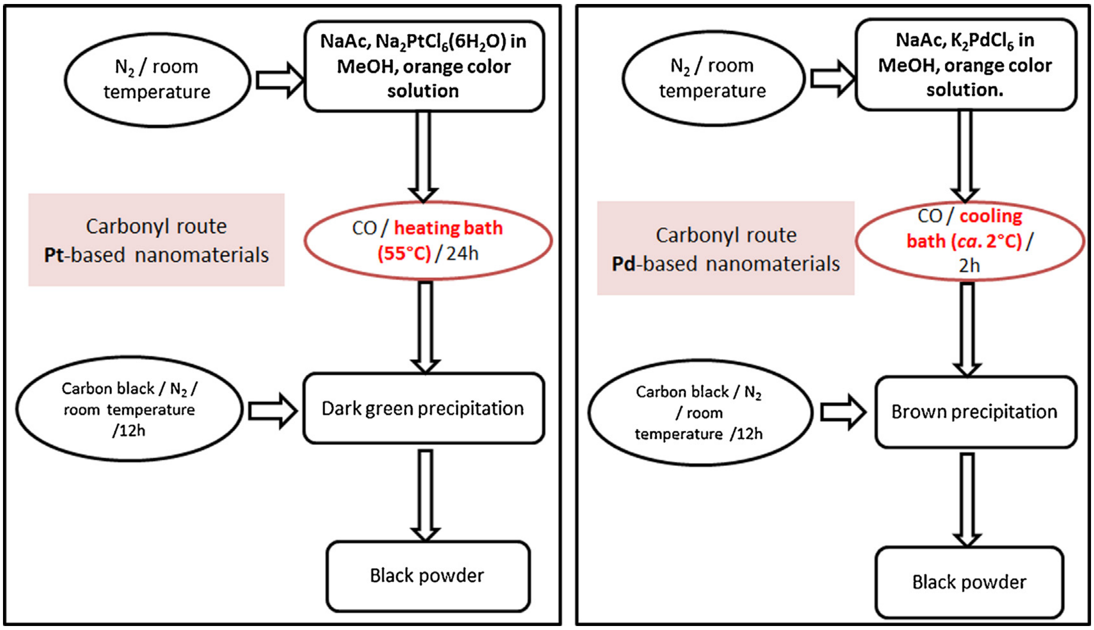

Scheme 1. Comparison of synthesis for Pt- and Pd-based nanomaterials *via* carbonyl route.

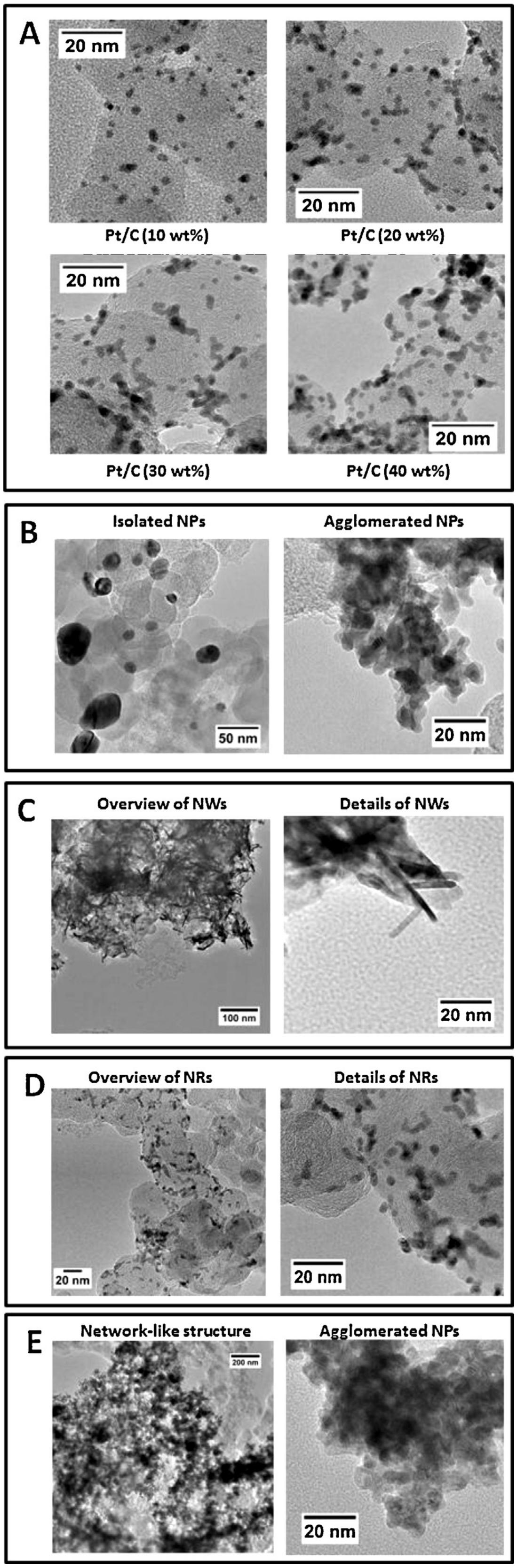

Fig. 1. TEM images for (A) Pt/C sample with metal mass-loading varying from 10 to 40 wt%, (B) Pd/C-1, (C) Pd/C-2, (D) Pd/C-3 and (E) Pd/C-4 catalysts.

The *p*XRD patterns of Pd/C catalysts show five typical Pd face-centred cubic (*fcc*) phase: (111), (200), (220), (311) and (222), as shown in Fig. 3A. It can be seen that the diffraction peak intensity for carbon (002) plane emerges at 25° following a trend: Pd/C-1 > Pd/C-2 > Pd/C-3 > Pd/C-4, corresponding to the increased sequence of Pd mass-loading from Pd/C-1 to Pd/C-4 samples. The peak at 34° in Pd/C (ETEK) sample is due to the presence of PdO (101) plane in the commercial sample [22]. By analysing the patterns *via* Williamson-Hall plot, Fig. 3B, the $\beta\cos\theta/\lambda$ value fluctuates with $4\sin\theta/\lambda$, where β is the integral peak width, θ the angle and λ the diffraction wavelength, the peak broadening is affected not only by the crystallite size (L_v), but also by micro-strains (ε) and stacking faults (α). The calculated lattice parameter (a), L_v, ε and α, for home-made and reference catalysts, are summarized in Table 2.

One can notice that, for the synthesized Pd samples, the value of the lattice parameter is very close to the reference catalyst Pd/C (ETEK). L_v value of Pd/C-1 is slightly higher, and those of home-made catalysts lower than that of the commercial Pd/C (ETEK). On the other hand, α and ε values of synthesized catalysts are higher than the reference one. These facts indicate different morphology of home-made catalysts with respect to Pd/C (ETEK). Among home-made catalysts, the trend of L_v is: Pd/C-3 < Pd/C-2 < Pd/C-4 < Pd/C-1, whereas α follows the opposite trend, namely, Pd/C-3 > Pd/C-2 > Pd/C-4 > Pd/C-1. It can be found that the trend of crystallite size is actually related to that of stacking fault. The variation of ε for the home-made catalysts from *ca.* 0.22% to *ca.* 0.37%, suggests a different trend from L_v and α.

Electrochemical behaviour of Pd/C catalysts with different structural morphology was further analysed, and compared with Pd/C (ETEK). Cyclic voltammograms (CVs) in acid medium are depicted in Fig. 4 (column A). The double-layer behaviour for all the catalysts is similar. The shape of hydrogen under potential deposition (H_{upd}) region for home-made catalysts is different from, not only among each other, but also to that of Pd/C (ETEK). The PdO reduction peak potential differs among home-made catalysts, and only Pd/C-3 shows a closer peak potential to the commercial one. The surface of H_{upd} regions, and PdO peaks shows opposite trend to L_v, and the same to α, suggesting that the surface electrochemistry of Pd is controlled by the morphology in acid. In alkaline medium, different surface adsorption behaviour can be also observed in CVs, as contrasted in Fig. 4 (column B). As regards to the hydrogen diffusion peak, that of Pd/C (ETEK) is centred at 400 mV *vs.* RHE, whereas this peak on home-made samples is positively shifted. The OH^- adsorption peak on Pd/C (ETEK) sample is at 630 mV *vs.* RHE, whereas it is positively (ex. Pd/C-4) or negatively (ex. Pd/C-1, Pd/C-2 and Pd/C-3) shifted on home-made catalysts. The PdO reduction peak potential for home-made catalysts is shifted to positive (ex. Pd/C-1, Pd/C-2 and Pd/C-3) or negative (ex. Pd/C-4) potential with respect to commercial one. The PdO reduction peak follows the same trend to that in acid, except for Pd/C-4 whose PdO reduction peak surface is larger than Pd/C-1, Pd/C-2 and Pd/C-3 but smaller than Pd/C (ETEK). The complex surface electrochemical behaviour in acid and alkaline of nanostructured generated Pd samples might be attributed to morphological parameter, with a consequence of the surface electronic modification. Indeed, in the CO-stripping process, in both acid (Fig. 5A) and alkaline (Fig. 5B) media, the CO oxidation surface process follows the same trend to that depicted for PdO reduction. In both media, the corresponding oxide reduction peak potential is similar between the home-made catalyst and commercial one. The CO-oxidation peak potential, on Pd/C-1 to Pd/C-4 catalysts is negatively shifted with respect to that on Pd/C (ETEK), in $HClO_4$ and KOH solutions. This phenomenon, suggests a surface electronic modification on the home-made samples. Again, this effect can be attributed to the different

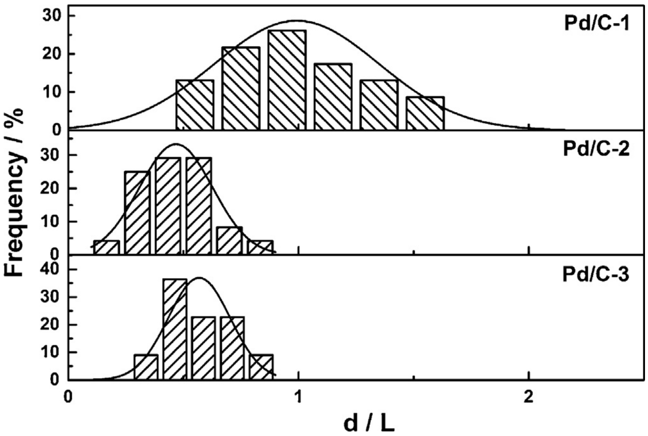

Fig. 2. Analysis of particle diameter (d) normalized by particle length (L) based on various TEM images for Pd/C-1, Pd/C-2 and Pd/C-3.

Table 2
Pd mass loading (Pd/wt%) from TGA results; lattice parameter (a/nm), crystallite size (L_v/nm), strain (ε/%) and stacking fault (α/%) values calculated from *p*XRD patterns; particle size (d) and morphology (Morph.) estimated based on TEM images; number of electron transfer (n), Tafel slope (|b| / mV dec^{-1} in the interval of 850–900 mV *vs.* RHE), electrochemical surface area (ECSA / m^2 g^{-1}$_{Pd}$), specific activity (SA / mA cm^{-2}$_{Pd}$) and mass activity (MA / mA mg^{-1}$_{Pd}$) at 850 ^{a} and 800 ^{b} mV *vs.* RHE.

	Pd/C-1	Pd/C-2	Pd/C-3	Pd/C-4	Pd/C (ETEK)
Pd	11.5	14.7	27.1	38.5	30
a	0.3891	0.3889	0.3891	0.3890	0.389
L_v	18	12	7	14	16
ε	0.25	0.37	0.22	0.28	0.02
α	1.47	1.98	2.20	1.93	0.90
Morph.	NPs	NWs	NRs	NPs	NPs
n ($HClO_4$)	3.3	4	3.9	3.9	3.6
n (KOH)	3.5	4	4	3.9	4
|b| ($HClO_4$)	55	66	69	61	57
|b| (KOH)	108	80	110	146	101
ECSA ($HClO_4$)	34	55	46	20	49
SA ($HClO_4$)	0.08 ^{a} 0.33 ^{b}	0.07 ^{a} 0.29 ^{b}	0.10 ^{a} 0.41 ^{b}	0.08 ^{a} 0.33 ^{b}	0.04 ^{a} 0.23 ^{b}
MA ($HClO_4$)	27 ^{a} 112 ^{b}	39 ^{a} 160 ^{b}	46 ^{a} 189 ^{b}	16 ^{a} 66 ^{b}	20 ^{a} 113 ^{b}
ECSA (KOH)	12	15	21	20	28.5
SA (KOH)	0.23 ^{a} 0.60 ^{b}	0.70 ^{a} 2.75 ^{b}	0.64 ^{a} 1.56 ^{b}	0.24 ^{a} 0.47 ^{b}	0.33 ^{a} 1.04 ^{b}
MA (KOH)	27 ^{a} 72 ^{b}	105 ^{a} 412 ^{b}	134 ^{a} 328 ^{b}	48 ^{a} 94 ^{b}	94 ^{a} 296 ^{b}

morphology and in good agreement with analysis of CVs curves, cf. Fig. 4.

The ORR polarization curves at 900 rpm are shown in Fig. 6A. Different rotating speeds are shown in Fig. S1 (supplementary content). Fig. 6A shows that the half-wave potential, $E_{1/2}$, of Pd/C-3 is shifted +18 mV from Pd/C (ETEK) catalyst. $E_{1/2}$ values for Pd/C-2; Pd/C-4; and Pd/C (ETEK) are close to each other (820-830 mV/RHE), while that for Pd/C-1 is the most negative one. The number of electron transfer (n value in Table 2) was estimated as *ca.* 3.3, 4, 3.9, 3.9 and 3.6 for Pd/C-1, Pd/C-2, Pd/C-3, Pd/C-4 and Pd/C (ETEK) sample, respectively. The reason why n value in Pd/C-1 and Pd/C (ETEK) is low than on other samples is probably associated with the H_2O_2 production in the ORR process. Mass-transfer corrected Tafel plot in Fig. 6B shows specific activity (the kinetic current density normalized by Pd active surface), in the interval of 900–850 mV vs. RHE. Pd/C-3 and Pd/C (ETEK) have the highest and lowest specific activity (SA), respectively. The Tafel slope (b) in this interval, listed in Table 2, of Pd/C-2 and Pd/C-3 was the highest, namely, 66 and 69 mV dec^{-1}, followed by b value on Pd/C-4, of *ca.* 61 mV dec^{-1}, whereas, that of Pd/C-1 and Pd/C (ETEK) decreased to *ca.* 55 and 57 mV dec^{-1}. This fact reflects a different ORR process on Pd/C-1 and Pd/C (ETEK), with respect to other samples. The mass activity at 850 and 800 mV *vs.* RHE in Table 2 confirmed the highest catalytic activity towards ORR on Pd/C-2 and Pd/C-3 samples. It is worth to compare the catalytic activity of our Pd NWs and NRs supported on carbon with other Pd-based nanomaterials toward ORR in acid solution. For example, the MA of $Pd_xCo_yNi_z$ trimetallic NPs, supported on carbon, was of *ca.* 2.6–3.2 mA mg^{-1}$_{Pd}$ at 0.8 V *vs.* RHE [23]. Carbon supported PdCo bimetallic NPs showed an ORR mass activity of *ca.* 20–170 mA mg^{-1}$_{Pd}$ at 0.8 V *vs.* RHE [24].

In 0.1 M KOH, Fig. 6C, $E_{1/2}$ of ORR polarization curves on Pd/C-3 is the highest potential, successively followed by Pd/C (ETEK), Pd/C-4, Pd/C-2 and Pd/C-1. The n on Pd/C-1 is 3.5, whereas that on other samples is close to 4. Taking the analysis of the number of electron charge transfer in acid into account, the electron transfer efficiency is constant or enhanced in alkaline solution. Tafel plot in Fig. 6D shows the highest SA values on Pd/C-2 and Pd/C-3 samples, followed by Pd/C (ETEK), Pd/C-4 and Pd/C-1 samples. As shown in Table 2, Pd/C-2 has the lowest b value of *ca.* 80 mV dec^{-1} among all the samples, followed by Pd/C (ETEK) with *ca.* 101 mV dec^{-1}. The Tafel slopes of Pd/C-1 and Pd/C-3 are close, namely *ca.* 108 and 110 mV dec^{-1}, For Pd/C-4, b = 146 mV dec^{-1}. The MA in Table 2 shows that the catalytic activity is enhanced on Pd/C-2 and Pd/C-3 samples with respect to other catalysts in this work. Compared with the catalytic activity towards ORR on nanostructured Pd in the literature [25,26], that on Pd/C-2 and Pd/C-3 catalysts is enhanced.

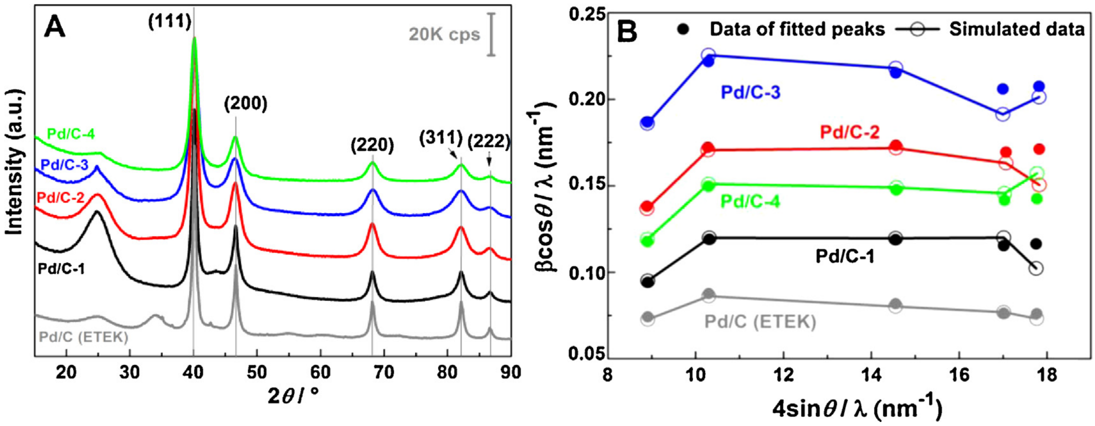

Fig. 3. (A) *p*XRD patterns of home-made catalysts. The peak at 34° is the (101) plane of PdO in the reference Pt/C (ETEK), (B) Williamson-Hall plot for Pd/C-1, Pd/C-2, Pd/C-3 and Pd/C-4 catalysts.

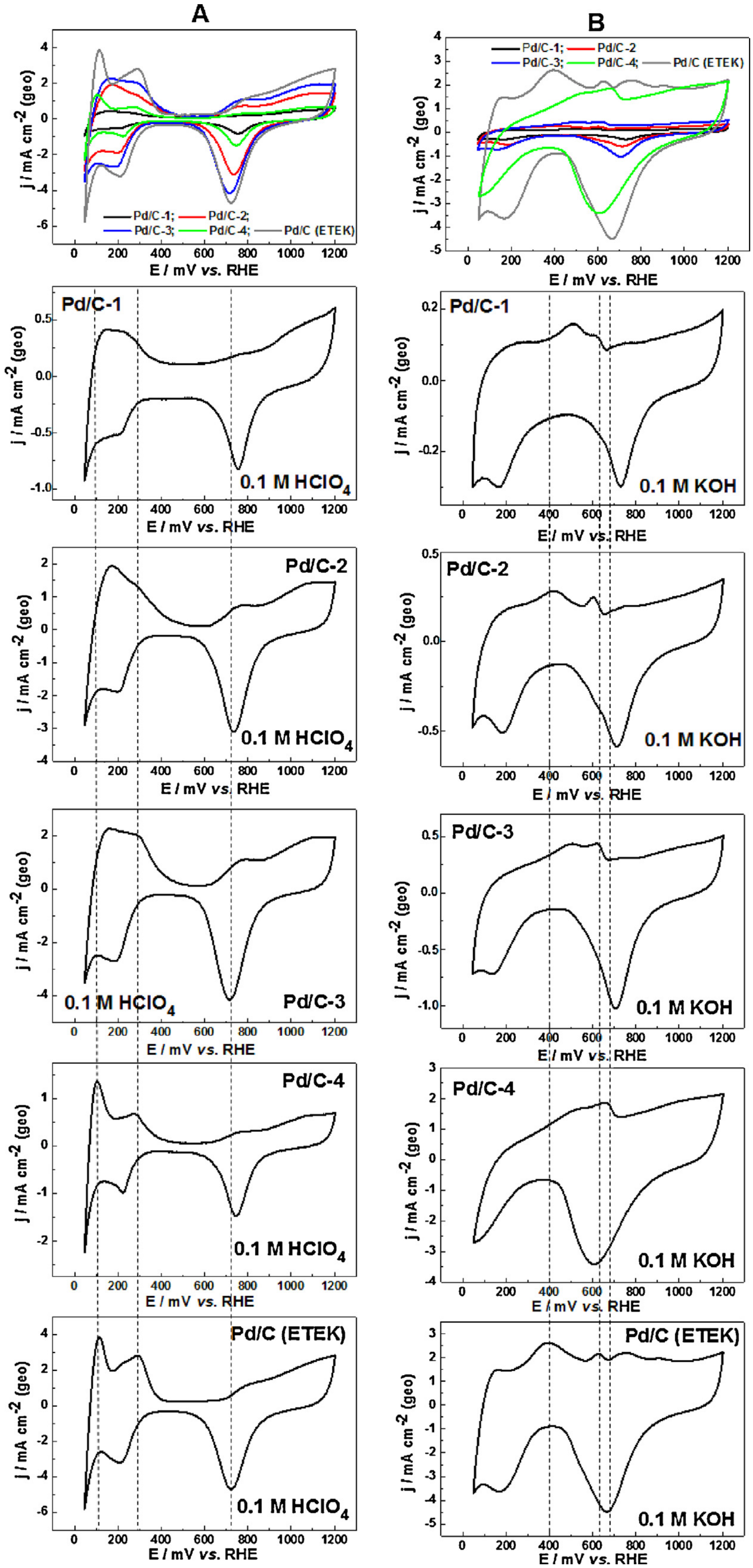

Fig. 4. Cyclic voltammograms, recorded at scan rate of 50 mV s^{-1} in N_2-saturated 0.1 M $HClO_4$ (column A) and 0.1 M KOH (column B).

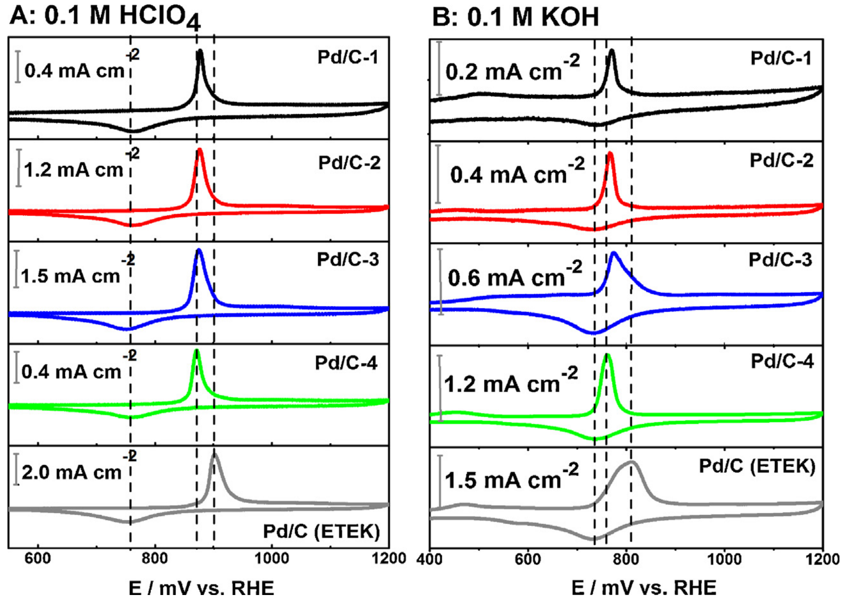

Fig. 5. CO-stripping voltammograms, recorded at scan rate of 5 mV s^{-1} in N_2-saturated 0.1 M $HClO_4$ (A) and 0.1 M KOH (B). The current density is normalized by geometric surface of working electrode.

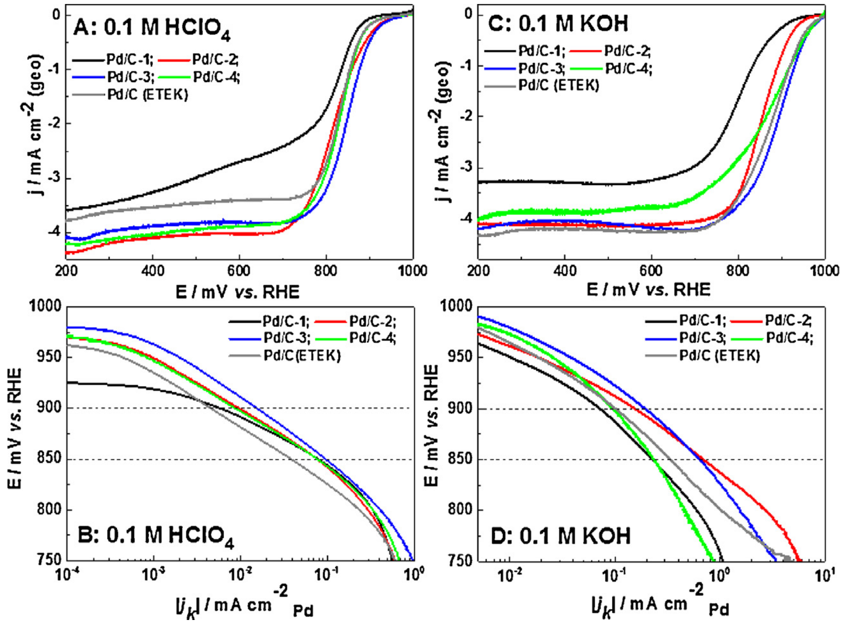

Fig. 6. (A) ORR polarization curves, recorded by linear sweep voltammograms at scan rate of 5 mV s^{-1} with a rotating speed of 900 rpm in O_2-saturated 0.1 M $HClO_4$, and (C) 0.1 M KOH. Mass transfer corrected Tafel plots, derived from ORR polarization curves at 900 rpm, for the catalysts in (B) 0.1 M $HClO_4$, and (D) 0.1 M KOH.

Considering the structural morphology, one can conclude that the ORR mass activity on nanowire-like in Pd/C-2 and nanorod-like in Pd/C-3 is improved, though with lower active surface area and mass loading with respect to commercial Pd/C (ETEK) [27] in acid and alkaline media. Highly agglomerated structures in Pd/C-1 and Pd/C-4 prepared *via* carbonyl chemical route show slight or no improvement towards ORR activity, possible due to highly reduced Pd active surface. It is interesting to note that on home-made catalysts, the ORR mass activity follows the same trend as the stacking faults (α), but in opposite sequence to the crystallite size (L_v). Pd/C-2 and Pd/C-3 is higher than Pd/C-1 and Pd/C-4, concomitantly indicating a connection between the catalytic activity towards ORR and the catalysts' morphology. It is worth to note that the different metal mass loadings were, indeed performed through the addition of different mass of carbon substrate with the same concentration of Pd chemical precursor solution. Thus, it is possible that the generation of various morphologies takes place on various nucleation sites of the supporting material. The test on other substrates needs further verification, and it is under current investigation in our laboratory

4. Conclusion

In this work, carbon supported Pd nanostructures were prepared *via* carbonyl chemical route generating various morphologies according to the mass loading, as revealed by TEM images. The obtained Pd catalysts were compared with Pt NPs catalysts, prepared *via* the same carbonyl chemical route, resulting in similar particle size and morphology. The surface electrochemistry in acid and alkaline media as well as the ORR, combined with the analyses of *p*XRD patterns, it comes out that the morphological effect has a positive impact towards the electrocatalytic ORR process, as compared with carbon supported reference catalyst. This study paves the way to better control the morphology changes induced by the chemical synthetic route *via* carbonyl, on the one hand; on the other hand the substrate' nature variation can shed light onto the nucleation process leading to morphological changes of the catalytic centres.

Acknowledgements

This work was in part supported by the European Union's Seventh Framework Program (FP7/2007–2013) for the Fuel Cell and Hydrogen Joint Technology Initiative under grant agreement nr. 303492–CathCat and University of Poitiers, France. JM M-H, and LA E-W thank Conacyt-MX for financial support through scholarships nr. 351743 and 234729, respectively. The authors thank Dr. Laure Timperman, at University of Tours (France), for the synthesis of Pt/C.

Appendix A. Supplementary data

Supplementary data associated with this article can be found, in the online version, at http://dx.doi.org/10.1016/j.electacta.2015.05.140.

References

[1] R. Rahul, R.K. Singh, M. Neergat, Effect of oxidative heat-treatment on electrochemical properties and oxygen reduction reaction (ORR) activity of Pd–Co alloy catalysts, J. Electroanal. Chem. 712 (2014) 223–229.
[2] M. Shao, J. Odell, M. Humbert, T. Yu, Y. Xia, Electrocatalysis on Shape-Controlled Palladium Nanocrystals: Oxygen Reduction Reaction and Formic Acid Oxidation, J. Phy. Chem. C 117 (2013) 4172–4180.
[3] S. Takenaka, N. Susuki, H. Miyamoto, E. Tanabe, H. Matsune, M. Kishida, Highly durable Pd metal catalysts for the oxygen reduction reaction in fuel cells; coverage of Pd metal with silica, Chem. Commun. 46 (2010) 8950–8952.
[4] M. Shao, T. Yu, J.H. Odell, M. Jin, Y. Xia, Structural dependence of oxygen reduction reaction on palladium nanocrystals, Chem. Commun. 47 (2011) 6566–6568.
[5] H. Gharibi, F. Golmohammadi, M. Kheirmand, Fabrication of MEA based on optimum amount of Co in PdxCo/C alloy nanoparticles as a new cathode for oxygen reduction reaction in passive direct methanol fuel cells, Electrochim. Acta 89 (2013) 212–221.
[6] S.-W. Kim, J. Park, Y. Jang, Y. Chung, S. Hwang, T. Hyeon, Y.W. Kim, Synthesis of Monodisperse Palladium Nanoparticles, Nano Lett. 3 (2003) 1289–1291.
[7] L.A. Gugliotti, D.L. Feldheim, B.E. Eaton, RNA-Mediated Metal-Metal Bond Formation in the Synthesis of Hexagonal Palladium Nanoparticles, Science 304 (2004) 850–852.
[8] N. Zheng, J. Fan, G.D. Stucky, One-Step One-Phase Synthesis of Monodisperse Noble-Metallic Nanoparticles and Their Colloidal Crystals, J. Am. Chem. Soc. 128 (2006) 6550–6551.
[9] Y. Xiong, J. Chen, B. Wiley, Y. Xia, S. Aloni, Y. Yin, Understanding the Role of Oxidative Etching in the Polyol Synthesis of Pd Nanoparticles with Uniform Shape and Size, J. Am. Chem. Soc. 127 (2005) 7332–7333.
[10] L. Ren, L. Yang, P. Yu, Y. Wang, L. Mao, Electrochemical Post-Treatment of Infinite Coordination Polymers: An Effective Route to Preparation of Pd Nanoparticles Supported onto Carbon Nanotubes with Enhanced Electrocatalytic Activity toward Ethanol Oxidation, ACS Appl. Mater. Interfaces 5 (2013) 11471–11478.
[11] J. Ge, W. Xing, X. Xue, C. Liu, T. Lu, J. Liao, Controllable Synthesis of Pd Nanocatalysts for Direct Formic Acid Fuel Cell (DFAFC) Application: From Pd Hollow Nanospheres to Pd Nanoparticles, J. Phy. Chem. C 111 (2007) 17305–17310.
[12] V. Mazumder, S. Sun, Oleylamine-Mediated Synthesis of Pd Nanoparticles for Catalytic Formic Acid Oxidation, J. Am. Chem. Soc. 131 (2009) 4588–4589.
[13] W. Zhou, M. Li, O.L. Ding, S.H. Chan, L. Zhang, Y. Xue, Pd particle size effects on oxygen electrochemical reduction, Int. J. Hydrogen Energy 39 (2014) 6433–6442.
[14] L. Xiao, L. Zhuang, Y. Liu, J. Lu, H.D. Abruña, Activating Pd by Morphology Tailoring for Oxygen Reduction, J. Am. Chem. Soc. 131 (2009) 602–608.
[15] N. Alonso-Vante, Carbonyl Tailored Electrocatalysts, Fuel Cells 6 (2006) 182–189.
[16] N. Alonso-Vante, Platinum and Non-Platinum Nanomaterials for the Molecular Oxygen Reduction Reaction, ChemPhysChem 11 (2010) 2732–2744.
[17] E.P. Kuendig, D. McIntosh, M. Moskovits, G.A. Ozin, Binary carbonyls of platinum $Pt(CO)_n$ (where n = 1-4). Comparative study of the chemical and physical properties of $M(CO)_n$ (where M = nickel, palladium, or platinum; n = 1-4), J. Am. Chem. Soc. 95 (1973) 7234–7241.
[18] Y. Luo, A. Habrioux, L. Calvillo, G. Granozzi, N. Alonso-Vante, Yttrium Oxide/Gadolinium Oxide-Modified Platinum Nanoparticles as Cathodes for the Oxygen Reduction Reaction, ChemPhysChem 15 (2014) 2136–2144.
[19] A. Habrioux, W. Vogel, M. Guinel, L. Guetaz, K. Servat, B. Kokoh, N. Alonso-Vante, Structural and electrochemical studies of Au-Pt nanoalloys, Phys. Chem. Chem. Phys. 11 (2009) 3573–3579.
[20] A.J. Bard, L.R. Faulkner, Electrochemical Methods: Fundamentals and Applications, Second Edition ed., John Wiley&Sons, New York, 2001.
[21] L. Timperman, PhD thesis, University of Poitiers, (2010).
[22] C.-J. Huang, F.-M. Pan, T.-C. Tzeng, C. Li, J.-T. Sheu, Growth and Field Emission of Reactive Sputtered Pd–PdO Core–Shell Nanoflakes on Platinum, J. Electrochem. Soc. 156 (2009) J28–J31.
[23] K.R. Lee, S.I. Woo, Promoting effect of Ni on PdCo alloy supported on carbon for electrochemical oxygen reduction reaction, Catal. Today 232 (2014) 171–174.
[24] D. Wang, H.L. Xin, H. Wang, Y. Yu, E. Rus, D.A. Muller, F.J. DiSalvo, H.D. Abruña, Facile Synthesis of Carbon-Supported Pd–Co Core–Shell Nanoparticles as Oxygen Reduction Electrocatalysts and Their Enhanced Activity and Stability with Monolayer Pt Decoration, Chem. Mater. 24 (2012) 2274–2281.
[25] K. Jukk, N. Alexeyeva, A. Sarapuu, P. Ritslaid, J. Kozlova, V. Sammelselg, K. Tammeveski, Electroreduction of oxygen on sputter-deposited Pd nanolayers on multi-walled carbon nanotubes, Int. J. Hydrogen Energy 38 (2013) 3614–3620.
[26] N. Alexeyeva, A. Sarapuu, K. Tammeveski, F.J. Vidal-Iglesias, J. Solla-Gullón, J.M. Feliu, Electroreduction of oxygen on Vulcan carbon supported Pd nanoparticles and Pd–M nanoalloys in acid and alkaline solutions, Electrochim. Acta 56 (2011) 6702–6708.
[27] A. Dector, F.M. Cuevas-Muñiz, M. Guerra-Balcázar, L.A. Godínez, J. Ledesma-García, L.G. Arriaga, Glycerol oxidation in a microfluidic fuel cell using Pd/C and Pd/MWCNT anodes electrodes, Int. J. Hydrogen Energy 38 (2013) 12617–12622.

Applied Catalysis B: Environmental 147 (2014) 756–763

Contents lists available at ScienceDirect

Applied Catalysis B: Environmental

journal homepage: www.elsevier.com/locate/apcatb

Mixed-oxide $Ti_{1-x}W_xO_2$ as support for (photo)-electrochemical processes

S. Mokrane-Soualah[a,b], A.S. Gago[a,1], A. Habrioux[a], N. Alonso-Vante[a,*]

[a] IC2MP UMR-CNRS 7285, University of Poitiers, 4 rue Michel Brunet, B27-BP633, 86022 Poitiers, France
[b] Laboratory of Electrochemistry, Corrosion and Energy Valorization, University of Béjaia, Rue de Targa Ouzemmour, 06000 Béjaia, Algeria

ARTICLE INFO

Article history:
Received 16 July 2013
Received in revised form 3 October 2013
Accepted 7 October 2013
Available online xxx

Keywords:
TiO_2
Sol–gel
Photoelectrochemistry
ORR
Substrate

ABSTRACT

In this study, mixed-oxides of $Ti_{1-x}W_xO_2$ ($0 \leq x \leq 0.3$) nanomaterials have been synthesized via a multistep sol–gel process. The effect of W doping on the anatase structure and on the electrical conductivity of the material was investigated. Photo-electrochemical action spectra and UV–vis spectroscopy were used to determine the bang-gap energy of the mixed-oxides. The electrochemical stability of these materials was also investigated before they were tested as substrate for platinum nanocatalysts for oxygen reduction reaction. The metal was deposited onto the support either via the chemical route (carbonyl method) or via UV-irradiation.

1. Introduction

The widely used conventional support of Pt-based catalyst is carbon black (Vulcan XC-72). This latter, in low temperature fuel cells, is known to undergo electrochemical oxidation to surface oxides species and to CO_2 [1]. As carbon corrodes, noble metal nanoparticles on carbon black will detach from the electrode or aggregate to larger particles resulting in Pt surface area loss, which subsequently lowers the performance of PEMFCs [2]. Therefore, many efforts have been made to search for new catalyst supports [3]. Metal–metal oxide catalysts have been investigated as possible co-catalysts that are believed to operate via the bifunctional mechanism [4–6]. Tungsten oxide has been considered as a support material for fuel cell catalysts [7,8]. Titania, a widely used catalyst support [9], is known to enhance the activity in many cases due to the strong interaction between the active phase and the support [10]. In most of these oxides the metal is in its highest oxidation state and these materials are large-gap semiconductors. However, these oxides can be partially reduced [11] or doped with other metal cations [12], resulting in metal-like oxides. TiO_2 can be doped with other cations to prepare $Ti_{1-x}M_xO_2$, where M is a metal from group V or greater. Hence, doped TiO_2 has the possibility of being both electrically conducting and kinetically stable in aqueous acid or alkaline media within a large electrode potential interval. The heteroatoms can be incorporated as a substituent of the titanium ion [13] or as an interstitial ion [14] of the titania lattice, or a surface-bound species, e.g., the surface wolframyl groups [15]. Depending on the nature and/or the history of sample preparation, the mode of incorporation of the heteroatom can change and, hence, the physical properties and the performances.

Various deposition techniques are available for the preparation of TiO_2 samples (powder or thin films), namely, magnetron sputtering [16], sol–gel [17], hydrothermal [18], chemical vapor deposition [19] or pulsed laser deposition [20]. Among them, sol–gel is of particular interest for its simplicity to obtain well-controlled stoichiometry doped TiO_2 oxides.

In the present work, tungsten was introduced to titania to obtain a mixed $Ti_{1-x}W_xO_2$ material, which was then characterized by various analytical and spectroscopic techniques. We are especially interested in the influence of W in the optoelectronic properties and in the interaction between platinum nanoparticles and the high-conducting mixed-oxide as support.

2. Experimental

2.1. Synthesis of materials by sol–gel synthesis

$Ti_{1-x}W_xO_2$ nanoparticles were synthesized via a sol–gel-based multistep synthesis involving firstly the dissolution of *tungsten VI* chlorides oxides $WOCl_4$ in isopropanol during 3 h under stirring at ambient temperature. Thereafter, the titanium isopropoxide (TIP) was added in this solution. Finally, after 16 h, a required quantity

---

[*] Corresponding author. Tel.: +33 54945 3625; fax: +33 54945 3580.
E-mail address: nicolas.alonso.vante@univ-poitiers.fr (N. Alonso-Vante).

[1] Present address: Institute of Technical Thermodynamics/Electrochemical Energy Technology, German Aerospace Center (DLR), Pfaffenwaldring 38-40, 70569 Stuttgart, Germany.

0926-3373/$ – see front matter © 2013 Elsevier B.V. All rights reserved.
http://dx.doi.org/10.1016/j.apcatb.2013.10.012

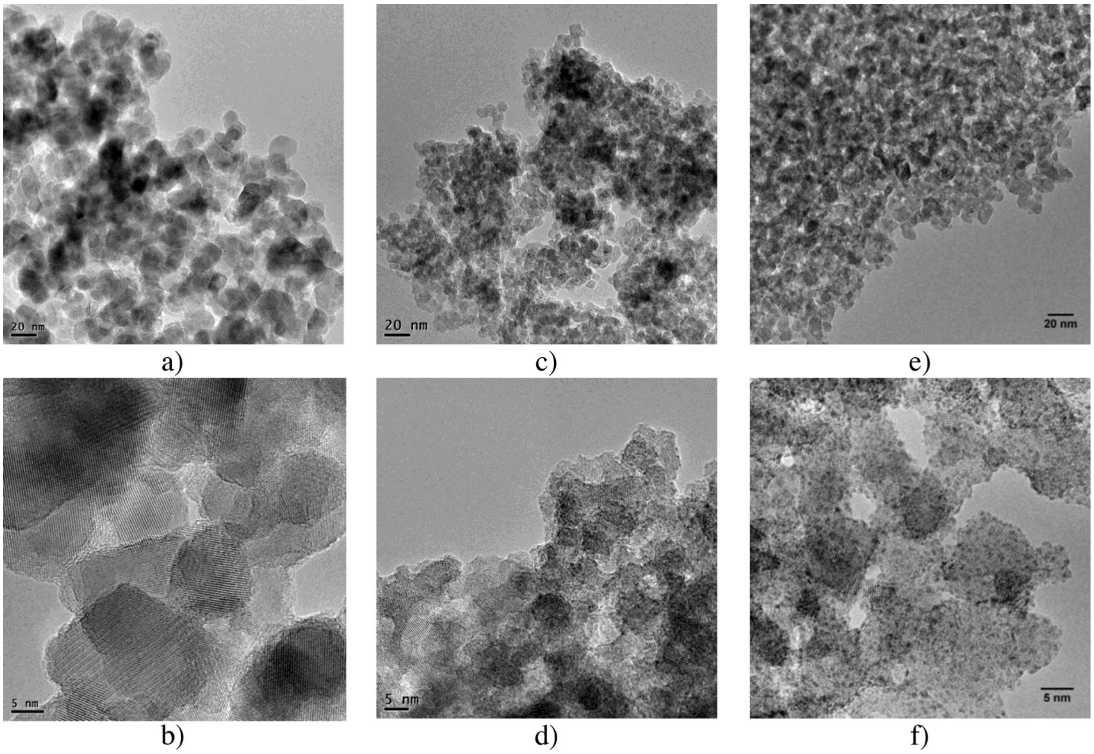

Fig. 1. TEM images of TiO_2 (a and b), $Ti_{0.95}W_{0.5}O_2$ (c and d) and $Ti_{0.7}W_{0.3}O_2$ (e and f) powders.

of water at 0 °C was added to hydrolyze the TIP to $Ti_{1-x}W_xO_2$. The powder was obtained after evaporation of the solvent and dried under primary vacuum, and later heat-treated, under air or nitrogen, at 450 °C, 1 h. The quantities of the chemical precursors vary according to the chosen molar ratio of Ti/W. For the sake of comparison, TiO_2 and WO_3 were independently synthesized using the sol–gel process.

2.2. Platinum nanoparticles supported onto oxides

For the synthesis of 8 wt.% Pt/oxide, platinum carbonyl $[Pt_3(CO)_6]_5{}^{2-}$ was prepared by mixing 50.12 mg $Na_2PtCl_6{\cdot}6H_2O$ with 44.24 mg sodium acetate (mol ratio of NaAc/Pt = 6) in methanol solution under CO atmosphere for 24 h. Subsequently, 200 mg of oxide $Ti_{0.8}W_{0.2}O_2$ was added to the above solution and stirred for another 12 h under nitrogen atmosphere. The final product ($Pt/Ti_{0.8}W_{0.2}O_2$) was collected on a Millipore filter membrane (dia. 0.22 μm pore size), washed with water and dried in vacuum at room temperature [21,22].

2.3. Characterization of photocatalyst

The morphology and size of particles was examined with a TEM on a JEOL JEM-2001 equipped with a LaB_6 filament. The samples were characterized under an accelerating voltage of 200 kV and a resolution of ca. 0.19 nm.

The synthesized materials were characterized by powder X-ray diffraction using a diffractometer, Bruker "D8 Advance", equipped with a linear detector fast VANTEC and a heating room Anton Paar (htk16) in the 2θ range of 15–70°. FullProf program suite was used for the Rietveld refinements.

Raman spectra were obtained with a spectrometer, Horiba Jobin Yvon "LabRam HR 800-UV", using 0.05 mW green laser Ar^+ (Melles Griot), within the wave number range of 50–1200 cm^{-1}. The spectrometer is gauged with a sample of silicon with a resolution of 0.5 cm^{-1}. The software LabSpec 5 allows for the acquisition and the treatment of the results.

The oxides were also analyzed by Diffuse Reflectance Spectroscopy with a spectrophotometer UV-Visible-PIR Varian "Cary 5000", double UV-Visible-PIR beam (spectral range from 175 to 3300 nm) equipped with a Praying Mantis^{TM}. To determine the conductivity of oxide powders, the impedance spectroscopy measurements were recorded at room temperature. An Autolab potentiostat with a Frequency Response Analysis system software (FRA) was used to record the impedance in the frequency range of 50 kHz to 1 Hz, at a potential of 0 V. The cell used was provided with a two-gold disk electrodes compartment covered by a sheet of carbon, Toray. A torque of 25 in.-pounds assured the electrical contact and reproducibility of the measurements of the various oxides powders. All generated data showed a non-frequency dependence.

2.4. Photoelectrochemical and electrochemical measurements

Photocurrent measurements were performed at room temperature in a photoelectrochemical cell (PEC) provided with three electrodes. A plate of glassy carbon served as counter electrode, and a reversible hydrogen electrode (RHE), connected to the cell compartment through a Luggin capillary, as a reference electrode. A solution 0.5 M H_2SO_4 was used as electrolyte. The working (photo)electrodes were prepared by spin coating (at 3500 rpm) using a suspension of the oxides in ethanol (5 mg/mL) and deposited on SnO_2:F (Solems) substrates of 0.5 cm^2. After ejection and evaporation of the solvent, a porous $Ti_{1-x}W_xO_2$ adherent thin film was formed. The samples were calcined afterwards, in air at 450 °C. The PEC was provided with a quartz window and was placed on an optical table on a support that allowed the displacement of all the system in X, Y and Z directions. The measurements were carried under UV–vis illumination and in darkness. The UV–vis source of light was from a Xenon lamp, Spectral products ASB-XE-175. Current-potential curves were performed in Ar-saturated electrolyte, from 0.1 to 2 V/RHE at 50 mV s^{-1}.

For the oxygen reduction reaction (ORR) measurements, the working electrode was a glassy carbon disk with a 3 mm diameter (geometric surface area, 0.071 cm^2) and polished with Al_2O_3 (5A) powder prior to catalyst deposition. The catalyst ink was prepared by dispersing 10 mg of catalysts, e.g., $Ti_{0.8}W_{0.2}O_2$, 8 wt.% Pt/$Ti_{0.8}W_{0.2}O_2$ (by carbonyl way) and 8 wt.% Pt/$Ti_{0.8}W_{0.2}O_2$ (by photodeposition), in 250 μL Nafion® (5 wt.% in water/aliphatic alcohol solution, Aldrich) and 1250 μL ultra pure water (18 MΩ-cm) in an ultrasound bath for 1 h. A drop of 3.0 μL of catalyst ink was deposited onto the working electrode surface and dried under nitrogen. Before the ORR measurements, cyclic voltammetry, in nitrogen-saturated electrolyte, was performed to clean and activate the electrode surface from 0.05 to 1.2 V/RHE at 50 mV s^{-1}. 20 cycles were necessary to stabilize the current–potential signal. Linear current–potential curves were recorded from 1.0 to 0.2 V/RHE in oxygen-saturated electrolyte at a 1600 rpm rotating speed. All electrochemical measurements were recorded with a Potentiostat, Autolab PGSTAT30.

3. Results and discussion

3.1. TEM characterization of the $Ti_{1-x}W_xO_2$ powders

Fig. 1 shows low and high magnification TEM images of some $Ti_{1-x}W_xO_2$ powders. For each sample the size of particles is clearly in the order of ca. 10 nm. Whatever the considered sample, TEM observations did not show the presence of larger particles. The particles seem to be regular in shape regardless of the W-content. From Fig. 1a, c and e, it seems that the addition of W is responsible for a slight decrease in the mean particle size. Furthermore, for high W-content (i.e. for $Ti_{0.7}W_{0.3}O_2$ sample), small particles are apparent (Fig. 1e). The presence of these particles could be attributed to the growth of small clusters at the surface of larger ones.

3.2. Phase identification in the prepared $Ti_{1-x}W_xO_2$ materials

The Fig. 2 summarizes the XRD patterns of the whole set of synthesized oxides, namely, $Ti_{0.7}W_{0.3}O_2$, $Ti_{0.8}W_{0.2}O_2$, $Ti_{0.9}W_{0.1}O_2$, $Ti_{0.95}W_{0.05}O_2$, $Ti_{0.99}W_{0.01}O_2$, and TiO_2. The vertical bars at the bottom show the diffraction peaks corresponding to the anatase and brookite phase of TiO_2. The anatase phase is the predominant phase on all synthesized samples. The visible peak at $2\theta = 31°$ corresponding to brookite phase disappears with the tungsten concentration (>1%). This result supports the fact that tungsten inhibits any phase change of anatase [23]. Moreover, up to a W content of 30 at.%, there is no formation of crystalline WO_3 phase, which can suggest that W could be built-in in the matrix of TiO_2. Structural analysis of the $Ti_{1-x}W_xO_2$ material with different W contents calcined at 450 °C suggests that the anatase phase of titanium dioxide does not change when reacting with a tungstate chemical precursor for W content lower than 30 at.%.

3.3. Structural characterization of $Ti_{1-x}W_xO_2$ materials and effect of the heat-treatment

In addition, tungsten is responsible for shifting diffraction peaks of anatase toward lower angles. Diffractograms shown in Fig. 2 were fitted by the Fullprof free software and Rietveld structure refinement. The average crystallite size as well as lattice parameters of $Ti_{1-x}W_xO_2$ with (0 at.% < W < 30 at.%) obtained from these simulations are summarized in Table 1. The lattice parameters ($a = b$, and c) show variations with the W-content. While the a-parameter monotonously increases with the W-content, the c-parameter decreases. As a result, the volume unit cell increases until 10 at.% W, and then remains nearly constant. Furthermore, it can be pointed out that the addition of a small amount of W (1 at.%) produces a slight shrinkage of both a, and c parameters (in comparison with TiO_2 sample) which could be associated with the substitution of Ti^{4+} by W^{6+}. As a result of this substitution, a defect formation occurs at the metal sites [24].

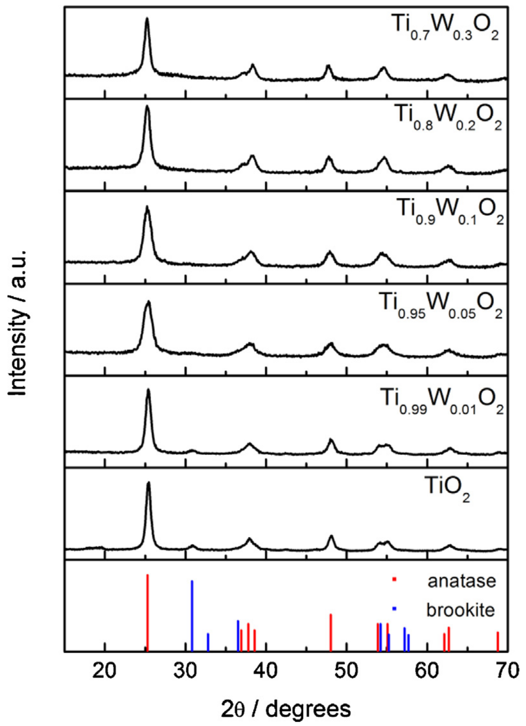

Fig. 2. XRD patterns of $Ti_{0.7}W_{0.3}O_2$, $Ti_{0.8}W_{0.2}O_2$, $Ti_{0.9}W_{0.1}O_2$, $Ti_{0.95}W_{0.05}O_2$, $Ti0_{.99}W_{0.01}O_2$ and TiO_2. Vertical bars at the bottom represent the diffraction peaks positions of anatase and brookite phases.

The effect of the calcination temperature was also in situ XRD examined on $Ti_{0.8}W_{0.2}O_2$ and the $Ti_{0.2}W_{0.8}O_2$ samples see Fig. 3. The as-prepared sample: $Ti_{0.8}W_{0.2}O_2$ shows broad diffraction patterns characteristic of the anatase crystal phase with a low crystallinity at ambient temperature as shown in Fig. 3 (lower panel). With the increase of the calcination temperature (i.e. 650 °C), the narrowing of the diffraction peaks was observed, thus crystallite growth of the titanium dioxide takes place. However, the appearance of a shoulder at 24° testifies of a phase change, which is clearly put in evidence when measuring the heat-treated sample at 30.3 °C, see upper panel of Fig. 3.

3.4. Strains analyses of $Ti_{1-x}W_xO_2$ materials

To complete the structural study of the $Ti_{1-x}W_xO_2$ materials ($x < 0.3$), Raman spectra were generated on those samples and contrasted in Fig. 4A. These results are consistent with the phase analysis realized from data obtained by XRD. All $Ti_{1-x}W_xO_2$ samples showed the characteristic peaks for the E_g, B_{1g}, A_{1g} and E_g modes of anatase, but their positions slightly deviate from those of bulk anatase at 145, 398, 519 and 639 cm^{-1} [25]. The samples with W content below 5 at.% show peaks at 247, 323 and 366 cm^{-1} that can be assigned to the A_{1g}, B_{1g}, and B_{2g} modes of brookite [26] (Fig. 4B). Other details observed in the Raman spectra is the broad emission peak centered at ca. 972 cm^{-1} for W-content higher than 1 at.% (Fig. 4C). The magnitude of this peak increases as the W content increases. There is no indication of other tungsten species, including crystalline WO_3. This is fairly in agreement with conclusions drawn from XRD experiments. Consequently, this peak is attributed to the W=O stretching mode of surface wolframyl entities [27]. In order to determine the effects of tungsten on the

Table 1
Characterization data of the different tungsten doped titanium oxide samples.

Sample	Crystallite size (XRD)/nm	a (= b)/Å	c/Å	Cell volume/Å^3	Crystallite size (Raman)/nm	Tensile stress/MPa	Compressive stress/MPA	E_{gap} (eV) Kubelka–Munk	E_{gap} (eV) action spectrum	Conductivity (mS/cm)
TiO_2	9.8	3.785	9.483	135.856	10.1	857	–	3.44	3.42	1.77×10^{-3}
$Ti_{0.99}W_{0.01}O_2$	10.5	3.784	9.478	135.712	9.4	791	–	3.31	–	45.4×10^{-3}
$Ti_{0.95}W_{0.05}O_2$	6.4	3.789	9.482	136.130	6.4	–	332	–	3.38	2.62
$Ti_{0.9}W_{0.1}O_2$	7.2	3.796	9.473	136.502	6.1	–	674	–	–	88.5
$Ti_{0.8}W_{0.2}O_2$	9.1	3.801	9.431	136.255	5.4	–	63	3.37	–	147.06
$Ti_{0.7}W_{0.3}O_2$	10.8	3.807	9.422	136.555	5.3	–	579	–	–	–
WO_3	–	–	–	430.059	–	–	–	2.91	3.05	–

microstructure of TiO_2, the frequency shift and full width at half maximum (FWHM) of the E_g mode at ca. 144 cm^{-1} are plotted in Fig. 5A. Within the W-content range from 0 to 30 at.%, the full-width at half-maximum of the peak increases from 12.6 to 29.9 cm^{-1}. At the same time, the E_g band is blue-shifted from 144.6 to 155.3 cm^{-1}. These data are consistent with a monotonous decrease of the mean crystallite size as the W content increases. There are apparently some discrepancies between XRD calculations and the Raman data since the crystallite size of anatase phase calculated from diffractograms continuously decreases up to a W content of 10 at.% and then increases. Such difference is due to the fact that XRD data reflect the overall size of crystallites including heavily tungsten-doped surfaces of TiO_2 nanocrystals observed for high W-content samples and that Raman data reflect the properties of the TiO_2 core for samples exhibiting wolframyl groups on their surface [24]. Our observed E_g mode blue-shift could be attributed to the effect of tungsten into the matrix of anatase and consequently associated with the metal-ions insertion [28]. Yang et al. [29] believe that the blue-shift of the peak could be caused by the residual compressive strain, while the broadening of the peak may be associated with defects such as dislocation and oxygen vacancies leading to a deteriorated crystal quality. The magnitude of the stress affecting TiO_2 grains has been estimated from Raman spectra using the procedure reported by Kim et al. [24]. For each sample, the crystallite size was first obtained from the E_g mode bandwidth by using the phonon confinement model [30]. The expected position of the E_g mode was then deduced from the calculated TiO_2 crystallite size. Finally, the difference between the expected and the observed E_g mode peak position was then used to estimate the nature (tensile or compressive) and the magnitude of the stress affecting the material by using the slope of 3.16 cm^{-1}/GPa [24,31]. Results obtained are summarized in Table 1. From Table 1 one observes that the stress affecting the sample can be either a tensile or a compressive one as a function of its composition. For low W content samples (i.e. W < 1 at.%), the stress affecting the anatase phase is a tensile one. This stress can be associated with the presence of the brookite phase suggesting the larger strain between TiO_2 grains [32]. The samples with W > 5 at.% are subjected to a compressive stress. This is due to the surface segregation of parasitic phases imposing large compressive strain to the TiO_2 layer, and to the lattice of TiO_2 that simultaneously experiences excessive defects. This latter effect is however balanced by the expansion of the anatase lattice.

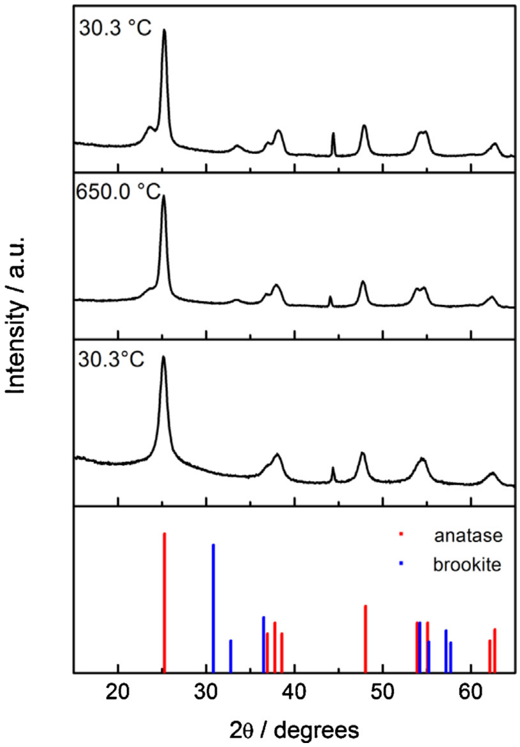

Fig. 3. XRD pattern evolution of $Ti_{0.8}W_{0.2}O_2$, during the in situ heat-treatment in air (30.3–650 °C), from bottom to upper panel.

From the Rietveld refinement results, we obtained the variations of the Ti—O bond distances with the W-content. The anatase structure can be described as edge-sharing of identical TiO_6 octahedral. The octahedral is elongated along the c-axis to result in four short equatorial Ti—O bonds and two long axial Ti—O bonds. Fig. 5B shows the variations of the Ti—O bond distances of anatase with the tungsten content. The axial bond remains more or less constant and decreases significantly for 30 at.% W, while the equatorial bond shows a monotonous increase with the increase of the W-content.

Based on the above discussion, it is very likely that two tungsten species are the lattice doping tungsten and the surface wolframyl group. When the W-content is low (i.e. lower than 5 at.%), most of the tungsten species are majorly inside the anatase lattice and substitute the titanium ions. From Raman experiments, the saturation point can be estimated to be between 1 and 5 at.% since the presence of wolframyl species is visible at W content higher than 5 at.%. This saturation range is slightly lower than other already published data [24,33,34]. In fact, at higher tungsten content (i.e. higher than 5 at.%), the additional tungsten atoms are responsible for the formation of surface bonded wolframyl groups, as evidenced by the growth of the 972 cm^{-1} peak in the Raman spectra. It can be seen in Table 1 that both a, and c parameters are slightly decreased by simply adding 1 at.% of W. Similar observations were done by Kim et al. [24]. The addition of 5 at.% of W, both a-, and c-parameters expand. This can be explained by the substitution of Ti^{4+} by W^{6+} in agreement with the explanation given by Kim et al. [24]. As the surface bound wolframyl groups become visible (i.e. for W content higher than 5 at.%), the lattice is expanded in the direction of a-parameter, whereas there is a shrinkage along the c-axis. As conclusion, it seems that surface groups are responsible for expanding the lattice along the a-axis, and the c-parameter decreases in order to keep the cell volume at a nearly constant value as shown in Table 1. Other causes such as surface hydration effect or repulsive interactions of the parallel surface defect dipoles can also be responsible for lattice volume changes [35,36]. However, the first

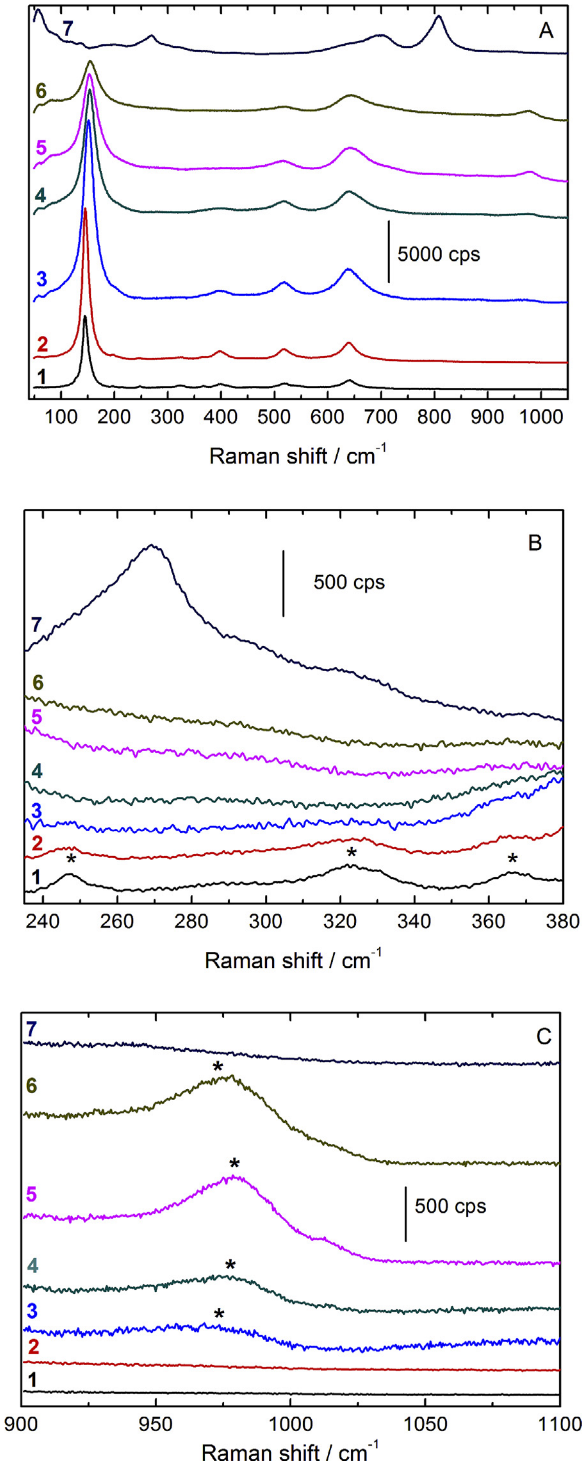

Fig. 4. (A) Raman spectra of oxides, and tungsten mixed-oxide in the spectral range of 40–1050 cm^{-1}. (B) Raman spectra in the energy interval of 240–380 cm^{-1} showing the evolution of the brookite phase. Bands associated to the A_{1g}, B_{1g}, and B_{2g} modes of brookite are marked with stars. (C) Raman spectra in the energy interval of 900–1100 cm^{-1} showing the evolution of wolframyl groups. The band attributed to the W═O stretching mode of surface wolframyl entities is marked with a star. **1**: TiO_2; **2**: $Ti_{0.99}W_{0.01}O_2$; **3**: $Ti_{0.95}W_{0.05}O_2$; **4**: $Ti_{0.9}W_{0.1}O_2$; **5**: $Ti_{0.8}W_{0.2}O_2$; **6**: $Ti_{0.7}W_{0.3}O_2$; **7**: WO_3.

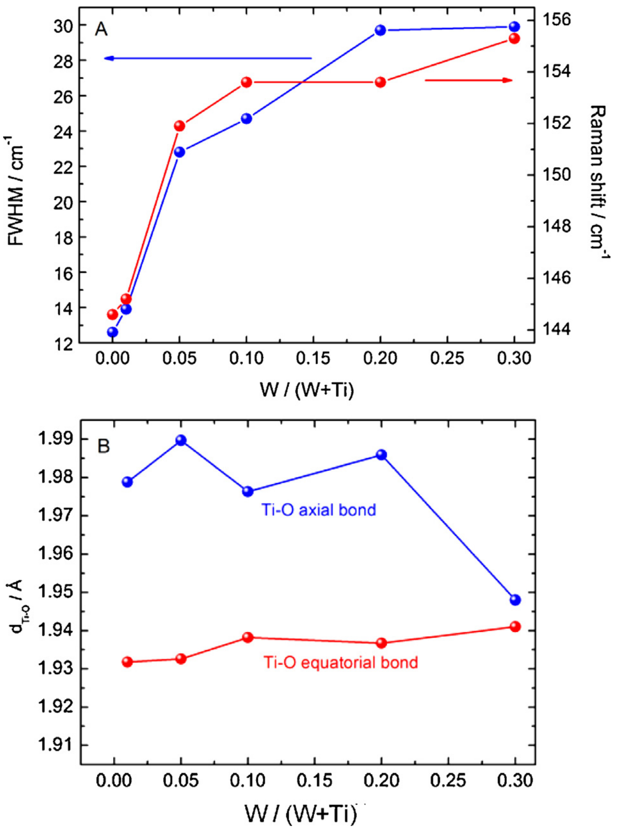

Fig. 5. (A) Variation of the peak position (red line) and the peak width (blue line) of the E_g band of titanium dioxide with the tungsten at.% content. (B) Variations of the Ti—O (axial–equatorial) bond distances of titanium dioxide with the tungsten at.% content. (For interpretation of the references to color in this figure legend, the reader is referred to the web version of the article.)

phenomenon would be responsible for a lattice contraction as the particle size decreases. Furthermore a lattice expansion would be observed as a result of the repulsive interaction between surface defect dipoles. Additionally, since the polarizability of the anatase lattice is low it is possible to conclude that repulsive interactions able of exerting a negative pressure on the crystal lattice are weak [35].

3.5. Light absorption properties

The samples of $Ti_{1-x}W_xO_2$ were measured by reflectance technique and then adjusted using a Kubelka–Munk transformation. Determination of the band-gap energy was essential to identify changes in the electronic structure of the oxides, which depends on the structural properties. Fig. 6A shows the reflectance spectra of TiO_2, $Ti_{0.99}W_{0.01}O_2$, $Ti_{0.8}W_{0.2}O_2$ and WO_3. One can see that all titanium-based oxides are transparent in the visible light region. Due to the fundamental absorption in the vicinity of band-gap, the reflectance increases abruptly as the wavelength reaches the visible range. The reflectance maximum decreases with the W-content, suggesting changes in the opto-electronic properties. Fig. 6B shows the direct transition Kubelka–Munk plot as a function of the photon energy allowing the estimation at the intercept of the threshold energies, namely, 3.31; 3.37; 3.44; and 2.91 eV for $Ti_{0.99}W_{0.01}O_2$, $Ti_{0.8}W_{0.2}O_2$, TiO_2, and WO_3, respectively. The apparent decrease in the overall band gap energy with the amount of tungsten doping testifies a shift to the visible region. Moreover, as discussed below, the increase of the conductivity (Table 1) with the tungsten content confers to such mixed-oxides a metal-like behavior. In other words, the increase in the conductivity is the result of the effect of the electronic state of W in the band structure of TiO_2 and can also be related to the constancy of the long Ti-O bond length in the crystal structure.

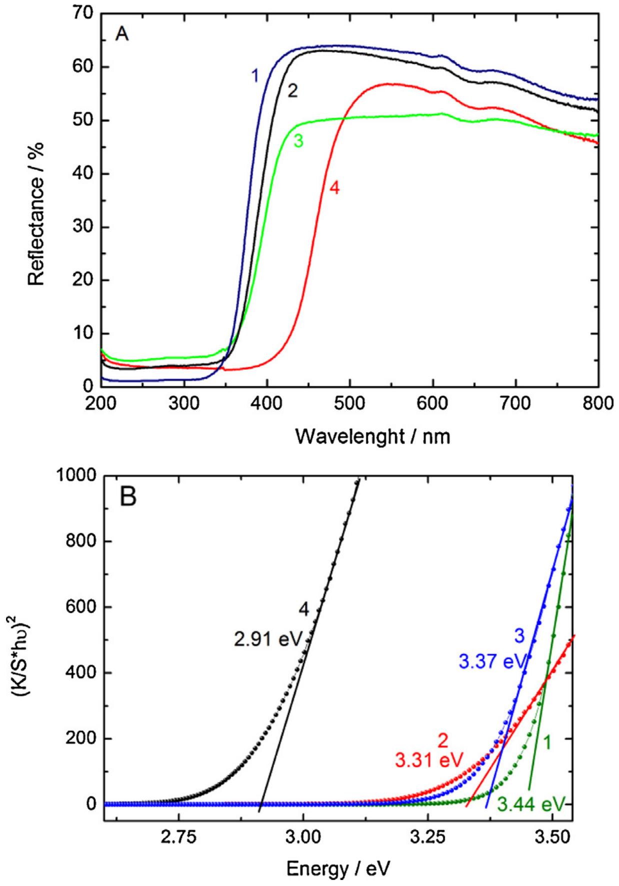

Fig. 6. (A) UV–visible diffuse reflectance spectra of selected samples **1**: TiO_2, **2**: $Ti_{0.99}W_{0.01}O_2$, **3**: $Ti_{0.8}W_{0.2}O_2$ and **4**: WO_3. (B) The corresponding Kubelka–Munk-transformed diffuse reflectance as a function of $h\nu$ for a direct allowed transition.

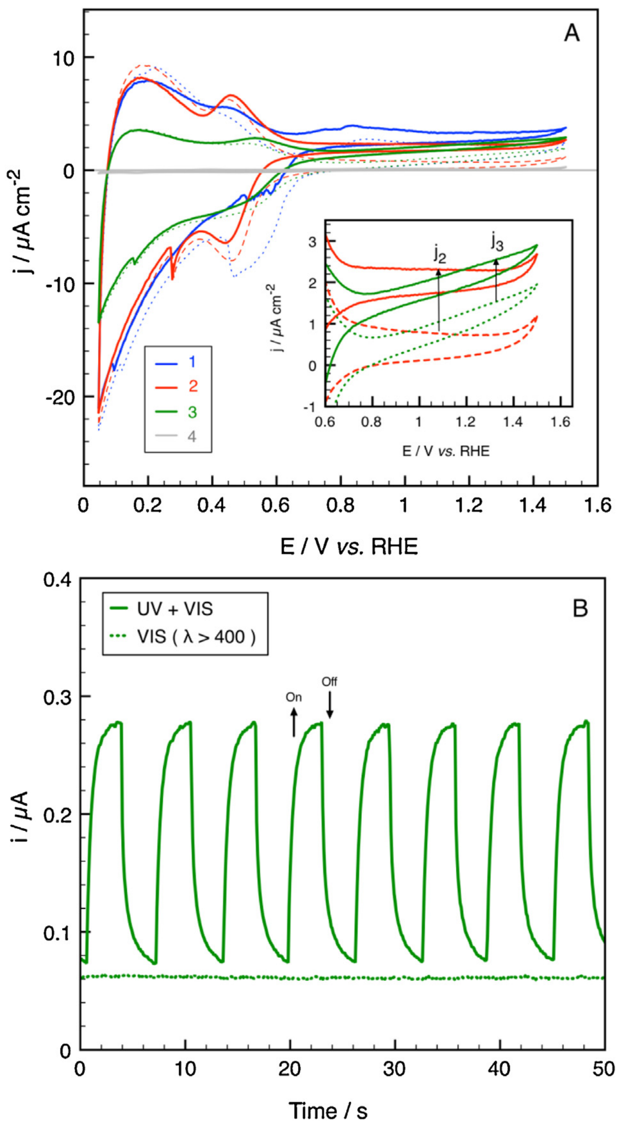

Fig. 7. (A) Current–potential characteristics of selected samples: **1**: $Ti_{0.95}W_{0.05}O_2$, (2) **2**: $Ti_{0.9}W_{0.1}O_2$, **3**: $Ti_{0.8}W_{0.2}O_2$ and **4**: SnO_2:F substrate in darkness (dashed lines) and under UV (full lines). The insert zooms the photo-response of **j**$_3$: $Ti_{0.8}W_{0.2}O_2$ and **j**$_4$: $Ti_{0.9}W_{0.1}O_2$. The periodic on-off photocurrent response of $Ti_{0.8}W_{0.2}O_2$ at $E = 1$ V vs. RHE, under UV and visible ($\lambda > 400$ nm) irradiation is shown in (B). Measurements were carried out in Ar-saturated 0.5 M H_2SO_4 electrolyte with a scan rate of 50 mV s^{-1}.

3.6. Photoelectrochemistry

The current–potential curves of $Ti_{0.95}W_{0.05}O_2$, $Ti_{0.9}W_{0.1}O_2$ and $Ti_{0.8}W_{0.2}O_2$ porous oxide films, measured in darkness and under UV–vis illumination are shown in Fig. 7A. The current responses are mainly dominated by the characteristic redox peaks of Ti^{4+} and Ti^{3+} (hydr)oxide species of TiO_2 occurring in the potential window from 0.05 and 0.6 V vs. RHE [37]:

$$Ti(OH)_2 + H^+ \leftrightarrow [Ti(OH)(H_2O)]^+ + e^- \leftrightarrow Ti(OH) + H_2O \qquad (1)$$

However, the electron–hole recombination increases with at.% of W-content and thus the photocurrent (i_{ph}) is greatly reduced. This fact allows ruling out the presence of amorphous WO_3 phase which would be responsible for increasing the magnitude of the photocurrent response [38]. This doping effect of 3d metals has been studied by DFT (density functional theory) calculations on TiO_2 (rutile) doped with W [39], Mo [40], Fe, Co, Ni, Mn [41]. According to such calculations a strong hybridization with the doping elements appears in the band gap of TiO_2 leading to the formation of intermediate energy states. As demonstrated in the present work, the consequence of such phenomenon is not the decrease of the fundamental energy gap of the mixed-oxide, cf. Fig. 6, but the increase of the electrical conductivity, cf. Table 1. The photogenerated electron–hole (e–h) pairs on $Ti_{0.8}W_{0.2}O_2$ only take place under UV irradiation, Fig. 7B. At a relatively high applied electrode potential (1 V vs. RHE) the recombination of e^-–h^+ pairs is evident under chopped illumination at intervals of 5 s. Nonetheless, as depicted in the insert of Fig. 7A, it is clear that the photo-response decreases with the increase of the W content. This is concomitant with the increase of the electronic conductivity, cf. Table 1, and further in good agreement with a similar trend observed in TiO_2 thin films doped with W, deposited by magnetron sputtering technique [16].

The modification of the band structure of TiO_2 by the insertion of W in the crystal structure was further studied by measuring i_{ph} with respect to wavelength of the incident photons, Fig. 8A. The direct band gap (E_g) of the oxides was estimated through $(i_{ph}{}^{*}h\nu)^2$ vs. $h\nu$ according the equation:

$$i_{ph} = A\frac{(h\nu - E_g)^n}{h\nu} \qquad (2)$$

where h is the Planck constant (6.63×10^{-34} J s), ν the photon frequency (Hz), n the order of optical transition and A is a constant that depends on the optical transition. For $n = 1/2$, see, Fig. 8B. For the reference materials WO_3 and thermal treated TiO_2 (anatase), a band gap of 3.05 eV and 3.32 eV was obtained, respectively. The intersection of the fitting line of $Ti_{0.8}W_{0.2}O_2$ was not straight forward (inset Fig. 8B), indicating again the introduction of intermediate states into the forbidden gap. Data are summarized in Table 1.

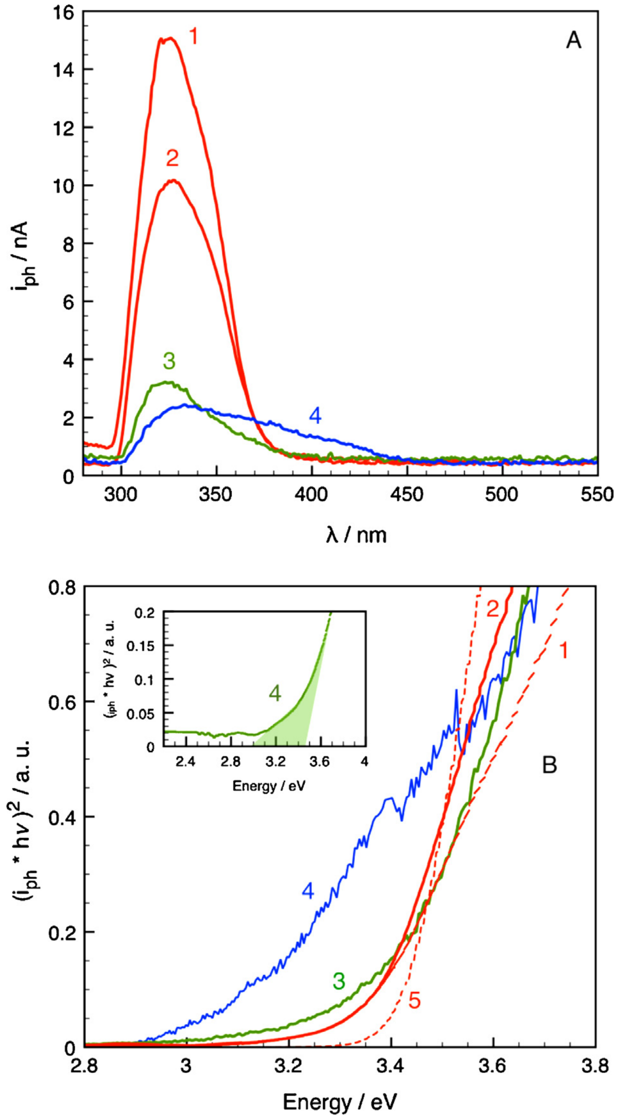

Fig. 8. (A) Photo-current action spectra of the selected samples: **1**: TiO_2 (thermal treated) **2**: TiO_2 (as prepared), **3**: $Ti_{0.8}W_{0.2}O_2$ and **4**: WO_3 porous film electrodes deposited on SnO_2:F substrate, measured at 1 V vs. RHE in Ar-saturated 0.5 M H_2SO_4 solution under UV–vis illumination. (B) Plots of $(i_{ph}{}^{*}h\nu)^2$ vs. $h\nu$ to determine the band gap (E_g). **5**: Commercial TiO_2 Degussa P25 with a ratio of anatase to rutile phases of 3:1 is plot for comparison. The inset shows the wide energy range of intersection for another electrode of **4**: $Ti_{0.8}W_{0.2}O_2$.

As a final point the current potential curves of porous $Ti_{0.8}W_{0.2}O_2$ electrode, measured up to 2 V vs. RHE at 20 mV s^{-1}, are shown in Fig. 9. Transpassive corrosion of the electrode during O_2-evolution was observed beyond 1.5 V vs. RHE in either darkness or under UV–vis illumination. In this sense the material exhibits similar stability than TiO_2 in acid medium, but with an enhanced metallic character. Consequently, the nanostructured powder of $Ti_{0.8}W_{0.2}O_2$ can be a promising ceramic substrate for electrocatalytic nanoparticles of Pt [42] or Ir-based [43] used as oxygen electrodes of PEM fuel cells and electrolyzers, respectively.

3.7. Oxygen reduction reaction (ORR)

Tafel plots extracted from ORR curves registered in an oxygen saturated acid electrolyte solution are summarized in Fig. 10. This figure contrasts the activity of two substrates: glassy carbon, and $Ti_{0.8}W_{0.2}O_2$ where it is clearly put in evidence the low catalytic activity of these substrate materials toward the ORR in 0.5 M H_2SO_4. The chemical route (carbonyl way) was used to deposit platinum nanoparticles both on Vulcan and on $Ti_{0.8}W_{0.2}O_2$ substrates. One can clearly see the enhancement of the reaction kinetics when platinum is deposited onto the oxide substrate. Furthermore, Tafel slopes determined for both samples show a slight deviation from the theoretical value of 120 mV dec^{-1} [44,45]. This result reflects different adsorption isotherms and could be related to different adsorption rates of oxygen on the catalyst surface [46]. Additionally, this fact is fairly in agreement with kinetic currents values calculated at 0.85 V vs. RHE for Pt/C and Pt/$Ti_{0.8}W_{0.2}O_2$ catalysts. They are respectively of 15 μA $cm^{-2}{}_{Pt}$ and 29 μA $cm^{-2}{}_{Pt}$ which means that a two-fold enhancement factor in the ORR kinetics can be obtained by depositing platinum onto tungsten doped titania substrate.

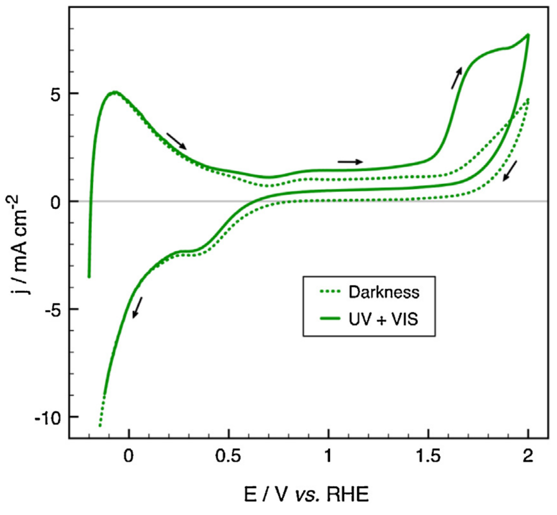

Fig. 9. Current–potential curves of $Ti_{0.8}W_{0.2}O_2$ electrode up to 2 V vs. RHE, in Ar-saturated 0.5 M H_2SO_4 solution in darkness (full line) and under UV–vis radiation (dashed line). The arrows indicate the sense of the potential sweep, which was performed at 20 mV s^{-1}.

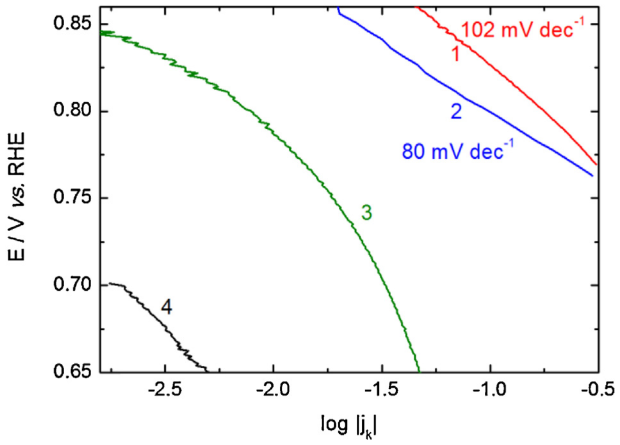

Fig. 10. Tafel plots obtained from ORR curves registered in an oxygen saturated electrolyte (H_2SO_4 0.5 M) at a scan rate of 5 mV s^{-1} with **1**: Pt/$Ti_{0.8}W_{0.2}O_2$, **2**: Pt/C, **3**: $Ti_{0.8}W_{0.2}O_2$, **4**: glassy carbon.

4. Conclusion

In this study TiO_2 nanomaterials containing different amount of tungsten have been synthesized via a multistep sol–gel process. These samples exhibit a composition dependent structure. Depending on the tungsten amount, lattice and surface doping species can be deduced. At low tungsten content W is mainly incorporated into the anatase lattice which results in the expansion of the TiO_2 lattice. At a high tungsten-content (i.e. W > 5 at.%), the formation of surface-bonded wolframyl groups takes place. These surface wolframyl groups are responsible for compressing the TiO_2 core thus a compressive strain. Furthermore, the magnitude of the photocurrent response under UV illumination decreases as the amount of tungsten doping species increases. This phenomenon can be explained by the reduction of the overall energy band gap and the introduction of intermediate states into the forbidden gap near the conduction band of TiO_2 as well as by the distortion of the anatase crystal caused by surface wolframyl groups leading to changes in the electronic structure of anatase. This is also responsible for increasing the electronic conductivity of the oxides up to 147 $mS\text{-}cm^{-1}$ for a tungsten content of 20 at.%. The latter property is of great interest for electrocatalytic applications since these materials can act as a substrate to deposit electrocatalytic nanomaterials such as platinum nanoparticles. Moreover the electrochemical stability of these W-TiO_2 nanomaterials up to potentials such as 1.5 V vs. RHE allows envisioning their application in a wide range of electrochemical energy conversion devices.

Acknowledgments

This work was partially supported by the European Union's Seventh Framework Programme (FP7/2007-2013) for the Fuel Cell and Hydrogen Joint Technology Initiative under grant agreement n° 303492 CathCat. Aldo Gago thanks CONACYT for financial support (Scholarship 305477).

References

[1] K.H. Kangasniemi, D.A. Condit, T.D. Jarvi, Journal of the Electrochemical Society 151 (2004) E125–E132.
[2] J. Liu, Z. Zhou, X. Zhao, Q. Xin, G. Sun, B. Yi, Physical Chemistry Chemical Physics 6 (2004) 134–137.
[3] R. Borup, J. Meyers, B. Pivovar, Y.S. Kim, R. Mukundan, N. Garland, D. Myers, M. Wilson, F. Garzon, D. Wood, P. Zelenay, K. More, K. Stroh, T. Zawodzinski, J. Boncella, J.E. McGrath, M. Inaba, K. Miyatake, M. Hori, K. Ota, Z. Ogumi, S. Miyata, A. Nishikata, Z. Siroma, Y. Uchimoto, K. Yasuda, K.-I. Kimijima, N. Iwashita, Chemical Reviews 107 (2007) 3904–3951.
[4] K. Lasch, L. Jörissen, J. Garche, Journal of Power Sources 84 (1999) 225–230.
[5] E.J. McLeod, V.I. Birss, Electrochimica Acta 51 (2005) 684–693.
[6] J.W. Long, R.M. Stroud, K.E. Swider-Lyons, D.R. Rolison, Journal of Physical Chemistry B 104 (2000) 9772–9776.
[7] P.K. Shen, A.C.C. Tseung, Journal of the Electrochemical Society 141 (1994) 3082–3090.
[8] M. Götz, H. Wendt, Electrochimica Acta 43 (1998) 3637–3644.
[9] L. Timperman, A. Lewera, W. Vogel, N. Alonso-Vante, Electrochemistry Communications 12 (2010) 1772–1775.
[10] M. Gopal, W.J. Moberly Chan, L.C. De Jonghe, Journal of Materials Science 32 (1997) 6001–6008.
[11] T. Ioroi, H. Senoh, S.-I. Yamazaki, Z. Siroma, N. Fujiwara, K. Yasuda, Journal of the Electrochemical Society 155 (2008) B321–B326.
[12] C.V. Subban, Q. Zhou, A. Hu, T.E. Moylan, F.T. Wagner, F.J. DiSalvo, Journal of the American Chemical Society 132 (2010) 17531–17536.
[13] L.G. Devi, B. Nagaraj, K.E. Rajashekhar, Chemical Engineering Journal 181–182 (2012) 259–266.
[14] M. Acikgoz, P. Gnutek, C. Rudowicz, Chemical Physics 402 (2012) 83–90.
[15] C.W. Lai, S. Sreekantan, International Journal of Hydrogen Energy 38 (2013) 2156–2166.
[16] G. Abadias, A.S. Gago, N. Alonso-Vante, Surface and Coatings Technology 205 (2011) S265–S270.
[17] Q. Li, D.J.G. Satur, H. Kim, H.G. Kim, Materials Letters 76 (2012) 169–172.
[18] D. Ke, H. Liu, T. Peng, X. Liu, K. Dai, Materials Letters 62 (2008) 447–450.
[19] A. Sobczyk-Guzenda, M. Gazicki-Lipman, H. Szymanowski, J. Kowalski, P. Wojciechowski, T. Halamus, A. Tracz, Thin Solid Films 517 (2009) 5409–5414.
[20] Y. Suda, H. Kawasaki, T. Ueda, T. Ohshima, Thin Solid Films 475 (2005) 337–341.
[21] S. Mokrane, L. Makhloufi, N. Alonso-Vante, Journal of Solid State Electrochemistry 12 (2008) 569–574.
[22] L. Timperman, Y.J. Feng, W. Vogel, N. Alonso-Vante, Electrochimica Acta 55 (2010) 7558–7563.
[23] S. Komornicki, M. Radecka, P. Sobaś, Journal of Materials Science: Materials in Electronics 15 (2004) 527–531.
[24] D.-S. Kim, J.-H. Yang, S. Balaji, H.-J. Cho, M.-K. Kim, D.-U. Kang, Y. Djaoued, Y.-U. Kwon, CrystEngComm 11 (2009) 1621–1629.
[25] T. Ohsaka, F. Izumi, Y. Fujiki, Journal of Raman Spectroscopy 7 (1978) 321–324.
[26] G.A. Tompsett, G.A. Bowmaker, R.P. Cooney, J.B. Metson, K.A. Rodgers, J.M. Seakins, Journal of Raman Spectroscopy 26 (1995) 57–62.
[27] F.D. Hardcastle, I.E. Wachs, Journal of Raman Spectroscopy 26 (1995) 397–405.
[28] Z.-M. Wang, G. Yang, P. Biswas, W. Bresser, P. Boolchand, Powder Technology 114 (2001) 197–204.
[29] Y. Yang, Q. Zhang, B. Zhang, W.B. Mi, L. Chen, L. Li, C. Zhao, E.M. Diallo, X.X. Zhang, Applied Surface Science 258 (2012) 4532–4537.
[30] S. Kelly, F.H. Pollak, M. Tomkiewicz, Journal of Physical Chemistry B 101 (1997) 2730–2734.
[31] D.G. Barton, M. Shtein, R.D. Wilson, S.L. Soled, E. Iglesia, Journal of Physical Chemistry B 103 (1999) 630–640.
[32] S. Kment, H. Kmentova, P. Kluson, J. Krysa, Z. Hubicka, V. Cirkva, I. Gregora, O. Solcova, L. Jastrabik, Journal of Colloid and Interface Science 348 (2010) 198–205.
[33] A. Fuerte, M.D. Hernández-Alonso, A.J. Maira, A. Martínez-Arias, M. Fernández-García, J.C. Conesa, J. Soria, G. Munuera, Journal of Catalysis 212 (2002) 1–9.
[34] M. Fernández-García, A. Martínez-Arias, A. Fuerte, J.C. Conesa, Journal of Physical Chemistry B 109 (2005) 6075–6083.
[35] G. Li, L. Li, J. Boerio-Goates, B.F. Woodfield, Journal of the American Chemical Society 127 (2005) 8659–8666.
[36] G. Li, J. Boerio-Goates, B.F. Woodfield, L. Li, Applied Physics Letters 85 (2004) 2059–2061.
[37] F.Y.L. Oliva, a.B. Avalle, E. Santos, O.R. Cámara, Journal of Photochemistry and Photobiology A: Chemistry 146 (2002) 175–188.
[38] S. Higashimoto, M. Sakiyama, M. Azuma, Thin Solid Films 503 (2006) 201–206.
[39] M. Aryanpour, R. Hoffmann, F.J. DiSalvo, Chemistry of Materials 21 (2009) 1627–1635.
[40] V.T.T. Ho, C.-J. Pan, J. Rick, W.-N. Su, B.-J. Hwang, Journal of the American Chemical Society 133 (2011) 11716–11724.
[41] M.S. Park, S.K. Kwon, B.I. Min, Physical Review B 65 (2002) 161201.
[42] S. Sharma, B.G. Pollet, Journal of Power Sources 208 (2012) 96–119.
[43] M. Carmo, D.L. Fritz, J. Mergel, D. Stolten, International Journal of Hydrogen Energy 38 (2013) 4901–4934.
[44] A. Damjanovic, V. Brusic, Electrochimica Acta 12 (1967) 615–628.
[45] A. Damjanovic, M.A. Genshaw, Electrochimica Acta 15 (1970) 1281–1283.
[46] S.M. Park, S. Ho, S. Aruliah, M.F. Weber, C.A. Ward, R.D. Venter, S. Srinivasan, Journal of the Electrochemical Society 133 (1986) 1641–1649.

Journal of
Materials Chemistry A

PAPER

View Article Online
View Journal | View Issue

Cite this: *J. Mater. Chem. A*, 2015, **3**, 11891

Electronic interaction between platinum nanoparticles and nitrogen-doped reduced graphene oxide: effect on the oxygen reduction reaction†

Jiwei Ma,‡[ad] Aurélien Habrioux,[a] Yun Luo,[a] Guadalupe Ramos-Sanchez,§[b] Laura Calvillo,[c] Gaetano Granozzi,[c] Perla B. Balbuena[b] and Nicolas Alonso-Vante*[a]

In this study, low-mass loadings (*ca.* 5 wt%) Pt/C catalysts were synthesized using the carbonyl chemical route allowing for the heterogeneous deposition of Pt nanoparticles on different carbon-based substrates. N-doped reduced graphene oxide, reduced graphene oxide, graphene oxide, graphite and Vulcan XC-72 were used for the heterogeneous deposition of Pt nanoparticles. The effect of the chemical nature of the carbon-based substrate on the Oxygen Reduction Reaction (ORR) kinetics at Pt nanoparticles surfaces was investigated. XPS results show that using N-doped reduced graphene oxide materials for the deposition of Pt nanoparticles leads to formation of Pt–N chemical bonds. This interaction between Pt and N allows for an electronic transfer from Pt to the carbon support. It is demonstrated that *ca.* 25% of the total amount of N atoms were bound to Pt ones. This chemical bond also revealed by the DFT analysis, induces changes in the oxygen adsorption energy at the platinum surface, engendering an enhancement of the catalyst activity towards ORR. In comparison with Vulcan XC-72, the mass activity at 0.9 V *vs.* RHE is 2.1 fold higher when N-doped reduced graphene oxide is used as substrate. In conjunction with the experimental results, DFT calculations describe the interaction between supported platinum clusters and oxygen where the support was modelled accordingly with the carbon-based materials used as substrate. It is demonstrated that the presence of N-species in the support although leading to a weaker O_2 adsorption, induces elongated O–O distances suggesting facilitated dissociation. Additionally, it is revealed that the strong interaction between Pt clusters and N-containing substrates leads to very slight changes of the cluster–substrate distance even when oxygen is adsorbed at the interfacial region, thus leading to a lower resistance for electron charge transfer and enabling electrochemical reactions.

Received 16th February 2015
Accepted 30th April 2015

DOI: 10.1039/c5ta01285f

www.rsc.org/MaterialsA

1. Introduction

To address environmental and energy challenges polymer electrolyte fuel cells (PEFCs)[1,2] represent power sources that are particularly interesting for applications in transportation and stationary power plants. For PEFCs, conventional electrocatalysts are generally based on Pt and Pt-alloy nanoparticles (NPs) supported on carbon black materials.[1,3] Though promising fuel cell performances are currently achieved, the Pt loading is still too high for large scale applications. Two routes to decrease catalyst cost are nowadays explored: (i) reducing Pt loading, and (ii) exploring non-noble metal catalysts. However, it is challenging to maintain catalyst activity, especially for the oxygen reduction reaction (ORR), when the Pt catalyst loading is reduced. Moreover, it is well-known that due to their low graphitization degree, carbon black materials are unstable and electrochemically oxidize at 0.97 V *vs.* RHE, as detected by differential electrochemical mass spectrometry (DEMS).[4]

---

[a] *IC2MP, UMR-CNRS 7285, University of Poitiers, 4 rue Michel Brunet, 86022 Poitiers, France. E-mail: nicolas.alonso.vante@univ-poitiers.fr*

[b] *Department of Chemical Engineering, Texas A&M University, College Station, TX 77843, USA*

[c] *Department of Chemical Sciences, University of Padova, Via Marzolo 1, 35131 Padova, Italy*

[d] *Faculty of Materials Science and Engineering, Hubei University, 430062 Wuhan, China*

† Electronic supplementary information (ESI) available: Views of 4 × 4, LOG and HOG graphene sheets considered for calculations, views of interaction of oxygen with Pt_4 clusters supported on different substrates, views of Pt_{38} clusters interacting with different substrates, views of positions of O_2 interacting with Pt_{38} clusters supported on N_3-doped graphene. See DOI: 10.1039/c5ta01285f

‡ Present address: J. Ma: Sorbonne Universités, UPMC Université Paris 06, UMR-CNRS 8234, PHENIX, F-75005, Paris, France.

§ Present address: G. Ramos-Sánchez: Cátedras Conacyt: Departamento de Química Universidad Autónoma Metropolitana – Iztapalapa.

Although the kinetics of the process is rather low, it is known to be responsible for reducing the cell durability by deteriorating the electrocatalytic activity of carbon-supported Pt NPs accompanied by Pt loss and agglomeration.[5–7] Challenges associated with the use of carbon black substrates can be addressed by developing improved support materials.[5] Therefore, in the past decades, extensive investigations have been focused on exploring alternative substrates, *e.g.* oxide-based[5,8–12] and graphene-like,[5,13–23] which might induce strong and beneficial catalyst–support interactions, thereby substantially enhancing catalytic activity while decreasing Pt loading.

Graphene meets the requirements for support materials due to its large surface area, high conductivity, good chemical and electrochemical stability.[24] As a result, it has been recognized as a promising support for low-temperature fuel cell electrocatalysts.[15] Graphene-based supports are commonly prepared by reducing graphene oxide (GO) *via* a chemical reduction method which eventually takes to reduced GO (RGO).[15,24] However, it is currently very challenging to control the supported-metal center morphology and dispersion. Recently, heteroatom-doped graphene materials have received much attention[24,25] as support for electrocatalysts, paving the way for the growth of catalytically active metals with controlled morphology and dispersion on the surface of graphene support.[21,24,26]

In this paper, low mass loading (*ca.* 5 wt%) Pt/C catalysts using either nitrogen-doped or undoped RGO-based materials as carbon support are prepared and electrochemically characterized with respect to ORR. Nitrogen-doped RGO (NRGO) has been intensively investigated as Pt catalyst support due to the possibility to control the composite catalyst functionality by rationalizing the high affinity between nitrogen groups and Pt atoms.[21,26–28]

To better understand the interaction between Pt NPs and graphene-like substrates, undoped RGO was also used for comparison. Different interaction modes between Pt NPs and NRGO were identified and ascribed to charge transfer between Pt NPs and the graphene support. These interactions are related to Pt–N interactions due to the presence of nitrogen groups on the NRGO surface, as also revealed by X-ray photoemission spectroscopy (XPS) results. This study points out the effect of a support-driven electronic modification of Pt on the activity of Pt active centers towards ORR. Density Functional Theory (DFT) calculations have been performed to understand electronic modifications of Pt NPs induced by graphene-based substrates, including the effects of the extent of oxidation of graphene and the doping with nitrogen. The electrocatalytic activities of NRGO and RGO supported low mass loading Pt NPs towards ORR were significantly higher compared to a benchmarking Pt/C catalyst showing great potential for applications in PEFCs.

2. Experimental

2.1 Synthesis of GO, RGO and NRGO

GO was synthesized according to the well-known Hummers method.[29] A mixture of 3.01 g of flaked graphite (Sigma-Aldrich) and 1.50 g of $NaNO_3$ (Sigma-Aldrich, ≥99.0%) was prepared and immersed into ice. Then, 69 mL of concentrated H_2SO_4 (Normapur, 95%) was added. Thereafter, 9 g of $KMnO_4$ (Sigma-Aldrich, ≥99.0%) was slowly added to keep the temperature of the reaction under 20 °C. After stabilization of the reaction temperature, the reaction media was heated at 35 °C and stirred for 30 min. 138 mL of ultra-pure water was then slowly added, producing an exothermic effect to 98 °C. Additional heating was also applied after addition of water to maintain the reaction temperature at 98 °C for 15 min. The reaction was then cooled by using a water bath until stabilization of the temperature. Then the reaction media was neutralized by slowly adding 100 mL of ultra-pure water and 10 mL of H_2O_2 (VWR, 33%), producing an exothermic effect. The system was then air cooled. The reaction media was filtrated by using an 80–100 μm filter, the fine and the rough part were collected. The fractions obtained were then let to settle to remove the supernatant. They were then centrifuged at 12 000 rpm for 10 minutes and the supernatant was removed. The residues were washed two times with HCl (Normapur, 37%) : H_2O, 1 : 3 (v/v) solution and subsequently, with ultra-pure water. The final residues were then dried at 50 °C. The graphite oxide was then collected for the following experiments and characterization.

To synthesize RGO, 150 mg of GO was dispersed into 100 mL of ultra-pure water. The suspension was magnetically stirred for 3 h and then sonicated for 1 h. 2 mL of an 8 M NaOH solution were then added into the suspension and magnetically stirred for 30 min. Subsequently, 1.2 g of $NaBH_4$ were added and the suspension was heated at 80 °C for 1 h. The powder was recovered by centrifugation at 12 000 rpm for 10 min and washed with ultra-pure water. Finally, the sample was obtained by centrifugation at 12 000 rpm for 10 min and dried at 60 °C for 48 h. Finally, the powder was calcined at 400 °C for 2 h under a reducing atmosphere (5% H_2 in N_2).

To synthesize NRGO material, 80 mg of GO was dispersed into 60 mL of ethanol and magnetically stirred for 3 h. GO was exfoliated by sonication for 2 h. 2 mL of water and 2 mL of ammonia were then added into the solution and heated at 80 °C, the mixture solution was finally transferred into a Teflon line autoclave (125 mL) and heated at 160 °C for 3 h.

2.2 Synthesis of Pt/C catalysts (C: graphite, Vulcan XC-72, RGO, NRGO)

Pt–carbonyl complex ($[Pt_3(CO)_6]_5^{2-}$) was synthesized through the reaction of $H_2PtCl_6 \cdot 6H_2O$ (99.95%, Alfa Aesar) and sodium acetate (anhydrous, 99%, Alfa Aesar) under a saturated CO atmosphere at *ca.* 55 °C for 24 h. Methanol (anhydrous, 99.8%, Sigma-Aldrich) was used as solvent and the solution was stirred until the color turned into black green.[30] The molar ratio between Na^+ and $[PtCl_6]^{2-}$ was fixed to 6. After the synthesis of the Pt–carbonyl complex, NRGO, RGO, graphite and Vulcan XC-72 (Cabot, pre-annealed at 400 °C under N_2 for 4 h) were respectively added to the carbonyl complex solution under an inert gas atmosphere and stirred for 12 h in order to obtain *ca.* 5 wt% Pt/C catalysts. The solvent was let to evaporate and the sample was rinsed with ultra-pure water. Finally, the powder was dried at 60 °C overnight. The mass loading of Pt in the investigated samples was determined by thermogravimetric analysis (TGA) and was 4.6 wt%, 4.4 wt%, 4.1 wt% and 4.8 wt% for Pt/NRGO, Pt/RGO, Pt/graphite and Pt/Vulcan catalysts, respectively.

2.3 Physical–chemical characterization

Raman spectroscopy (RS) was used to characterize the chemical status of the carbon atoms of the different supports investigated in this study. A Horiba Jobin Yvon Labram HR800UV RS spectrometer, equipped with an Ar^+ (Melles Griot) laser as illumination source and a CCD cooled detector, was used. The RS instrument was coupled to an Olympus microscope with analyzed region of 100× microscope objective. The wavelength of the laser was 514.5 nm and the power 0.04 mW. The spectra were recorded at a resolution of 1 cm^{-1}. Simulations were performed by using Fityk software.[31]

The supported Pt catalysts were analyzed by transmission electron microscopy (TEM) (JEOL JEM-2100) operating under 200 kV.

XPS measurements were performed with a KRATOS AXIS ULTRA DLD using monochromatic Al K_α radiation (1486.6 eV, 150 W) as exciting source. The pressure during analysis was 6.0×10^{-8} Pa. The binding energy (BE) of the target elements (Pt 4f, N 1s and C 1s) was determined with a pass energy of 20 eV and the resolution was *ca.* 0.4 eV. Spectrometer energy calibration was carried out using a gold sample (Au 4f at 84 eV). The N 1s and Pt 4f photoemission lines were separated into chemical-shifted components (after Shirley background removal) using Voigt shaped peaks, imposing a FWHM in the 0.8–1.4 eV range, except for the metallic Pt component where an asymmetrical shape was used. In the case of the C 1s peak, seven different components were considered (although not all of them are present in all materials). An asymmetrical shape[32] was used for the sp^2 component, whereas symmetrical Voigt functions were used for the sp^3 component and the C–O and C–N functional groups.

2.4 Electrochemical characterization

Electrocatalytic inks of supported Pt NPs were prepared as follows: 10 mg catalysts, 250 μL Nafion® solution (5 wt% in water/aliphatic alcohol solution, Sigma-Aldrich) and 1250 μL Milli-Q water (18.2 MΩ cm) were mixed and sonicated for 1 h. Thereafter, 3 μL of the mixture were taken and dropped on a glassy carbon electrode, previously polished with alumina 5A. Then it was dried in a stream of inert gas at room temperature for 30 min.

The electrochemical measurements were carried out in a three-electrode one-compartment cell by using a potentiostat (Autolab PGSTAT 30). The electrolyte was prepared from H_2SO_4 (99.6% Suprapur, Merck) and Milli-Q water (18.2 MΩ cm). A plate of glassy carbon and a reversible hydrogen electrode (RHE) with a Luggin capillary were used as counter and reference electrode, respectively. A rotating disk electrode (RDE) served as working electrode. The catalysts were evaluated at 25 °C with cyclic voltammetry (CV) and linear sweep voltammetry (LSV) techniques, in N_2- and O_2-saturated 0.5 M H_2SO_4, for CV and ORR measurements, respectively. The samples were cycled between 0.05 and 1.2 V *vs.* RHE at a scan rate of 50 mV s^{-1}, and ORR was studied at 900 rpm using a scan rate of 5 mV s^{-1}.

2.5 DFT models and methods

First, a single graphene 4 × 4 layer was used to model the interaction between a small metallic cluster (Pt_4) with the graphenic network. The GO was modelled according to the most stable configuration reported by Lahaye *et al.*[33] Two oxidation degrees denoted as low oxidation graphene (LOG) and high oxidation graphene (HOG) were simulated. In both of them one side of the graphene layer is covered with hydroxyl groups while on the other only epoxy groups are present. The number of hydroxyl groups in one side of LOG is 4 and the number of epoxy groups in the other side is also 4, while for HOG there are double amount of functional groups in each side. Nitrogen was added to the graphene and GO systems in the form of pyridinic N: replacing one C atom by one N and eliminating one neighboring carbon; this structure is called G-1N. By doing so, dangling bonds naturally arise, which were eliminated by adding hydrogen atoms. To investigate the effect of a higher doping degree, two more pyridinic N sites were added (G-3N), then the interaction with the Pt_4 cluster was analyzed. The structures of the substrates are provided as ESI.† Fig. S1† depicts the graphene sheet, LOG, and HOG systems. In all the cases of modification of the graphene structure, atomic positions, and cell size and shape were allowed to change while for the interaction with the metallic cluster only atomic positions were allowed to change during DFT optimization.

In order to explore the effect of the cluster size on the metal–support interactions, we also report DFT calculations of Pt_{38} deposited on graphene and G-3N (3% at N). In addition, to allow more N atoms in contact with the larger cluster, we built a new graphene structure with a higher N concentration (6% at N) that was called G-6N.

The electronic structure calculations were performed using the DFT approach with the projector augmented wave (PAW) pseudopotential for the inert core electrons and plane-wave basis set for the valence orbitals,[34,35] as implemented in the Vienna *ab initio* Simulation Package (VASP).[36,37] The generalized gradient approximation (GGA) in the form of the PBE exchange correlation functional was used. The plane wave basis was set up to a kinetic energy cut-off of 400 eV. The integration of the Brillouin-zone was performed using 5 × 5 × 1 Monkhorst–Pack grid[38] with Γ points included for the 4 × 4 graphene sheet and doped and functionalized supports while 3 × 3 × 1 for the 7 × 7 graphene sheet and doped systems. For DOS calculations the *k*-points were augmented to 9 × 9 × 1 and 5 × 5 × 1 respectively. For the partial occupancies the Methfessel-Paxton of first order with a smearing width of 0.2 was used. A conjugate-gradient algorithm is used to relax the atoms into their ground state. The convergence criteria for the electronic self-consistence loop is that the total energy change between two steps is smaller than 1×10^{-4} eV and 1×10^{-3} eV for atomic relaxation respectively.

3. Results and discussion

3.1 Physical–chemical characterization

Raman analysis of the carbon supports. Results obtained for Vulcan, GO, RGO, NRGO and graphite supports in the spectral region of 900–1700 cm^{-1} are shown in Fig. 1. This spectral region presents several overlapping bands. The first one, placed at *ca.* 1190–1200 cm^{-1}, is observed for all investigated carbon-based materials except for graphite support. The origin of this vibrational mode is currently not fully understood. It has been successively associated to nanocrystalline diamond,[39] hexagonal diamond[40] and sp^3 rich phase.[41,42] The band located at *ca.* 1350 cm^{-1} corresponds to the well-known D mode. The appearance of the D-band (A_{1g} symmetry) is the consequence of the symmetry breakdown for carbon atoms located at the edge of graphite sheets.[43] The third broad band, centered at *ca.* 1500 cm^{-1}, has been associated to the presence of amorphous sp^2 phase.[44] The G-band is centered at *ca.* 1580–1590 cm^{-1}. This band (corresponding to the E_{2g} symmetry) is of particular interest since it provides information about the in-plane vibration of sp^2-bonded carbon atoms.[45] For graphite, NRGO and RGO materials, another band can be identified at *ca.* 1620 cm^{-1}. It corresponds to the D′ mode. This D′ mode is not identified in Vulcan and GO samples because it probably interferes strongly with the G mode that clearly complicates the interpretation of the parameters characterizing the G band (Table 1). The D and D′ bands are defect-induced bands. It is clearly deduced that the graphitic structure of all samples, except graphite, possesses a high degree of interstitial disorder along the *c*-axis between the crystallite planes.[45] This assertion is based on the observation of the intensity of the band centered at *ca.* 1500 cm^{-1} which essentially reaches a high intensity for RGO, NRGO, GO and Vulcan samples. In addition, the previously mentioned materials contain more sp^3 rich phases than graphite, since the intensity of their 1200 cm^{-1} band is larger.

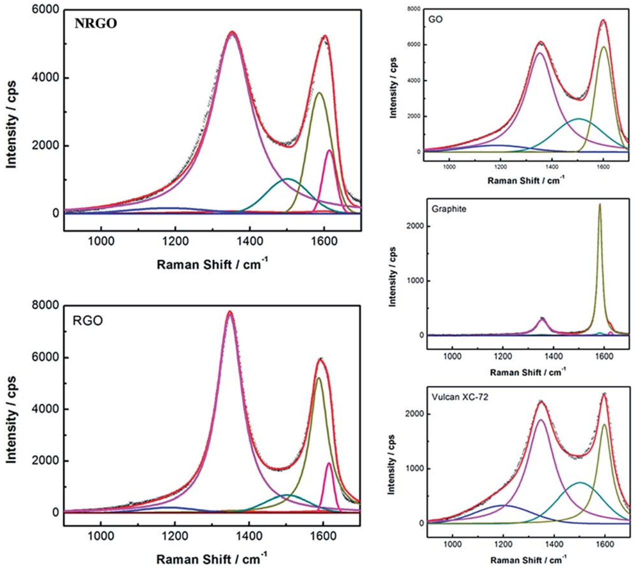

Fig. 1 Raman spectra of NRGO, RGO, GO, Graphite and Vulcan substrates.

Table 1 Raman parameters obtained, after curve fitting, for all investigated samples. I_D and I_G respectively correspond to D and G bands positions. $\omega_{1/2D}$ and $\omega_{1/2G}$ respectively correspond to full-width at half-maximum (FWHM) of D and G bands. L_a represents the in-plane crystallite size and is determined from eqn (1)

	Vulcan	Graphite	GO	RGO	NRGO
ν_D (cm^{-1})	1350	1354	1353	1348	1352
$\omega_{1/2D}$ (cm^{-1})	131	30	70	41	65
ν_G (cm^{-1})	1598	1583	1602	1588	1587
$\omega_{1/2G}$ (cm^{-1})	66	10.7	39	30	37
I_D/I_G	2.1	0.3	2.4	2.1	3.7
L_a (nm)	8.0	56.1	7.0	8.0	4.6

The fitting of different spectra was performed. Lorentzian line shapes were used for D and G bands,[45,46] whereas Gaussian ones were used to fit D′ band[46,47] as well as the bands centered at *ca.* 1200 cm^{-1} [45,48] and 1500 cm^{-1}.[45] For the replication, positions of D and G bands were set by taking into account the second order Raman spectrum and particularly the positions of 2D (*ca.* 2700 cm^{-1}) and D + G (*ca.* 2940 cm^{-1}) bands (data not shown). As a result of the fit, several parameters were extracted and presented in Table 1. The I_D/I_G and $I_{D'}/I_G$ values respectively correspond to integrated intensity ratios of D to G bands and of D′ to G bands.

An upward shift of the G-band of all samples can be observed with respect to the position of the G-band for the graphite sample. This shift probably results from the high degree of disorder of Vulcan, GO, RGO and NRGO materials. It is in fact well-known that the G band of disordered solids is shifted to higher Raman wave numbers than the G band of ordered ones.[49] However, it can be noticed that the graphitic structure of RGO and NRGO materials is relatively more ordered than the graphitic structure of GO (G-band located at 1602 cm^{-1}), since the G-bands of RGO and NRGO are respectively located at 1588 and 1587 cm^{-1}. As the upward shift of G-band increases, it becomes difficult to separate G and D′ bands. As a result, for Vulcan and GO materials, the observed band includes both G and D′ ones and it can be considered that the magnitude of the shift is directly related to the percentage of contribution of D'.[50] The highly disordered character of both Vulcan and GO samples is moreover in fair agreement with the observed D and G line-widths of these two samples (Table 2). The decrease in both line widths is an evidence for the increase of the ordering degree for RGO and NRGO materials. I_D/I_G ratio allows evaluating the graphitization degree of a carbon-based material. The I_D/I_G is used as an indicator of the amount of defects in the carbon-based materials as well as to evaluate the in-plane crystallite size (L_a) which is a measure of the inter-defects distance. One of the relations describing the evolution of L_a with the integrated intensity ratio of G to D bands is the following one:[51]

$$L_a(\mathrm{nm}) = 2.4\times10^{-10}\lambda_{\mathrm{laser}}^4\frac{I_G}{I_D} \tag{1}$$

λ_{laser} is the laser wavelength in nm.

From the L_a values calculated for all investigated samples, it can be deduced that all samples except graphite have a low

Table 2 Deconvolution of the C 1s XPS data into single chemical components for the carbon substrates and Pt/C catalysts. For each single chemical component, the BE (eV), FWHM (eV) and amount (%) values are given

	C sp^2	C sp^3	C–N	Alcohols	Epoxy groups	Carbonyl groups	Carboxylic groups
Graphite	284.2 eV 0.52 86.5%	285.3 eV 1.4 7.5%	—	286.4 eV 1.4 5.1%	—	287.9 eV 1.2 0.9%	—
GO	284.1 eV 1.33 49.8%	—	—	286.2 eV 1.03 38.8%	287 eV 0.77 2.7%	287.9 eV 1.37 7.0%	288.9 eV 1.4 1.7%
NRGO	284.4 eV 0.83 64.8%	—	285.5 eV 1.3 17.1%	286.4 eV 1.19 5.0%	287.2 eV 1.03 4.2%	288.0 eV 1.4 6.7%	288.9 eV 1.4 2.2%
Vulcan	284.4 eV 0.85 93.7%	285.6 eV 1.2 4.1%	—	286.3 eV 0.7 2.2%	—	—	—
Pt/graphite	284.2 eV 0.53 87.6%	285.3 eV 1.3 4.1%	—	286.3 eV 1.4 6.0%	—	287.9 eV 1.4 2.3%	—
Pt/RGO	284.2 eV 0.72 92.5%	285.6 eV 0.8 3.8%	—	286.3 eV 0.6 1.6%	287 eV 1.4 2.1%	—	—
Pt/NRGO	284.3 eV 0.88 67.5%	—	285.4 eV 1.3 14.7%	286.4 eV 1.06 5.0%	287.2 eV 0.85 3.5%	287.9 eV 1.25 6.4%	288.9 eV 1.4 2.9%
Pt/Vulcan	284.2 eV 0.89 89.9%	285.4 eV 1.4 3.5%	—	286.3 eV 1.0 6.6%	—	—	—

crystallite size and do not possess extended graphitic domains. Additionally the broadness of the D-band of these samples (GO, RGO, NRGO, Vulcan) can reflect a broad distribution of in-plane crystallite size. It comes as no surprise that graphite possesses larger in-plane crystallites (56.1 nm). The oxidation of graphite allowing to obtain GO is responsible for an extremely high decrease of the in-plane crystallite size (L_a value, see Table 1) which cannot be restored by chemical treatments leading to formation of RGO and NRGO materials. This assertion is highly supported by the evolution of L_a values from sample-to sample (Table 1). It can be noticed that L_a value for NRGO material (4.6 nm) is lower than L_a value for GO material (7.0 nm). This is probably due to the grafting of N-containing chemical groups at the surface of the basal planes of carbon.

TEM analysis of the Pt/C catalysts. TEM images of Pt/NRGO, Pt/RGO, Pt/Graphite and Pt/Vulcan catalysts are shown in Fig. 2. From TEM micrographs we observed that Pt NPs were highly dispersed on the NRGO and Vulcan substrates, while Pt NPs deposited onto RGO and graphite substrates were agglomerated. The higher graphitization degree of graphite, as revealed by Raman spectra, is probably responsible for a decrease of nucleation sites that favor the formation of large agglomerates due to a higher effective surface energy responsible for increasing the free energy barrier.[18,52] The mean particle sizes for Pt/NRGO and Pt/Vulcan are 2.8 ± 1.2 nm and 2.0 ± 1.0 nm, respectively (see Fig. 2a and d). Due to the large agglomeration degree of Pt NPs onto RGO and onto graphite, it was difficult to estimate the size of isolated Pt NPs.

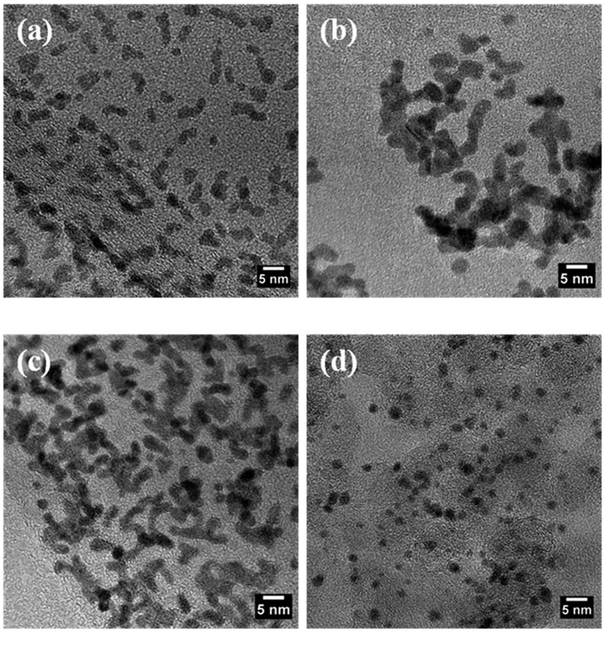

Fig. 2 TEM images of Pt/NRGO (a), Pt/RGO (b), Pt/graphite (c) and Pt/Vulcan (d) nanomaterials.

XPS analysis of the Pt/C catalysts. In order to investigate the surface chemical status of Pt and substrate atoms in the investigated Pt/C samples, XPS measurements were carried out. The C 1s, N 1s and Pt 4f XPS data are shown in Fig. 3, as well as the deconvolution of the experimental profiles into single chemical components. The BEs, FWHMs and relative amounts (%) of the different components in the different samples are reported in Tables 2–4, where the nature of each component is also briefly described. This process can furnish interesting information on the nature of the oxygen and nitrogen groups of the different carbon supports and their effect on the electronic properties of platinum.

In order to make a reliable deconvolution process, an accurate cross check of the BE and FWHM associated to each single components with literature data is needed. In this respect, we can also capitalize on the results of our previous studies on related systems (RGO[53,54] and N-HOPG[55–57]).

Table 3 Deconvolution of the N 1s XPS data into single chemical components for the NRGO and Pt/NRGO materials. For each single chemical component, the BE (eV), FWHM (eV) and amount (%) values are given

	Pt–N	Pyridinic	Pyrrolic	Graphitic	NO_x
NRGO	—	398.4	399.7	401.2	402.7
		1.4	1.38	1.19	1.4
		42.6%	46.4%	6.5%	4.5%
Pt/NRGO	397.7	398.7	399.8	401.2	402.5
	1.0	1.4	1.36	1.07	1.4
	25.1%	35.2%	28.6%	5.0%	6.1%

Table 4 Deconvolution of the Pt 4f XPS data into single chemical components for the Pt/C catalysts. For each single chemical component, the BE (eV), FWHM (eV) and amount (%) values are given

	Pt^0	Pt^{2+}	Pt^{4+}
Pt/graphite	71.0	72.2	74.6
	0.9	1.4	1.6
	65.7%	26.5%	7.8%
Pt/Vulcan	71.2	72.4	74.1
	1.0	1.4	1.5
	54.5%	31.5%	14%
Pt/RGO	70.9	72.2	73.9
	0.9	1.5	1.6
	66%	21%	13%
Pt/NRGO	71.2	72.1	73.7
	1.0	1.6	1.8
	40.2%	41.6%	18.2%

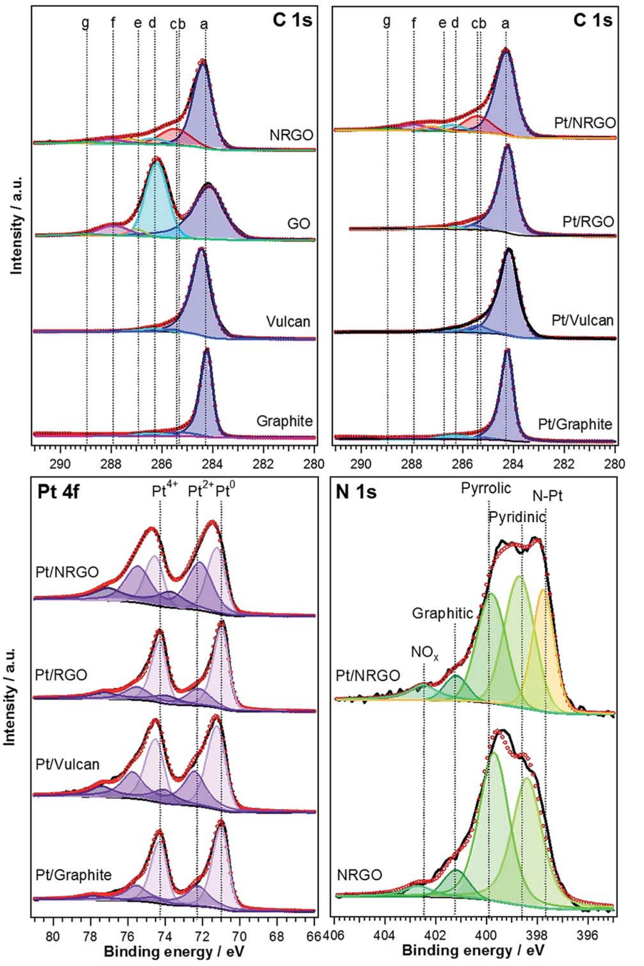

Fig. 3 Deconvolution of the C 1s, Pt 4f and N 1s photoemission lines of the carbon supports and of the Pt/C catalysts into single chemical components. The raw data is represented by a solid black line, whereas the fit is represented by red cycles. Assignation of components in C 1s photoemission line: (a) C sp^2, (b) C sp^3, (c) C–N, (d) alcohols, (e) epoxy, (f) carbonyl, (g) carboxylic groups.

Regarding the C 1s region, the main peak is always centered at 284.2 eV and it is associated to sp^2 hybridized carbon atoms (C sp^2). A minor component centered at 285.3 eV is also observed in some samples and it is associated to sp^3 hybridized carbon atoms (C sp^3). The Graphite samples (graphite and Pt/graphite) show also two minor components at 286.4 and 287.9 eV, attributed to tertiary alcohols and carbonyl groups, respectively, whereas the Vulcan samples (Vulcan and Pt/Vulcan) contain only a small amount of tertiary alcohols (286.3 eV). As expected, the GO sample contains a large amount of surface oxygenated groups, mainly tertiary alcohols (286.2 eV, *ca.* 38.8%), which are strongly reduced in samples containing RGO and NRGO. In fact, the fit of the C 1s photoemission line for NRGO confirms the presence of a graphitic sp^2 core whose basal planes are decorated by a small amount of oxygen functional groups, like tertiary alcohols (286.3 eV, *ca.* 5%) and epoxy (287 eV, 4.2%) groups. Small amounts of carbonyl and/or carboxylic groups, which are usually decorating the edges/holes of the basal plane, are also persisting in NRGO. Finally, the deconvolution process also reveals the presence of C–N bonds (peak centered at 285.4 eV). The nature of the C–N bonds will be discussed below with the analysis of the N 1s region. Only minor changes in the C 1s composition are found when passing from the clean substrates to the corresponding Pt/C catalysts (see Table 2).

The N 1s photoemission line can be separated into four components centered at 398.7, 399.8, 401.2 and 402.5 eV which are ascribed to pyridinic, pyrrolic, graphitic (substitutional), and oxidized nitrogen, respectively.[58] From the peak areas analyses (see Table 3), the main components of the N 1s lines are pyridinic and pyrrolic species. Pyridinic nitrogen is bonded to two carbon atoms and donates one p electron to the aromatic π system (C–N═C), whereas pyrrolic N atoms, incorporated into five-membered heterocyclic rings, are bonded to two carbon atoms and donate two p-electrons to the π-conjugated system. In the case of the Pt/NRGO sample, an additional component at 397.7 eV had to be included in the fit. To the best of our knowledge, no such a low BE component has been so far reported in literature for the N 1s peak in related systems. We suggest a correlation of such component with the effects of a strong Pt–N interaction. However, it is rather difficult to relate it to a specific type of N atom. It is interesting to highlight that this Pt–N component contributes significantly (25.1%) to the whole N 1s peak area.

Regarding the Pt 4f region, the spectra contain two peaks, which correspond to Pt $4f_{7/2}$ and $4f_{5/2}$ states from the spin–orbital splitting, and each peak was deconvoluted into three different Pt oxidation states (Pt^0, Pt^{2+} and Pt^{4+}) to identify the predominant oxidation state of Pt. As seen in Table 4, Pt^0 is the predominant oxidation state in all the Pt catalysts (around 54–66%) except in the Pt/NRGO, where the Pt^0 and Pt^{+2} species are comparable. The higher amount of Pt^{+2} species in the Pt/NRGO sample could also be interpreted as an evidence of the Pt–N interaction. This effect has been already reported in ref. 62. On the other hand, all samples present a variable amount of Pt^{+2} and Pt^{+4} species, deduced from the Pt $4f_{7/2}$ peaks at 72.1–74.6 eV. Their presence in all the samples can be attributed to the contact of the Pt NPs surface with air giving rise to Pt oxide phases. The fact that there is a considerable amount of oxidized species could be attributed to the small size of the Pt NPs (determined by TEM), resulting in a high percentage of Pt atoms on the surface of the NPs. A decrease in the amount of oxidized species can be observed for Pt/graphite and Pt/RGO samples. This can be associated with the formation of Pt islands resulting from the coalescence of small Pt nanoparticles leading to the formation of nanostructures possessing a higher crystallite size and consequently showing a different interaction with oxygen from the air. We note that the presence of oxides in supported Pd nanoparticles has been recently reported based on X-ray photoelectron spectroscopy analysis.[59] The presence of positively charged Pt ions could also suggest that there is an electron transfer from the Pt NPs to the underlying carbon support. The electron transfer from the Pt NPs to the carbon support has already been confirmed by theoretical calculations and experimental observations.[60–62] Moreover, there is a positive shift of around 0.3 eV of the Pt^0 component for the Pt/NRGO sample (71.2 eV), compared with the Pt/RGO sample (70.9 eV). This shift in the BE could confirm the electronic transfer from the Pt NPs to the carbon support through the N groups and be related to the Pt–N interactions observed in the N 1s photoemission at the lowest BE. In the literature, the Pt core-level f-band modification associated to N-doping effects has already been observed,[28,62] and it has been stated that the N functional groups might increase the electron affinity of the substrate, facilitating the Pt electron donation behavior, which may be the main reason for the improved Pt catalytic activity and durability of the N-doped Pt/C systems compared to the undoped Pt/C ones. We come back to this point in our DFT analysis in a later section.

3.2 Electrochemical measurements

The electrocatalytic properties of the prepared graphene-supported Pt nanocatalysts were studied using cyclic voltammetry (CV) and rotating-disk electrode (RDE). Results are shown in Fig. 4. Fig. 4a shows CV curves of the investigated electrocatalysts in the potential range varying from 0.05 to 1.2 V RHE^{-1}. The CV curves showed two distinctive potential regions associated with hydrogen adsorption/desorption process (H_{upd}) between 0.05 and 0.4 V RHE^{-1}, and with Pt oxidation beyond 0.7 V RHE^{-1}, where H_{upd} refers to the under-potential deposition of hydrogen. Platinum electrochemical surface area (ESA) values, calculated from H_{upd} region, assuming a charge transfer of 210 μC cm^{-2} on Pt surface,[63] were 34 m^2 g^{-1}, 28 m^2 g^{-1} and 20 m^2 g^{-1} for Pt/NRGO, Pt/RGO and Pt/graphite catalysts, respectively, indicating that the utilization of Pt/NRGO and Pt/RGO were approaching that of conventional Pt/Vulcan catalyst with 30 m^2 g^{-1} (see Table 5). Additionally, in comparison with Pt/Vulcan, Pt/RGO, Pt/graphite and Pt/NRGO showed higher potentials for the Pt oxide reduction peak, revealing that the Pt surface can be reduced at higher potentials, which can lead to an enhancement of the ORR activity. It should be noticed that the –OH formation at the surface of Pt/NRGO catalyst is to some extent inhibited in comparison with the other catalysts. The inhibition for H_2O activation is well-known to be responsible for enhancing the activity of Pt towards ORR.[64] This fact is greatly supported by XPS results with a down-shift BE of Pt 4f electrons. A similar effect was previously reported and contributes to the beneficial strong interaction between Pt–C hybridization.[5,18]

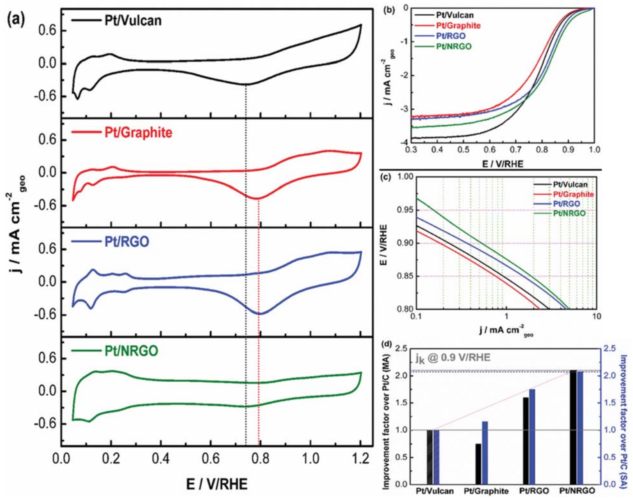

Fig. 4 Comparison of catalytic properties of carbon supported Pt electrocatalysts. (a) CV curves recorded at 25 °C in N_2-saturated 0.5 M H_2SO_4 at a scan rate of 50 mV s^{-1}. (b) ORR curves in an O_2-saturated 0.5 M H_2SO_4 at a scan rate of 5 mV s^{-1} and a rotating rate of 900 rpm. (c) Tafel slopes extracted from ORR polarization curves. (d) Relative mass activity (MA, black color) and relative specific activity (SA, blue color) at 0.9 V *vs.* RHE for the investigated electrocatalysts. Mass and specific activities are given as kinetic current densities (j_k) normalized to the loading amount and electrochemical surface active area (ESA) of Pt, respectively.

Table 5 Electrochemical active surface area (ESA), half-wave potential ($E_{1/2}$) and Tafel slopes calculated from the H_{upd} and ORR polarization curves of carbon supported Pt electrocatalysts

	ESA ($m^2\ g^{-1}$)	$E_{1/2}$ (V *vs.* RHE)	Tafel slope (mV dec^{-1})
Pt/NRGO	34	0.825	95.3
Pt/RGO	28	0.820	81.4
Pt/graphite	20	0.785	84.6
Pt/Vulcan	30	0.795	85.2

The ORR polarization curves obtained with the investigated samples are shown in Fig. 4b. It can be seen that Pt/NRGO shows a remarkably high electrocatalytic activity towards ORR in acid medium since the half-wave potential was *ca.* 0.825 V RHE^{-1} and largely higher than what can be obtained (*ca.* 0.795 V RHE^{-1}) with the conventional Pt/Vulcan catalyst, whereas half-wave potentials were respectively 0.820 V RHE^{-1} and 0.785 V RHE^{-1} for Pt/RGO and Pt/Graphite catalysts (see Table 5). Further kinetic information on the electron–transfer reaction mediated by the Pt/NRGO, Pt/RGO, Pt/Graphite catalysts in comparison with Pt/Vulcan catalyst, is shown in Fig. 4c. It shows Tafel plots after mass-transfer correction. The Tafel slopes indicate that the reaction pathway and the rate-determining step are similar for Pt/RGO (81.4 mV dec^{-1}), Pt/graphite (84.6 mV dec^{-1}) and Pt/Vulcan (85.2 mV dec^{-1}) catalysts, whereas a small variation of the Tafel slope can be observed with Pt/NRGO (95.3 mV dec^{-1}) materials (see Table 5). This can be associated with a different adsorption isotherm and with a different rate determining step. The kinetic current was calculated from the ORR curves according to the Koutecky-Levich equation[65] as follows:

$$\frac{1}{j} = \frac{1}{j_{\text{d}}} + \frac{1}{j_{\text{k}}} \tag{2}$$

where j is the measured current, j_{d} is the diffusion-limiting current, and j_{k} is the kinetic current. The kinetic current was calculated by the equation:

$$j_{\text{k}} = \frac{j \times j_{\text{d}}}{j_{\text{d}} - j} \tag{3}$$

Additionally, it is obvious that the kinetic current densities of Pt/NRGO and Pt/RGO are higher than that of Pt/Vulcan highlighting the improved ORR activities on graphene-supported Pt catalysts.

The mass and specific activities at 0.9 V RHE^{-1} for all the investigated catalysts are reported in Fig. 4d. It can be observed that Pt/NRGO exhibits a mass activity, which is 2.1-fold higher than that of conventional Pt/Vulcan catalyst. Moreover, Pt/RGO displays a mass activity, which is 1.6-fold higher than that of Pt/Vulcan catalyst. In contrast, Pt/Graphite shows the lowest mass activity in reason of the low utilization of Pt in this sample. This is in agreement with the calculated ESA values.[66] Interestingly, the specific activities of Pt/NRGO, Pt/RGO and Pt/Graphite are higher than that obtained with conventional Pt/Vulcan catalyst. This difference in ORR activity most likely arises from the electronic modification of Pt generated by the substrate effect.

3.3 Theoretical considerations

Properties of the support. The presence of the functional groups and dopants affect the geometric and electronic properties of the carbon support. The geometric changes are very small leading to a slight increase in the lattice parameters and bond distances. However, the changes in the electronic structure are more evident as the functional groups and nitrogen are more electronegative as shown by their Bader charges (ESI Table S1†). Therefore, the Density of States (DOS) of the studied systems present interesting features as depicted in Fig. 5. The electronic population distribution of graphene is observed in Fig. 5a. The addition of pyridinic N leads to the formation of new states especially at the Fermi level (Fig. 5a′). These new states will be responsible for enhancement of the electric conductivity as they increase the metallic behavior of the system. Another peak at ∼−1.0 eV (below the Fermi level) may be responsible for a higher number of electrons available for transfer during the interactions of the surface with metallic clusters or molecules. The electronic structure of graphene oxide changes significantly as the amount of functional groups is raised (Fig. 5b, b′, c, and c′). When the quantity of oxygenated functional groups is higher (HOG) the system becomes semiconductor with a band gap close to ∼3.0 eV (Fig. 5c); for LOG conditions the system is still metallic but O and OH almost discrete states are present below and above the vicinity of the Fermi level (Fig. 5b). The addition of a single N atom (∼3 at.%) causes changes in the DOS of GO, under LO conditions there is broadening of the distribution of states near the Fermi level but the influence is less dramatic since the system was already

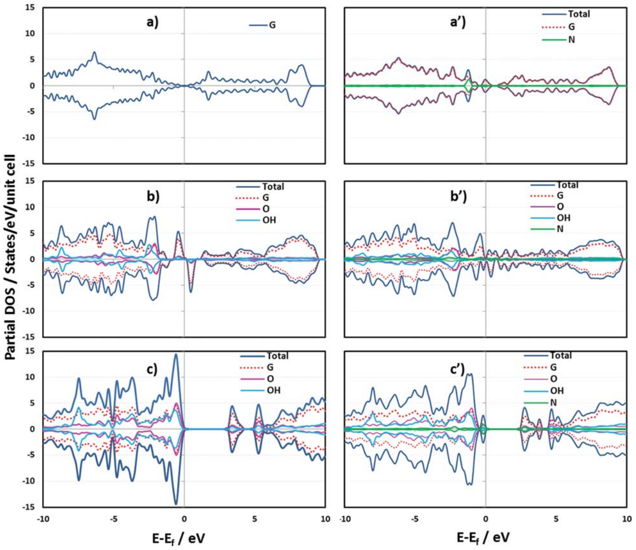

Fig. 5 Partial DOS (in states/eV) for the studied support materials: (a) Graphene, (a′) N-doped graphene, (b) LOG, (b′) N-doped LOG, (c) HOG and (c′) N-doped HOG. Positive and negative DOS branches represent spin up and down electrons respectively. The horizontal axis displays relative energies $E - E_{\text{f}}$ (in eV) where E_{f} is the Fermi level.

metallic (Fig. 5b′), but for HOG the band gap decreases by ~0.5 eV (Fig. 5c′).

Interaction of the substrate with Pt_4. A Pt_4 cluster was relaxed in the tetrahedral geometry, and once optimized it was allowed to interact with the support. Fig. S2† depicts the Pt_4 cluster interacting with O_2, and supported clusters interacting with nitrogen doped supports. Fig. S3† depicts the interaction of the cluster with LOG and HOG. The interaction energy (E_{int}) of the cluster with the support was calculated as the energy difference between the separated systems and the resultant geometry after the relaxation procedure. Table 6 indicates that E_{int} varies depending on the structure of the support and the participating site. Several structures and sites were analyzed; however, as the size of the cluster is very small and has a low cohesive energy, in some cases the deformation of the cluster is very large. It should be noted that the interaction energy calculated in this way does not take into account cluster deformation which is observed as a consequence of this interaction. Nevertheless, the interaction of the support with this small cluster is strong and all effects resultant from this interaction are enhanced with respect to the unsupported cluster. For example, reactivity trends of CO adsorption on supported clusters are qualitatively well represented,[67,68] while quantitative information can be obtained analyzing the interaction of the support with a larger cluster, as reported in a later section.

The weakest metal–substrate interaction is obtained with the intrinsic sites of the graphene layer (Table 6); stronger effects depend on the specific site and closeness of the metallic sites from the functional groups that decorate the support. In the case of the structures doped with nitrogen (G-1N and G3-N) the interaction energy is more than twice that obtained with graphene (Table 6). Stronger metal–support interaction energies represent advantages in fuel cell electrocatalysts where the mobility and aggregation of the cluster is one of the main problems associated to durability. The stronger metal–support interactions for N-doped graphene are in agreement with the TEM images of the N-doped support revealing well distributed particles while all other samples show evidence of particle agglomeration. The interaction of the cluster with three nitrogen atoms-support (G-3N) not only enhances the interaction energy but leads to a higher charge transfer from the cluster to the support as shown by the average Pt charge in Table 6, in agreement with the observations reported by Gracia Espino *et al.*[69] in core–shell Pt–Ni clusters. The extent of charge transfer is a very important property for the catalytic activity because electron transfer from the metal directed towards the support may limit the metallic surface ability to provide electrons for the chemical or electrochemical reduction reactions. Stronger metal–support interaction energy is found for GO in all of the oxidation states and in presence of functional groups. The degree of oxidation also affects the interactions: in LOG the smaller amount of functional groups allows the cluster atoms to interact mostly with carbon atoms; whereas in the HOG the cluster is able to mostly interact with the functional groups instead of carbon. Therefore, in the OH side of LOG, when the cluster is interacting totally with carbon atoms the interaction energy is stronger than in graphene but the charge transfer is similar to that in graphene. Conversely, in the O side of HOG the cluster is totally in contact with the epoxy groups and not interacting with carbon atoms. At these conditions, the interaction energy is weaker but the charge transfer is very high. The most significant charge transfer is obtained in the O side of the LOG, where the cluster interacts with carbon atoms in the support but also with oxygen atoms of the epoxy groups. Therefore, in general the oxygen functional groups enhance the metal–substrate interaction strength and lead to higher charge transfer but an excessive amount of oxygenated groups as in HOG offers disadvantages. This is primarily because of the HOG semiconducting behavior discussed above and secondly because of the higher feasibility of oxidation and formation of CO_2. The addition of nitrogen to GO slightly modifies the interaction energy strength and enhances the charge transfer but only when the cluster interacts directly with the nitrogen atom, in any other case the behavior is very similar to the non-nitrogenated substrates.

Under the effect of O_2 adsorption the deformation of the cluster was found to be more severe, thus only the simulations in which the cluster retains its original shape are reported. The adsorption was modeled by addition of O_2 directly on one of the bridge sites of the cluster. It is worth mentioning that in the unsupported cluster the adsorption of oxygen is the strongest compared to those on any of the supported clusters. The

Table 6 DFT calculated interaction of Pt_4 with the various supports and changes in O_2 adsorption energy

		$S–Pt_4$			$S–Pt_4–O_2$			
		E_{int}/eV	Pt–C/Å	Pt charge/a.u.	Oxygen Ads/eV	O–O distance	O_2 charge	O–Pt
Pt_4				0.0	−1.97	1.438	−0.61	1.971–1.974
Graphene		−1.15	2.28 (Bridge)	+0.10	−1.33	1.396	−0.57	1.989–2.037
G-1N		−2.74	2.04(2.15 – N)	+0.26	−1.41	1.430	−0.64	1.898–1.948
G-3N		−2.43	(2.13 – N)	+0.44	−1.50	1.451	−0.65	1.891–1.931
LOG	OH side	−2.67	2.18	+0.16	−1.33	1.386	−0.57	1.960–2.095
	O Side	−7.85	2.23(2.01 – O)	+0.98	−1.26	1.493	−0.63	1.902–1.923
HOG	OH side	−1.89	2.25(2.01 – O)	+0.55				
	O Side	−2.01	(2.14 – O)	+0.78	−1.35	1.398	−0.56	2.028–1.988
LOG-N		−2.8	2.12(2.10 – N)	+0.34				
HOG-N		−2.16		+0.89				

distance Pt–O_2 also changes. Two Pt–O distances are reported in Table 6 (last column): the first corresponds to the oxygen adsorbed on a Pt atom not interacting with the support while the second corresponds to the Pt atom interacting directly with the support. On the unsupported Pt cluster both of them are equal, but in the supported clusters the first is shorter and the second larger, indicating that the interaction of Pt with the support causes weaker oxygen adsorption (larger Pt–O distance) especially near the Pt–support interface. The charge transferred from the cluster to the adsorbate is higher when the cluster is only donating electrons to the O_2 molecule. The presence of the C support diminishes the O_2 adsorption energy (Table 6 and Fig. S2†) and also reduces the amount of charge that is transferred from the cluster to O_2 because the cluster is also donating charge to the support. Therefore the distances O–Pt are larger and the O–O distance is shorter (Table 6 and Fig. S2-a, and -b†) *i.e.* the reduction of O_2 is more difficult.

The interaction of Pt_4 with N-doped graphene causes stronger O_2 adsorption than that in Pt_4–graphene but still weaker than that on the unsupported cluster. The Pt–O distances are shorter than those in Pt_4–graphene and the unsupported case. Also the charge transfer to the adsorbate (Table 6) is even higher than that in the unsupported case. Moreover, a higher number of dopant N atoms (G-3N) enhances this charge transfer to O_2 leading to an elongated O–O distance indicating that the mere presence of nitrogen is able to facilitate the O–O bond breaking, again in agreement with the analysis of Gracia Espino *et al.*[69] For the interaction with GO, the charge transferred from Pt_4 to O_2 is lower indicating that the presence of oxygenated species in the support (because of the oxygen higher electronegativity) causes electron retention. Part of these electrons are needed for the cluster–substrate interaction; therefore, especially in the O-side of the HOG in which the cluster interacts totally with oxygen atoms and not with carbon atoms the charge transfer is the lowest and the O–O distance becomes only slightly higher than its gas phase value while the Pt–O distances are large. Especial attention deserves the LOG in the O-side (Fig. S3b†) which presents higher charge transfer to O_2 and the largest O–O distance; in this case the Pt_4 cluster interacts with epoxy groups but with carbon atoms as well. This scenario seems to be favorable for O_2 reduction suggesting that a lower amount of decorating functional groups is more favorable for reactivity. Note that the geometry of the cluster also changes significantly in this case.

The analysis of the interaction of a small cluster with doped and functionalized supports led us to conclude that charge transfer from the support to the adsorbed molecule is a very important property. If the dopant or functional groups retain the electrons very strongly, the cluster will have a limited capacity to donate electrons to O_2 but if the cluster can receive electrons from the support and is able to donate them during the catalytic reaction then the catalytic activity could be enhanced.

The experimental results of N-doped graphene reported nitrogen concentrations close to 15 at.%. In the simulations reported so far, the N concentration was close to 3 at.% N. The simulations in this section are aimed to better represent the effect of the N-doped support on a more realistic nanoparticle size and higher N concentrations. A Pt_{38} cluster $\sim$0.8 nm diameter was allowed to interact with a 7 × 7 graphene layer. To model the interaction with N-doped graphene support two degrees of doping were used: 3N-doped (N 3 at.%) and 6N-doped (N 6 at.%). The 3N-doped was simulated by eliminating one carbon atom and exchanging the carbon atoms with dangling bonds by N. For the 6N-doped three carbon atoms were eliminated and the formed carbon dangling bonds were exchanged with pyridinic nitrogen. The influence of oxygenated functional groups is supposed to be minimal according to the experimentally found low concentration of oxygenated species. For the cluster Pt_{38} interacting with the 3N-doped graphene, the three nitrogen atoms interact only with one Pt atom while the other Pt atoms are interacting with carbon atoms (Fig. S4-c†); on the other hand on the 6N-doped support each nitrogen interacts with a platinum atom at the interface, so six out of seven Pt atoms at the interface are interacting with nitrogen (Fig. S4-d†). It is important to point out that the DFT results suggest the formation of Pt–N bonds observed both in the Pt_4 and Pt_{38} models (Fig. S2-c and -d, and S4-c and -d† respectively), in agreement with the conclusions from our XPS experiments and also with previous calculations.[69]

Properties of the support. Fig. 6 shows the density of states of the graphene sheet compared with those of the doped graphene with various N concentrations. As discussed above, new states arise near the Fermi level and those are enhanced with a higher N concentration. There is also a higher charge transfer from carbon atoms to nitrogen being reflected on the total charge of the graphitic structure. Table S2† reports the total charge donated as the amount of nitrogen increases. The interaction energy was calculated as in the previous section. However, here we included the deformation effects of both support and cluster. Table S2† shows that for graphene the interaction energy is very weak even becoming slightly positive if the deformation is not taken into account, also charge transfer occurs, but graphene donates a small amount of charge to the cluster. For N-doped graphene the interaction energy without considering deformation effects is stronger compared to pure graphene and is enhanced as the N concentration increases. However if the deformation is taken into account the interaction energies of the cluster with the two N-doped substrates are comparable but very strong in comparison to that of the cluster supported on graphene, thus confirming the strong cluster–support interaction in the N-doped substrate.

Also the charge transfer follows the same trend observed in Pt_4 in which the Pt cluster donates charge to N and carbon atoms. In ESI Fig. S4,† the geometry of the Pt_{38} cluster is depicted showing the main (111) and (100) planes. The clusters interact with the support through one of the (111) planes, and as the number of N atoms increases the cluster becomes closer to the support due to strong Pt–N interactions. We acknowledge that for this cluster size, other morphologies may also be present in fuel cell environments. Previous DFT studies of growth of Pt clusters[70] have determined that clusters evolve from icosahedral type (approximately 13–38 atoms) towards fcc-

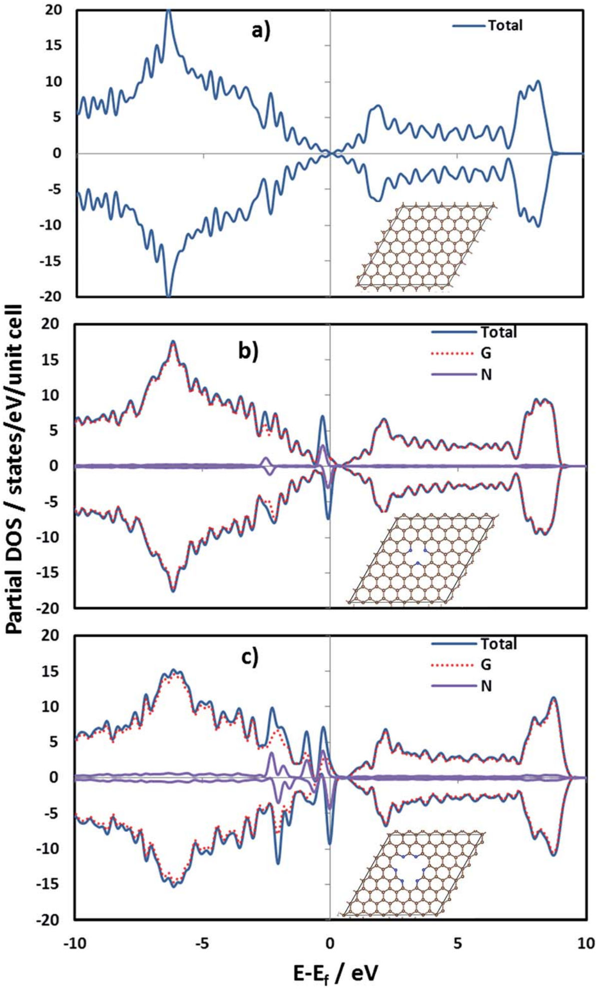

Fig. 6 Partial DOS (in states/eV) of the support (a) graphene, (b) 3N-doped graphene and (c) 6N-doped graphene. Insets show the structure, carbon atoms in brown and nitrogen in blue spheres.

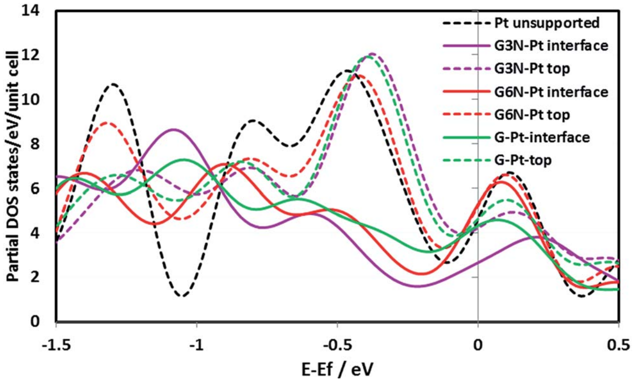

Fig. 7 Partial density of states (in states/eV) *vs.* relative energies $E - E_f$ where E_f is the energy of the Fermi level. Contributions of Pt atoms at the top of the cluster and at the interface are separated for the supported cluster. The DOS for the unsupported cluster (involving all atoms) is also shown.

like (>38 atoms). Thus we may expect a mixture of icosahedral and fcc-like clusters at this cluster size.

Electronic properties of the supported Pt_{38} cluster. The partial DOS of the cluster is depicted in Fig. 7. To identify contributions from interfacial atoms and atoms in the top of the cluster they are shown separately. In the unsupported case there are no interfacial atoms; therefore both sides of the cluster, as the cluster is symmetrical, are the same. For the supported cluster, the partial DOS of interfacial atoms are very different to those of the atoms located at the top of the cluster (far from the support). Moreover, the DOS at the top of the cluster are shifted slightly towards more positive values than the unsupported cluster. For the atoms in the upper part of the cluster a relatively large shift toward the Fermi level is found with respect to the DOS of the unsupported cluster when the cluster interacts with graphene, and with G-3N and G-6N. On the other hand, the interaction of G-6N with the cluster atoms at the interface with the substrate leads to higher changes. These changes are expected to have an effect on the catalytic behavior of the nanoparticles, O_2 and O adsorption (key stages in the oxygen reduction) as discussed in the next section.

Table 7 reports the calculated O_2 and O adsorption energies on top of the cluster. The O_2 adsorption energies in the various systems are very comparable. However, they are weaker compared to the case of the unsupported cluster. On the other hand, the O–O distance is shorter in the unsupported cluster while the effect of the support facilitates O_2 dissociation leading to slightly longer O–O distances. Although these differences are small, and the changes in charge transfer to the adsorbate are also small, the supported cases always lead to higher charge transfer in comparison to graphene.

The presence of nitrogen makes the extent of the charge donation from the cluster to the adsorbed molecule slightly lower in comparison to the trends observed for the small Pt_4 cluster.

We also evaluated the adsorption of atomic oxygen, to have a measure of the interactions with the ORR intermediate species. The strongest O adsorption is found on the unsupported cluster, whereas it is slightly weaker on all supported clusters; however the differences between doped and non-doped are small and no significant differences are observed as the concentration of dopant is increased. On the other hand, the charge transfer from the cluster to the adsorbed molecule is higher on supported clusters; however, the extent of charge donation seems to be smaller as the N concentration in the support increases. Finding materials that adsorb oxygenated compounds slightly weaker than on Pt may represent advantages for the oxygen reduction reaction. This is especially important for the OH species which can poison the catalyst if strongly adsorbed. Therefore the interaction of the supported metallic cluster may be beneficial because of the weaker adsorption of oxygenated species. In addition, as the interaction of the cluster with the support is higher in the doped support, this will provide enhanced stability.

Finally, given that the influence of the support can be greater or lower depending on the location of the O_2 adsorption site on the nanoparticle surface. To probe this statement we allowed O_2 adsorption in two additional sites, one at the middle of the cluster and another in a site in which one of the oxygen atoms is

Table 7 Adsorption energies and properties of O_2 and O on Pt_{38} unsupported and over the supports discussed in this study

	Pt_{38}–O_2							Pt_{38}–O				
		d/Å		Charges (e)					Charges (e)			
	E_{ads} (eV)	O–O	Pt–O	G	N	Pt	O_2	E_{ads} (eV)	G	N	Pt	O
Pt_{38}	−1.42	1.401	1.953	—	—	0.5764	−0.5764	−4.98	—	—	0.6760	−0.6760
G–Pt_{38}	−1.39	1.410	1.956	0.1318	—	0.4993	−0.6310	−4.79	0.1032	—	0.5836	−0.6865
G3N–Pt_{38}	−1.38	1.411	1.948	2.8106	−3.0126	0.8221	−0.6199	−4.83	2.7955	−3.033	0.9275	−0.6900
G6N–Pt_{38}	−1.31	1.410	1.953	5.9439	−6.3993	1.0685	−0.6128	−4.81	5.9056	−6.3406	1.1208	−0.6859

interacting directly with a Pt atom located at the interface (ESI, Fig. S5† depicts the sites for O adsorption in the three cases). The position of oxygen is similar in the supported clusters *i.e.* in the same type of cluster facet (111), bridge site in atoms with similar connectivity; the only difference is in the closeness respect to the support). We note that the spin polarization distribution in both Pt_4 and Pt_{38} may be also affected by the adsorption of the oxygenated species probably also affecting their reactivity.

The values for O_2 adsorption reported in Table 8 indicate that the effect of the support is accentuated when the molecules are closer to the support. Two values for adsorption energy are reported, one calculated without considering the changes in geometry after adsorption and the second including the geometry changes. Results for adsorption on the top of the cluster without cluster reconstruction the results have already been discussed in the previous section. For O_2 locations at the middle of the cluster surface the adsorption in all cases is weaker (than in the unsupported case and that in the top of the cluster); among them the G-3N is considerably weaker than all the others. At the cluster–support interface the G-3N support leads to the lowest adsorption energy. In the G and G-6N supports, even though the initial site and geometry for oxygen adsorption in the three supports was the same, the oxygen molecule tends to migrate from the interface to the middle leading to adsorption in a hollow site (Fig. 8). After migration the adsorption is stronger (even stronger than in the supported case for Pt_{38}–G and very similar to the unsupported case in Pt_{38} G-6N). In order to compare the O_2 adsorption in the same site, a new simulation in a hollow site in the G-3N was performed (value in parenthesis in Table 8). In that case the O–O distance is longer and the charge transferred to the O_2 molecule is larger, confirming an additional higher effect owed to the N-doped support. When the reconstruction is taken into account the same trends are observed. However the O_2 adsorption on top of the G–Pt_{38} is stronger than that in the unsupported case, while for O_2 adsorptions closer to the support the presence of N-species in the support leads to a weaker O_2 adsorption.

To investigate this point, it is useful to examine the interactions between the cluster and the support. In some cases the adsorption of O_2 has an effect on the separation between the cluster and the support. When adsorption is allowed in the top or in the middle of the cluster the changes in cluster–support separation for all the supports are negligible; however, when O_2 is very close to the interface the distance cluster–support is elongated, especially in the undoped graphene-supported cluster where the changes lead to the an almost total separation of the cluster from the support. In contrast, in the G-3N case only two of the interacting platinum atoms are slightly more separated from the support and in the G-6N support the connectivity of the cluster remained the same (Fig. 8). Therefore, this confirms that the strong interaction with the nitrogen-doped support besides enhancing the catalytic activity may also lead to a higher stability. Moreover, the differences in catalytic activity of Pt on the N-doped support can also be related to a stronger metal–substrate interaction which leads to no changes in the cluster–support separation in the presence of oxygen. On the contrary, the separation between the cluster and support in the non-doped system could lead to a higher resistance for electron transfer. Interestingly, the interaction of the cluster with only pyridinic nitrogen does not lead to a further enhancement of the catalytic activity; the presence of carbon and nitrogen atoms interacting with the cluster is the best option to enhance both the catalytic activity and stability of the nanoparticle for cathodes in fuel cells, *cf.* Section 3.2.

Table 8 O_2 adsorption energy (in eV) in Pt_{38} as a function of the adsorption site. The first value is the total adsorption energy and the second value (after the slash) is the adsorption energy taking into account the deformation of both cluster and support. Value in parenthesis for adsorption at the interface in the Pt_{38}–G-3N corresponds to the hollow site

	Top	Middle			Interface		
$Pt_{38\text{-unsupported}}$	−1.42/−1.96	E_{ads}	O–O/Å	B.C/e^-	E_{ads}	O–O/Å	B.C/e^-
Pt_{38}–1G	−1.39/−2.01	1.37/−1.97	1.4093	−0.62	−1.90/−2.18	1.4827	−0.73
Pt_{38} G–3N	−1.38/−1.96	1.19/−1.63	1.4092	−0.61	−0.97/−1.27, (−1.71/−2.18)	1.3813, (1.4896)	−0.55, (−0.75)
Pt_{38} G–6N	−1.31/−1.82	−1.33/−1.87	1.4051	−0.61	−1.43/−2.03	1.4837	−0.74

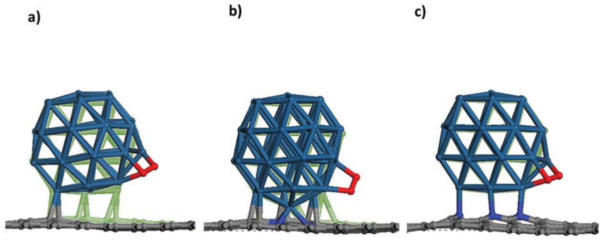

Fig. 8 Final configuration of the adsorption of oxygen at the cluster–support interface (Pt, C and O in blue, gray and red spheres respectively). The initial geometry of the supported cluster without oxygen is depicted in the back as green shadows. (a) Pt_{38}–G, (b) Pt_{38}–G-3N and (c) Pt_{38}–G-6N.

4. Conclusions

In this study, low-mass loading catalysts (*ca.* 5 wt% Pt/C) were synthesized *via* the carbonyl chemical route allowing for the heterogeneous deposition of Pt nanoparticles onto different carbon-based substrates. N-doped RGO, RGO, GO graphite and Vulcan XC-72 were used as substrates. Raman spectroscopy showed that except for graphite all the graphitic materials investigated in this study presented low inter-defect lengths. On the N-doped material, the XPS data analysis revealed that the N 1s photoemission line can be deconvoluted into different chemical signatures namely, pyridinic, pyrrolic, graphitic and oxidized nitrogen. The main components were pyridinic and pyrrolic species. The examination of Pt 4f photoemission peaks showed that a non-negligible amount of Pt atoms (25%) are chemically bound to N atoms, which was confirmed by the DFT analysis. This strong interaction between Pt clusters and N atoms allows for an electronic transfer from Pt to the carbon support, also predicted by our DFT calculations. Electrochemical measurements have shown that NRGO as substrates led to an increase in the mass activity of the catalyst at 0.9 V *vs.* RHE. This can be related to changes in the oxygen adsorption energy at the platinum surface. DFT calculations show that the molecular and atomic oxygen adsorption is weaker for the N-containing substrates. The DFT results reveal that the O–O distance is much elongated in the case of the N-doped substrates, which suggests lower barriers for O_2 dissociation. This is a first point to explain the increased electrocatalytic activity of Pt/NRGO toward the ORR. It should be added that the weaker O_2 and O adsorption suggest that other oxygenated compounds, such as OH may also be weaker on the catalysts supported in the N-doped substrates, which would further enhance the catalytic activity given that strongly adsorbed OH is a well-known catalyst poison. Additionally, in contrast to the non-doped systems, calculations have shown that the strong interaction between Pt clusters and N-doped graphene led to no changes in cluster–support separation with the presence of adsorbed molecular oxygen. We suggest that this stronger interaction may be responsible for a decrease in the resistance for electron transfer between the cluster and the substrate facilitating the electrochemical reactions. All results obtained in this study are of major importance and lay the basis for the development and demonstration of new cathode architectures for low temperature proton exchange membrane fuel cells.

Acknowledgements

JM thanks the fellowship of "Ministère de l'Enseignement Supérieur et de la Recherche". GRS thanks CONACYT (Mexico) for the postdoctoral fellowship. The authors thank Mrs C. Canaff for her technical assistance with XPS measurements. This work was partially supported by the European Union's Seventh Framework Programme (FP7/2007–2013) for the Fuel Cell and Hydrogen Joint Technology Initiative under grant agreement nr. 303492 CathCat.

Notes and references

1 M. K. Debe, *Nature*, 2012, **486**, 43–51.
2 H. A. Gasteiger, S. S. Kocha, B. Sompalli and F. T. Wagner, *Appl. Catal., B*, 2005, **56**, 9–35.
3 J. Wu and H. Yang, *Acc. Chem. Res.*, 2013, **46**, 1848–1857.
4 A. Manzo-Robledo, A. C. Boucher, E. Pastor and N. Alonso-Vante, *Fuel Cells*, 2002, **2**, 109–116.
5 J. Ma, A. Habrioux and N. Alonso-Vante, *ChemElectroChem*, 2014, **1**, 37–46.
6 F. Hasche, M. Oezaslan and P. Strasser, *Phys. Chem. Chem. Phys.*, 2010, **12**, 15251–15258.
7 Y.-C. Park, K. Kakinuma, M. Uchida, D. A. Tryk, T. Kamino, H. Uchida and M. Watanabe, *Electrochim. Acta*, 2013, **91**, 195–207.
8 A. Lewera, L. Timperman, A. Roguska and N. Alonso-Vante, *J. Phys. Chem. C*, 2011, **115**, 20153–20159.
9 L. Timperman, A. Lewera, W. Vogel and N. Alonso-Vante, *Electrochem. Commun.*, 2010, **12**, 1772–1775.
10 J. Ma, A. Habrioux and N. Alonso-Vante, *J. Solid State Electrochem.*, 2013, **17**, 1913–1921.
11 V. T. T. Ho, C.-J. Pan, J. Rick, W.-N. Su and B.-J. Hwang, *J. Am. Chem. Soc.*, 2011, **133**, 11716–11724.
12 C. V. Subban, Q. Zhou, A. Hu, T. E. Moylan, F. T. Wagner and F. J. DiSalvo, *J. Am. Chem. Soc.*, 2010, **132**, 17531–17536.
13 K. Gong, F. Du, Z. Xia, M. Durstock and L. Dai, *Science*, 2009, **323**, 760–764.
14 E. Yoo, T. Okata, T. Akita, M. Kohyama, J. Nakamura and I. Honma, *Nano Lett.*, 2009, **9**, 2255–2259.
15 C. Huang, C. Li and G. Shi, *Energy Environ. Sci.*, 2012, **5**, 8848–8868.
16 M. Liu, R. Zhang and W. Chen, *Chem. Rev.*, 2014, **114**, 5117–5160.
17 R. Siburian, T. Kondo and J. Nakamura, *J. Phys. Chem. C*, 2013, **117**, 3635–3645.
18 J. Ma, A. Habrioux, C. Morais, A. Lewera, W. Vogel, Y. Verde-Gómez, G. Ramos-Sanchez, P. B. Balbuena and N. Alonso-Vante, *ACS Catal.*, 2013, **3**, 1940–1950.
19 P. Xu, L. Dong, M. Neek-Amal, M. L. Ackerman, J. Yu, S. D. Barber, J. K. Schoelz, D. Qi, F. Xu, P. M. Thibado and F. M. Peeters, *ACS Nano*, 2014, **8**, 2697–2703.

20 D. He, K. Cheng, H. Li, T. Peng, F. Xu, S. Mu and M. Pan, *Langmuir*, 2012, **28**, 3979–3986.

21 D. He, Y. Jiang, H. Lv, M. Pan and S. Mu, *Appl. Catal., B*, 2013, **132–133**, 379–388.

22 G. He, Y. Song, K. Liu, A. Walter, S. Chen and S. Chen, *ACS Catal.*, 2013, **3**, 831–838.

23 J. Ma, A. Habrioux, N. Guignard and N. Alonso-Vante, *J. Phys. Chem. C*, 2012, **116**, 21788–21794.

24 H. Wang, T. Maiyalagan and X. Wang, *ACS Catal.*, 2012, **2**, 781–794.

25 J. Bai, Q. Zhu, Z. Lv, H. Dong, J. Yu and L. Dong, *Int. J. Hydrogen Energy*, 2013, **38**, 1413–1418.

26 A. Zahoor, M. Christy, Y. J. Hwang, Y. R. Lim, P. Kim and K. S. Nahm, *Appl. Catal., B*, 2014, **147**, 633–641.

27 H. Wang, M. Xie, L. Thia, A. Fisher and X. Wang, *J. Phys. Chem. C*, 2013, **5**, 119–125.

28 Y. Zhou, R. Pasquarelli, T. Holme, J. Berry, D. Ginley and R. O'Hayre, *J. Mater. Chem.*, 2009, **19**, 7830–7838.

29 W. S. Hummers and R. E. Offeman, *J. Am. Chem. Soc.*, 1958, **80**, 1339.

30 N. Alonso-Vante, *Fuel Cells*, 2006, **6**, 182–189.

31 M. Wojdyr, *J. Appl. Crystallogr.*, 2010, **43**, 1126–1128.

32 S. Doniach and M. Sunjic, *J. Phys. C: Solid State Phys.*, 1970, **3**, 285.

33 R. J. W. E. Lahaye, H. K. Jeong, C. Y. Park and Y. H. Lee, *Phys. Rev. B: Condens. Matter Mater. Phys.*, 2009, **79**, 125435.

34 P. E. Blochl, *Phys. Rev. B: Condens. Matter Mater. Phys.*, 1994, **50**, 17953–17979.

35 G. Kresse and D. Joubert, *Phys. Rev. B: Condens. Matter Mater. Phys.*, 1999, **59**, 1758–1775.

36 G. Kresse and J. Furthmuller, *Comput. Mater. Sci.*, 1996, **6**, 15–50.

37 G. Kresse and J. Hafner, *Phys. Rev. B: Condens. Matter Mater. Phys.*, 1993, **48**, 13115–13118.

38 H. J. Monkhorst and J. D. Pack, *Phys. Rev. B: Solid State*, 1976, **13**, 5188–5192.

39 J. Schwan, S. Ulrich, V. Batori, H. Ehrhardt and S. R. P. Silva, *J. Appl. Phys.*, 1996, **80**, 440–447.

40 J. Kohanoff, *Comput. Mater. Sci.*, 1994, **2**, 221–232.

41 R. E. Shroder, R. J. Nemanich and J. T. Glass, *Phys. Rev. B: Condens. Matter Mater. Phys.*, 1990, **41**, 3738–3745.

42 M. Veres, S. Tóth and M. Koós, *Diamond Relat. Mater.*, 2008, **17**, 1692–1696.

43 M. A. Pimenta, G. Dresselhaus, M. S. Dresselhaus, L. G. Cancado, A. Jorio and R. Saito, *Phys. Chem. Chem. Phys.*, 2007, **9**, 1276–1290.

44 L. C. Nistor, J. Landuyt, V. G. Ralchenko, T. V. Kononenko, E. D. Obraztsova and V. E. Strelnitsky, *Appl. Phys. A: Mater. Sci. Process.*, 1994, **58**, 137–144.

45 T. Jawhari, A. Roid and J. Casado, *Carbon*, 1995, **33**, 1561–1565.

46 E. F. Antunes, A. O. Lobo, E. J. Corat, V. J. Trava-Airoldi, A. A. Martin and C. Veríssimo, *Carbon*, 2006, **44**, 2202–2211.

47 V. Mennella, G. Monaco, L. Colangeli and E. Bussoletti, *Carbon*, 1995, **33**, 115–121.

48 X. M. Tang, J. Weber, S. N. Mikhailov, C. Müller, W. Hänni and H. E. Hintermann, *J. Non-Cryst. Solids*, 1995, **185**, 145–150.

49 A. Cuesta, P. Dhamelincourt, J. Laureyns, A. Martínez-Alonso and J. M. D. Tascón, *Carbon*, 1994, **32**, 1523–1532.

50 R. Vidano and D. B. Fischbach, *J. Am. Ceram. Soc.*, 1978, **61**, 13–17.

51 L. G. Cancado, K. Takai, T. Enoki, M. Endo, Y. A. Kim, H. Mizusaki, A. Jorio, L. N. Coelho, R. Magalhaes-Paniago and M. A. Pimenta, *Appl. Phys. Lett.*, 2006, **88**, 163106.

52 C. Galeano, J. C. Meier, V. Peinecke, H. Bongard, I. Katsounaros, A. A. Topalov, A. Lu, K. J. J. Mayrhofer and F. Schüth, *J. Am. Chem. Soc.*, 2012, **134**, 20457–20465.

53 C. Mattevi, G. Eda, S. Agnoli, S. Miller, K. A. Mkhoyan, O. Celik, D. Mastrogiovanni, G. Granozzi, E. Garfunkel and M. Chhowalla, *Adv. Funct. Mater.*, 2009, **19**, 2577–2583.

54 M. Favaro, S. Agnoli, C. Di Valentin, C. Mattevi, M. Cattelan, L. Artiglia, E. Magnano, F. Bondino, S. Nappini and G. Granozzi, *Carbon*, 2014, **68**, 319–329.

55 M. Favaro, L. Perini, S. Agnoli, C. Durante, G. Granozzi and A. Gennaro, *Electrochim. Acta*, 2013, **88**, 477–487.

56 M. Favaro, S. Agnoli, L. Perini, C. Durante, A. Gennaro and G. Granozzi, *Phys. Chem. Chem. Phys.*, 2013, **15**, 2923–2931.

57 W. Ju, M. Favaro, C. Durante, L. Perini, S. Agnoli, O. Schneider, U. Stimming and G. Granozzi, *Electrochim. Acta*, 2014, **141**, 89–101.

58 T. Sharifi, G. Hu, X. Jia and T. Wågberg, *ACS Nano*, 2012, **6**, 8904–8912.

59 E. Gracia-Espino, G. Hu, A. Shchukarev and T. Wågberg, *J. Am. Chem. Soc.*, 2014, **136**, 6626–6633.

60 D.-H. Lim and J. Wilcox, *J. Phys. Chem. C*, 2011, **115**, 22742–22747.

61 T. Holme, Y. Zhou, R. Pasquarelli and R. O'Hayre, *Phys. Chem. Chem. Phys.*, 2010, **12**, 9461–9468.

62 Y. Zhou, T. Holme, J. Berry, T. R. Ohno, D. Ginley and R. O'Hayre, *J. Phys. Chem. C*, 2009, **114**, 506–515.

63 T. J. Schmidt, H. A. Gasteiger, G. D. Stäb, P. M. Urban, D. M. Kolb and R. J. Behm, *J. Electrochem. Soc.*, 1998, **145**, 2354–2358.

64 Y. Bing, H. Liu, L. Zhang, D. Ghosh and J. Zhang, *Chem. Soc. Rev.*, 2010, **39**, 2184–2202.

65 A. J. Bard and L. R. Faulkner, *Electrochemical methods. Fundamentals and applications*, Wiley, New York, 2001.

66 M. Uchida, Y.-C. Park, K. Kakinuma, H. Yano, D. A. Tryk, T. Kamino, H. Uchida and M. Watanabe, *Phys. Chem. Chem. Phys.*, 2013, **15**, 11236–11247.

67 G. Ramos-Sanchez and P. B. Balbuena, *Phys. Chem. Chem. Phys.*, 2013, **15**, 11950–11959.

68 G. Ramos-Sánchez and P. B. Balbuena, *J. Electroanal. Chem.*, 2014, **716**, 23–30.

69 E. Gracia-Espino, X. Jia and T. Wågberg, *J. Phys. Chem. C*, 2014, **118**, 2804–2811.

70 A. Nie, J. Wu, C. Zhou, S. Yao, C. Luo, R. C. Forrey and H. Cheng, *Int. J. Quantum Chem.*, 2007, **107**, 219–224.

Electrochimica Acta 179 (2015) 108–118

Contents lists available at ScienceDirect

Electrochimica Acta

journal homepage: www.elsevier.com/locate/electacta

Review

The Effect of Support on Advanced Pt-based Cathodes towards the Oxygen Reduction Reaction. State of the Art

Yun Luo, Nicolas Alonso-Vante [1],*

IC2MP, UMR-CNRS 7285, University of Poitiers, 4 rue Michel Brunet, 86022 Poitiers, France

A R T I C L E I N F O

Article history:
Received 23 December 2014
Received in revised form 15 April 2015
Accepted 16 April 2015
Available online 21 April 2015

Keywords:
Substrates
Stability
Activity
Platinum
Nanoalloys

A B S T R A C T

This work summarizes the advanced materials developed by various research groups for improving the stability of platinum (Pt), and Pt-based catalysts center toward the oxygen reduction reaction (ORR) in acid medium. The ORR stability enhancement of Pt catalytic center can be classified according to the different nature of the supporting materials, namely, carbon-, oxide-based-, and oxide-carbon composites. The enhancement and stability of a catalytic center can be related to either its electronic modification induced by a strong interaction with the support, another metal (alloy), or to geometric effects. In addition, other parameters come into play, the size, the morphology of the catalytic center, the temperature, the dispersion, and mass loading, along with the measuring methods. This mini-review mainly focusses on the stability improvement, depending on the substrate nature. This latter can be further modified *via* functionalization or by the chemical interaction nature between the substrate and catalyst.

Contents

1. Introduction

Besides the electrocatalytic activity of nanomaterials for the oxygen reduction reaction (ORR), the stability of any catalytic center is still a major issue in low temperature fuel cell systems, such as proton-exchange membrane fuel cell (PEMFC), in particular for the best known catalyst: platinum (Pt) [1,2]. It is well known that degradation and contamination of Pt active sites result in a decrease of catalysts' performance in PEMFC [3,4]. Indeed, the conventional support of Pt-based nanoparticles (NPs) is carbon black. The corrosion of this support starting at 0.97 V *vs.* RHE (reversible hydrogen electrode) [5] leads nanoparticles to detach and aggregate into larger ones resulting in a loss of active surface area [6–9], hence lowering the performance of the electrochemical generator [2,6,9,10]. Efforts have been devoted to enhance the stability of this kind of catalysts *via* various methods, which can be divided into two routes, namely with or without Pt surface modification.

The first strategy, referring to Pt electronic modification, was to tailor Pt center in Pt-M with M = transition metals or rare earth

---

* Corresponding author. Tel.: +33 5 4945 3625; fax: +33 5 4945 3580.
E-mail address: Nicolas.Alonso.Vante@univ-poitiers.fr (N. Alonso-Vante).

[1] ISE Member

http://dx.doi.org/10.1016/j.electacta.2015.04.098

elements. The Pt alloyed rare earth (RE) bulk model confirmed the prediction of highly efficient and stable catalysts towards ORR [11–14]. And Pt_xY nanoalloy showed excellent ORR kinetic and durability [15]. Pt-M nanoalloys, where M could be Co, Ni, Cu, Fe, etc. [16–22], also showed a high ORR activity and/or stability. One explanation for such an ORR enhancement in such Pt-based nanoalloy is the “ligand effect” and “geometric effect” [22–25]. Another phenomenon that favors the ORR stability is the strong metal-substrate interaction (SMSI) between Pt NPs and the substrate. In fact, strong interaction of Pt centers with the graphitic domain of carbon materials, such as carbon nanotube (CNT) and reduced graphene oxide (RGO) sheet supported Pt catalysts, was observed [26–29]. Oxides were also identified as good candidates to support Pt-based NPs basically because of their better corrosion-resistance with respect to carbon materials [5]. Pt supported by oxides can be prepared *via* a chemical and/or photochemical route [30–32]. Both methods, reveal that SMSI in Pt and oxide should be responsible for the enhanced catalytic activity and/or stability towards ORR [30,33,34]. As defined by Tauster et al. [35,36], SMSI is related to formation of an interfacial bond occurring between the metal and the metal of the oxide’s surface. The modification of the metal electronic structure which takes place is also induced by strain effects [37]. Compared with carbon materials, the conductivity of pure oxides may limit their application as cathodic substrate materials. Therefore, doped oxides and oxide-carbon composites become attractive supports for catalytic nanoparticles [32,38,39] In fact, SMSI can be also identified in oxide-carbon composite supported Pt NPs [40]. The ORR stability was enhanced with respect to carbon black supported Pt NPs [39]. Recently, another type of interaction, between oxide clusters and Pt center supported by carbon black, was observed for ORR stability enhancement. Such an interaction is induced by micro-strain between oxide nanoclusters and Pt [41,42], leading to Pt surface change.

Besides Pt surface modification, other parameters could come to play. Norskov et al. predicted that, based on density function theory (DFT) calculation, the ORR surface specific activity (SA), defined as kinetic current normalized by Pt active surface, should be enhanced with increasing particle size in the range of 2–30 nm and maximum mass activity (MA), defined as kinetic current normalized by Pt mass, should be observed on particles of 2–4 nm in $HClO_4$ [43]. In addition particle-size effect in Pt-based catalysts towards both ORR activity and stability were observed [44,45]. Octahedral Pt-Ni facetted (111) dominant [18,46,47], Au cluster stabilized Pt [48] and Pt-based core-shell NPs [49,50] showed an enhanced ORR activity and stability with respect to the Pt center. Moreover, Pt NPs dispersion, mass-loading, substrate conductivity, working condition (*e.g.* temperature), *etc.*, affect the ORR process [51–55].

Since the Pt surface modification has a positive influence on the ORR process, this mini-review summarizes recent experimental progress obtained so far by various research groups using modified Pt centers and various substrates’ nature to anchor or hybridize the catalytic center. Other parameters (*e.g.* NPs size/morphology effect, temperature, and working condition will be mentioned but not discussed in detail.

Table 1

Low graphitized carbon supported Pt NPs towards ORR stability.

Catalyst	Particle diameter[a] / Shape	Durability test parameters					Durability test results		Ref.
		Cycles	Potential interval[b]	Electrolyte and electrochemical cell	Scan rate[c]	Temperature	Initial value[d]	Remaining value[e]	
Pt_xY/GCE	9/ Spherical	9,000	0.6–1.0	O_2-saturated 0.1 M $HClO_4$ in half-cell.	50	23 °C	MA = 3050	MA = 63%	[15]
Pt/GCE[*]	N.M.						MA = 500[f]	N.M.	
$Pt_{1.5}Ni$/CB	11/ Octahedral	4,000	0.6–1.0	0.1 M $HClO_4$ in half-cell.	50	N.M.	MA = 1200[f]	MA = 84%	[18]
PtNi/CB	12/ Octahedral						MA = 1700[f]	MA = 55%	
$PtNi_{1.5}$CB	13/ Octahedral						MA = 1100[f]	MA = 34%	
Pt/CB[*]	N.M.						MA = 150	N.M.	
$Pt_{2.5}Ni$/CB	9/ Octahedral	5,000	0.65–1.0	O_2-saturated 0.1 M $HClO_4$ in half-cell.	70	N.M.	MA = 3300	MA = 60%	[47]
Pt/CB[*]	N.M.						MA = 200	MA = 67%	
Pt_3Co/CB -700	7.2/ Spherical	5,000	0.05–1.0	N_2-saturated 0.1 M $HClO_4$ in half-cell.	50	RT	MA = 520	MA = 73%[f]	[16]
Pt/CB[*]	4.4/ Spherical						MA = 60	N.M.	
$PtCu_3$ 600C/CB	2.65/ N.M.	30,000	0.5–1.0	H_2/N_2-saturated 0.1 M $HClO_4$ in MEA.	100	80 °C	MA = 303	MA = 83%	[21]
$PtCu_3$ 800C/CB	4.2 / N.M.						MA = 530	MA = 40%	
$PtCu_3$ 950C/CB	5.4 / N.M.						MA = 320	MA = 97%	
Pt/CB[*]	2.9 / N.M.						MA = 160	MA = 81%	
Pt_3Pd/CB	11.3/ Octahedral	2,000	0.4–0.9	O_2-saturated 0.1 M $HClO_4$ in half-cell.	50	RT	ECSA = 54	ECSA = 98%	[61]
Pt_3Pd/CB	3.9/ Spherical						ECSA = 61	ECSA = 43%	
Pt/CB[*]	N.M.						ECSA = 95	ECSA = 47%	
$PtCu_3$/CB (ordered)	N.M.	7,000	0.6–1.2	0.1 M $HClO_4$in half-cell.	1000	N.M.	MA = 580	MA = 72%	[22]
$PtCu_3$/CB (disordered)	N.M.						MA = 450	MA = 67%	
Pt/Au	3–5/ Spherical	30,000	0.6–1.1	O_2-saturated 0.1 M $HClO_4$in half-cell.	50	RT	N.M.	H_{upd} = 100%	[48]
Pt/CB[*]	N.M.						N.M.	H_{upd} = 55%	
Pd@Pt	5/ Spherical	60,000	0.7–0.9	0.1 M $HClO_4$in MEA.	N.M.	80 °C	MA = 300	MA = 81%	[49]
Pt/CB[*]	3.5/N.M.						MA = 130	MA = 32%	

N.M. = not mentioned in literature.

MEA = membrane electrode assembly.

RT = room temperature.

[a] nm.

[b] V vs. RHE.

[c] $mV\,s^{-1}$.

[d] ORR mass activity (MA) @ 0.9 V vs. RHE / $mA\,mg^{-1}{}_{Pt}$; Hydrogen under-potential deposition (H_{upd})/cm^2; Electrochemical surface area (ECSA) / $m^2\,g^{-1}{}_{Pt}$.

[e] Normalized by the initial value.

[f] Data not provided in the literature, these ones were estimated from figures.

[*] Reference catalyst to compare with the catalytic activity of alloyed Pt NPs.

2. Carbon-based substrate for Pt NPs

2.1. Low graphitized carbons

Metal black NPs, *e.g.* Pt, Ru, *etc.* have been investigated as model systems for various electrocatalytic reactions. In this sense, novel unsupported alloys made of Pt and rare earth elements have been synthesized via physical methods, *e.g.* Pt_xY nanoalloy coated on glassy carbon electrode (GCE), showed excellent ORR activity and stability (in Table 1 and Fig. 1) [15]. Moreover, low graphitized carbons are widely used as supports for catalytic NPs.

Carbon black (CB), *e.g.* from Vulcan and Ketjen, are the most widely used supporting materials for catalysts' nanoparticles towards ORR. The enhancement of ORR activity and stability of carbon black supported Pt NPs is essentially based on the design of the catalytic center. In platinum nanoalloys, two main concepts, in the control of Pt catalytic center, are devised: the "geometric" and/or "ligand effect", where the Pt electronic modification change Pt catalytic performance. In the presence of alloyed 3d transition metals, and rare earth elements, *e.g.* Yttrium (Y), Gadolinium (Gd), with Platinum, the geometric effect can be related to a change of the Pt-Pt inter-atomic distance. The 3d transition metals or rare earth elements which can leach out during the electrochemical activation of platinum in acid medium, leading to pure Pt skin and thus altering the Pt-Pt atomic distance [15,16,18,56]. Such Pt-Pt atomic distance is more compressed in Pt_xY nanoalloy than on pure Pt. A similar phenomenon takes place on the Pt-M (M = 3d transition, metals) *e.g.*, Pt-Cu [15,57]. The surface de-alloying process of Y atoms in Pt_xY leads to close packed Pt atoms forming a Pt overlayer skin on alloyed Pt-Y core. Therefore, on Pt-M (M = transition, and rare earth metals) nanoalloys, the ligand effect can be attributed to a Pt electronic modification induced by M metals [12,14,58–60]. The ORR process that occurs at the Pt surface can be rationalized as follows: First the activation of O_2 molecule on Pt surface, involving one H^+ and e^- transfer, form adsorbed OOH. Secondly, this surface adsorbed species dissociates into O and OH. If the electronic structure of the catalytic center changes, the adsorption/desorption energy of the species changes as well. Based on DFT calculation the process of adsorption of OOH and desorption of O and OH, for example at Pt_3Y, is smaller in comparison to that of pure Pt surface atoms, leading to an enhanced ORR activity and stability [12].

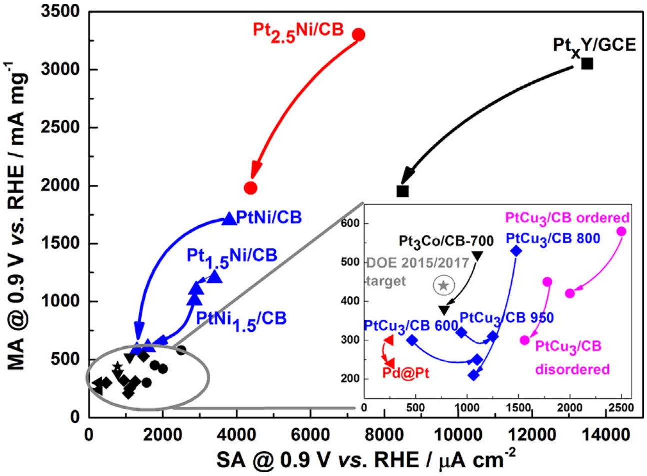

Fig. 1. ORR activity before and after stability test: surface specific activity (SA) *vs.* mass activity (MA). The degradation is shown by an arrow for Pt_xY/GC [15]; $Pt_{2.5}Ni/CB$ [47]; $Pt_{1.5}Ni/CB$, $PtNi/CB$ and $PtNi_{1.5}/CB$ [18]; (inset) for Pt_3Co/CB-700 [16]; $PtCu_3/CB$ 600C, $PtCu_3/CB$ 800C and $PtCu_3/CB$ 950C [21]; $PtCu_3/CB$ (ordered) and $PtCu_3/CB$ (disordered) [22]; Pt/Pd/CB [49]; DOE 2015/2017 target [3].

The ORR activity of Pt-M (M = transition metals and rare earth elements), as well as stability tests performed on various CB substrates are summarized in Table 1. The selected system was based on the ORR activity with respect to DOE (department of energy, USA) 2015 (MA = 440 mA/mg_{Pt}) / 2017 (SA = 770 μA/cm^2_{Pt}) targets [3]. The Pt-M catalysts listed in the Table are more efficient for the ORR with respect to the DOE target. Before the stability test, it can be seen that the ORR mass activity (MA) on Pt-M is higher with respect to Pt taken as a reference catalyst. Likewise, one can notice that the ORR mass activity on Pt-M on CB or GCE supports follows such DOE's trend. Indeed, the initial MA value of catalysts in the decreasing order are: octahedral $Pt_{2.5}Ni$ supported on CB ($Pt_{2.5}Ni/CB$) [47] > Pt_xY supported on GCE (Pt_xY/GCE) [15] > PtNi supported on CB (PtNi/CB) [18] > $Pt_{1.5}Ni$ supported on CB ($Pt_{1.5}Ni/CB$) [18] > $PtNi_{1.5}$ supported on CB ($PtNi_{1.5}/CB$) [18] > ordered $PtCu_3$ supported on CB ($PtCu_3/CB$ ordered) [22] > $PtCu_3$, annealed at 800 °C, supported on CB ($PtCu_3/CB$-800) [21] > Pt_3Co, annealed at 700 °C, supported on CB (Pt_3Co/CB-700) [16] > carbon black supported $PtCu_3$, annealed at 950 °C, supported on CB ($PtCu_3/CB$ 950) [21] > $PtCu_3$, annealed at 600 °C, supported on CB ($PtCu_3/C$ 600C) [21]. Unfortunately, in order to have a complete picture of the stability measurements on Pt-Y [15], Pt-Ni [18,47], Pt-Co [16] materials, measurements on Pt reference materials are needed. Furthermore, different working conditions employed differ, *cf.* columns 3–6 of Table 1. We can only assess that Pt_xY/GCE [15] retains the highest ORR mass activity among Pt-M (M = transition, and rare earth metals) centers, *e.g.*, PtNi/CB [18], $PtNi_{1.5}/CB$ [18], $Pt_{2.5}Ni/CB$ [47] and Pt_3Co/CB-700 [16]. Furthermore, tunable ORR kinetic and stability related to Pt and Ni ratio could be generated on octahedral Pt-Ni nanoalloy [18]. The different ORR kinetics on Pt-Ni catalysts with different Pt/Ni ratio was associated with the Pt surface morphological change as a result of leaching of Ni during ORR [18]. The MA on other nanoalloys such as Pt_3Co/CB-700 catalyst was reported to be around 73% after 5,000 potential cycles [16], ordered $PtCu_3/CB$ remained 72% after 7,000 cycles [22] and for $PtCu_3/CB$ annealed at 950 °C it was 97% ORR after 30,000 cycles [21]. Nevertheless, as compared to Pt_xY/GC [15] and $Pt_{2.5}Ni/CB$ [47] nanoalloys, the initial ORR activity of $PtCu_3$ [21] is lower by a factor of *ca.* 10.

The MA *vs.* the SA at 0.9 V *vs.* RHE, and stability for the ORR on various catalysts supported onto carbon are contrasted in Fig. 1. The loss of activity is marked by an arrow. Since different durability working conditions were reported, one should not directly compare ORR stability between different catalysts. However, one can appreciate two groups of catalysts, namely the most performant ones, *e.g.*, Pt_xY/GCE [15], $Pt_{2.5}Ni/CB$ [47], $Pt_{1.5}Ni/CB$ [18] and PtNi/CB [18], and the less performant ones, *e.g.* $PtNi_{1.5}/CB$ [18], ordered $PtCu_3/CB$ [22], Pt_3Co/CB-700 [16] and annealed $PtCu_3/CB$ catalysts [21]. Considering the DOE 2015/2017 target as a reference for the most performant catalysts, the ORR kinetics before and after stability tests is higher than the reference. For the less performant catalysts, the ORR activity after stability tests is lower than the reference. This picture shows us that ligand and/or geometric effect can also be correlated to the materials particles' size/morphology. Among octahedral shaped PtNi nanoalloys, the $Pt_{2.5}Ni/CB$, with the smallest diameter (*cf.* Table 1), delivered the highest initial MA and SA [18,47] supporting the favorable effect of particle size towards ORR.

The tuning of Pt active center activity was devoted to control the morphology of nanoparticles. In this connection, Zou et al. [46] reported that octahedral Pt_3Ni NPs with dominant (111) facet showed an enhanced ORR activity with respect to Pt_3Ni nanocubes. Similarly, Park et al. observed that the ORR stability on octahedral ones was improved [61] as compared to spherical Pt_3Pd/CB catalyst, *cf.* Table 1. Moreover, the high activity and stability of catalysts can be favored by engineering core-shell structures.

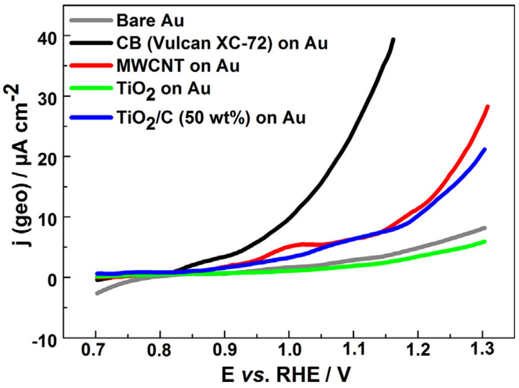

Fig. 2. Anodic polarization curves obtained by potential cycling at scan rate of 2 mV s^{-1}, from 0.7 to 1.3 V *vs.* RHE, in N_2-saturated 0.1 M $HClO_4$, for bare Au electrode, CB (Vulcan XC-72, pretreated at 400 °C under N_2 for 4 h), MWCNT (purification following the method in reference [101]) on Au electrode, TiO_2 (prepared *via* sol-gel route in [32]), TiO_2-C composite (50 wt% TiO_2, prepred *via* sol-gel route in [32]) coated on Au electrode.

The data shown in Fig. 1 contrast Pt-M (M = transition or rare earth metals) catalysts having an induced core-shell structure developed by leaching or dealloying process, *e.g.*, on Pt_xY/GCE [15], Pt_3Co/CB [16], Pt_xNi/CB [18] and $PtCu_3$/CB [21,22]. It thus turns out that the increased activity can be associated with the electronic effect induced by micro-strained Pt overlayer atoms as a result of leaching/dealloying [15,16,18,21,22]. An alternative way to stabilize Pt catalytic centers can be obtained from, *e.g.* Au cluster or by core-shell morphology, where the Pt is not alloyed [48,49,62]. It was reported that Pt/Au [48] and Pd@Pt [49] supported on CB showed no active surface area degradation after 30,000 potential cycles for the former and 19% loss of MA after 60,000 cycles for the latter. Pt/CB used as reference under the same conditions showed 45% and 68% loss, respectively, *cf.* Table 1. It is thus clear, that data shown in Fig. 1, indicates that these kinds of catalyst having non-alloyed cores possess an enhanced stability but lower ORR activity.

2.2. High-graphitized carbon

Other types of carbons, such as carbon nanotube (CNT) and reduced graphene oxide (RGO) were reported as substrates to favor the ORR process of Pt NPs [26,28,29,63]. As shown in Fig. 2, the onset corrosion potential for high graphitized carbon (*e.g.* multi-walled CNT) is higher than that for low graphitized carbon (*e.g.* CB). Thus, improvement of ORR stability on Pt/(high graphitized carbon) catalyst was reported, see Table 2 and Fig. 4. The corrosion resistance of the substrate minimize Pt NPs agglomeration.

Another mechanism for such an activity enhancement revealed that a SMSI is also responsible for stabilizing Pt NPs [26,64]. Recently, Alonso-Vante et al. reported the interaction between Pt center and graphitic domain of carbon materials [26,65]. For such a comparison, care was taken in controlling the size/morphology of Pt NPs (*cf.* Fig. 3A-C), obtained *via* the carbonyl chemical route synthesis [26,65,66]. Using CO as a molecular probe, a series of experiments were done on well-defined substrate conditions. Fig. 3D shows the CO-stripping voltammograms on Pt/CB (CB = Vulcan XC-72), Pt/MWCNT (MWCNT = multi-walled carbon nanotube) and Pt/HOPG (HOPG = highly oriented pyrolytic graphite). The oxidation of carbon monoxide is shifted to negative potential and it is a function of the degree of graphitization of the substrates as revealed by the Raman spectroscopy (*cf.* insets of Fig. 3D). These results, indeed, disclose that the ratio of the D-band (disordered band) intensity with the G-band (graphitic band) decreases. The favorable interaction of Pt NPs onto graphitic domains of carbon was further verified *via* XPS analysis (not shown here).

Table 2 summarizes the ORR stability on CNT or graphene supported Pt NPs. It is noticeable that the ORR stability of CNT or graphene supported Pt NPs is enhanced with respect to Pt/CB reference catalysts. As an example, the remaining ECSA of Pt/MWCNT [26], which measured up to 3,000 cycles, was 68% whereas the reference Pt/C catalyst was 25%. The origin of stability on this kind of systems can be related to both the higher corrosion potential of substrate and the SMSI effect developed by the hybridization of *d*-orbitals of Pt with sp^2 domains of carbon. Strasser et al. [63] also reported an enhanced

Table 2
ORR stability on multi-walled carbon nanotube (MWCNT), functionalized graphene sheet (FGS) and reduced graphene oxide/carbon black (RGO/CB) supported Pt NPs.

Active Center	Particle diameter[a]/ shape	Durability test parameters					Durability test results		Ref.
		Cycles	Potential interval[b]	Electrolyte and electrochemical cell	Scan rate[c]	Temperature	Initial value[d]	Remaining value[e]	
Pt/MWCNT	2.2/Spherical	3,000	0.05–1.2	N_2-saturated 0.5 M H_2SO_4in half-cell.	50	25 °C	N.M.	ECSA = 68%	[26]
Pt/CB (R1)*	1.9/Spherical							ECSA = 25 %	
Pt/MWCNT	2.9/Spherical	10,000	0.5–1.0	0.1 M $HClO_4$in half-cell.	50	RT	ECSA = 47 ± 12 MA = 120 ± 20	ECSA = 105% MA = 90%	[63]
Pt/CB (R2)*	2.5/Spherical						ECSA = 53 ± 4 MA = 150 ± 10	ECSA = 74% MA = 66%	
Pt/FGS	5.5/Spherical	5,000	0.6–1.1	N_2-saturated 0.5 M H_2SO_4in half-cell.	50	RT	ECSA = 108 MA = 39	ECSA = 68% MA = 50%	[28]
Pt/CB (R3)*	6.9/Spherical						ECSA = 75 MA = 65[e]	ECSA = 40% MA = 35%	
Pt/RGO/CB	5/Spherical	20,000	0.6–1.1	0.1 M $HClO_4$in half-cell.	100	RT	ECSA = 56.4 MA = 170[f]	ECSA = 95% MA = 69%[f]	[29]
Pt/CB (R4)*	3/Spherical						ECSA = 58.9 MA = 170[f]	ECSA = 50%[f] MA = 35%[f]	

N.M. = not mentioned.
RT = room temperature.
[a] nm.
[b] V vs. RHE.
[c] mV s^{-1}.
[d] ORR mass activity (MA) @ 0.9 V vs. RHE / mA mg$^{-1}{}_{Pt}$; electrochemical surface area (ECSA) / m^2 g$^{-1}{}_{Pt}$.
[e] Normalized by the initial value.
[f] Data not provided in the literature, these ones were estimated from figures.
[*] Reference catalyst to compare ORR stability.

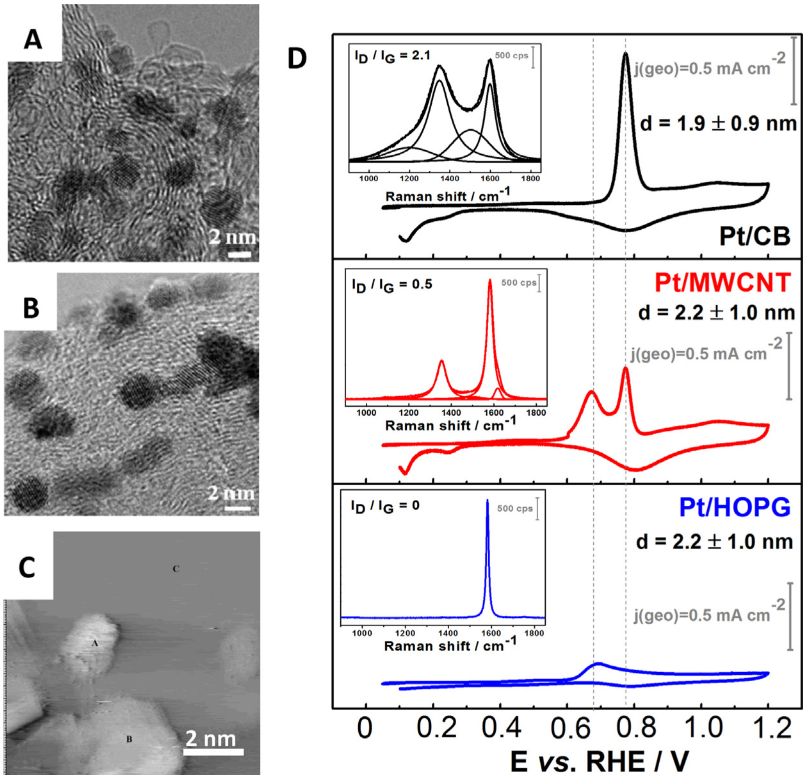

Fig. 3. TEM images for Pt/CB (A) and Pt/MWCNT (B). Reprinted with permission from [26]. Copyright (2013) American Chemical Society. STM image for Pt/HOPG sample (C), zone A and B represent Pt NPs and zone C for HOPG. CO-stripping voltammograms (D) for Pt/CB, Pt/MWCNT and Pt/HOPG; (insets) Raman spectra for CB, MWCNT and HOPG. Data extracted from [26,65].

ORR stability after 10,000 cycles on Pt/MWCNT with respect to Pt/CB catalyst. In this work the MA of Pt/MWCNT remained 90% with no degradation of ECSA, whereas the remaining ECSA and MA were 74% and 66% on Pt/CB, respectively. Reduced graphene oxide (RGO) and CB composite were reported as a more durable substrate than CB for Pt NPs [29]. It was reported that ECSA showed only a loss of 5% on Pt/RGO/CB catalyst after 20,000 cycles, while the active surface area of Pt/RGO and Pt/CB, as reference catalysts, remained respectively around 50% and 60%. In spite of the relatively low initial activity of Pt/RGO/CB catalyst towards the ORR, the remaining MA after stability test was of 69%. Under the same conditions Pt/CB degradation is higher and the remaining MA is 35%. Additionally, functionalized graphene sheet (FGS) supported Pt NPs showed an enhanced ORR stability in comparison to the commercial Pt/C catalyst after 5,000 cycles. The extent of the electrochemical surface area variation of the various Pt NPs- carbon systems with the number of cycles is contrasted in Fig. 4. One can further notice that Pt/CB reported in the literature strongly differ, probably because of different sources and different cycling potential intervals. One can, however, state that Pt NPs can be positively stabilized on carbon with graphitic domains.

3. Oxide-based materials

3.1. Pure-, doped-oxides

Wide band-gap semiconducting oxides, such as TiO_2, SnO_2, and WO_3 [32,34,39,67–71], are good candidates as supports for Pt NPs, not only because of their corrosion resistance with respect to carbon-based materials (*cf.* Fig. 2), but also because of their strong interaction with metallic particles inducing the so-called SMSI effect for the ORR activity as well as stability enhancement [33]. SMSI was reported between Pt and oxides, *e.g.*, TiO_2, SiO_2, CeO_2, and so on [72–75]. This phenomenon is defined as an interfacial interaction between the catalytic metal and the metal of the oxide resulting in an electronic structure modification of the catalytic metal [35,36]. Taking Pt/TiO_2 system as an example, DFT calculation indicated a strong interfacial reaction between Pt and Ti atoms forming a metal-metal bond [76]. The modification of Pt electronic structure can also be associated with a charge transfer at the interfacial Pt-Ti alloy [40]. Hwang et al. attested [33],*via* X-ray absorption near edge structure (XANES) data, Fig. 5A, charge transfer from oxide ($Ti_{0.7}Mo_{0.3}O_2$) to Pt NPs. Compared with Pt/C catalyst and PtCo/C catalyst, dramatic decrease of number of unfilled *d*-states could be observed in Pt/$Ti_{0.7}Mo_{0.3}O_2$, Fig. 5B. Thus indicating that electron donation from oxide to Pt takes place.

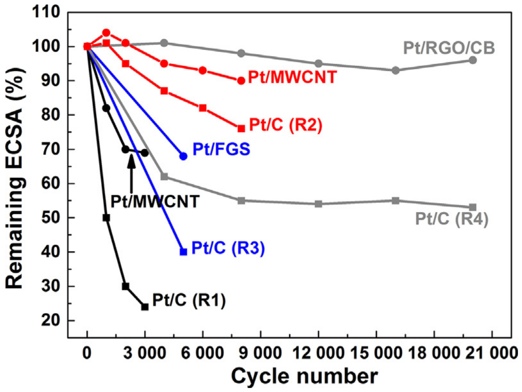

Fig. 4. Electrochemical surface area evolution for Pt/MWCNT compared with Pt/CB (R1) [26] and [63], Pt/RGO/CB compared with Pt/CB (R4) [29] and Pt/FGS compared with its Pt/CB (R3) [28].

However, some reports revealed that, besides charge transfer, lattice strain effect should also be taken into account as an important factor enhancing the ORR activity [37]. In this sense, Kim et al. described that charge transfer from Cr-TiO_2 to Pt (Pt/Cr-TiO_2) takes place as a result of a strong OH adsorption on Pt surface leading to a decrease of ORR activity [37]. Nevertheless, ORR activity on Pt/Cr-TiO_2 was improved with respect to the reference Pt/C. To put in evidence such phenomena (SMSI and/or strain effects), Pt NPs were deposited onto oxides using either the photo-deposition, or depositing *via* a chemical route [32,39,40,77,78].

With respect to Pt NPs supported onto doped-oxides, the activity and stability vis-à-vis the ORR are summarized in Table 3 and Fig. 6. For Pt/TiO_2, and Pt/$Nb_{0.25}Ti_{0.75}O_2$ [34,38], the initial specific activities are lower than the reference Pt/CB. After 2,500 potential cycles, SA value on Pt/TiO_2 and Pt/$Nb_{0.25}Ti_{0.75}O_2$ catalyst remain respectively 52% and 41%, whereas the loss on the reference Pt/CB attains 96 %. When considering, the ECSA evolution, after stability tests, Pt/TiO_2 and Pt/$Nb_{0.25}Ti_{0.75}O_2$ materials preserve, respectively, 44% and 45%, i.e., more stability than the loss of 93% recorded for Pt/CB. It should also be noted that ORR stability between Pt/TiO_2 and Pt/$Nb_{0.25}Ti_{0.75}O_2$ catalyst is very close, but ORR activity is obviously enhanced on Pt/$Nb_{0.25}Ti_{0.75}O_2$ with respect to Pt/TiO_2. Besides, doped oxides can improve the ORR activity and enhance stability of Pt [79]. Sn doped TiO_2 can also be applied as substrate for Pt center towards ORR. Hou et al., reported that the enhanced ORR activity on Pt/$Ti_{0.7}Sn_{0.3}O_2$ is due to its high conductivity with respect to Pt/TiO_2 [79]. After 500 potential cycles, the remaining ECSA for Pt/$Ti_{0.7}Sn_{0.3}O_2$ was 62%, whereas for Pt/CB catalyst it was only 26%. Enhanced ORR activity and stability on Pt/$Ti_{0.7}Mo_{0.3}O_2$ was also obtained [30,33]. Indeed, after 5,000 potential cycles, the ORR activity on Pt/$Ti_{0.7}Mo_{0.3}O_2$ was 92%, whereas Pt/CB decreased to 50%. It revealed that a strong bonding between Pt and oxide is at the origin of the SMSI effect, preventing Pt NPs from agglomeration [33]. Pt NPs on Nb- and Sb-doped SnO_2 showed enhanced effect on stabilizing Pt NPs after stability test with respect to carbon supported Pt NPs [51,80]. The authors claimed that enhanced stability should be attributed to SMSI. In Fig. 6 one can notice that it is very difficult to compare ORR stability between Pt/Oxide catalysts due to the different stability test procedures. Nevertheless, it can be concluded that Pt centers on oxides are more stable than on carbon or carbon-oxide composite as substrate, see below, attributing to both higher corrosion potential and SMSI.

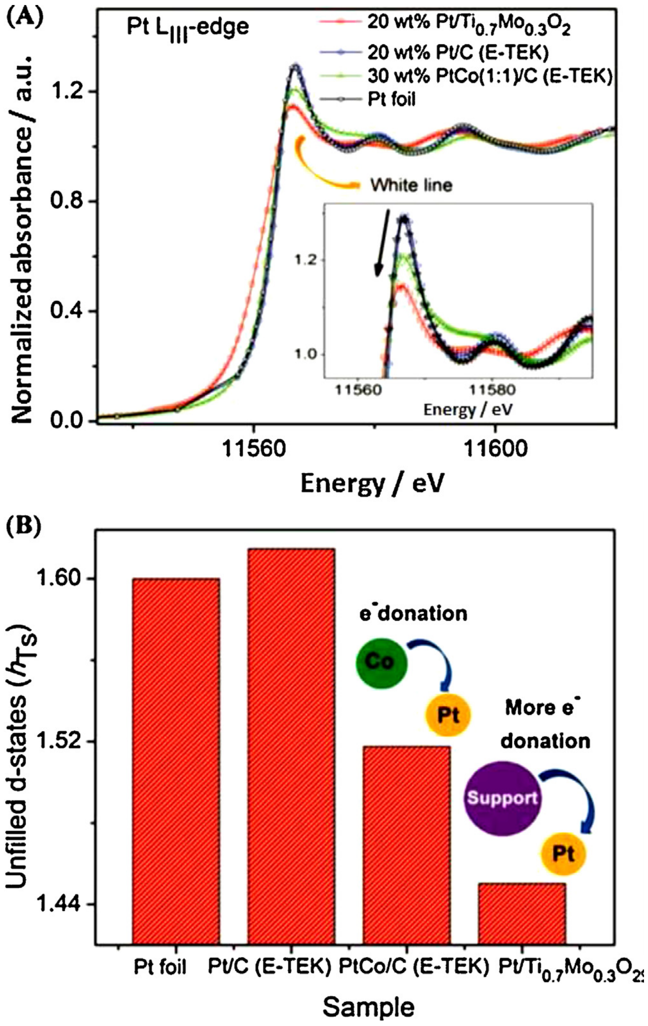

Fig. 5. Pt L_{III}-edge XANES spectra (A) and variation in unfilled *d*-states for Pt/$Ti_{0.7}Mo_{0.3}O_2$ and Pt-based NPs on carbon. Reprinted with permission from [33]. Copyright (2011) American Chemical Society.

3.2. Oxide-modified catalytic center

Oxide-modified Pt center supported by carbon can be essentially synthesized *via* a chemical route [41,42]. Such system is significant for Pt-based catalyst with rare-earth (RE) elements. Alloyed Pt-RE has been predicted for its excellent ORR activity and stability [12–14,58]. The synthesis of Pt-RE nanoalloy is a great challenge *via* soft chemical route as compared to the relatively facile chemical synthesis of Pt-Ni and Pt-Co nanoalloys [16,18]. The reason is that the reduction potential of RE elements is very negative (*ca.* -2 V) [82]. Therefore, co-reduction of RE and Pt in aqueous solution is not appropriate for Pt-RE nanoalloy synthesis. Results from various groups confirm that chemical co-reduction of Pt and Y precursors lead to Y-oxide in Pt catalysts [41,42,83,84]. Surprisingly, ORR activity and stability of Pt-Y_2O_3/C was enhanced in comparison to Pt/C catalyst [41,42,83,84]. This phenomenon can be, however, associated to the interaction of amorphous RE-oxide cluster interacting with Pt surface atoms [41,42]. Our group recently observed enhanced ORR activity as well as stability with Y_2O_3 and Gd_2O_3 modified Pt center on CB, noted as Pt-Y_2O_3/C and Pt-Gd_2O_3/C, with respect to the reference Pt/C [42]. It was found that ORR activity was actually enhanced after heat-treatment, even though no evidence of modification of the Pt electronic structure and formation of Pt-Y or Pt-Gd alloy could be assessed yet [41,42]. Thus, such an effect should be distinguished from SMSI, since no Pt electronic modification can be brought to light. As shown in Fig. 7A, the micro-strain value, estimated from Williamson-Hall plots based on XRD data, was enhanced from as-prepared to heat-treated Pt-M_2O_3/C (M = Y and Gd) samples. Conversely, such a phenomenon decreased from as-prepared to heat-treated Pt/C sample. Compared with Pt/C sample, the TEM images showed that the Pt NPs was much less agglomerated after heat-treatment in Pt-M_2O_3/C (M = Y and Gd) samples. The ORR stability, evaluated from remaining active surface and kinetic current (Fig. 7B), was found more stable for Pt-M_2O_3/C (M = Y and Gd) samples after heat-treatment, than for Pt/C sample after heat-treatment. These results confirm the effect of rare earth oxides in stabilizing the Pt center. In fact, a decreased micro-strain value and ORR activity was found, however, in TiO_2-CB supported Pt NPs (Pt/TiO_2/C) after heat-treatment, which could be related to a Pt center healing process [85]. Therefore, an increased micro-strain value and ORR activity/stability in Pt-M_2O_3/C (M = Y and Gd) systems can be associated to the presence of surface oxide clusters on Pt surface defects serving as nano-supports. Besides,

Table 3
Titanium oxide (TiO_2), Niobium doped titanium oxides ($Nb_{0.25}Ti_{0.75}O_2$), Tin doped titanium oxide ($Ti_{0.7}Sn_{0.3}O_2$) and Nb-/Sb- doped tin oxide ($Sn_{0.96}Nb_{0.04}O_{2-\delta}$ / $Sn_{0.96}Nb_{0.04}O_{2-\delta}$) supported Pt NPs towards ORR stability.

Active Center	Particle diameter[a]/ shape	Durability test parameters					Durability test results		Ref.
		Cycles	Potential interval[b]	Electrolyte and electrochemical cell	Scan rate[c]	Temperature	Initial value[d]	Remaining value[e]	
Pt/TiO_2	3–5/Spherical	2,500	0.6–1.4	0.5 M H_2SO_4in half-cell.	50	N.M.	ECSA = 31.2 SA = 2300	ECSA = 44% SA = 52%	[34,38]
Pt/$Nb_{0.25}Ti_{0.75}O_2$	3–4/Spherical						ECSA = N.M. SA = 2970	ECSA = 45% SA = 41%	
Pt/CB (R1)*	2–3/Spherical						ECSA = 56.4 SA=3180	ECSA = 7% SA = 4%	
Pt/(Nb-TiO_2)	2.3/Spherical	1,000	0.05–1.2	N_2-saturated 0.1 M $HClO_4$in half-cell.	50	80°C	ECSA = 36	ECSA = 73%	[81]
Pt/(C-TiO_2)(R2)*	2.3/Spherical						ECSA = 24	ECSA = 8%	
Pt/$Ti_{0.7}Sn_{0.3}O_2$	2.4/Spherical	500	0.6–1.2	0.5 M H_2SO_4	N.M.	N.M.	ECSA = 43.6	ECSA = 62%	[79]
Pt/CB (R3)*	N.M.						ECSA = 66.9	ECSA = 26%	
Pt/$Ti_{0.7}Mo_{0.3}O_2$	N.M./Dendrite	5,000	0.2–1.2	O_2-saturated 0.5 M H_2SO_4in half-cell.	N.M.	25°C	ECSA = 81.1 MA = 3.1	MA = 92%	[30]
Pt*	N.M./Dendrite						ECSA = 81.1 MA = 0.75	MA = 75%	
Pt/CB (R4)*	N.M.						ECSA = 71.2 MA = 0.55	MA = 50%	
Pt/$Ti_{0.7}Mo_{0.3}O_2$	3–4/Spherical	1,000	0.0–1.1	0.5 M H_2SO_4in half-cell.	50	25°C	SA = 800[f]	SA = 92%	[33]
Pt/CB (R5)*	3–4/Spherical						SA = 100[f]	SA = 49%	
Pt/$Sn_{0.96}Nb_{0.04}O_{2-\delta}$	2.8 ± 0.4/N.M.	4,000	0.9–1.3	N_2-saturated 0.1 M $HClO_4$in half-cell.	N.M	25°C	ECSA = 79.7	ECSA = 90%[f]	[51,80]
Pt/$Sn_{0.96}Nb_{0.04}O_{2-\delta}$	2.7 ± 0.5/N.M.						ECSA = 68.6	ECSA = 88%[f]	
Pt/CB (R6)*	2.2 ± 0.5/N.M.	1,000					ECSA = 80.7	ECSA = 38%[f]	

N.M. = not mentioned.
RT = room temperature.
[a] nm.
[b] V vs. RHE.
[c] $mV\,s^{-1}$.
[d] ORR specific (SA) and mass activity (MA) @ 0.9 V vs. RHE / $mA\,mg^{-1}{}_{Pt}$; electrochemical surface area (ECSA)/$m^2\,g^{-1}{}_{Pt}$.
[e] Normalized by the initial value.
[f] Data not provided in the literature, these ones were estimated from figures.
* Reference catalyst to compare ORR stability.

XPS (X-ray photoelectron spectroscopy) analyses revealed that the surface Pt/M ratio, for Pt-M_2O_3/C (M = Y and Gd) catalysts, increased after heat-treatment. This further proves the micro-strain change induced Pt surface modification. These results give insights to understand that RE oxides are different source of favorable interaction with Pt centers.

3.3. Oxide-carbon composite

Another kind of catalyst substrate material is the oxide-carbon composite (M_xO_y/C). Using chemical route, *e.g.*, sol-gel chemical process [39], the oxides are synthesized in the presence of carbon to form the composite. The composite revealed enhanced corrosion resistance with respect to carbon (e.g. CB), as shown in Fig. 2. It is worth to note that, depending on the mass ratio of oxide to carbon, the composite shows a similar relative powder conductivity to that of carbon [5]. For instance, in the range of 0–20 wt% TiO_2/C, the conductivity of the composite is close to that of CB [5]. The in-situ synthesis of the oxides favors an intimate contact in such a way as to form an ohmic junction at the oxide-carbon interface [86–88]. Oxides in the composites are interesting [5,89], in spite of their low conductivity (large-gap materials) [41,42,90,91] since they serve as anchoring points of catalytic centers. As shown recently, the deposition of Pt NPs was selectively performed onto the oxides of the oxide-carbon composite (Pt/M_xO_y/C), using UV light [92,93] or a chemical route [94,95]. This system proved to be efficient to enhance the ORR activity and stability [39,41,92,96]. Such a phenomenon, as described by Tauster et al. [35,36] is due to an important interaction of the catalytic center with the metal of the oxide sites of the composite named SMSI. Although Koudelka et al. claimed the absence of SMSI in Pt/TiO_2 prepared *via* photo-deposition, due to the absence of any shift of the binding energy (BE) of Pt *4f* peak in XPS [97]. Recent works, however, confirm SMSI based on modified Pt electronic structure in presence of TiO_2 [32,39,40,92,94,98–100]. Results generated in our group, revealed that the BE of Pt *4f* peak is negatively shifted in Pt/TiO_2/C and Pt/WO_3/C, whereas no shift was observed on Pt/C [40].

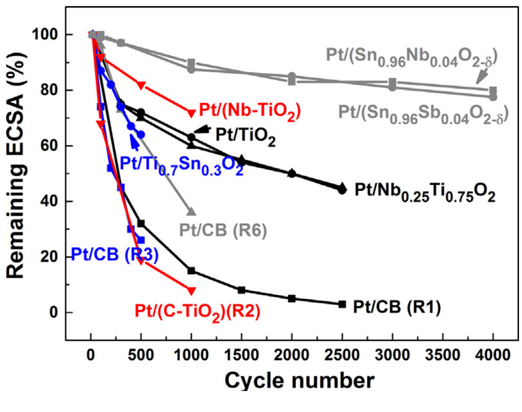

Fig. 6. Electrochemical surface area degradation for Pt/TiO_2 and Pt/$Nb_{0.25}Ti_{0.75}O_2$ compared with Pt/CB (R1) [34,38], Pt/(Nb-TiO_2) compared Pt/(C-TiO_2) (R2) [81], Pt/$Ti_{0.7}Sn_{0.3}O_2$ compared Pt/CB (R3) [79], Pt/($Sn_{0.96}Nb_{0.04}O_{2-\delta}$) and Pt/($Sn_{0.96}Sb_{0.04}O_{2-\delta}$) compared Pt/CB (R6) [51,80].

From Fig. 8, where ECSA degradation is depicted, composites supported Pt NPs show less ECSA loss with respect to reference Pt/CB catalysts. Table 4 summarizes some results on oxide-carbon composites supported Pt NPs towards ORR stability. From this

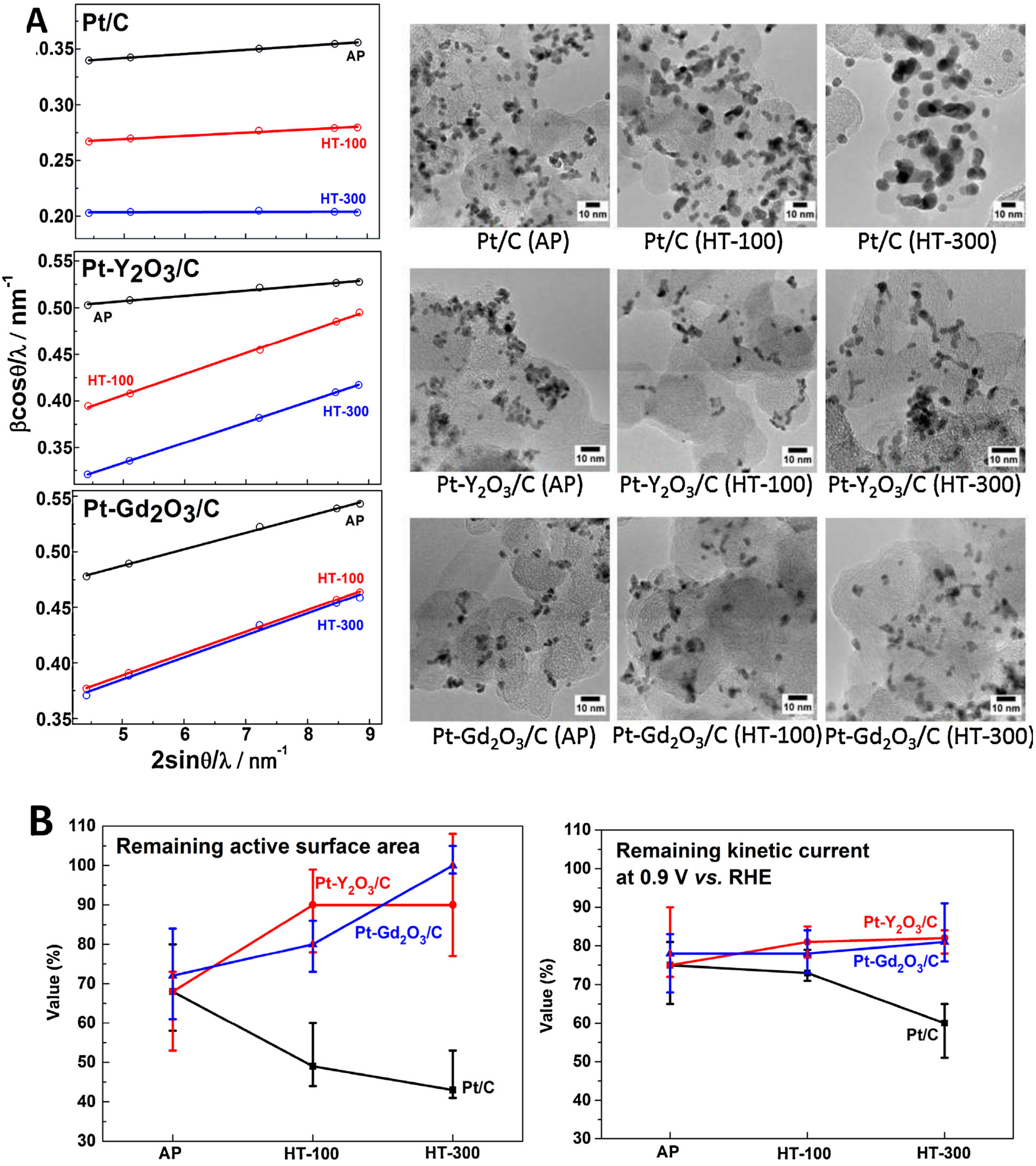

Fig. 7. Williamson-Hall plots and TEM images (A) and ORR stability, measured by cycling 6,000 potential cycles from 0.6 to 0.95 V *vs.* RHE at scan rate of 50 mV s^{-1} in N_2-saturated 0.1 M $HClO_4$ (B) for as-prepared (AP), heat-treated at 100 °C and 300 °C (HT-100 and HT-300) Pt/C, Pt-Y_2O_3/C and Pt-Gd_2O_3/C samples. Data extracted from [42].

Table, it can be seen that the loss of ECSA in Pt/M_xO_y/CB catalysts is less than in reference Pt/CB catalyst. For Pt/TiO_2/CB prepared *via* photo-deposition, it was reported that ECSA remains at 42%, whereas it decreases to 28% on Pt/CB after 3,000 potential cycles [92]. Besides, Wang et al. reported similar trends, where ECSA decreased by 78% and 51%, respectively on Pt/TiO_2/CB and Pt/CB catalyst prepared by chemical route [96]. Moreover, Pt/SnO_2/CB shows enhanced stability with respect to reference Pt/C during 3,500 potential cycles [39]. And Pt/ZnO/CB shows more ECSA loss within 2,000 potential cycles, but more Pt active sites after 3,500 cycles remain in comparison to reference Pt/CB catalyst [39]. It is clear that ZnO in Pt/ZnO/CB is not stable in acid medium. SMSI in Pt/SnO_2/CB was probed by CO-stripping via *in-situ* infra-red (FTIR) spectroscopy. The FTIR results confirmed that oxide-carbon composites influence the electronic effect of the catalytic center, therefore influencing their activity and durability.

Table 4
Titanium oxide (TiO_2)-carbon, Yttrium oxide (Y_2O_3)-carbon and Gadolinium oxide (Gd_2O_3)-carbon composite supported Pt NPs towards ORR stability.

Active Center	Particle diameter[a] /shape	Durability test parameters					Durability test results		Ref.
		Cycles	Potential interval[b]	Electrolyte and electrochemical cell	Scan rate[c]	Temperature	Initial value[d]	Remaining value[e]	
$Pt/TiO_2/CB$	N.M./Spherical	3,000	0.05–1.2	N_2-saturated 0.5 M H_2SO_4in half-cell.	50	25 °C	N.M.	ECSA = 42%	[92]
Pt/CB (R1)*	N.M./Spherical						N.M.	ECSA = 28%	
$Pt/TiO_2/CB$	3.5/Spherical	1,000	0.53–1.13	0.5 M H_2SO_4in half-cell.	N.M.	25 °C	ECSA = 72.7	ECSA = 78%	[96]
Pt/CB (R2)*	2.85/Spherical						ECSA = 81.5	ECSA = 51%	
$Pt/SnO_2/CB$	N.M.	3,500	0.05–1.2	N_2-saturated 0.5 M H_2SO_4in half-cell.	50	25 °C	ECSA = 89.5	ECSA = 60 ± 3%	[39]
Pt/ZnO/CB	N.M.						ECSA = 17.8	ECSA = 50 ± 2%	
Pt/CB (R3)*	N.M.						ECSA = 37.8	ECSA = 50 ± 3%	

N.M. = not mentioned.
[a] nm.
[b] V vs. RHE.
[c] $mV s^{-1}$.
[d] Electrochemical surface area (ECSA) / $m^2 g^{-1}_{Pt}$.
[e] Normalized by initial value.
* Reference catalyst to compare ORR stability.

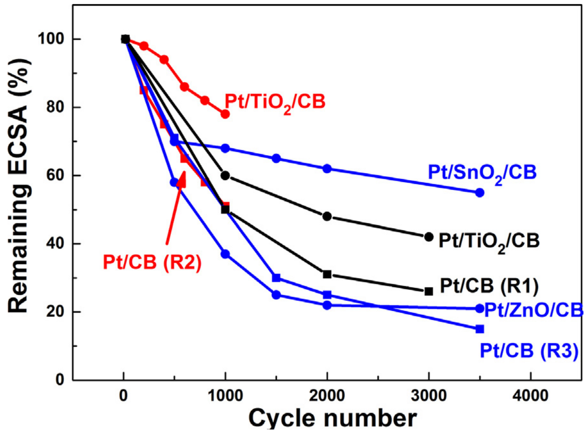

Fig. 8. $Pt/TiO_2/CB$ compared with reference Pt/CB catalyst [92,96]; $Pt/SnO_2/CB$ and Pt/ZnO/CB compared with reference Pt/CB catalyst [39].

4. Summary and outlook

We have made an analysis of the various substrates used to support nanoparticles of platinum or alloyed platinum. The examination of such catalyst/substrate systems toward the oxygen reduction reaction was assessed in three parts according to the nature of the substrates, namely carbon, oxide, oxide-carbon composites. Besides the electronic modification of the catalytic center to create more active catalytic centers with less massif material is the search of the ideal substrate (good conductivity and stability) to stand the harsh electrochemical conditions of the cathode when submitted to the on-off condition of low temperature fuel cells. Electronic modification is attained using the hybridization phenomenon, as in the case of the interaction of sp^2 of graphitic domains, and/or the metal oxide with the metal d-orbitals, and/or the effect of oxide clusters (e.g. rare-earth oxides) decorating the catalytic center. However, efforts need to be expanded in the design of the catalytic center modification either via substrate-metal interaction and/or by the catalytic center modification itself.

Acknowledgement

This work was partially supported by the European Union's Seventh Framework Programme (FP7/2007-2013) for the Fuel Cell and Hydrogen Joint Technology Initiative under grant agreement n8 303492 CathCat, and the University of Poitiers.

Appendix A. Supplementary data

Supplementary data associated with this article can be found, in the online version, at http://dx.doi.org/10.1016/j.electacta.2015.04.098.

References

[1] Y.E. Seidel, R.W. Lindstroem, Z. Jusys, M. Gustavsson, P. Hanarp, B. Kasemo, A. Minkow, H.J. Fecht, R.J. Behm, Stability of nanostructured Pt/glassy carbon electrodes prepared by colloidal lithography, J. Electrochem. Soc. 155 (2008) K50–K58.
[2] P.J. Ferreira, G.J. la O', Y. Shao-Horn, D. Morgan, R. Makharia, S. Kocha, H.A. Gasteiger, Instability of Pt/C electrocatalysts in proton exchange membrane fuel cells - A mechanistic investigation, J. Electrochem. Soc. 152 (2005) A2256–A2271.
[3] M.K. Debe, Electrocatalyst approaches and challenges for automotive fuel cells, Nature 486 (2012) 43–51.
[4] J. Ge, J. St-Pierre, Y. Zhai, PEMFC cathode catalyst contamination evaluation with a RRDE-methyl methacrylate, Int. J. Hydrogen Energy 39 (2014) 18351–18361.
[5] J. Ma, A. Habrioux, N. Alonso-Vante, The Effect of Substrates at Cathodes in Low-temperature Fuel Cells, ChemElectroChem 1 (2014) 37–46.
[6] J. Speder, A. Zana, I. Spanos, J.J.K. Kirkensgaard, K. Mortensen, M. Arenz, On the influence of the Pt to carbon ratio on the degradation of high surface area carbon supported PEM fuel cell electrocatalysts, Electrochem. Commun. 34 (2013) 153–156.
[7] J. Speder, A. Zana, I. Spanos, J.J.K. Kirkensgaard, K. Mortensen, M. Hanzlik, M. Arenz, Comparative degradation study of carbon supported proton exchange membrane fuel cell electrocatalysts – The influence of the platinum to carbon ratio on the degradation rate, J. Power Sources 261 (2014) 14–22.
[8] K.J.J. Mayrhofer, J.C. Meier, S.J. Ashton, G.K.H. Wiberg, F. Kraus, M. Hanzlik, M. Arenz, Fuel cell catalyst degradation on the nanoscale, Electrochem. Commun. 10 (2008) 1144–1147.
[9] Y. Shao, G. Yin, Y. Gao, Understanding and approaches for the durability issues of Pt-based catalysts for PEM fuel cell, J. Power Sources 171 (2007) 558–566.
[10] C.W.B. Bezerra, L. Zhang, H. Liu, K. Lee, A.L.B. Marques, E.P. Marques, H. Wang, J. Zhang, A review of heat-treatment effects on activity and stability of PEM fuel cell catalysts for oxygen reduction reaction, J. Power Sources 173 (2007) 891–908.
[11] S.J. Yoo, K.-S. Lee, S.J. Hwang, Y.-H. Cho, S.-K. Kim, J.W. Yun, Y.-E. Sung, T.-H. Lim, Pt3Y electrocatalyst for oxygen reduction reaction in proton exchange membrane fuel cells, Int. J. Hydrogen Energy 37 (2012) 9758–9765.

[12] J. Greeley, I.E.L. Stephens, A.S. Bondarenko, T.P. Johansson, H.A. Hansen, T.F. Jaramillo, J. Rossmeisl, I. Chorkendorff, J.K. Nørskov, Alloys of platinum and early transition metals as oxygen reduction electrocatalysts, Nat. Chem. 1 (2009) 552–556.

[13] P. Malacrida, M. Escudero-Escribano, A. Verdaguer-Casadevall, I.E.L. Stephens, I. Chorkendorff, Enhanced activity and stability of Pt-La and Pt-Ce alloys for oxygen electroreduction: the elucidation of the active surface phase, J. Mater. Chem. A 2 (2014) 4234–4243.

[14] S.J. Yoo, S.J. Hwang, J.-G. Lee, S.-C. Lee, T.-H. Lim, Y.-E. Sung, A. Wieckowski, S.-K. Kim, Promoting effects of La for improved oxygen reduction activity and high stability of Pt on Pt-La alloy electrodes, Energy Environ. Sci. 5 (2012) 7521–7525.

[15] P. Hernandez-Fernandez, F. Masini, D.N. McCarthy, C.E. Strebel, D. Friebel, D. Deiana, P. Malacrida, A. Nierhoff, A. Bodin, A.M. Wise, J.H. Nielsen, T.W. Hansen, A. Nilsson, E.L. StephensIfan, I. Chorkendorff, Mass-selected nanoparticles of PtxY as model catalysts for oxygen electroreduction, Nat. Chem. 6 (2014) 732–738.

[16] D. Wang, H.L. Xin, R. Hovden, H. Wang, Y. Yu, D.A. Muller, F.J. DiSalvo, H.D. Abruña, Structurally ordered intermetallic platinum–cobalt core–shell nanoparticles with enhanced activity and stability as oxygen reduction electrocatalysts, Nat. Mater. 12 (2013) 81–87.

[17] H. Yang, W. Vogel, C. Lamy, N. Alonso-Vante, Structure and Electrocatalytic Activity of Carbon-Supported Pt–Ni Alloy Nanoparticles Toward the Oxygen Reduction Reaction, J. Phy. Chem. B 108 (2004) 11024–11034.

[18] C. Cui, L. Gan, M. Heggen, S. Rudi, P. Strasser, Compositional segregation in shaped Pt alloy nanoparticles and their structural behaviour during electrocatalysis, Nat. Mater. 12 (2013) 765–771.

[19] J. Kim, Y. Lee, S. Sun, Structurally Ordered FePt Nanoparticles and Their Enhanced Catalysis for Oxygen Reduction Reaction, J. Am. Chem. Soc. 132 (2010) 4996–4997.

[20] A. Marcu, G. Toth, R. Srivastava, P. Strasser, Preparation, characterization and degradation mechanisms of PtCu alloy nanoparticles for automotive fuel cells, J. Power Sources 208 (2012) 288–295.

[21] K.C. Neyerlin, R. Srivastava, C. Yu, P. Strasser, Electrochemical activity and stability of dealloyed Pt–Cu and Pt–Cu–Co electrocatalysts for the oxygen reduction reaction (ORR), J. Power Sources 186 (2009) 261–267.

[22] N. Hodnik, C. Jeyabharathi, J.C. Meier, A. Kostka, K.L. Phani, A. Recnik, M. Bele, S. Hocevar, M. Gaberscek, K.J.J. Mayrhofer, Effect of ordering of PtCu$_3$ nanoparticle structure on the activity and stability for the oxygen reduction reaction, Phys. Chem. Chem. Phys. 16 (2014) 13610–13615.

[23] L. Su, W. Jia, C.-M. Li, Y. Lei, Mechanisms for Enhanced Performance of Platinum-Based Electrocatalysts in Proton Exchange Membrane Fuel Cells, ChemSusChem 7 (2014) 361–378.

[24] E. Antolini, J.R.C. Salgado, M.J. Giz, E.R. Gonzalez, Effects of geometric and electronic factors on ORR activity of carbon supported Pt–Co electrocatalysts in PEM fuel cells, Int. J. Hydrogen Energy 30 (2005) 1213–1220.

[25] S. Koh, P. Strasser, Electrocatalysis on Bimetallic Surfaces: Modifying Catalytic Reactivity for Oxygen Reduction by Voltammetric Surface Dealloying, J. Am. Chem. Soc. 129 (2007) 12624–12625.

[26] J. Ma, A. Habrioux, C. Morais, A. Lewera, W. Vogel, Y. Verde-Gómez, G. Ramos-Sanchez, P.B. Balbuena, N. Alonso-Vante, Spectroelectrochemical Probing of the Strong Interaction between Platinum Nanoparticles and Graphitic Domains of Carbon, ACS Catal. 3 (2013) 1940–1950.

[27] X. Wang, W. Li, Z. Chen, M. Waje, Y. Yan, Durability investigation of carbon nanotube as catalyst support for proton exchange membrane fuel cell, J. Power Sources 158 (2006) 154–159.

[28] R. Kou, Y. Shao, D. Wang, M.H. Engelhard, J.H. Kwak, J. Wang, V.V. Viswanathan, C. Wang, Y. Lin, Y. Wang, I.A. Aksay, J. Liu, Enhanced activity and stability of Pt catalysts on functionalized graphene sheets for electrocatalytic oxygen reduction, Electrochem. Commun. 11 (2009) 954–957.

[29] Y. Li, Y. Li, E. Zhu, T. McLouth, C.-Y. Chiu, X. Huang, Y. Huang, Stabilization of High-Performance Oxygen Reduction Reaction Pt Electrocatalyst Supported on Reduced Graphene Oxide/Carbon Black Composite, J. Am. Chem. Soc. 134 (2012) 12326–12329.

[30] T.-T. Nguyen, V.T.T. Ho, C.-J. Pan, J.-Y. Liu, H.-L. Chou, J. Rick, W.-N. Su, B.-J. Hwang, Synthesis of Ti$_{0.7}$Mo$_{0.3}$O$_2$ supported-Pt nanodendrites and their catalytic activity and stability for oxygen reduction reaction, Appl. Catal., B 154–155 (2014) 183–189.

[31] J. Ma, E. Valenzuela, A.S. Gago, J. Rousseau, A. Habrioux, N. Alonso-Vante, Photohole Trapping Induced Platinum Cluster Nucleation on the Surface of TiO$_2$ Nanoparticles, J. Phy. Chem. C (2013) .

[32] L. Timperman, A. Lewera, W. Vogel, N. Alonso-Vante, Nanostructured platinum becomes alloyed at oxide-composite substrate, Electrochem. Commun. 12 (2010) 1772–1775.

[33] V.T.T. Ho, C.-J. Pan, J. Rick, W.-N. Su, B.-J. Hwang, Nanostructured Ti$_{0.7}$Mo$_{0.3}$O$_2$ Support Enhances Electron Transfer to Pt: High-Performance Catalyst for Oxygen Reduction Reaction, J. Am. Chem. Soc. 133 (2011) 11716–11724.

[34] S.-Y. Huang, P. Ganesan, B.N. Popov, Titania supported platinum catalyst with high electrocatalytic activity and stability for polymer electrolyte membrane fuel cell, Appl. Catal. B 102 (2011) 71–77.

[35] S.J. Tauster, S.C. Fung, R.L. Garten, Strong metal-support interactions. Group 8 noble metals supported on titanium dioxide, J. Am. Chem. Soc. 100 (1978) 170–175.

[36] S.J. Tauster, Strong metal-support interactions, Acc. Chem. Res. 20 (1987) 389–394.

[37] J.-H. Kim, S. Chang, Y.-T. Kim, Compressive strain as the main origin of enhanced oxygen reduction reaction activity for Pt electrocatalysts on chromium-doped titania support, Appl. Catal., B 158–159 (2014) 112–118.

[38] S.-Y. Huang, P. Ganesan, B.N. Popov, Electrocatalytic activity and stability of niobium-doped titanium oxide supported platinum catalyst for polymer electrolyte membrane fuel cells, Appl. Catal. B 96 (2010) 224–231.

[39] B. Ruiz Camacho, C. Morais, M.A. Valenzuela, N. Alonso-Vante, Enhancing oxygen reduction reaction activity and stability of platinum via oxide-carbon composites, Catal. Today 202 (2013) 36–43.

[40] A. Lewera, L. Timperman, A. Roguska, N. Alonso-Vante, Metal–Support Interactions between Nanosized Pt and Metal Oxides (WO$_3$ and TiO$_2$) Studied Using X-ray Photoelectron Spectroscopy, J. Phy. Chem. C 115 (2011) 20153–20159.

[41] Y. Luo, A. Habrioux, L. Calvillo, G. Granozzi, N. Alonso-Vante, Yttrium Oxide/Gadolinium Oxide-Modified Platinum Nanoparticles as Cathodes for the Oxygen Reduction Reaction, ChemPhysChem 15 (2014) 2136–2144.

[42] Y. Luo, A. Habrioux, L. Calvillo, G. Granozzi, N. Alonso-Vante, Thermally Induced Strains on Catalytic Activity and Stability of Pt-M$_2$O$_3$ (M = Y or Gd) Catalysts Towards Oxygen Reduction Reaction (ORR), ChemCatChem (2014) , doi:http://dx.doi.org/10.1002/cctc.201500130.

[43] G.A. Tritsaris, J. Greeley, J. Rossmeisl, J.K. Nørskov, Atomic-Scale Modeling of Particle Size Effects for the Oxygen Reduction Reaction on Pt, Catal. Lett. 141 (2011) 909–913.

[44] C. Zhang, S.Y. Hwang, Z. Peng, Size-dependent oxygen reduction property of octahedral Pt-Ni nanoparticle electrocatalysts, J. Mater. Chem. A 2 (2014) 19778–19787.

[45] P. Trogadas, T.F. Fuller, The Effect of Uniform Particle Size Distribution on Pt Stability, ECS Trans. 41 (2011) 761–773.

[46] J. Zhang, H. Yang, J. Fang, S. Zou, Synthesis and Oxygen Reduction Activity of Shape-Controlled Pt$_3$Ni Nanopolyhedra, Nano Lett. 10 (2010) 638–644.

[47] S.-I. Choi, S. Xie, M. Shao, J.H. Odell, N. Lu, H.-C. Peng, L. Protsailo, S. Guerrero, J. Park, X. Xia, J. Wang, M.J. Kim, Y. Xia, Synthesis and Characterization of 9nm Pt–Ni Octahedra with a Record High Activity of 3.3 A/mgPt for the Oxygen Reduction Reaction, Nano Lett. 13 (2013) 3420–3425.

[48] J. Zhang, K. Sasaki, E. Sutter, R.R. Adzic, Stabilization of Platinum Oxygen-Reduction Electrocatalysts Using Gold Clusters, Science 315 (2007) 220–222.

[49] K. Sasaki, H. Naohara, Y. Cai, Y.M. Choi, P. Liu, M.B. Vukmirovic, J.X. Wang, R.R. Adzic, Core-Protected Platinum Monolayer Shell High-Stability Electrocatalysts for Fuel-Cell Cathodes, Angewandte Chemie International Edition 49 (2010) 8602–8607.

[50] D. Wang, H.L. Xin, Y. Yu, H. Wang, E. Rus, D.A. Muller, H.D. Abruña, Pt-Decorated PdCo@Pd/C Core–Shell Nanoparticles with Enhanced Stability and Electrocatalytic Activity for the Oxygen Reduction Reaction, J. Am. Chem. Soc. 132 (2010) 17664–17666.

[51] H. Yano, T. Akiyama, M. Watanabe, H. Uchida, High durability of Pt/graphitized carbon catalysts for polymer electrolyte fuel cells prepared by the nanocapsule method, J. Electroanal. Chem. 688 (2013) 137–142.

[52] L. Timperman, Y.J. Feng, W. Vogel, N. Alonso-Vante, Substrate effect on oxygen reduction electrocatalysis, Electrochim. Acta 55 (2010) 7558–7563.

[53] K.H. Kangasniemi, D.A. Condit, T.D. Jarvi, Characterization of Vulcan Electrochemically Oxidized under Simulated PEM Fuel Cell Conditions, J. Electrochem. Soc. 151 (2004) E125–E132.

[54] L.M. Roen, C.H. Paik, T.D. Jarvi, Electrocatalytic Corrosion of Carbon Support in PEMFC Cathodes, Electrochem. Solid-State Lett. 7 (2004) A19–A22.

[55] Y. Senoo, K. Kakinuma, M. Uchida, H. Uchida, S. Deki, M. Watanabe, Improvements in electrical and electrochemical properties of Nb-doped SnO$_{2-\delta}$ supports for fuel cell cathodes due to aggregation and Pt loading, RSC Adv. 4 (2014) 32180–32188.

[56] M. Watanabe, D.A. Tryk, M. Wakisaka, H. Yano, H. Uchida, Overview of recent developments in oxygen reduction electrocatalysis, Electrochim. Acta 84 (2012) 187–201.

[57] P. Strasser, S. Koh, T. Anniyev, J. Greeley, K. More, C. Yu, Z. Liu, S. Kaya, D. Nordlund, H. Ogasawara, M.F. Toney, A. Nilsson, Lattice-strain control of the activity in dealloyed core–shell fuel cell catalysts, Nat. Chem. 2 (2010) 454–460.

[58] M. Escudero-Escribano, A. Verdaguer-Casadevall, P. Malacrida, U. Grønbjerg, B.P. Knudsen, A.K. Jepsen, J. Rossmeisl, I.E.L. Stephens, I. Chorkendorff, Pt$_5$Gd as a Highly Active and Stable Catalyst for Oxygen Electroreduction, J. Am. Chem. Soc. 134 (2012) 16476–16479.

[59] V.R. Stamenkovic, B.S. Mun, K.J.J. Mayrhofer, P.N. Ross, N.M. Markovic, Effect of Surface Composition on Electronic Structure, Stability, and Electrocatalytic Properties of Pt-Transition Metal Alloys: Pt-Skin versus Pt-Skeleton Surfaces, J. Am. Chem. Soc. 128 (2006) 8813–8819.

[60] H. Yang, N. Alonso-Vante, J.-M. Léger, C. Lamy, Tailoring, Structure, and Activity of Carbon-Supported Nanosized Pt–Cr Alloy Electrocatalysts for Oxygen Reduction in Pure and Methanol-Containing Electrolytes, J. Phy. Chem. B 108 (2004) 1938–1947.

[61] Y.-W. Lee, A.R. Ko, D.-Y. Kim, S.-B. Han, K.-W. Park, Octahedral Pt-Pd alloy catalysts with enhanced oxygen reduction activity and stability in proton exchange membrane fuel cells, RSC Adv. 2 (2012) 1119–1125.

[62] Z. Wen, J. Liu, J. Li, Core/Shell Pt/C Nanoparticles Embedded in Mesoporous Carbon as a Methanol-Tolerant Cathode Catalyst in Direct Methanol Fuel Cells, Adv. Mater. (Weinheim Ger.) 20 (2008) 743–747.

[63] F. Hasche, M. Oezaslan, P. Strasser, Activity, stability and degradation of multi walled carbon nanotube (MWCNT) supported Pt fuel cell electrocatalysts, Phys. Chem. Chem. Phys. 12 (2010) 15251–15258.

[64] Y. Shao, S. Zhang, C. Wang, Z. Nie, J. Liu, Y. Wang, Y. Lin, Highly durable graphene nanoplatelets supported Pt nanocatalysts for oxygen reduction, J. Power Sources 195 (2010) 4600–4605.

[65] J. Ma, A. Habrioux, N. Guignard, N. Alonso-Vante, Functionalizing Effect of Increasingly Graphitic Carbon Supports on Carbon-Supported and TiO_2–Carbon Composite-Supported Pt Nanoparticles, J. Phy. Chem. C 116 (2012) 21788–21794.

[66] N. Alonso-Vante, Carbonyl Tailored Electrocatalysts, Fuel Cells 6 (2006) 182–189.

[67] E. Kang, S. An, S. Yoon, J.K. Kim, J. Lee, Ordered mesoporous WO_{3-X} possessing electronically conductive framework comparable to carbon framework toward long-term stable cathode supports for fuel cells, J. Mater. Chem. 20 (2010) 7416–7421.

[68] A. Bauer, K. Lee, C. Song, Y. Xie, J. Zhang, R. Hui, Pt nanoparticles deposited on TiO_2 based nanofibers: Electrochemical stability and oxygen reduction activity, J. Power Sources 195 (2010) 3105–3110.

[69] Z. Yan, W. Wei, J. Xie, S. Meng, X. Lü, J. Zhu, An ion exchange route to produce WO_3 nanobars as Pt electrocatalyst promoter for oxygen reduction reaction, J. Power Sources 222 (2013) 218–224.

[70] F. Takasaki, S. Matsuie, Y. Takabatake, Z. Noda, A. Hayashi, Y. Shiratori, K. Ito, K. Sasaki, Carbon-Free Pt Electrocatalysts Supported on SnO_2 for Polymer Electrolyte Fuel Cells: Electrocatalytic Activity and Durability, J. Electrochem. Soc. 158 (2011) B1270–B1275.

[71] A. Rabis, E. Fabbri, A. Foelske, M. Horisberger, R. Kötz, T.J. Schmidt, Durable Oxide-Based Catalysts for Application as Cathode Materials in Polymer Electrolyte Fuel Cells (PEFCs), ECS Trans. 50 (2013) 9–17.

[72] B.H. Chen, J.M. White, Properties of platinum supported on oxides of titanium, J. Phy. Chem. 86 (1982) 3534–3541.

[73] R. Lamber, Strong metal-support interaction in the system of platinum on quartz glass in a reducing atmosphere, Thin Solid Films 128 (1985) L29–L32.

[74] A.K. Datye, D.S. Kalakkad, M.H. Yao, D.J. Smith, Comparison of Metal-Support Interactions in Pt/TiO_2 and Pt/CeO_2, J. Catal. 155 (1995) 148–153.

[75] H. Yoshitake, Y. Iwasawa, Active sites and reaction mechanisms for deuteration of acrolein on TiO_2-, Y_2O_3- ZrO_2-, CeO_2 and Na/SiO_2-supported platinum catalysts, J. Chem. Soc., Faraday Trans. 88 (1992) 503–510.

[76] D.-e. Jiang, S.H. Overbury, S. Dai, Structures and Energetics of Pt Clusters on TiO_2: Interplay between Metal–Metal Bonds and Metal–Oxygen Bonds, J. Phy. Chem. C 116 (2012) 21880–21885.

[77] W. Vogel, L. Timperman, N. Alonso-Vante, Probing metal substrate interaction of Pt nanoparticles: Structural XRD analysis and oxygen reduction reaction, Applied Catalysis A: General 377 (2010) 167–173.

[78] L. Timperman, N. Alonso-Vante, Oxide Substrate Effect Toward Electrocatalytic Enhancement of Platinum and Ruthenium–Selenium Catalysts, Electrocatalysis 2 (2011) 181–191.

[79] Y. Gao, M. Hou, Z. Shao, C. Zhang, X. Qin, B. Yi, Preparation and characterization of $Ti_{0.7}Sn_{0.3}O_2$ as catalyst support for oxygen reduction reaction, J. Energ. Chem. 23 (2014) 331–337.

[80] K. Kakinuma, Y. Chino, Y. Senoo, M. Uchida, T. Kamino, H. Uchida, S. Deki, M. Watanabe, Characterization of Pt catalysts on Nb-doped and Sb-doped $SnO_{2-\delta}$ support materials with aggregated structure by rotating disk electrode and fuel cell measurements, Electrochim. Acta 110 (2013) 316–324.

[81] I. Savych, J. Bernard d'Arbigny, S. Subianto, S. Cavaliere, D.J. Jones, J. Rozière, On the effect of non-carbon nanostructured supports on the stability of Pt nanoparticles during voltage cycling: A study of TiO_2 nanofibres, J. Power Sources 257 (2014) 147–155.

[82] A.J. Bard, L.R. Faulkner, Electrochemical Methods: Fundamentals and Applications, Second Edition ed., John Wiley&Sons, New York, 2001.

[83] M.K. Jeon, P.J. McGinn, Carbon supported Pt–Y electrocatalysts for the oxygen reduction reaction, J. Power Sources 196 (2011) 1127–1131.

[84] K.G. Nishanth, P. Sridhar, S. Pitchumani, Enhanced oxygen reduction reaction activity through spillover effect by Pt–$Y(OH)_3$/C catalyst in direct methanol fuel cells, Electrochem. Commun. 13 (2011) 1465–1468.

[85] W. Vogel, L. Timperman, N. Alonso-Vante, Probing metal substrate interaction of Pt nanoparticles: Structural XRD analysis and oxygen reduction reaction, Appl. Catal. A 377 (2010) 167–173.

[86] J. Ma, A. Habrioux, N. Alonso-Vante, Enhanced H.E.R ORR behavior on photodeposited Pt nanoparticles onto oxide–carbon composite, J. Solid State Electrochem. 17 (2013) 1913–1921.

[87] T.J. Fabish, M.L. Hair, The dependence of the work function of carbon black on surface acidity, J. Colloid Interface Sci. 62 (1977) 16–23.

[88] E.C.H. Sykes, F.J. Williams, M.S. Tikhov, R.M. Lambert, Nucleation, Growth, Sintering, Mobility, and Adsorption Properties of Small Gold Particles on Polycrystalline Titania, J. Phy. Chem. B 106 (2002) 5390–5394.

[89] X. Liu, J. Chen, G. Liu, L. Zhang, H. Zhang, B. Yi, Enhanced long-term durability of proton exchange membrane fuel cell cathode by employing Pt/TiO_2/C catalysts, J. Power Sources 195 (2010) 4098–4103.

[90] T. Masuda, H. Fukumitsu, K. Fugane, H. Togasaki, D. Matsumura, K. Tamura, Y. Nishihata, H. Yoshikawa, K. Kobayashi, T. Mori, K. Uosaki, Role of Cerium Oxide in the Enhancement of Activity for the Oxygen Reduction Reaction at Pt–CeO_x Nanocomposite Electrocatalyst - An in Situ Electrochemical X-ray Absorption Fine Structure Study, J. Phy. Chem. C 116 (2012) 10098–10102.

[91] D.R. Ou, T. Mori, K. Fugane, H. Togasaki, F. Ye, J. Drennan, Stability of Ceria Supports in Pt–CeO_x/C Catalysts, J. Phy. Chem. C 115 (2011) 19239–19245.

[92] J. Ma, A. Habrioux, A. Gago, N. Alonso-Vante, Towards Understanding the Essential Role Played by the Platinum-Support Interaction on Electrocatalytic Activity, ECS Trans. 45 (2013) 25–33.

[93] F. Zhang, J. Chen, X. Zhang, W. Gao, R. Jin, N. Guan, Y. Li, Synthesis of Titania-Supported Platinum Catalyst: The Effect of pH on Morphology Control and Valence State during Photodeposition, Langmuir 20 (2004) 9329–9334.

[94] J. Shim, C.-R. Lee, H.-K. Lee, J.-S. Lee, E.J. Cairns, Electrochemical characteristics of Pt–WO_3/C and Pt–TiO_2/C electrocatalysts in a polymer electrolyte fuel cell, J. Power Sources 102 (2001) 172–177.

[95] S. Beak, D. Jung, K.S. Nahm, P. Kim, Preparation of Highly Dispersed Pt on TiO_2-Modified Carbon for the Application to Oxygen Reduction Reaction, Catal. Lett. 134 (2010) 288–294.

[96] Z.-Z. Jiang, Z.-B. Wang, Y.-Y. Chu, D.-M. Gu, G.-P. Yin, Ultrahigh stable carbon riveted Pt/TiO_2-C catalyst prepared by in situ carbonized glucose for proton exchange membrane fuel cell, Energy Environ. Sci. 4 (2011) 728–735.

[97] M. Koudelka, A. Monnier, J. Sanchez, J. Augustynski, Correlation between the surface composition of Pt/TiO_2 catalysts and their adsorption behaviour in aqueous solutions, J. Mol. Catal. 25 (1984) 295–305.

[98] L. Xiong, A. Manthiram, Synthesis and characterization of methanol tolerant Pt/TiO_x/C nanocomposites for oxygen reduction in direct methanol fuel Cells, Electrochim. Acta 49 (2004) 4163–4170.

[99] N.R. de Tacconi, C.R. Chenthamarakshan, K. Rajeshwar, W.-Y. Lin, T.F. Carlson, L. Nikiel, W.A. Wampler, S. Sambandam, V. Ramani, Photocatalytically Generated Pt / C–TiO_2 Electrocatalysts with Enhanced Catalyst Dispersion for Improved Membrane Durability in Polymer Electrolyte Fuel Cells, J. Electrochem. Soc. 155 (2008) B1102–B1109.

[100] N.R. de Tacconi, K. Rajeshwar, W. Chanmanee, V. Valluri, W.A. Wampler, W.-Y. Lin, L. Nikiel, Photocatalytically Generated Bimetallic (Pt–Au /C–TiO_2) Electrocatalysts for Polymer Electrolyte Fuel Cell Applications, J. Electrochem. Soc. 157 (2010) B147–B153.

[101] A. Orfanidi, M.K. Daletou, S.G. Neophytides, Preparation and characterization of Pt on modified multi-wall carbon nanotubes to be used as electrocatalysts for high temperature fuel cell applications, Appl. Catal. B 106 (2011) 379–389.

Electrochimica Acta 141 (2014) 89–101

Contents lists available at ScienceDirect

Electrochimica Acta

journal homepage: www.elsevier.com/locate/electacta

Pd Nanoparticles deposited on nitrogen-doped HOPG: New Insights into the Pd-catalyzed Oxygen Reduction Reaction

Wenbo Ju[a,2], Marco Favaro[b,2], Christian Durante[b], Lorenzo Perini[b], Stefano Agnoli[b], Oliver Schneider[a,c,*], Ulrich Stimming[a,d,e], Gaetano Granozzi[b,1]

[a] *Department of Physics E19, Technische Universität München, James-Franck-Str.1, 85748, Garching, Germany*
[b] *Department of Chemical Science, Università degli Studi di Padova, Via Marzolo 1, 35131, Padova, Italy*
[c] *Institute of Informatics VI, Technische Universität München, Boltzmannstr.3, 85748, Garching, Germany*
[d] *Institute of Advanced Study (IAS), TechnischeUniversität München, Lichtenbergstr. 2a, 85748 Garching, Germany*
[e] *TUM CREATE Ltd., 1 CREATE Way, #10-02CREATE Tower, Singapore 138602, Singapore*

ARTICLE INFO

Article history:
Received 18 November 2013
Received in revised form 25 June 2014
Accepted 25 June 2014
Available online 11 July 2014

Keywords:
Oxygen reduction reaction
Electrocatalysis
Substrate effect
XPS
Nitrogen doped HOPG

ABSTRACT

The combination of surface science and electrochemistry is an effective method to approach a fundamental understanding of electrocatalytic systems, especially of the catalyst/support assemblies. Extrinsic chemical defects in the support can affect the performances and this topic is much investigated in recent electrocatalyst research. In this work, nitrogen functional groups are introduced into the outermost layers of highly oriented pyrolytic graphite (HOPG) by ion implantation with a beam energy of 100 eV. Palladium nanoparticles (Pd NPs) are then electrochemically deposited onto both pure and nitrogen doped HOPG (N-HOPG). Pd^{2+} species located at the interface between the NPs and the nitrogen-rich surface were observed in the latter case. The supported Pd NPs on N-HOPG show the same electrocatalytic activity for oxygen reduction reaction (ORR) as compared with those supported on pure HOPG. However, the stability of Pd NPs on N-HOPG towards potential cycling decreases strongly due to the existence of Pd^{2+} at the interface, which can accelerate the dissolution of Pd atoms. This result is contradictory to results on supported Pt NPs from the literature where the merit of the N-doping was outlined.

1. Introduction

Supported metal nanoparticles (NPs), as the most common heterogeneous catalysts and electrocatalysts, have attracted a significant amount of research. A single supported NP in contact with an electrolyte is a complex system whose general performances, such as activity, selectivity and stability, depend on many factors, i.e. surface composition, facets, lower-coordinated atoms and defects, size effects, support effects, specific properties of the electrochemical interface, electrolyte composition, and other parameters [1]. To achieve the goal of developing electrocatalysts with optimized efficiency and durability, the knowledge of the whole set of parameters included in the electrocatalytic processes is essential. Therefore, a surface science and electrochemistry (EC) approach to characterize the catalyst/support assembly at the nano-scale is fundamental to achieve a full understanding of an electrocatalytic system under investigation.

There is still an open debate on the influence of a support material on the catalytic performance of supported metal NPs [2]. Significant progress has been made in the past ten years especially in theoretical description of the elementary steps of electrocatalytic reactions. Both geometrical and electronic effects have been reported and been explained theoretically [3–5]. The introduction of tailored defects onto the support surface can improve the dispersion of metal NPs so as to reduce the amount of catalyst without compromising the electrochemical performance [2]. The defects can act as trapping sites for anchoring the metal NPs in order to prevent the decrease in the surface area caused by the agglomeration of metal NPs [6,7]. A charge transfer and electronic interactions between support and catalyst can modify the electronic structure of supported metal NPs, and thus can influence their activity for some specific reactions such as CO oxidation and O_2 reduction [8–10]. A lattice strain introduced into supported metal NPs by adjusting to the lattice structure of the support material can lead to a change

---

* Corresponding author. Tel.: +498928918105; fax: +498928918107.
E-mail addresses: oliver_m.schneider@tum.de (O. Schneider), gaetano.granozzi@unipd.it (G. Granozzi).

[1] 1Tel: +390498275158, Fax: +390498275161

[2] 2W. Ju and M. Favaro contributed equally to this work and should be considered first authors

http://dx.doi.org/10.1016/j.electacta.2014.06.141
0013-4686/

of the electronic structure, and further to a change in the catalytic activity and particle stability [3,11,12]. Additionally, extrinsic chemical defects can modulate the electronic properties of the support material, as well as change the catalyst/support interfacial interaction, which can affect the stability and activity of supported catalyst [13–16].

Highly oriented pyrolytic graphite (HOPG) is the most suitable sp^2-carbon model substrate. Its weak binding to the noble metal NPs leads to the prevalent localization of supported metal NPs at steps and defects [17–19]. Particle-support interaction takes place nearly exclusively by van-der-Waals forces, and strain and ligand effect play no role with this support material [20]. When nitrogen functional groups are introduced by ion implantation into the HOPG surface, the support morphology as well as its electronic properties are modified. Several chemical defects, i.e. trapped N^+ and $N_2{}^+$ ions in carbon vacancies, C-sp^2-N defects (*pyridinic*, *pyrrolic* and N *substitutional*) and -C≡N terminal groups have been identified by a high resolution X-ray photoemission spectroscopy (XPS) analysis [21,22]. Several studies have reported a beneficial influence of N-HOPG on the electrochemical activity of supported NPs: Zhou et al. [14] observed a significant enhancement of N-HOPG onto the catalytic activity and durability of supported Pt NPs for the methanol oxidation reaction (MOR). They used N ion implanation at an implantation energy of 100 eV and electrodeposited Pt using a single pulse deposition from a rather diluted solution of H_2PtCl_6 in diluted perchloric acid. The particle size distribution on HOPG was very large and most particles had sizes between 5 nm and 30 nm. On the N-HOPG, on the other hand, most particles had a size of around 2 nm. Zhou et al. combined in a subsequent study results from theoretical calculations with impedance and work function measurements [15]. They were able to correlate an increased downward band bending at the surface to the optimal deposition potential used in their study. They also found a shift in the core level f-electron levels due to the doping by XPS, and identified Pt^{2+} and Pt^{4+} species formed. From this, they concluded that a charge transfer from Pt particles to the support is possible. Holme et al. [16] reported a down shift of the Pt d-band center when Pt particles sit on N-HOPG compared to undoped HOPG, which weakens the adsorption bonding towards atomic oxygen and therefore increases the activity for ORR. These calculation were done for Pt clusters, and the effect of nanoparticle size was not considered. Palladium and its alloys could be an alternative to Pt-based ORR catalysts. Similar to Pt, it binds the oxygen slightly too strong, which is why a manipulation of the d-band by support effects is desirable [23,24]. In recent work, palladium (Pd) NPs were evaporated from a high-purity metal rod onto HOPG and nitrogen-doped HOPG under ultra-high vacuum (UHV) [7]. Their electrocatalytic activity for the oxygen reduction reaction (ORR) was observed to be almost independent of the nitrogen implantation, but depended mainly on the amount of Pd deposited. However the nitrogen ion implantation was carried out with 500 eV nitrogen ions and the derived N-defects were mostly buried below the surface [7]. On the other hand, the enhanced electrocatalytic activity of the Pt/N-HOPG system was obtained on an implanted sample obtained with 100 eV nitrogen ions [14], so that the N-derived defects are more surface-localized.

Therefore, the N-HOPG supports were prepared in this work by ion implantation with a beam energy of 100 eV. The Pd NPs were electrochemically deposited with the potentiostatic double-pulse technique, which provides a high control of the NPs sizes and particle density. The final Pd/N-HOPG specimens have been then thoroughly characterized by Surface Science tools, namely tapping-mode atomic force microscopy (AFM) and X-ray photoemission (XPS). The electrochemical behavior of pure HOPG, N-HOPG, Pd/HOPG and Pd/N-HOPG was investigated in acidic media with respect to the ORR behavior. The general results provide new insights that are in part contradictory to literature data.

2. Experimental

2.1. Preparation and characterization of N-HOPG samples

Clean HOPG samples (MikroMasch, ZYB grade) were prepared by cleaving the surface with a scotch tape, followed by a thermal annealing cycle from 500 °C to 800 °C after the transfer into the Ultra High Vacuum (UHV) environment. The UHV preparation chamber (base pressure $< 5 \times 10^{-9}$ mbar), was equipped with a double anode X-ray source (Omicron), a hemispherical electron analyzer (VG Scienta) and an ion gun (Thermo VG Scientific) for the implantation process. The N-HOPG samples were prepared by ion implantation using a cold plasma produced in a 2.2×10^{-6} mbar background of N_2, a beam energy of 100 eV (which is close to the lower limit at which a stable beam can be achieved) and an exposure duration of 45 min, with an incidence angle of the ion beam equal to 45° with respect to the sample surface. The ionic current measured during the ion implantation was 1.5 μA and the total dose of implanted argon and nitrogen was around 1×10^{16} ion cm^{-2}. The nitrogen amount was determined normalizing the intensity of the N *1s* XPS peak by the integrated area of the C *1s* photoemission line, obtaining a nitrogen dose of 7.5 at%. The *in-situ* XPS measurements were performed at room temperature, using non-monochromatized Mg-Kα radiation ($h\nu = 1253.6$ eV) and a pass energy of 50 eV and 20 eV for the survey and the single spectral windows, respectively. The calibration of the binding energy (BE) scale was carried out using Au *4f* as reference. The XPS peaks of carbon and nitrogen were deconvoluted into individual components (after Shirley background removal), using a Doniach-Sunich function for the sp^2-C component and symmetrical Voigt functions for the "molecular-like" components. The χ^2 minimization was ensured by the use of a nonlinear least squares routine.

The *ex-situ* atomic force microscopy (AFM) images were taken in tapping mode (TM-AFM) with a Veeco Nanoscope V, using a phosphorus(n) doped silicon (P:Si) cantilever (RTESPA, Bruker) with a resonance frequency in the range of 345-384 kHz and a spring constant of 20-80 N/m. The AFM images were evaluated with WSxM 5.0 image analysis software [25]. The size of electrodeposited nanoparticles was determined as the height of particles, as the convolution between AFM tip and particle leads to a strong overestimation of the particle size.

The Monte Carlo simulations have been carried out using the SRIM-013 (Stopping and Range of Ion in Matter) package [26].

2.2. Electrochemical deposition and characterization

Electrochemical experiments, such as metal deposition, electrochemical characterization, activity and stability measurements, were performed in glass cells with a standard three electrode arrangement by use of a Potentiostat-Galvanostat (Autolab PGSTAT 30). Peroxymonosulfuric acid (Caro's acid) was prepared with H_2SO_4 (95~97%, Merck, p.a.) and H_2O_2 (30%, Merck, p.a.) at a volume ratio of 1:1. All glassware was cleaned in Caro's acid and rinsed extensively with deionized water obtained from a Milli-Q water purification system (Millipore, 18.2 MΩcm, 3 ppm total organic carbon). Hg/Hg_2SO_4 (Schott, B3610) in 0.1 M H_2SO_4 reference electrodes ($E_{ref} = 660$ mV vs. SHE) and Pd wires (Ögussa) as counter electrodes were utilized in all experiments. Potentials in this paper have been converted to the standard hydrogen electrode (SHE) scale by adding 66omV. Pure HOPG and N-HOPG samples, which were encapsulated in a Teflon tape with a 0.126 cm^2 geometric area exposed to the electrolyte, were used as substrates. The solutions were prepared from H_2SO_4 (96%, Merck, Suprapur), $Pd(NO_3)_2$ ($Pd(NO_3)_2$ solution, 16.27%, Mateck), and Na_2SO_4 (99.5%, Merck) with deionized water. The pH value was measured by a pH-meter (Voltcraft, pH-100ATC).

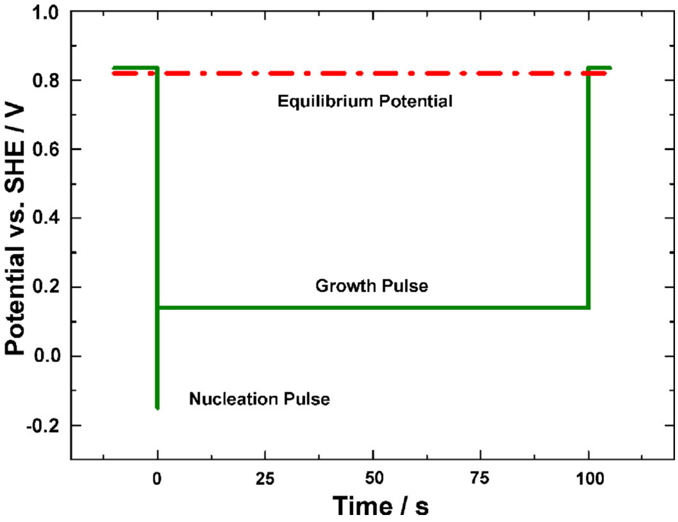

Fig. 1. Double-pulse potential for the Pd deposition applied in this study. A short nucleation pulse of 10ms at E = -140 mV precedes a long growth pulse of 100s at E = 150 mV. The equilibrium potential of Pd^{2+}/Pd is around 820 mV.

Cyclic voltammetry (CV) and electrochemical impedance spectroscopy (EIS) measurements for pure HOPG and N-HOPG were carried out at room temperature in Ar saturated 0.1 M Na_2SO_4 + *x*mM H_2SO_4 (pH = 3) solution. The CVs were measured in a potential range from -0.64 to 1.96 V on the HOPG electrodes, and from -0.14 to 1.46 V on the N-HOPG electrodes. All scan rates were 100 mV/s. The EIS was performed at the open circuit potentials (OCPs) of both HOPG and N-HOPG, which were 0.654 V and 0.584 V, respectively. 50 values of impedance were captured at frequencies from 10 kHz to 0.1 Hz.

Pd deposition was performed from an aqueous solution of 0.5 mM $Pd(NO_3)_2$ in 0.1 M H_2SO_4. The solution was deaerated with argon (Ar) gas, but the solutions were unstirred during the electrochemical experiments. The potentiostatic double-pulse technique was applied for particle deposition. A short nucleation pulse of 10ms at E = -140 mV preceded a long growth pulse of 100s at E = 150 mV. Before and after Pd deposition, the potential was kept at 845 mV, which is about 25 mV more positive than the equilibrium potential of Pd^{2+}/Pd ($E_{eq}\approx$820 mV), to avoid further deposition. After deposition, the sample was removed from the cell and rinsed with deionized water. Fig. 1 shows the double-pulse procedure for the Pd deposition. The amount of Pd deposited was estimated from the deposition charge. Electrochemical deposition of metals on HOPG typically leads to three-dimensional growth, and the shape of the particles can be approximated as hemispherical [17,18], therefore the particle height can be considered equal to the particle radius.

The electrochemical properties of Pd NPs supported on HOPG and N-HOPG were investigated by CV measurements in Ar saturated 0.1 M Na_2SO_4 + *x* mM H_2SO_4 (pH = 3) solution, in order to preserve the stability under polarization of the PdO overlayer formed at elevated potentials, according to the corresponding Pourbaix diagrams [27]. The potential range from 0.26 V to 1.46 V was applied in the CV at a scan rate of 50 mV/s. The CV measurements on HOPG and N-HOPG were performed in the same conditions in order to obtain baselines. The active area of supported Pd was determined by integrating the current of the Pd surface monoxide layer reduction from cyclic voltammetry (424 μC/cm^2) [28]. Repeated cycling under these conditions served for evaluation of the Pd particle stability. The electrocatalytic activity for ORR was measured in O_2 saturated 0.1 M Na_2SO_4 + *x* mM H_2SO_4 (pH = 3) solution, both for bare and Pd-containing HOPG and N-HOPG. CV was performed in the potential range from 0.765 V to 0.275 V at a scan rate of 5 mV/s. As the binding forces of Pd NPs to HOPG and N-HOPG are extremely weak, all activity measurements were carried out in a half-cell setup without any stirring. Experiments using a RDE or RRDE setup could also not be carried out due to the impossibility of machining single-crystalline HOPG with the accuracy required for mounting in an RDE holder.

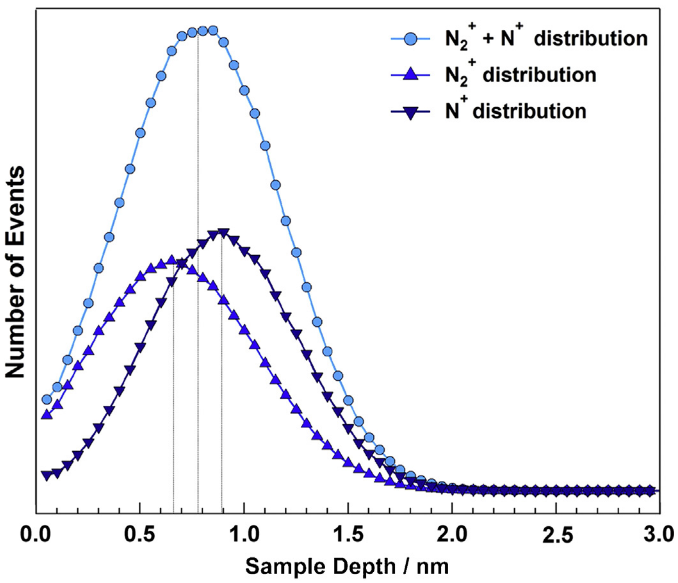

Fig. 2. Implanted nitrogen profiles obtained with Monte Carlo simulation of the implantation process.

3. Results and Discussion

3.1. Monte Carlo simulation of the implantation process

For a quantitative estimation of the distribution of the morphological and chemical defects introduced by the implantation process, Monte Carlo simulations of the nitrogen implantation process have been carried out assuming the Kinchin-Pease modeling[29] of the ion-target atoms interaction. Under the experimental conditions of the present study, the nitrogen plasma contains both N^+ and N_2^+ ionic species [21]. Fig. 2 reports the N^+ and N_2^+ ion distributions in the HOPG target, simulated in two distinct runs with a kinetic energy of 100 eV. The N^+ distribution is centered at 9 Å (where the origin of the abscissa axis represents the topmost layer of the HOPG) with a Full Width at Half Maximum (FWHM) of 6 Å, while the N_2^+ distribution is located closer to the surface, with a projected range (R_p) of 6.7 Å and a straggling of 8 Å. The sum of the two single distributions, that represents the experimental conditions of the ion implantation, is finally characterized by a R_p of 7.9 Å and a FWHM of 10.3 Å, as can be observed from the Fig. 2.

Fig. 2 shows that the morphological defects distribution (coupled with the mass and energy deposition induced by the collision processes) has the maximum located on the topmost layer because of the low kinetic energy of the incoming ions; for this reason, the induced re-hybridization sp^2-sp^3 takes place almost exclusively at the surface of the sample. Furthermore, since the graphite lattice constant perpendicular to the plane is equal to 3.35 Å [30], the R_p of the total ion distribution is located in the second and in the third layer of the sample. Then, the Pd NPs deposited on N-HOPG will be well-dispersed (by the interaction with the morphological defects) and well-interacting with the nitrogen-based chemical defects (as will be documented in the following sections).

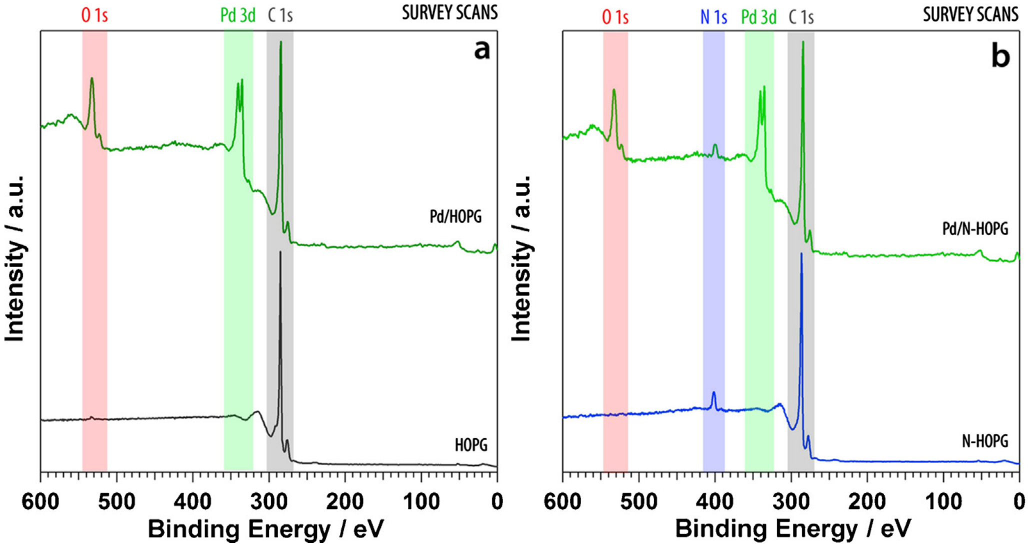

Fig. 3. XPS survey scans taken in the 0~600 eV spectral region for HOPG and Pd/HOPG (a) and for N-HOPG and Pd/N-HOPG (b). In the figure the single spectral regions for the core level photoionization of C (*1s*), Pd (*3d*), N (*1s*) and O (*1s*) are highlighted.

3.2. XPS characterization of N-HOPG and Pd/N-HOPG

In order to characterize the chemical changes induced by the ion implantation, we have carried out a XPS investigation. In the large interval measurements (surveys reported in Fig. 3), the photoionization peak of the C *1s* (284.4 eV) is observed as main feature in all the analyzed samples. Concerning the N-HOPG samples, the N *1s* peak is centered at 400.0 eV, while the surveys relative to the Pd/HOPG and to the Pd/N-HOPG systems show the presence of the Pd *3d* peak (335 eV) and of the O *1s* peak (531.0 eV). For the last two mentioned, the presence of the O *1s* features is imputable to C-O groups present at the step edges and bound to the surface morphological defects after the metal deposition in the aqueous media.

In order to get more precise information about the chemical identity of the defects induced by the ion implantation, the C *1s* and N *1s* energy regions have been recorded with high resolution and the corresponding peaks have been fitted with Voigt functions imposing a FWHM in the 1.0-1.4 eV range.

Fig. 4 reports the multi-peak analysis of the C *1s* signals for pure HOPG (a), N-HOPG (b) and Pd/N-HOPG (c) samples. For the N-HOPG system, the presence of three components is clearly visible, one centered at 284.4 eV which can be attributed to sp^2 hybridized carbon (sp^2-C) forming the pure graphitic lattice, one at 285.5 eV, connected to sp^3 hybridized carbon (sp^3-C) and therefore tetragonally coordinated carbon clusters [31,32] and finally the third at 286.5 eV, which, according to literature, can be assigned to C-N bonds [33].

From these data, we can deduce that N-doping can induce chemical defects (the C-N signal accounts for 12% of the total C *1s* photoemission line) whose characteristics have been studied in further detail by analyzing the N *1s* XPS signals, as reported in Fig. 5a and 5b. Five different components have been identified [21], centered at 398.1 eV, 400.2 eV and 401.2 eV, corresponding to sp^2 C-N defects, which can be described as *pyridinic* (N1), *pyrrolic* (N3) and *N substitutional* (N4, or N graphitic) defects, respectively [22,34]. The component centered at 398.9 eV matches with–C≡N terminal groups (N2). Finally, the component centered at 402.7 eV can be attributed to a N^+ ion trapped into a carbon vacancy (N5). However, for a correct fitting procedure of the XPS peaks of the Pd/HOPG and the Pd/N-HOPG samples, it is necessary to introduce further small components in the high-BE energy tail of the C *1s* (C = O and C(O)OH, centered respectively at 287.8 eV and at 288.9 eV) and of the N *1s* (NO_x at 403.8 eV). The oxygen contamination, as already discussed above, is probably due to the oxidation of samples after the metal deposition in the aqueous environment.

Fig. 6 shows the Pd *3d* XPS data for the same metal coverage deposited on pure HOPG and N-HOPG. No further electrochemical experiments aside from Pd deposition were carried out on these samples before XPS. The Pd $3d_{5/2}$ photoemission peak shows a FWHM ($\Delta E = 1.8$ eV) compatible with the presence of both metal Pd and Pd^{2+} species (centered at 335.1 eV and at 336.2 eV, respectively

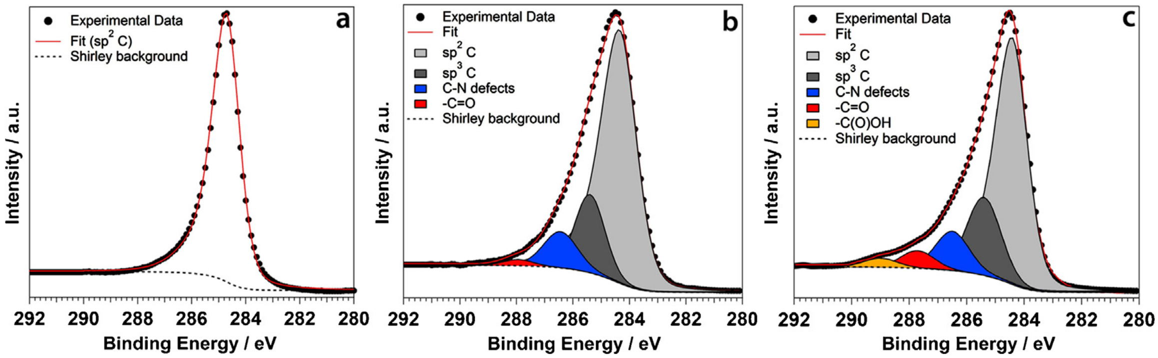

Fig. 4. Core level photoemission lines of C *1s* and relative deconvolution into single chemical components for pure HOPG (a), N-HOPG (b) and Pd/N-HOPG (c).

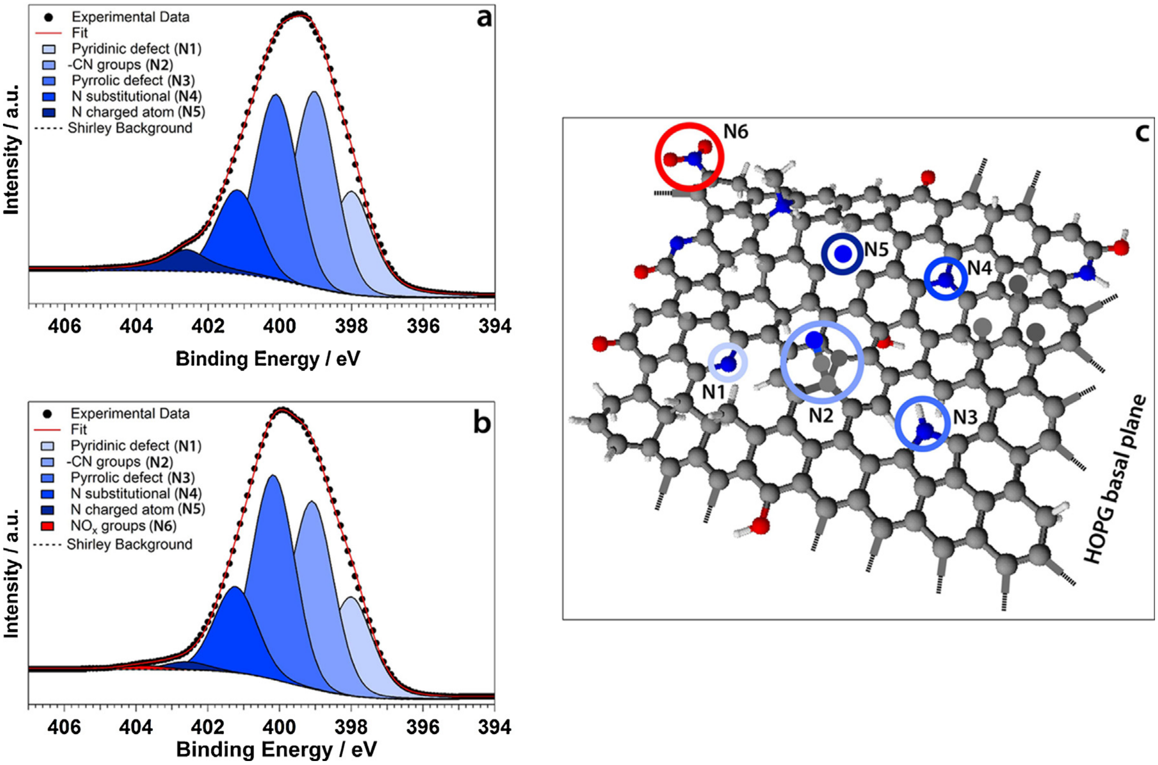

Fig. 5. Core level photoemission lines and relative deconvolution into single chemical components of N 1s for N-HOPG (a) and Pd/N-HOPG (b). Graph c reports a pictorial model of the surface with the nitrogen-based defects.

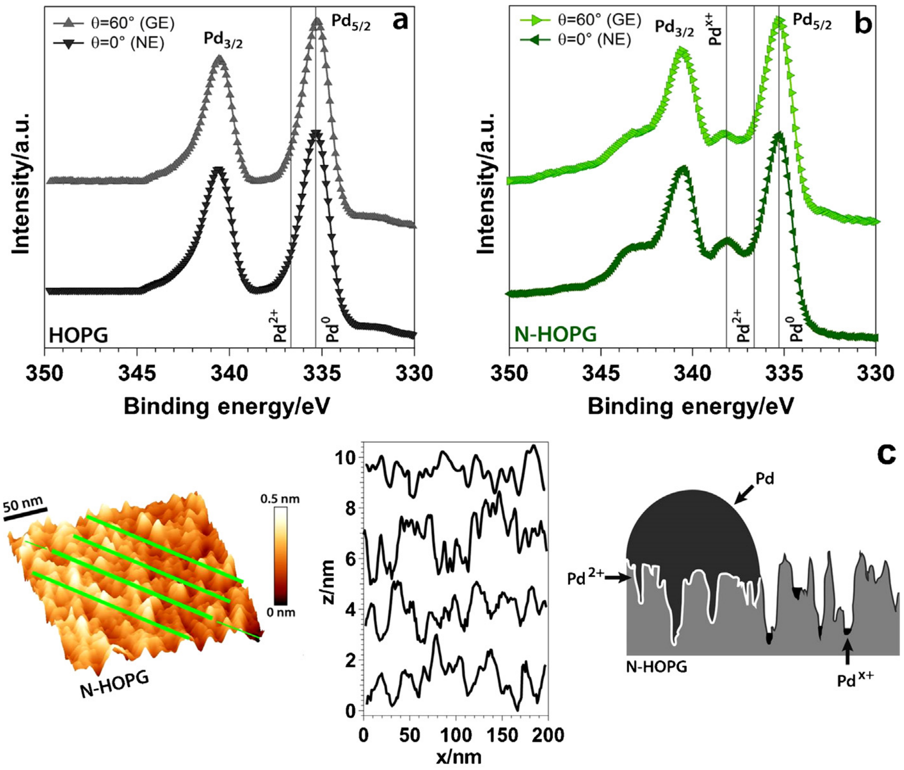

Fig. 6. Pd *3d* peaks for the Pd/HOPG (a) and for the Pd/N-HOPG systems (b), taken under normal (0°) and grazing (60°) acquisition angles. (c) 3D Height (Z) profile from AFM topography of N-HOPG and pictorial model representing the Pd/N-HOPG system. The presence of a thin interfacial layer rich in Pd^{2+} and in Pd^{x+} is well supported by the angle-resolved core level spectroscopy of the Pd 3d peaks.

[35]). The presence of Pd^{2+} species, that characterize both the deposition of pure and N-doped HOPG, can be attributed to oxidation of Pd due to the air exposure after the EC deposition. Moreover, on the N-HOPG, the electron withdrawing power of the nitrogen functional groups (due to the high difference of the electronegativity of C, N and Pd, equal to 2.50, 3.05 and 2.25 with respect to the Pauling scale, respectively) leads to a charge transfer between the metal NPs and the nitrogen surface defects. The oxidation of metal Pd to Pd^{2+} at the interface between the metal NPs and the nitrogen-rich surface is well-represented in the pictorial model reported in the Fig. 6c.

Interestingly, the Pd *3d* peak for the Pd/N-HOPG sample taken under normal emission conditions (0° with respect to the normal to the sample surface, Fig. 6b) shows a further component centered at 338.1 eV, which is partially attenuated when the take-off angle approximates the grazing emission (60° off the normal to the sample surface). For this reason, this component cannot be present at the surface of the Pd particles but rather be attributed to very small Pd nanoclusters decorating surface defect sites (the lateral size of these small clusters have to be not more than 2-3 nm, since the photoelectron mean free path for the photoelectrons coming from the Pd 3d core level, in the condition of the measurements reported in this work, is equal to 1.2 nm). In these clusters, hosted in the subnanometric pits induced by the ion implantation, the coordination by the nitrogen functional groups leads to the formation of Pd^{x+} species with $x = 2–4$ at the interface to the substrate.

In order to observe the formation of highly oxidized Pd^{x+} ions, it is necessary that the Pd atoms trapped in the surface defect sites interact with a large number of electron withdrawing groups. As a proof of that, in a previous study on Pd deposited on HOPG implanted with N ions at 500 eV (with a $R_p = 18.2$ Å) [7], we did not observe such photoemission feature in the Pd 3d spectra; due to the higher implantation energy, the interface between the Pd NPs and the substrate was in that case constituted by an amorphous carbon layer, with a lower amount of nitrogen groups. Hence, in order to observe the high binding energy component in the Pd 3d spectrum (that means the presence of Pd^{x+} species), it is necessary to have a surface whose topmost layer is rich in strong electron withdrawing groups. This phenomenology is also supported by findings reported in literature; in particular, Seo et al. observed the same component at high BE after the Pd deposition on graphene sheets functionalized by surface epoxy, hydroxyl and carboxyl groups [35]. This is in line with literature reports on Pt on N-HOPG, where oxidized Pt species due to charge transfer to the support were observed as well [15].

3.3. AFM characterization

In order to characterize the surface morphology of the samples, we have performed ex-situ AFM measurements. Fig. 7 shows the surface of pure HOPG (at two different magnifications) before and after the nitrogen implantation. As can be observed by comparing

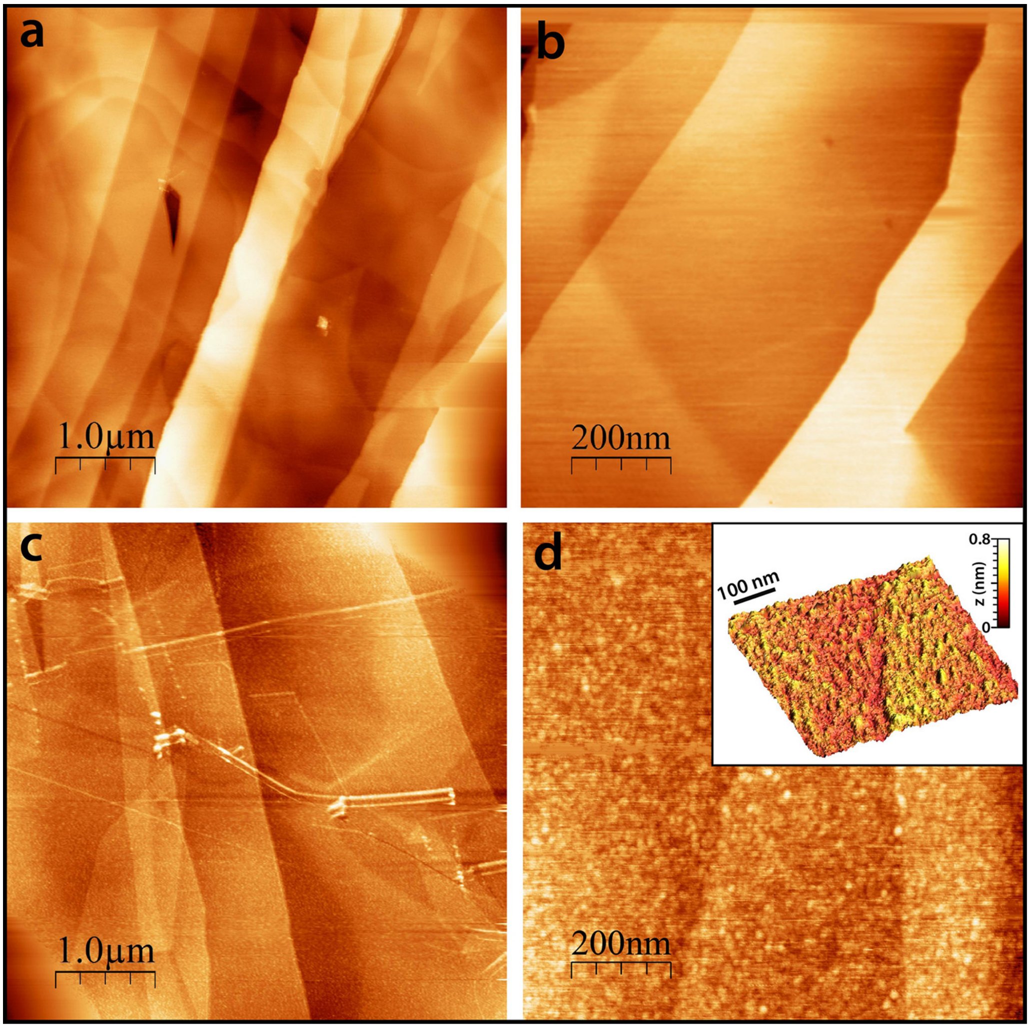

Fig. 7. AFM images reporting the results obtained on pure and N-HOPG (a,b and c,d, respectively). The inset reported in d shows a 3D magnification of the sample surface after the ion implantation.

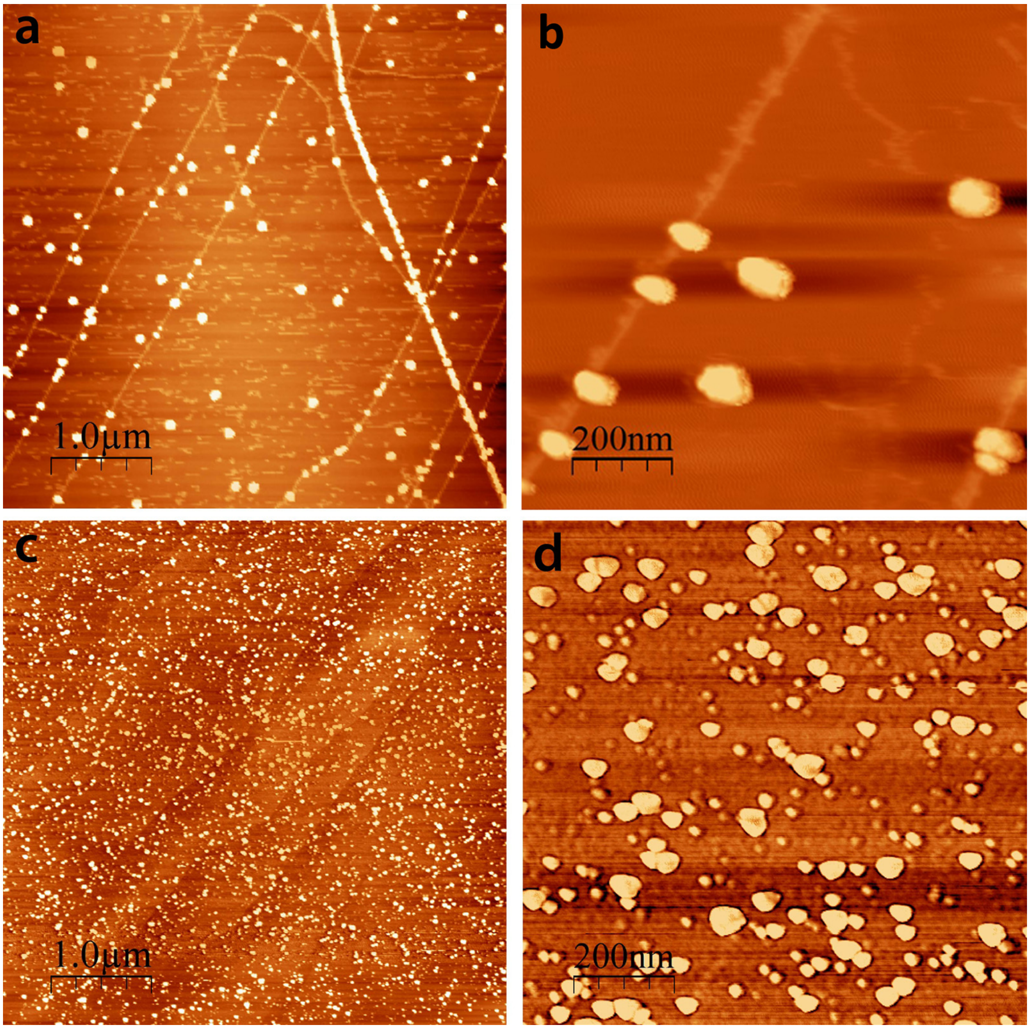

Fig. 8. AFM images obtained after the deposition of Pd on pure HOPG and N-HOPG (a,b and c,d, respectively). The comparison between Figure a and Figure c shows the high dispersion and decrease of the NP size that can be reached by the chemical (and morphological) modification of the HOPG surface.

Fig. 7a and 7c, the long range morphology is preserved; on the other hand, the high magnification images (Fig. 7b and 7d) of pure and N-HOPG confirm the predictions of the Monte Carlo simulation: the topmost layer undergoes an amorphization induced by the ion implantation, as also highlighted by the inset reported in Fig. 7d showing a 3D projection of the surface after the nitrogen implantation.

Fig. 8 shows the AFM topography of the Pd/HOPG and of the Pd/N-HOPG (at two different magnifications). The deposition charge was very similar for both samples, indicating that the total amount of Pd deposited is the same. The AFM data reveal that the nucleation of Pd is facilitated on the N-doped surfaces; consequently, for the same coverage and under the same deposition conditions, a higher NPs density is observed with respect to corresponding NPs grown on pure HOPG (cf. Fig. 8a and 8c). At the same time, the average size of Pd NPs deposited onto N-HOPG (d = 8.1 ± 3.1 nm, Fig. 8c) is smaller with respect to the NPs grown on pure HOPG (d = 13.4 ± 2.0 nm, Fig. 8a), but with a wider size distribution. This is in line with the usual behaviour of metals electrodeposited on HOPG at room temperature, which leads to an inhomogeneous distribution of 3D islands, with a higher nucleation density on step edges than on terraces, and a wide size distribution [6,36]. On the pure HOPG support the NPs on terraces, not trapped by low-coordinated sites (within the TSK or Kossel-Stranski model), are weakly bonded to the substrate and consequently they may diffuse and be captured by other NPs or substrate step edges (that, acting as low-coordination sites, can bind efficiently the metal NPs). On the other hand, on N-HOPG samples, the presence of low coordination sites formed even on the terraces by the ion bombardment, reduces the mobility of NPs and permits an extended nucleation (as well documented from the comparison between Fig. 8b and 8d). Both the improved dispersion and the smaller particle sizes are in agreement with observations in literature for Pt, where, however, the particle sizes on N-HOPG were around 2 nm instead of 8 nm in this work. This is due to the different electrochemical behaviour of the Pd electrolyte and the different electrodeposition protocol applied. Even after a long time electrochemical growth pulse (as long as 100s in this work), although some NPs coalesce due to the relatively short interparticle distance, the NPs on N-HOPG are still widely dispersed with a much higher particle density as compared with that of NPs on HOPG.

3.4. Electrochemical characterization and activity for ORR

The typical CV curves of HOPG and N-HOPG under deaerated conditions are shown in Fig. 9a. The currents measured on both electrodes are normalized to the geometric area of 0.126 cm^2. The pure HOPG exhibits a chemical inertia in pH = 3 solution with a potential window as wide as 1.85 V. When the potential is above 1.6 V and below -0.25 V, the oxygen evolution reaction

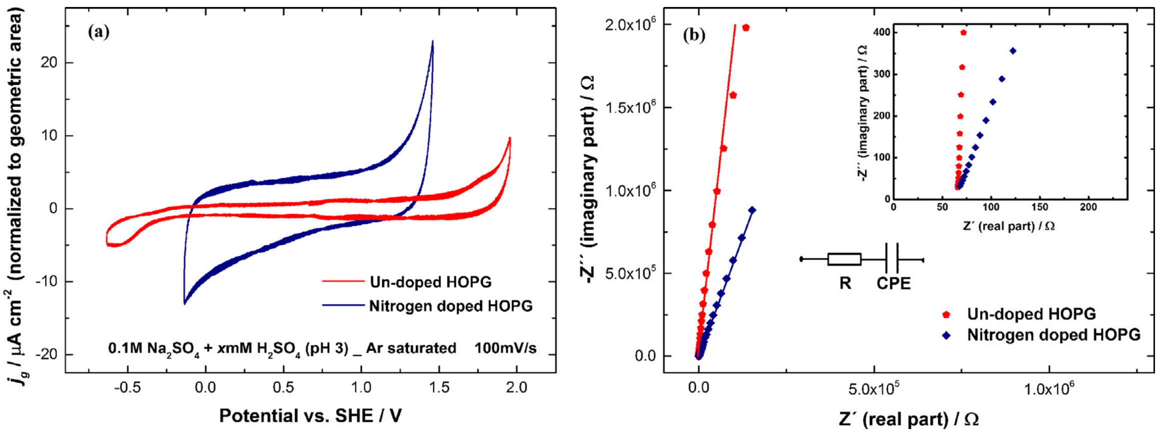

Fig. 9. (a) Cyclic voltammetry of HOPG and N-HOPG in different potential ranges in Ar saturated 0.1 M Na_2SO_4 + xmM H_2SO_4 (pH = 3) solution. Both currents are normalized to the geometric area of the electrode of 0.126 cm^2. The scan rate is 100 mV/s; (b) Nyquist plots of HOPG and N-HOPG in Ar saturated 0.1 M Na_2SO_4 + xmM H_2SO_4 (pH = 3) solution at open circuit potential. The x- and y-axis are plotted in linear scale. The inset corresponds to a zoom for the same plot in the high frequency region from 10k to 500 Hz The electrode/electrolyte interface is simulated as the inserted circuit diagram.

(OER) and hydrogen evolution reaction (HER) occur on its surface, respectively. As compared with pure HOPG, the N-HOPG electrode behaves more active for OER and HER. The onset potentials for HER and OER on the N-HOPG surface are about 0 V and 1.2 V, respectively. Therefore it can be already expected that N-HOPG shows also an increased activity for the ORR. The current density during double-layer charging at the N-HOPG/electrolyte interface is almost 4 times higher than that at HOPG/electrolyte interface. From the currents in the double layer region, capacitance values of C_{dl} = 38.9 ± 1.4 µF/cm^2 for N-HOPG and C_{dl} = 8.5 ± 0.2 µF/cm^2 for HOPG can be derived. The impedance behavior of HOPG and N-HOPG at pH = 3 is shown as Nyquist plots in Fig. 9b (the inset corresponds to a zoom for the same plot in the high frequency region from 10k to 500 Hz). Both EIS measurements were carried out at the OCP of each sample. The almost linear behavior in the Nyquist plot demonstrates the absence of significant Faradaic processes in both cases. Due to the significant tilt in the curve especially for N-HOPG, the electrode/electrolyte interface is simulated by an equivalent circuit with a CPE (constant phase element) and R_e representing the double layer capacitance and the electrolyte resistance, respectively. The impedance expressed in terms of a CPE is

$$Z(\omega)_{CPE} = R_e + \frac{1}{(j\omega)^{\alpha}Q} \qquad \text{(Eq. 1)}$$

where R_e is a resistance, ω is an angular frequency, and α and Q are the CPE parameters which are independent of frequency [37]. Brug et al. [38] developed a relationship for a blocking electrode between the effective interfacial capacitance C_{eff} and the CPE parameter Q as

$$C_{eff} = [QR_e^{1-\alpha}]^{1/\alpha} \qquad \text{(Eq. 2)}$$

When the value of α is closer to unity, the surface of the electrode is more approaching the ideal 2-D surface. From linear fits of the logarithm of the (absolute) imaginary part of the impedance as function of ln(ω), the value of α and Q for HOPG and N-HOPG are obtained as α_{HOPG} = 0.977, $\alpha_{\text{N-HOPG}}$ = 0.896, Q_{HOPG} = 0.79 × 10^{-6} s$^{\alpha}$/Ωcm^2 and $Q_{\text{N-HOPG}}$ = 1.71 × 10^{-6} s$^{\alpha}$/Ωcm^2, respectively. From the results full impedance spectra were calculated from Eq.1 and are included in Fig. 9b as solid lines. For HOPG a slight deviation of the measured data from linearity is seen at low frequencies, pointing to the presence of some parasitic faradaic reactions (maybe due to trace oxygen in the Ar gas). The results for the CPE parameters indicate that the HOPG surface is very flat and close to the ideal capacitance behavior, while the lower α for N-HOPG is consistent with its higher roughness seen in AFM. Calculation of C_{eff} based on Eq.2 leads to very similar values for both materials (5.01 µF/cm^2 for HOPG and 4.75 µF/cm^2 for N-HOPG). The higher interfacial capacitance of N-HOPG obtained by cyclic voltammetry is therefore mainly attributed to the higher roughness compared to the pure HOPG and to a lesser extent to the contribution of introduced chemical defects.

N-HOPG shows an enhanced activity for OER and HER as well as an increased double-layer capacitance compared with pure HOPG because of the surface modifications from the nitrogen doping process. A pure HOPG surface, as an extremely smooth surface with a low defect density, performs more like a semi-metal on the terrace region due to the low electronic density of states (EDOS) near the Fermi level [39]. Through the nitrogen implantation process, the HOPG surface becomes rougher and nitrogen functional groups are introduced at the HOPG surface. The defect and step regions have a higher EDOS such that the electrons with suitable energy are able to transfer to a redox system with a higher probability [21]. Furthermore, nitrogen functional groups can significantly reduce the hydrophobic effects of pure HOPG and increase the EDOS near the Fermi level [40]. Both modifications can enhance the activity of N-HOPG for some redox reactions such as OER and HER. Additionally, the enhanced EDOS could improve the screening of an external electric field, so that the capacitance of N-HOPG electrode in contact with an electrolyte solution is much greater than that of pure HOPG in addition to the contribution from surface roughening [40]–this is however not supported by the impedance data.

Pd NPs supported on HOPG (Pd/HOPG) and on N-HOPG (Pd/N-HOPG) exhibit different CV plots in the potential range from 0.26 to 1.46 V (Fig. 10). The current traces of the pure substrates (dashed curves in Fig. 10) show that the contribution of the Pd to the total capacitance of the specimens is negligible, whereas the contribution of the support to the Faradaic processes is minor. Although the onset potentials of Pd oxidation and Pd monoxide (PdO) reduction for both samples are located at equal values, the current densities measured during the cathodic scan in the potential range of 0.26 V - 0.4 V do not show an agreement for the two types of samples, which indicates that some other reactions apart from the PdO reduction are involved on the Pd/N-HOPG sample in this potential range. The N-HOPG substrate behaves almost inert in Ar saturated 0.1 M H_2SO_4 in this potential range, which can be concluded from its almost flat CV curve in Fig. 10. The CV of Pd/N-HOPG was captured by increasing the potential from a starting value of 0.45 V anodically to 1.45 V, and lowering it then in the cathodic sweep to 0.26 V, finally returning to 0.45 V. The Pd oxidation and the OER are the

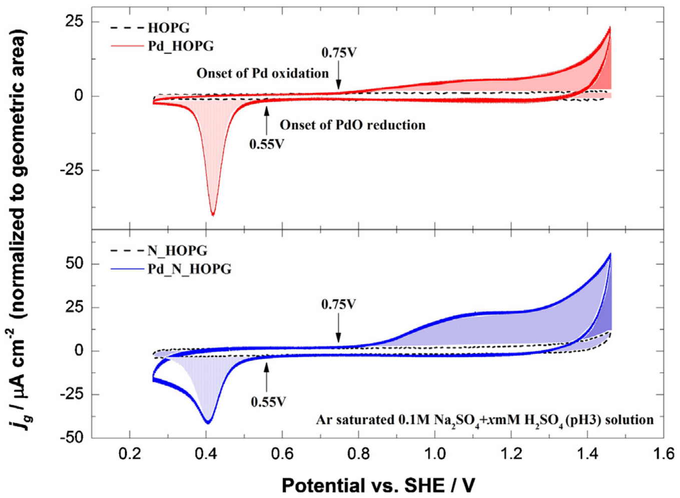

Fig. 10. Cyclic voltammetry of Pd/HOPG and Pd/N-HOPG in Ar saturated 0.1 M $Na_2SO_4 + x$mM H_2SO_4 (pH = 3) solution. The potential is scanned from 0.26 V to 1.46 V at 50 mV/s. The CVs of HOPG and N-HOPG are plotted as the baselines. The onset potential of Pd oxidation is at around 0.75 V, and the onset potential of Pd monoxide reduction is at around 0.55 V. The charge transfer in both anodic and cathodic scans is shown as the integration over the shadow region.

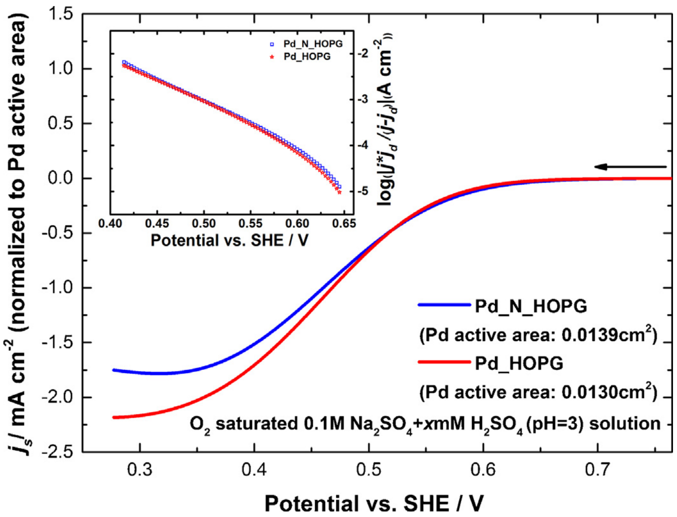

Fig. 11. Specific current density for ORR on Pd_HOPG and Pd/N-HOPG electrodes with decreasing potential in O_2 saturated 0.1 M $Na_2SO_4 + x$ mM H_2SO_4 (pH = 3) solution. The x-axis is the overpotential corresponding to the OCP of each electrode immersed in the working electrolyte. The arrow indicates the direction of the potential scan, which is at a scan rate of 5 mV/s. The inserted diagram shows the mass-transfer corrected Tafel plot of ORR. The kinetic current density is obtained from equation 3.

two major reactions occurring during the anodic scan up to 1.45 V, which introduces two main products, PdO and O_2, at the electrode. Many authors have reported that nitrogen-doped graphene is an active metal-free electrocatalyst for ORR in both alkaline and acidic solutions [41–46]. This has also been observed in previous work [21]. Liu et al. [41] reported that the ORR catalyzed by nitrogen-doped graphene foam occurs at 0.83 V vs. RHE in O_2 saturated 0.1 M $HClO_4$. In our work, the N-HOPG catalyzed ORR occurs in the O_2 saturated pH 3 solution when the potential is lower than 0.6 V (not shown). The ORR current density on N-HOPG is around -12 μA/cm^2 at 0.26 V vs.SHE, while only -2 μA/cm^2 on HOPG. Therefore, the ORR directly on the N-HOPG substrate cannot be neglected in the potential range of 0.26 V - 0.4 V when adsorbed O_2 formed at the Pd during the anodic scan and transferred to the nitrogen functional groups still is present during the cathodic sweep.

The reduction peak of PdO on HOPG support is a typical Gaussian curve with a peak potential of 0.42 V. When the potential is more negative than 0.29 V, the reduction process is almost complete. The active area of Pd NPs on HOPG is evaluated by the transferred charge during PdO reduction. The reduction peak of PdO on N-HOPG support is asymmetric with an excess charge transfer compared to that during the PdO reduction, which is attributed to the ORR catalyzed by N-HOPG in this potential range. In order to evaluate the active area of Pd NPs on N-HOPG, the excess charge transfer contributed from ORR should be eliminated mathematically. The active area is approximately determined by the charge integrated over a Gaussian curve, which is fitted based on the right half peak (shown as the shadow region in the cathodic scan of Pd/N-HOPG).

The transferred charge in the anodic scan on Pd/HOPG (the contribution of the support has been subtracted for the data analysis, the charge is integrated over the shadowed region shown in Fig. 10) is nearly 1.5 times of the charge transferred during PdO reduction in the cathodic scan. The excess charge in the anodic scan is attributed to the charge transfer with the OER and the decreasing of the Pd active area due to dissolution and agglomeration. In the case of Pd/N-HOPG, the transferred charge in the anodic scan, corrected for the contributions from double-layer charging and reactions related to the substrate in absence of Pd, is almost 3 times the charge transferred during the PdO reduction process, and is almost 2.3 times the total charge transferred during the cathodic scan (containing contributions of PdO reduction and ORR). Besides the charge transfer during the OER, the excess charge in the anodic scan of Pd/N-HOPG suggests that the loss of Pd active area is more serious compared to the Pd/HOPG. This issue is discussed below in the stability measurement. An alternative to the explanation of the reduction process occurring at lower potential than the normal PdO reduction peak by adsorbed oxygen reduction reaction could be correlated to the small Pd NPs suggested by the XPS data (see above). One could imagine that the oxide on such clusters is more stable than on larger Pd NPs and therefore reduced at lower potentials. However, the intensity of the corresponding signal in XPS suggests that these smaller particles are much less prevalent than the larger particles, and cannot explain the large currents observed.

In Fig. 11, the specific ORR current density of each sample is plotted versus the applied potential, after subtracting the currents measured on bare HOPG and N-HOPG under identical conditions from the raw data. The corrected current density increases first exponentially from the onset potential until it approaches the diffusion-limited current density due to the sluggish mass transport of O_2, that itself is time-dependent under the applied experimental conditions. Generally, it is well accepted in practice that the contribution of mass transport can be neglected for low overpotentials where the measured current density is less than 10% of the diffusion limited current density [18,47]. In order to work with a larger potential range and to eliminate the influence from diffusion limitation of the reactant, the data in Fig. 11 were analyzed using the well-known equation:

$$\frac{1}{j} = \frac{1}{j_k} + \frac{1}{j_d} \qquad \text{(Eq. 3)}$$

where j is the measured current density, j_k and j_d are kinetic and limiting current densities, respectively. In this case the maximum current densities, i.e. peak current densities of the respective curves in Fig. 11 were taken instead of j_d. For linear sweep voltammetry of an irreversible, one electron transfer reduction reaction with planar diffusion geometry [48], one can show that this approach is reliable for potentials well positive of the peak potential. Also for the situation in this work it is believed that the approach is valid, even though in the beginning hemispherical diffusion is expected for the individual Pd nanoparticles. The mass-transfer corrected

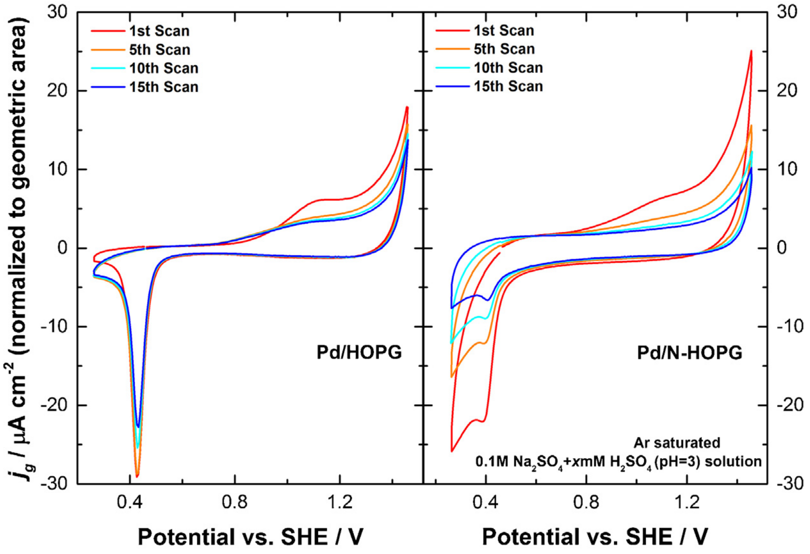

Fig. 12. The potential cycles of Pd/HOPG (left) and Pd/N-HOPG (right) in the stability measurements in Ar saturated 0.1 M Na_2SO_4 + x mM H_2SO_4 (pH = 3) solution. The potential applied during the measurements is from 0.26 V to 1.46 V at a scan rate of 50 mV/s. The current is normalized to the geometric area of the electrode.

Tafel plots of ORR are shown in the inserted graph of Fig. 11. When the potential is more negative than 0.55 V, the Tafel slopes of both electrodes are around (105 ± 3) mV/dec. In a four-electron transfer mechanism of O_2 reduction, the Tafel slope should be around 120 mV/dec [49,50]. Hence, the measured Tafel slopes from our experiments indicate that some H_2O_2 is produced.

The specific current densities for ORR on both Pd/HOPG and Pd/N-HOPG do not show a relevant difference and therefore it is possible to conclude that the nitrogen functional groups do not affect the activity of supported Pd NPs for ORR in these experiments, different to some reports of Pt NPs supported on nitrogen doped graphite [14,16,51]. Holme et al. [16] investigated theoretically that pyramidal Pt_4 cluster supported on pyridinic and pyrrolic nitrogen defects of N-HOPG had a weaker binding to oxygen atoms than that on pristine HOPG because of larger electron transfer from Pt on nitrogenous defects. As the Pt-O binding energy is a little stronger than the optimal value [23], the slightly weakened binding of Pt to oxygen atoms points to a more active catalyst for ORR and methanol oxidation reaction (MOR). This conclusion was also supported by some experimental works [14,51]. As a member of Pt group, Pd was expected to present the same behavior as Pt when it was supported on nitrogenous defects. The XPS data of Pd/N-HOPG shows that, besides the Pd^0 state, the +2 oxidation state and even higher oxidation states are also observed. These increased oxidation states of Pd in nitrogen-containing carbon systems are reported by many authors [52–54] as caused by the formation of Pd-O and Pd-N bonds. However, the Pd supported on HOPG, which can only form Pd-O bonds, shows much less higher oxidation states than that on N-HOPG. Therefore, the higher Pd oxidation states of Pd/N-HOPG are mainly caused by interaction with the nitrogenous defects The electron transfer from Pd onto the nitrogenous defects is confirmed by this data. On Pd/N-HOPG, the position of the Pd^0 *3d* was not affected by the doping process, but that the particle-support interface was altered. There are several aspects to be considered in the interpretation of these results: For one, any support effect is weakened gradually with the increase of thickness [55]. The estimated operation range of a support effect is within a few atomic layers [56–59]. In the case of Pd nanostructures, the support effect is assumed to play a role only when the thickness of nanostructure is equal or less than 10ML (around 2~3 nm). But the majority of electrochemically deposited Pd NPs in the experiments discussed in this paper have an average height larger than 2 nm, different to literature studies on Pt. The average height of Pd NPs on HOPG is (13.4 ± 2.0) nm, and of Pd NPs on N-HOPG is (8.1 ± 3.1) nm. The nitrogen functional groups influence the properties of Pd atoms nearby the support-particle interface, as clearly demonstrated by the additional XPS peaks, while the upper part of Pd NPs on N-HOPG possesses the same electrochemical properties as compared to that on HOPG. As a result, the Pd NPs on both supports exhibit the same intrinsic activity for ORR. Another contributing effect may be the modification of the support/Pd interface: Even though the dispersion of the particles is–in line with literature reports- improved by the introduction of defect sites, the total binding strength of larger particles still might be mainly due to van-der-Waals interactions, and the presence of Pd ions at the interface could diminish the electronic interaction even for smaller particles. This is in agreement with earlier findings for much smaller Pd NPs evaporated on N-HOPG (even though produced at higher implantation currents), where also for such small particles no effect of the surface functionalization on the ORR was observed [7]. In fact it was even postulated in literature that surface functionalization can weaken the support/particle interaction by diminishing the van-der-Waals forces [60]. Particle size can significantly influence the activity of NPs, especially, when it shrinks to several nanometers. The electrocatalytic activity of Pd NPs for ORR decreases with shrinking of particle size, when the particle size is smaller than a critical value. The onset potential of ORR becomes more negative in parallel [49]. In this work, although the average particle sizes of Pd NPs supported on HOPG and N-HOPG are different, the onset potential of ORR in both measurements are similar, suggesting that the particle size effect can be neglected. Therefore it can be excluded that the negative particle size effects cancel out a positive support effect.

In order to test the stability of the Pd NPs on the studied systems, potential cycles have been performed on Pd/HOPG and Pd/N-HOPG electrodes. The CV plots of both samples are shown in Fig. 12. From the reduction peak of PdO, the loss of Pd active area during the potential cycles can be observed directly. The peak current density at the reduction peak of PdO on HOPG decreases gradually from -3.66 μA/cm^2 in the 1st scan down to -2.87 μA/cm^2 in the 15th scan, however, the value of Pd/N-HOPG decreases from -2.78 μA/cm^2 in the 1st scan down to -0.83 μA/cm^2 in the 15th scan. Obviously, the loss rate of Pd active area on N-HOPG is much higher than that on HOPG. For Pd/N-HOPG, the second reduction process at lower potentials in the cathodic scan is even more pronounced than that

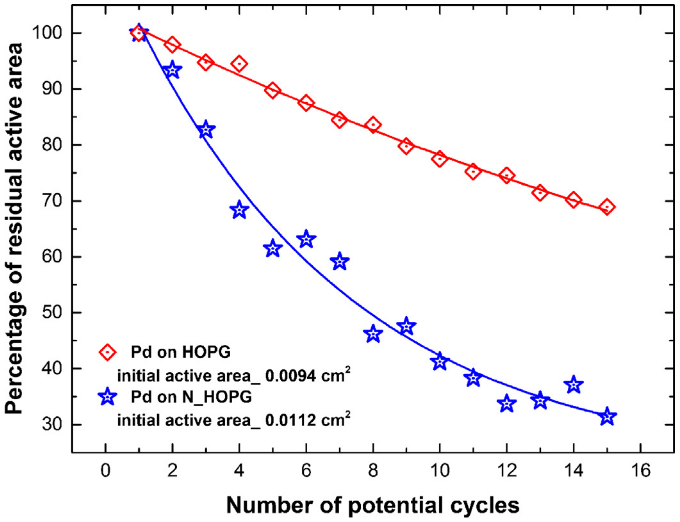

Fig. 13. The degeneration of the Pd active area of supported Pd particles in the stability measurements. The initial active areas of the Pd on HOPG and on N-HOPG are 0.0094 cm^2 and 0.0112 cm^2, respectively. The initial active area is fixed as the 100%. The residual active area after potential cycles is normalized to the initial area in percentage. The residual active area versus the number of potential cycles is fitted to the exponential decay function shown as the solid lines.

for the sample shown in Fig. 10, and shows a clear decrease with decreasing Pd coverage. In line with the explanations above, at decreasing Pd coverage less O_2 will be transferred to the nitrogen functional groups and be available for subsequent reduction.

The active area of Pd NPs, which is determined from the transferred charge during PdO reduction, is used in order to compare the loss rate of Pd quantitatively. The initial active areas of Pd on HOPG and N-HOPG are 0.0094 cm^2 and 0.0112 cm^2, respectively. The active area decreases exponentially (Fig. 13). After 15 cycles, on Pd/HOPG 69% of Pd active area remains, but the Pd/N-HOPG only keeps 31% of initial Pd active area. This indicates that the Pd supported on N-HOPG has a lower stability as compared with that on HOPG.

The coalescence of Pd NPs on N-HOPG is a considerable reason of the rapid loss of Pd active area. Based on the AFM images, the Pd NPs disperse more densely on N-HOPG with a shorter average interparticle distance (AID) compared with the situation on HOPG support. The insufficient separation of NPs can cause a high probability for coalescence, since only a short distance needs to be bridged in order to establish an interparticle contact [61]. However, the geometric and chemical defects on N-HOPG, introduced by the ion implantation process, seem to be effective obstacles against the migration of Pd NPs on the surface as the wide dispersion and high density of Pd NPs are observed even after a relatively long electrochemical deposition process, where otherwise agglomeration should have been observed already.

According to the Pourbaix diagram of Pd, PdO is thermodynamically stable at elevated potentials in presence of acidic solution of pH larger than 2 [27]. However, the corrosion and the restructuring of the Pd surface are accelerated in potential cycles, which has been ascribed to the repeated formation and reduction of a surface Pd oxide [62]. Aside from the formation of PdO in the potential range applied in this experiment, the dissolution of Pd into solution occurs in the form of $[Pd(H_2O)_4]^{2+}$ [63]. The loss of surface area of Pd/HOPG, which has been investigated by AFM measurements, is correlated mainly to the loss of Pd from the surface (dissolution and detachment) and in part to agglomeration. As the surface properties of the Pd NPs are not altered on N-HOPG, as demonstrated by XPS and ORR data above, the difference in stability should arise from other contributions besides the losses of Pd ions into the electrolyte from dissolution of surface PdO. For the short AID, the redeposition of dissolved Pd atoms onto the more stable neighbored NPs (Ostwald ripening) is a possible contributor of the catalyst degradation. Otherwise, the results in this work indicate that the cationic Pd^{2+} present between the Pd and N-HOPG interface should be considered as a trigger of rapid degradation. By the angle-resolved core level XPS of the Pd *3d* peaks, the presence of a thin interfacial layer rich in Pd^{2+} has been observed. The particle-support interfacial layer can be attacked easily by the acidic solution, and nitrogen functional groups interacting with the particles may be electrochemically oxidized, thus accelerating the loss of Pd atoms and entire particles. In conclusion, the introduction of nitrogen functional groups improves the dispersion of deposited Pd particles but reduces the stability towards potential cycling strongly.

4. Conclusions

N-HOPG was prepared by ion implantation with a beam energy of 100 eV. According to Monte Carlo simulations, the center of the distribution of the nitrogen-based chemical defects is located in the second and third layers. The AFM images show that the surface of HOPG undergoes an amorphization, and shows more low-coordinated sites on the terraces modified by the ion bombardment, which can enhance the nucleation of Pd NPs. Through the XPS characterization, Pd^{2+} species located at the interface between the metal NPs and the nitrogen-rich surface were observed as a result of a charge transfer from the Pd atoms to the nitrogen functional groups, which can be explained with the higher electron affinity of the nitrogen functional groups compared to Pd clusters.

In the electrochemical characterization, pure N-HOPG shows an enhanced activity for OER and HER as well as an increased double-layer capacitance compared with pure HOPG due to the surface roughening and extrinsic functional groups introduction. The supported Pd NPs on N-HOPG do not show an enhanced activity for ORR as compared with those on HOPG in agreement with XPS data. This is the case despite a clear interaction between support and Pd nanoparticles indicated by the additional Pd^{x+} signals. The major cause of this is assigned to the relatively large particle size, and possibly an effect of the charged Pd species at the interface. Among the elemental catalysts, Pt approaches the peak value of volcano plot for oxygen reduction activity most closely, but the oxygen binding force to Pt atom is a little too strong. When Pt is supported on pyridinic and pyrrolic nitrogen defects, Pt, can show an enhanced oxygen reduction activity. Pd, as a member of Pt group, has even a slightly stronger binding force with oxygen than Pt. The lack of theoretical work about Pd on nitrogen doped carbon hinders the further understanding of this catalyst, but it is possible that the N doped defects can form some kinds of chemical interactions with the Pd atoms, which leads to a change of the valence band. The XPS in our work shows the existence of a Pd-cation layer at the interlayer of Pd NPs and N-HOPG, which correlates to the rapid degradation of Pd active area observed in the electrochemical measurements. Therefore, the stability of Pd NPs supported on N-HOPG is worse than on pure HOPG, which is influenced by many factors like the average interparticle distance. However, the presence of Pd^{2+} at the particle-support interfacial layer is considered to be a very significant reason of accelerating the dissolution of Pd atoms as well as the detachment of entire Pd NPs, which reduces the stability of supported Pd particles during potential cycling strongly.

Acknowledgment

We acknowledge financial support from Deutscher Akademischer Austauschdienst (DAAD) within the Vigoni bilateral program, from the Fuel Cell and Hydrogen Initiative - Joint Undertaking

(FCH-JU) within the CathCat project under contract No. 303492, and from the Carl von Linde foundation at Technische Universität München. WJ thanks for the financial support of the China Scholarship Council. MF thanks Fondazione Cariparo for a PhD fellowship. We would like to thank Dr. Tine Brülle and Dr. Hadwig Sternschulte for helpful discussions.

References

[1] A.S. Bandarenka, M.T.M. Koper, Structural and electronic effects in heterogeneous electrocatalysis: Toward a rational design of electrocatalysts, Journal of Catalysis, in press.

[2] B.R. Cuenya, Synthesis and catalytic properties of metal nanoparticles: Size, shape, support, composition, and oxidation state effects, Thin Solid Films 518 (2010) 3127–3150.

[3] B. Hammer, J.K. Nørskov, Theoretical surface science and catalysis—calculations and concepts, in: H.K. Bruce, C. Gates (Eds.), Advances in Catalysis, Academic Press, 2000, pp. 71–129.

[4] J. Greeley, J.K. Norskov, L.A. Kibler, A.M. El-Aziz, D.M. Kolb, Hydrogen evolution over bimetallic systems: understanding the trends, Chemphyschem: a European journal of chemical physics and physical chemistry 7 (2006) 1032–1035.

[5] N.M. Marković, P.N. Ross Jr., Surface science studies of model fuel cell electrocatalysts, Surface Science Reports 45 (2002) 117–229.

[6] L. Perini, C. Durante, M. Favaro, S. Agnoli, G. Granozzi, A. Gennaro, Electrocatalysis at palladium nanoparticles: Effect of the support nitrogen doping on the catalytic activation of carbonhalogen bond, Applied Catalysis B: Environmental 144 (2014) 300–307.

[7] M. Favaro, S. Agnoli, L. Perini, C. Durante, A. Gennaro, G. Granozzi, Palladium nanoparticles supported on nitrogen-doped HOPG: a surface science and electrochemical study, Physical Chemistry Chemical Physics 15 (2013) 2923–2931.

[8] H. Häkkinen, S. Abbet, A. Sanchez, U. Heiz, U. Landman, Structural, electronic, and impurity-doping effects in nanoscale chemistry: supported gold nanoclusters, Angew Chem. Int. Ed. 42 (2003) 1297–1300.

[9] D. Pillay, G.S. Hwang, Growth and structure of small gold particles on rutile TiO_{2}(110), Physical Review B 72 (2005) 205422.

[10] S. Laursen, S. Linic, Oxidation Catalysis by Oxide-Supported Au Nanostructures: The Role of Supports and the Effect of External Conditions, Physical Review Letters 97 (2006).

[11] N.M. Marković, C.A. Lucas, V. Climent, V. Stamenković, P.N. Ross, Surface electrochemistry on an epitaxial palladium film on Pt(111): surface microstructure and hydrogen electrode kinetics, Surface Science 465 (2000) 103–114.

[12] L.A. Kibler, A.M. El-Aziz, D.M. Kolb, Electrochemical behaviour of pseudomorphic overlayers: Pd on Au(1 1 1), Journal of Molecular Catalysis A: Chemical 199 (2003) 57–63.

[13] T. Kondo, T. Suzuki, J. Nakamura, Nitrogen Doping of Graphite for Enhancement of Durability of Supported Platinum Clusters, The Journal of Physical Chemistry Letters 2 (2011) 577–580.

[14] Y. Zhou, R. Pasquarelli, T. Holme, J. Berry, D. Ginley, R. O'Hayre, Improving PEM fuel cell catalyst activity and durability using nitrogen-doped carbon supports: observations from model Pt/HOPG systems, Journal of Materials Chemistry 19 (2009) 7830.

[15] Y. Zhou, T. Holme, J. Berry, T.R. Ohno, D. Ginley, R. OíHayre, Dopant-induced electronic structure modification of HOPG surfaces: implications for high activity fuel cell catalysts, J. Phys. Chem. C 114 (2010) 506–515.

[16] T. Holme, Y. Zhou, R. Pasquarelli, R. O'Hayre, First principles study of doped carbon supports for enhanced platinum catalysts, Physical chemistry chemical physics: PCCP 12 (2010) 9461–9468.

[17] T. Brülle, U. Stimming, Platinum nanostructured HOPG–Preparation, characterization and reactivity, Journal of Electroanalytical Chemistry 636 (2009) 10–17.

[18] T. Brülle, W. Ju, P. Niedermayr, A. Denisenko, O. Paschos, O. Schneider, U. Stimming, Size-dependent electrocatalytic activity of gold nanoparticles on HOPG and highly boron-doped diamond surfaces, Molecules (Basel, Switzerland) 16 (2011) 10059–10077.

[19] R.T. Pötzschke, C.A. Gervasi, S. Vinzelberg, G. Staikov, W.J. Lorenz, Nanoscale studies of Ag electrodeposition on HOPG (0001), Electrochimica Acta 40 (1995) 1469–1474.

[20] I. Lopez-Salido, D.C. Lim, R. Dietsche, N. Bertram, Y.D. Kim, Electronic and Geometric Properties of Au Nanoparticles on Highly Ordered Pyrolytic Graphite (HOPG) Studied Using X-ray Photoelectron Spectroscopy (XPS) and Scanning Tunneling Microscopy (STM), J. Phys. Chem. B 110 (2006) 1128–1136.

[21] M. Favaro, L. Perini, S. Agnoli, C. Durante, G. Granozzi, A. Gennaro, Electrochemical behavior of N and Ar implanted highly oriented pyrolytic graphite substrates and activity toward oxygen reduction reaction, Electrochimica Acta 88 (2013) 477–487.

[22] D. Usachov, O. Vilkov, A. Gruneis, D. Haberer, A. Fedorov, V.K. Adamchuk, A.B. Preobrajenski, P. Dudin, A. Barinov, M. Oehzelt, C. Laubschat, D.V. Vyalikh, Nitrogen-doped graphene: efficient growth, structure, and electronic properties, Nano letters 11 (2011) 5401–5407.

[23] J.K. Norskov, J. Rossmeisl, A. Logadottir, L. Lindqvist, J.R. Kitchin, T. Bligaard, H. Jónsson, Origin of the overpotential for oxygen redcution at a fuel-cell cathode, J. Phys. Chem. B 108 (2004) 17886–17892.

[24] I.E.L. Stephens, A.S. Bondarenko, U. Grønbjerg, J. Rossmeisl, I. Chorkendorff, Understanding the electrocatalysis of oxygen reduction on platinum and its alloys, Energy & Environmental Science 5 (2012) 6744.

[25] I. Horcas, R. Fernandez, J.M. Gomez-Rodriguez, J. Colchero, J. Gomez-Herrero, A.M. Baro, WSXM: a software for scanning probe microscopy and a tool for nanotechnology, The Review of scientific instruments 78 (2007) 013705.

[26] J.F. Ziegler, M.D. Ziegler, J.P. Biersack, SRIM–The stopping and range of ions in matter (2010), Nuclear Instruments and Methods in Physics Research Section B: Beam Interactions with Materials and Atoms 268 (2010) 1818–1823.

[27] M.J.N. Pourbaix, J.V. Muylder, N. de Zoubov, Electrochemical Properties of the Platinum Metals, Platinum Metals Rev. 3 (1959) 100–106.

[28] M. Grdeń, M. Łukaszewski, G. Jerkiewicz, A. Czerwiński, Electrochemical behaviour of palladium electrode: Oxidation, electrodissolution and ionic adsorption, Electrochimica Acta 53 (2008) 7583–7598.

[29] G.H. Kinchin, R.S. Pease, The displacement of atoms in solids by radiation, Rep. Prog. Phys. 18 (1955) 1–51.

[30] Y. Baskin, L. Meyer, Lattice Constants of Graphite at Low Temperatures, Physical Review 100 (1955) 544.

[31] D. Wei, L. Y., Y. Wang, H., Zhang, L., Huang, G. Yu, Synthesis of N-Doped Graphene by Chemical Vapor Deposition and Its Electrical Properties, Nano letters, 9 (2009) 1752-1758.

[32] T.S. Wang, J.J. Ding, R. Cheng, H.B. Peng, X. Lu, Y.T. Zhao, Diamond-Like Carbon produced by highly charged ions impact on highly oriented pyrolytic graphite, Nuclear Instruments and Methods in Physics Research Section B: Beam Interactions with Materials and Atoms 272 (2012) 15–17.

[33] C. Zhang, L. Fu, N. Liu, M. Liu, Y. Wang, Z. Liu, Synthesis of nitrogen-doped graphene using embedded carbon and nitrogen sources, Advanced materials 23 (2011) 1020–1024.

[34] N. Hellgren, J. Guo, Y. Luo, C. Såthe, A. Agui, S. Kashtanov, J. Nordgren, H. Ågren, J.-E. Sundgren, Electronic structure of carbon nitride thin films studied by X-ray spectroscopy techniques, Thin Solid Films 471 (2005) 19–34.

[35] M.H. Seo, S.M. Choi, J.K. Seo, S.H. Noh, W.B. Kim, B. Han, The graphene-supported palladium and palladium–yttrium nanoparticles for the oxygen reduction and ethanol oxidation reactions: Experimental measurement and computational validation, Applied Catalysis B: Environmental 129 (2013) 163–171.

[36] C. Binns, S.H. Baker, C. Demangeat, J.C. Parlebas, Growth, electronic, magnetic and spectroscopic properties of transition metals on graphite, Surface Science Reports 34 (1999) 105–170.

[37] M.E. Orazem, B. Tribollet, Electrochemical Impedance Spectroscopy, John Wiley & Sons, Inc, USA, 2008, pp. 523.

[38] G.J. Brug, A.L.G. Van den Eeden, M. Sluyters-Rehbach, J.H. Sluyters, The analysis of electrode impedances complicated by the presence of a constant phase element, J. Electroanal. Chem. 176 (1984) 275–295.

[39] K.K. Cline, M.T. McDermott, R.L. McCreery, Anomalously slow electron transfer at ordered graphite electrodes: influence of electronic foactors and reactive sites, J. Phys. Chem. 98 (1994) 5314–5319.

[40] M.F. Juarez, L. Mohammadzadeh, W. Schmickler, The double-layer capacity of nitrogen-doped graphite, Electrochemistry Communications 36 (2013) 50–52.

[41] J. Liu, K. Sasaki, S.M. Lyth, Electrochemical Oxygen Reduction on Metal-Free Nitrogen-Doped Graphene Foam in Acidic Media, ECS Transactions 58 (2013) 1529–1540.

[42] K.R. Lee, K.U. Lee, J.W. Lee, B.T. Ahn, S.I. Woo, Electrochemical oxygen reduction on nitrogen doped graphene sheets in acid media, Electrochemistry Communications 12 (2010) 1052–1055.

[43] L. Feng, L. Yang, Z. Huang, J. Luo, M. Li, D. Wang, Y. Chen, Enhancing electrocatalytic oxygen reduction on nitrogen-doped graphene by active sites implantation, Scientific reports 3 (2013) 3306.

[44] L. Lai, J.R. Potts, D. Zhan, L. Wang, C.K. Poh, C. Tang, H. Gong, Z. Shen, J. Lin, R.S. Ruoff, Exploration of the active center structure of nitrogen-doped graphene-based catalysts for oxygen reduction reaction, Energy & Environmental Science 5 (2012) 7936.

[45] Y. Shao, S. Zhang, M.H. Engelhard, G. Li, G. Shao, Y. Wang, J. Liu, I.A. Aksay, Y. Lin, Nitrogen-doped graphene and its electrochemical applications, Journal of Materials Chemistry 20 (2010) 7491.

[46] L. Qu, Y. Liu, J.-B. Baek, L. Dai, Nitrogen-Doped Graphene as Efficient Metal-Free Electrocatalyst for Oxygen Reduction in Fuel Cells, ACS Nano 4 (2010) 1321–3126.

[47] J.A. Poirier, G.E. Stoner, Microstructural Effects on Electrocatalytic Oxygen Reduction Activity of Nano-Grained Thin-film Platinum in Acid Media, J. Electrochem. Soc. 141 (1994) 425–430.

[48] R.S. Nicholson, I. Shain, Theory of Stationary Electrode Polarography: Single Scan and Cyclic Methods Applied to Reversible, Irreversible, and Kinetic Systems, Analytical chemistry 36 (1964) 706–723.

[49] H. Erikson, A. Kasikov, C. Johans, K. Kontturi, K. Tammeveski, A. Sarapuu, Oxygen reduction on Nafion-coated thin-film palladium electrodes, Journal of Electroanalytical Chemistry 652 (2011) 1–7.

[50] H. Erikson, M. Liik, A. Sarapuu, J. Kozlova, V. Sammelselg, K. Tammeveski, Oxygen reduction on electrodeposited Pd coatings on glassy carbon, Electrochimica Acta 88 (2013) 513–518.

[51] S.C. Roy, P.A. Christensen, A. Hamnett, K.M. Thomas, V. Trapp, Direct methanol fuel cell cathodes with sulfur and nitrogen-based carbon functionality, J. Electrochem. Soc. 143 (1996) 3073–3079.

[52] M. Hasik, A. Bernasik, A. Drelinkiewicz, K. Kowalski, E. Wenda, J. Camra, XPS studies of nitrogen-containing conjugated polymers-palladium systems, Surface Science 507-510 (2002) 916–921.

[53] V.B. Parambhath, R. Nagar, S. Ramaprabhu, Effect of nitrogen doping on hydrogen storage capacity of palladium decorated graphene, Langmuir 28 (2012) 7826–7833.
[54] X. Xu, Y. Li, Y. Gong, P. Zhang, H. Li, Y. Wang, Synthesis of palladium nanoparticles supported on mesoporous N-doped carbon and their catalytic ability for biofuel upgrade, JACS 134 (2012) 16987–16990.
[55] L.A. Kibler, Hydrogen electrocatalysis, Chemphyschem: a European journal of chemical physics and physical chemistry 7 (2006) 985–991.
[56] A. Roudgar, A. Groß, Local reactivity of thin Pd overlayers on Au single crystals, Journal of Electroanalytical Chemistry 548 (2003) 121–130.
[57] M. Baldauf, D.M. Kolb, A hydrogen adsorption and absorption study with ultrathin Pd overlayers on Au(111) and Au(100), Electrochimica Acta 38 (1993) 2145–2153.
[58] M. Baldauf, D.M. Kolb, Formic acid oxidation on ultrathin Pd films on Au(hkl) and Pt(hkl) electrodes, J. Phys. Chem. 100 (1996) 11375–11381.
[59] L.A. Kibler, Dependence of electrocatalytic activity on film thickness for the hydrogen evolution reaction of Pd overlayers on Au(1 1 1), Electrochimica Acta 53 (2008) 6824–6828.
[60] W.B. Schneider, U. Benedikt, A.A. Auer, Interaction of platinum nanoparticles with graphitic carbon structures: a computational study, Chemphyschem: a European journal of chemical physics and physical chemistry 14 (2013) 2984–2989.
[61] J.C. Meier, C. Galeano, I. Katsounaros, J. Witte, H.J. Bongard, A.A. Topalov, C. Baldizzone, S. Mezzavilla, F. Schuth, K.J. Mayrhofer, Design criteria for stable Pt/C fuel cell catalysts, Beilstein journal of nanotechnology 5 (2014) 44–67.
[62] J. Llopis, Corrosion of Platinum Metals and Chemisorption, Catalysis Reviews 2 (1969) 161–220.
[63] J.F. Llopis, J.M. Gamboa, L. Victori, Radiochemical study of the anodic behaviour of palladium, Electrochimica Acta 17 (1972) 2225–2230.

Applied Catalysis B: Environmental 144 (2014) 300–307

Contents lists available at ScienceDirect

Applied Catalysis B: Environmental

journal homepage: www.elsevier.com/locate/apcatb

Electrocatalysis at palladium nanoparticles: Effect of the support nitrogen doping on the catalytic activation of carbon—halogen bond

Lorenzo Perini, Christian Durante, Marco Favaro, Stefano Agnoli, Gaetano Granozzi, Armando Gennaro*

Department of Chemical Sciences, University of Padova, Via Marzolo, 1, 35131 Padova, Italy

ARTICLE INFO

Article history:
Received 20 May 2013
Received in revised form 2 July 2013
Accepted 8 July 2013
Available online 17 July 2013

Keywords:
Doped glassy carbon
Electrocatalysis
Palladium
Nitrogen doping
Benzyl chloride

ABSTRACT

Pd nanoparticles (NPs) were deposited electrochemically on three differently modified glassy carbon (GC) supports: pristine GC, nitrogen implanted GC and Ar implanted GC. The aim of such an approach is to discriminate whether the electrocatalytic activity of Pd NPs toward the activation of carbon—halogen bond is preferentially driven by chemical or morphological defects. Modified GC electrodes were prepared by ion implantation whereas Pd was deposited according to a double-step potential deposition in a 1 mM $PdSO_4 + 0.1$ M H_2SO_4 solution.

The electrodes were fully characterized by X-ray photoemission spectroscopy, which allowed the identification of several different N-based defects. Pd NPs morphology, dimension and distribution were investigated by scanning electron microscopy. The outcomes indicate that the electrodeposition of Pd NPs on nitrogen-implanted GC results in smaller catalyst particle sizes and higher particle dispersion with respect to pristine GC. The palladium nitrogen-implanted electrode was tested in the electrochemical reduction of benzyl chloride, showing that Pd NPs result in a much higher catalytic activity than bulk Pd and Pd NPs loaded on the pristine GC electrode.

1. Introduction

Activation of the carbon—halogen (C—X) bond is a highly explored field in organic electrochemistry since it finds huge application in organic synthesis [1,2], in the control over radical polymerization [3,4], in pollutant degradation [5–7] and in mechanistic investigation on dissociative electron transfer (DET) [8–11]. The main drawback associated with the electrochemical activation of C—X is the very negative potentials required, and this is particularly true in the case of organic chlorides, which represent the most investigated ensemble among organic molecules containing a nucleofuge group. This has boosted over the last decade the research of electrode materials active toward the C—X bond breaking, and, so far, Ag, Cu and Pd were found to possess extraordinary electrocatalytic properties [12–16]. However, attempts to improve catalytic activity by changing from bulk electrode to nanoparticles (NPs) dispersed on a support, or by introducing a second or a third metal have not yet led to the desired improvements [17,18].

In principle, the catalytic activity can be increased either by a fine dispersion of the NPs or by modulating the electronic properties of the catalyst NPs by interaction with support chemical or morphological defects; as an example, a way to enhance the durability of the catalyst support assembly in the case of oxygen reduction is to strengthen the catalyst NPs support interaction by introducing into the substrate defects that can act as trapping sites for anchoring the catalyst NPs [19,20]. In this regard, Minguzzi et al. have recently observed that the electrochemical activation of a carbon surface in acidic media introduces oxygen functional groups which enhances the stability and the electrocatalytic activity of Ag NPs toward the C—X bond activation [21].

Among various forms of carbon, glassy carbon (GC) is the most important for use as an electrode in electrochemistry, since it shows very low electrical resistivity, it is non-porous and impermeable to gases, it has high chemical resistance and the widest potential range observed for graphitic carbon electrodes and, last but not least, it can be easily polished and managed [22]. This renders GC an optimal material for a basic investigation on how the chemical modifications of the support can affect the activity of the loaded catalyst. The chemical modification (hereafter referred to as doping) of a GC surface is generally performed by the adsorption or by the covalent bonding (grafting) of molecular catalyst or electronic mediators. Another option is to synthetize a doped GC by thermolysis of suitable carbon precursors (usually polymers) containing the desired heteroatoms [22,23] or by the mixture of resins and an inorganic source of heteroatoms, such as boric acid and ammonia [24]. In the present case, following a different approach, nitrogen

---

* Corresponding author. Tel.: +39 049 8275132; fax: +39 049 8275829.
E-mail address: armando.gennaro@unipd.it (A. Gennaro).

0926-3373/$ – see front matter © 2013 Elsevier B.V. All rights reserved.
http://dx.doi.org/10.1016/j.apcatb.2013.07.023

functional groups have been introduced on a GC support by N_2^+ and N^+ ion implantation, producing a modified N-GC support. Here it will be shown that the presence of nitrogen functional groups on the carbonaceous support can influence the nucleation and growth of metal NPs and promote their catalytic activity toward activation of the C—X bond.

In the present case, palladium was employed as metal NPs because of its excellent hydrogenation ability, which makes it an excellent catalyst in the electrochemical dechlorination of organic chlorides in aqueous media or organic–aqueous mixture [25–27]. The Pd NPs electrochemical deposition on N-GC (Pd@N-GC) has been carried out in a 1 mM $PdSO_4$ + 0.1 M H_2SO_4 solution by a double-step potential deposition.

The N_2^+ and N^+ ion implantation, besides the introduction of new functional groups, leads to the formation of an increased number of morphological defects; this open a new issue about the possibility of disentangling the effects connected to the presence of new functional groups from those deriving from the morphological defects introduced by ion implantation. In order to discriminate between the two effects, we have performed the deposition of Pd also on pristine GC (Pd@GC) and on an Ar^+ implanted GC (Pd@Ar-GC) samples, and used them as an internal reference to gauge the results. In particular, Ar-implantation determines relevant morphological defects, consisting in a re-hybridization of carbon atoms from C_{sp^2} to C_{sp^3}, but cannot induce chemical defects [28].

The prepared GC electrodes were fully characterized by X-ray photoelectron spectroscopy (XPS) and scanning electron microscopy (SEM), and the electrochemical reactivity was tested for the reduction of benzyl chloride, which so far is considered as a standard test molecule for investigating carbon—halogen bond activation.

2. Experimental

2.1. Chemicals

CH_3CN, (WWR, HPLC grade) was distilled over CaH_2 under a N_2 atmosphere. Tetraethylammonium tetrafluoroborate ($TEABF_4$) (Fluka, >98%) was recrystallized twice from EtOH and dried in a vacuum oven at 70 °C. Benzyl chloride (Fluka, ≥99.5%) and $PdSO_4$ (Alfa Aesar, 99.95%) were high-purity reagents and were used without further purification. Deionized water used for the experiments was previously twice distilled from $KMnO_4$.

2.2. Preparation and characterization of Ar-GC and N-GC substrates

The N- and Ar-GC samples were prepared by using the ion beam produced by the ion gun (Thermo VG Scientific) under the same conditions: 2.2×10^{-6} mbar background of N_2 or Ar, a beam energy of 500 eV and exposure time of 10 min, with an incidence angle of the ion beam equal to 45° with respect to the sample surface (the ion current measured during this treatment was 2.0 μA and the total dose of implanted atoms was around 5×10^{16} ion cm^{-2}). The nitrogen/argon dose was evaluated to be about 15 at%.

The XPS characterization of the samples was performed in a UHV chamber (base pressure $<5 \times 10^{-9}$ mbar), equipped with a double anode X-ray source (Omicron), a hemispherical electron analyzer (VG Scienta). All XPS measurements were performed at room temperature, using non-monochromatic Mg-Kα radiation ($h\nu$ = 1253.6 eV) and a pass energy of 50 eV and 20 eV for the survey and high-resolution spectra, respectively. The calibration of the binding energy (BE) scale was carried out using Au 4f as reference. The N 1s and C 1s peaks were deconvoluted into individual components (after Shirley background removal) using symmetrical Voigt functions, whereas the Pd 3d photoemission peaks were deconvoluted into chemical-shifted components using Doniach–Sunjich shape functions. In both cases, the χ^2 minimization was ensured by the use of the nonlinear least-squares routines.

SEM investigations were performed with a dual-beam FEI Nova 600i instrument, with a semi-in-lens cold cathode field emission scanning electron microscope source.

2.3. Electrochemical instrumentation

Electrochemical measurements were carried out either by use of a computer-controlled Autolab PGSTAT30 potentiostat or an EG&G PARC Model 273/A potentiostat. The electrocatalytic activity of the nanostructured surfaces for benzyl chloride reduction was investigated by means of cyclic voltammetry (CV) and was carried out in a three-electrode cell with a GC, either modified or unmodified, or Pd disk as working electrode. The counter electrode and the reference electrode were a Pt wire and Ag|AgI|Bu_4NI (0.1 M) in CH_3CN, respectively. The latter was calibrated after each experiment against the ferrocenium/ferrocene couple. The potentials measured against the Ag|AgI|I^- reference electrode were converted to the SCE scale, to which all potentials in the paper are referred, by using $E^0_{Fc+/Fc} = 0.391$ V vs. SCE in CH_3CN [12]. The working electrodes were built from a GC plate (Tokai GC-20) and 2-mm diameter Pd wire (Alfa Aesar, 99.999%) and were polished to a mirror finish with silicon carbide papers of decreasing grain size (Struers, grit: 500, 1000, 2400, 4000) followed by diamond paste (3-, 1-, 0.25-μm particle size). They were then cleaned in ethanol in an ultrasonic bath for about 5 min. In several cases a slight passivation of the Pd electrode, resulting in a poor reproducibility of the data, was observed during the electrocatalytic experiments. When this happened, the electrode was activated by CVs until cathodic discharge.

The Pd NPs on GC, Ar-GC and N-GC were freshly prepared before each experiment by electrodeposition of Pd on an exposed area of 3-mm diameter GC disk. The GC samples (8 mm diameter) were either clamped in a Kel-F mask or enveloped in Teflon tape. The electrochemical deposition of Pd NPs was carried out in a three-electrode cell containing 1 mM $PdSO_4$ solution in 0.1 M H_2SO_4. GC, Ar-GC and N-GC disks were set as working electrode, while the counter electrode and the reference electrode were a Pt wire and a Hg|Hg_2SO_4|K_2SO_4 saturated electrode, respectively. The reference electrode was separated from the working electrode compartment through a salt bridge which avoided any contamination of the working electrode. The conversion of the potential measured vs. Hg|Hg_2SO_4|SO_4^{2-} to the SCE scale is obtained by addition of +0.373 V to the measured value. All experiments were carried out at 25 °C.

3. Results and discussion

3.1. Preparation of Pd nanoparticles (NPs) on pristine and doped GCs

We first investigated the redox reactions of palladium on GC by CV in 1 mM $PdSO_4$ + 0.1 M H_2SO_4 solution. The first negative-going scan obtained under these conditions shows no well-defined cathodic peak for the reduction of Pd^{2+} to Pd(0). CV obtained starting at an initial potential of 0.3 V vs. SCE and scanning in the negative direction at variable negative potential limits indicate that Pd deposition starts at a potential more negative than −0.05 V vs. SCE, which coincides with the equilibrium potential. This was confirmed by the appearance of a PdO peak on the reverse scan and by XPS measurements revealing the presence of Pd over the GC surface. A similar experiment has been carried out at N-GC, though in

Table 1
Optimized deposition conditions for Pd NPs on various GC supports.

	E_r (V)[a,b]	t_r (s)[c]	E_{nu} (V)[b]	t_{nu} (s)	E_{grow} (V)[b]	t_{grow} (s)	Q (C)[d]
GC	0.3	10	−0.25	0.1	−0.077	50	2.74E−4
Ar-GC	0.3	10	−0.25	0.1	−0.077	50	2.75E−4
N-GC	0.3	10	−0.25	0.1	−0.127	50	2.78E−4

[a] Resting potential.
[b] Potentials are vs. SCE.
[c] Resting time.
[d] Values obtained from the mean of at least 5 different experiments.

this case the deposition of Pd started at a more negative potential than at pure GC (−0.1 V vs. SCE). On the basis of these results, Pd NPs were deposited on GC by a potentiostatic double-step deposition method, since this method allows better control over the dimension and dispersion of metal NPs; the optimized deposition conditions are summarized in Table 1. The first step (nucleation) was set at a sufficiently negative potential ($E_{nu} = -0.25$ V vs. SCE) to allow the deposition process to be controlled only by diffusion and, as a consequence, instantaneous nucleation of Pd takes place. In the second step (growth) the potential was set at $E_{grow} = -0.077$ V vs. SCE for GC and Ar-GC and $E_{grow} = -0.127$ V vs. SCE for N-GC. At these potentials the process is kinetically controlled and the Pd NPs grow without further nucleation of new sites. The solution was oxygen-free and unstirred during the depositions. The deposition current was recorded and integrated in order to determine the total deposition charge (Table 1). The results indicate that a comparable amount of charge is consumed for all three samples and therefore the mass of Pd loaded over the three different GCs is fairly similar.

Pd NPs deposited on GC and modified GCs show the typical electrochemical behavior of palladium nanostructured electrode (Fig. 1) [29,30], which is characterized by a hydrogen adsorption peak labeled as 1c and a hydrogen desorption peak 1a, a zone labeled as **a** where hydrogen evolution occurs and a zone **b** due to the oxidation of hydrogen atoms adsorbed during the negative-going scan onto the Pd(0) NPs, a zone **c** due to the formation of PdO and the zone **d** due to PdO reduction.

3.2. Morphological and chemical characterization of Pd NPs on pristine and doped GCs

We first investigated the different GCs surface chemistry by means of XPS: in Fig. 2a the survey spectra of the different samples after the electrochemical deposition of Pd (see Table 1) are shown. The surveys for all three samples clearly show similar features that account for the presence of Pd, carbon and oxygen, while nitrogen is present only in the case of Pd@N-GC. In this case, from the analysis of N 1s and C 1s XPS peaks, we can determine an overall surface stoichiometry of $C_{0.85}N_{0.15}$. Furthermore, while in Pd@Ar-GC we observe only morphological defects, consisting of a re-hybridization from C_{sp^2} to C_{sp^3}, in Pd@N-GC, we can distinguish between different chemical defects; by deconvoluting the N 1s XPS peak (Fig. 2b), we can single out the presence of pyridinic (398.0 eV), —C≡N terminal groups (398.9 eV), pyrrolic (400.1 eV), N graphitic defects (401.2 eV) and N^+ ion trapped into carbon vacancies (402.6 eV) [28,31]. A further component present at high BE (404 eV) can be assigned to the interaction between nitrogen and oxygen with the formation, of NO_x groups, though in a very limited amount. Although GC has a randomly oriented structure over large dimensions, it contains a graphitic microcrystalline structure; therefore, we may assume that the effect of the ion implantation would increase the number of defects on the graphitic structures, resulting in an increased numbers of edges. If so, it is reasonable to assume that nitrogen groups are placed nearby these new edges of the graphitic microstructure. A pictorial view of nitrogen defects is proposed in Fig. 3.

Fig. 2c shows the Pd 3d XPS spectra for the same Pd loading (see Table 1) deposited onto Ar-GC, N-GC and GC. As can be seen, the Pd 3d photoemission peak presents a full width at half maximum (FWHM) compatible with the presence of both metal Pd and Pd^{2+}

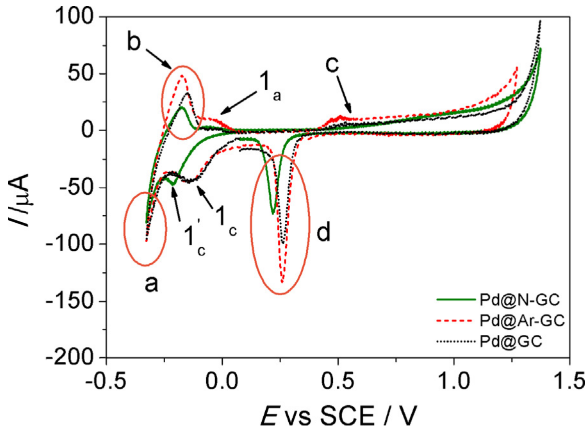

Fig. 1. Cyclic voltammetry of Pd NPs deposited on pristine and modified GCs in 0.1 M H_2SO_4 solution; scan rate 200 mV s^{-1}.

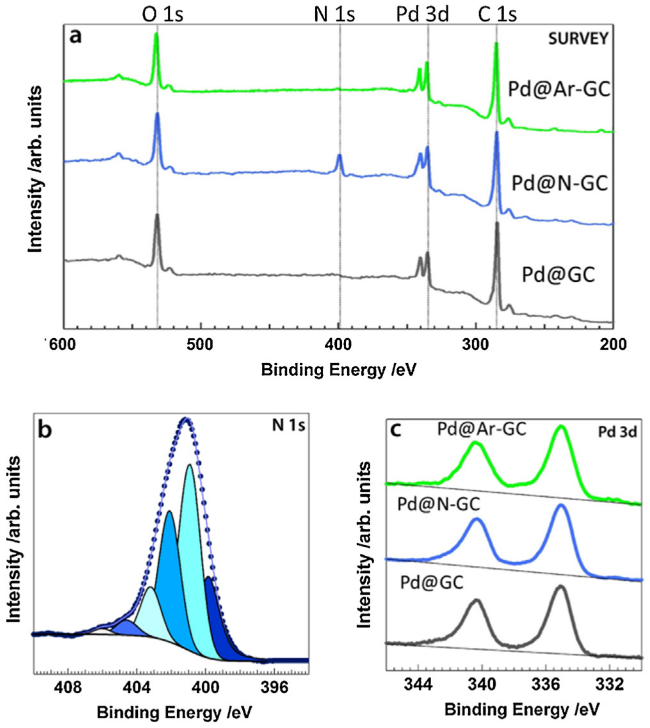

Fig. 2. XPS data of Pd@Ar-GC, Pd@N-GC, Pd@GC for the same Pd loading (see Table 1): (a) survey wide scans; (b) N 1s XPS peak and relative deconvolution by means of chemically shifted components in Pd@N-GC; and (c) Pd 3d XPS peaks.

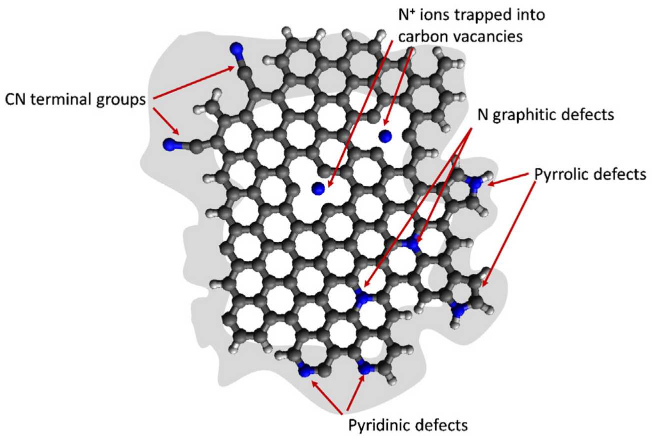

Fig. 3. Ball-and-stick model of the different chemical species obtained after ion implantation in GC according to the XPS N 1s data reported in Fig. 2b. The evidenced area corresponds to edge defects.

species (BE $Pd^0 = 335.1$ eV, BE $Pd^{2+} = 336.2$ eV), and no significant change is observed in the three cases.

The morphological surface characterization of Pd NPs on doped and undoped GC supports was carried out by SEM (Figs. 4 and 5). The electrochemical deposition of Pd on GC has been carried out at three different deposition time: 25, 50 and 150 s, and results in the formation of NPs of an average dimension depending on the time of the growing step (t_{grow}). NPs deposited for 25 s have a typical Volmer–Weber growth and average dimension of 23 nm (Fig. 4a and b). The increase of the growing step period from 25 to 50 s increases the Pd amount loaded over the GC support and changes the Pd NPs dimensions according to a Gaussian distribution centered at 40 nm (Fig. 4c and d). It is worth noting that in this case NPs agglomerates of 100–300 nm sizes are also present as a result of the preferential growth of Pd NPs over the preexisting metal seeds. At a deposition time of 150 s the distribution of the particle size assumes a maxima at 45 nm. In this case the growth of NPs agglomerates is even more emphasized (Fig. 4e and f).

In Fig. 5a comparative panel for Pd@GC, Pd@Ar-GC and Pd@N-GC deposited at the same growing period of 50 s, at two different magnification scale is reported. SEM images of Pd@Ar-GC show Pd NPs with smaller sizes (centered at 25 nm) and narrower dispersion (Fig. 5d–f) with respect to Pd@GC (Fig. 5a–c). Also in the case of Pd@Ar-GC some large size Pd agglomerates are visible, though to a lesser extent than for Pd@GC. In the case of Pd@N-GC, roughly spherical Pd NPs with average sizes of 21 nm are more regularly distributed with respect to both Pd@GC and Pd@Ar-GC (Fig. 5g–i).

The surface area of the Pd NPs loaded on pristine GC (geometric area 0.076 cm^2) and modified GCs have been estimated from the integrated charge in the electrochemical formation of a full monolayer of PdO [32,33]. This method is based on the identification of the upper potential limit at which oxygen is chemisorbed in a monoatomic layer with a one to one correspondence with the surface Pd atoms. This method has been preferred over the one based on CO stripping, since the N-GC support has shown an anomalous behavior in the presence of carbon monoxide.

CVs at variable positive potential limits have been performed (Fig. 6a) and then the integrated charge for the formation of PdO has been plotted vs. the inversion potential (Fig. 6b). The potential for a complete formation of a PdO monolayer corresponds to the point where the straight line changes its slope. The integrated charge at this potential allows obtaining the Pd NPs surface area according to Eq. (1):

$$Q_0 = 2eN_A\Gamma_0 A \qquad (1)$$

where N_A is the Avogadro constant and Γ_0 is the surface concentration of atomic oxygen, which corresponds to the number of Pd atoms, N_{Pd}, exposed per unit surface area. From the N_{Pd} per unit surface area, it is possible to calculate the reference charge q_0^s, which in the case of Pd is ca. 420 C/cm^2. The real surface area is therefore

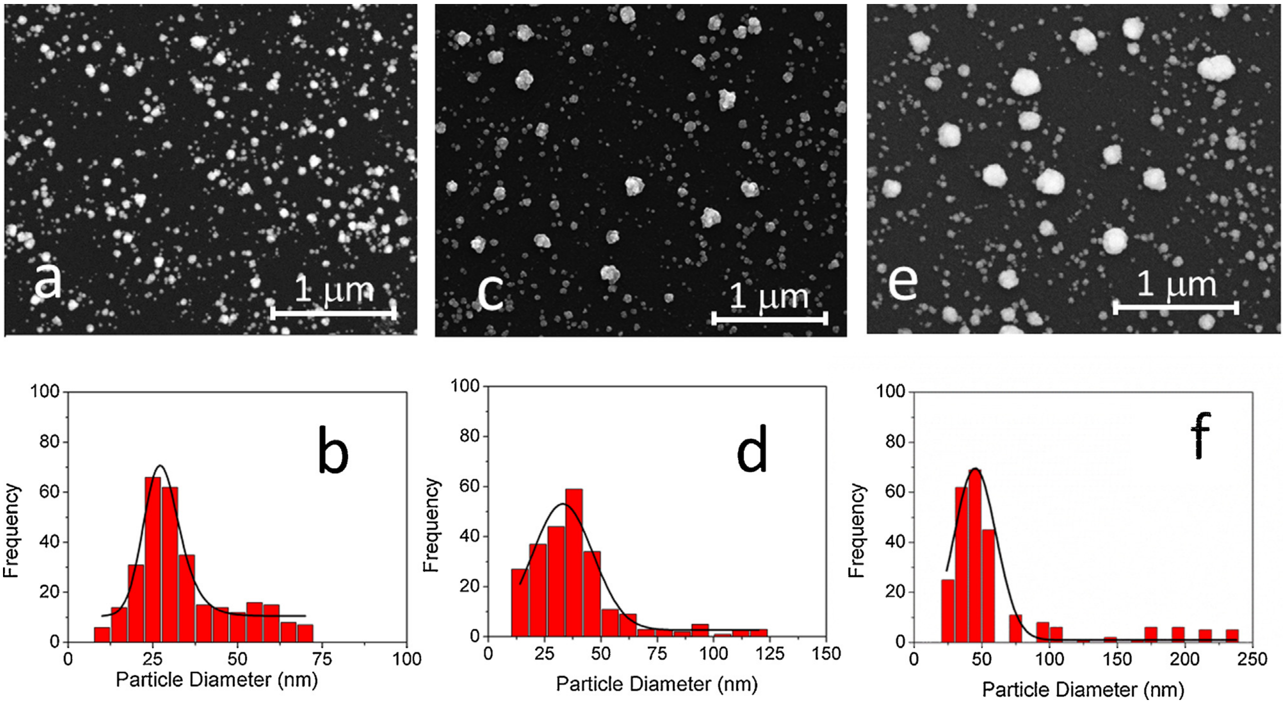

Fig. 4. SEM images and particle size distributions for Pd@GC at different growth time: (a and b) $t_{grow} = 25$ s; (c and d) $t_{grow} = 50$ s; (e and f) $t_{grow} = 150$ s.

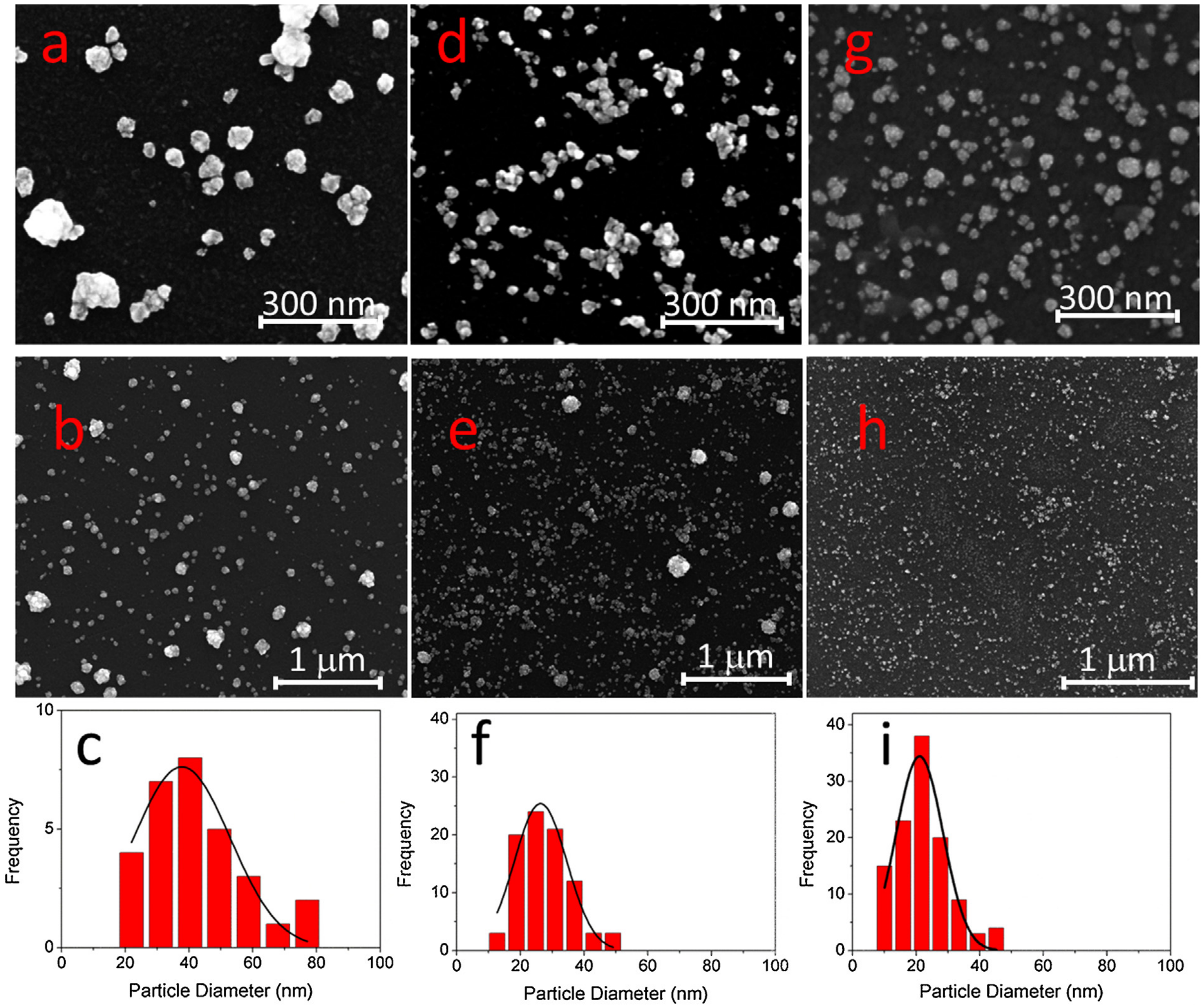

Fig. 5. SEM images at two different magnifications and particle size distributions for: (a–c) Pd@GC; (d–f) Pd@Ar-GC and (g–i) Pd@N-GC obtained at the same Pd loading (see Table 1).

obtained from the ratio of the integrated charge and the reference charge as indicated in Eq. (2):

$$A = \frac{Q_0}{q_0^s} \tag{2}$$

The estimated area for Pd@N-GC was 0.110 cm^2, which is higher than the area calculated for Pd@GC and Pd@Ar-GC, 0.089 and 0.085 cm^2, respectively.

In conclusion, it is evident that a mere morphological effect of the GC support is not sufficient to justify such differences in terms of surface area, metal NPs dimension and dispersion, but it must be related to the presence of nitrogen functional groups and a much stronger interaction between the chemical defect sites of GC and Pd [34]. A similar result has been observed for Pt NPs deposited on N-doped HOPG [35,36], where it was claimed the N-doping is responsible for a decrease in Pt NPs size and an increase in NPs dispersion.

3.3. Electrocatalytic activity of Pd NPs on pristine and doped GCs

The electrocatalytic activity of Pd NPs was tested for the reduction of benzyl chloride, chosen as a model process for the electroreduction of organic halides. The mechanism of activation of organic halides is generally analyzed in the framework of dissociative electron transfer (DET) to C—X bonds. Whether the activation occurs at an inert or catalytic electrode, two reaction pathways are possible for the reductive cleavage of R—X to $R^\bullet$ and X^-. These are a stepwise mechanism, involving an intermediate radical anion, $R{-}X^{\bullet -}$, which further decomposes to $R^\bullet$ and X^- (Eqs. (3) and (4)) and a concerted mechanism, where electron transfer (ET) and bond breaking occur in a single step (Eq. (5)). Whichever of the two mechanism is followed, a $R^\bullet$ radical is formed that is generally more easily reducible than R—X and readily undergoes a second ET (Eq. (6)). Therefore, the process involves two successive one-electron transfers leading to the carbanion R^-, which is then rapidly protonated by any proton donor BH present in solution (Eq. (7)).

$$R{-}X + e^- \rightleftarrows R{-}X^{\bullet -} \tag{3}$$

$$R{-}X^{\bullet -} \rightarrow R^\bullet + X^- \tag{4}$$

$$R{-}X + e^- \rightarrow R^\bullet + X^- \tag{5}$$

$$R^\bullet + e^- \rightarrow R^- \tag{6}$$

$$R^- + BH \rightarrow R{-}H + B^- \tag{7}$$

The transfer coefficient α, which allows the attribution of the reduction mechanism, has been determined by voltammetric analysis. If the peak potential E_p varies linearly with log υ, with slope $\partial E_p / \partial \log \upsilon$, Eq. (8) can be used to calculate the transfer coefficient,

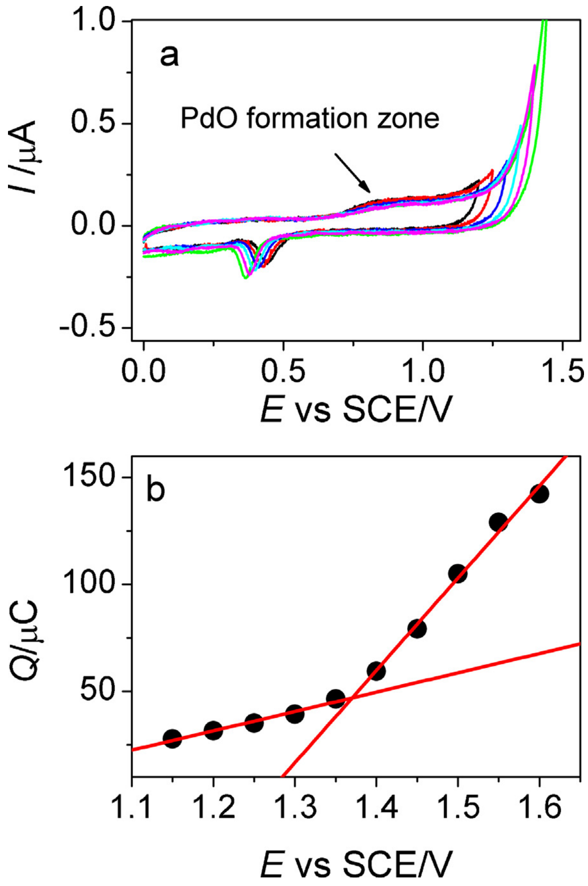

Fig. 6. (a) Cyclic voltammograms at Pd@N-GC electrode in 0.1 M H_2SO_4 with different positive potential limits. (b) Integrated charge for the formation of PdO at Pd@N-GC electrode as a function of the positive potential limit.

α. Alternatively, α can be calculated by Eq. (9), where $E_{p/2} - E_p$ is the peak width [37].

$$\frac{\partial E_p}{\partial \log \upsilon} = -\frac{1.151RT}{\alpha F} \qquad (8)$$

$$E_{p/2} - E_p = \frac{1.857RT}{\alpha F} \qquad (9)$$

The reduction mechanism of benzyl chloride on bulk Pd and GC has previously been reported [12], showing that, on both electrodes, the reduction of benzyl chloride follows a concerted mechanism that is typically characterized by an ET coefficient $\alpha \ll 0.5$.

The CVs of benzyl chloride on GC and bulk Pd in $CH_3CN + TBABF_4$ are reported in Fig. 7. Generally, the peak potential is the benchmark for the electrocatalytic properties, and GC is so far considered a non-catalytic electrode [38]. Therefore, the catalytic activity, expressed as $\Delta E_p = E_p^{Pd} - E_p^{GC}$, indicates that bulk Pd exhibits a remarkable electrocatalytic effect of 0.33 V with respect to GC (Table 2).

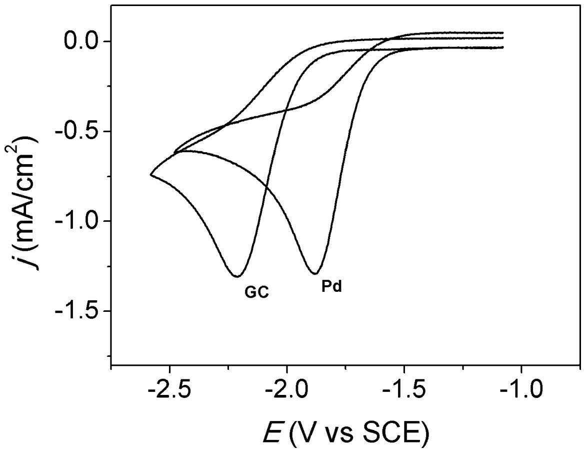

Fig. 7. Cyclic voltammetry of 2 mM benzyl chloride recorded in $CH_3CN + 0.1$ M $TBABF_4$ at GC and bulk Pd electrodes.

Fig. 8a shows CV of benzyl chloride reduction at Pd@GC electrodes at different Pd deposition times. From Fig. 8a it is clear that the overpotential for benzyl chloride reduction depends on the Pd surface coverage since, as the deposition time of Pd increases from 25 to 150 s, the reduction peak shifts to a more positive potential and the peak current increases. The best performance is observed at Pd@GC deposited for 150 s ($E_p = -1.87$ V vs. SCE), which shows comparable electrocatalytic activity with respect to bulk Pd ($E_p = -1.88$ V vs. SCE). Therefore, it appears that the catalytic activity of Pd over a non-modified GC depends more on the Pd loading and nanoparticles size than on the morphology of the metal catalyst.

The electrochemical behavior of Pd@Ar-GC ($t_{grow} = 50$ s) is also reported in Fig. 8b. As previously discussed, Pd NPs on Ar-GC are smaller and more uniformly dispersed than on pristine GC; however, besides a little difference of peak current, which may be associated with a different active surface area, Pd@Ar-GC shows similar catalytic activity and reduction mechanism with respect to Pd@GC (Table 2). These results assert that, even though Ar-GC has an increased number of defects with respect to pristine GC and the Pd NPs size is sensibly different between the two samples, the catalytic activity is not influenced by the morphology of the supports. Furthermore, it must be stressed that both Pd@GC and Pd@Ar-GC do not show better performance in terms of catalytic activity with respect to bulk Pd, and this, also considering the benefit of employing a small amount of catalyst, puts a limit on the practical advantage of using a nanostructured electrode with respect to a bulk one.

Table 2
Voltammetric data for benzyl chloride reduction (2 mM) in $CH_3CN + 0.1$ M $TEABF_4$, measured at 0.1 V s^{-1}.

Cathode	E_p [a] (V)	α	ΔE_p [b] (V)	A (cm^2)	M-CA[c] (mA g^{-1})	S-CA[d] (mA cm^{-2})
GC	−2.21	0.30		0.071[e]	–	–
Pd	−1.88	0.26	0.33	0.031[e]	–	1.262
Pd@GC	−1.93	0.19	0.28	0.089[f]	7.2E+05	1.217
Pd@Ar-GC	−1.93	0.23	0.28	0.085[f]	6.6E+05	1.156
Pd@N-GC	−1.78	0.33	0.43	0.110[f]	9.0E+05	1.269

[a] Potentials are referred to SCE.
[b] See $\Delta E_p = E_p^{Pd} - E_p^{GC}$.
[c] Mass catalytic activity with respect to the mass of Pd electrodeposited.
[d] Specific catalytic activity.
[e] Geometric area.
[f] Real surface area.

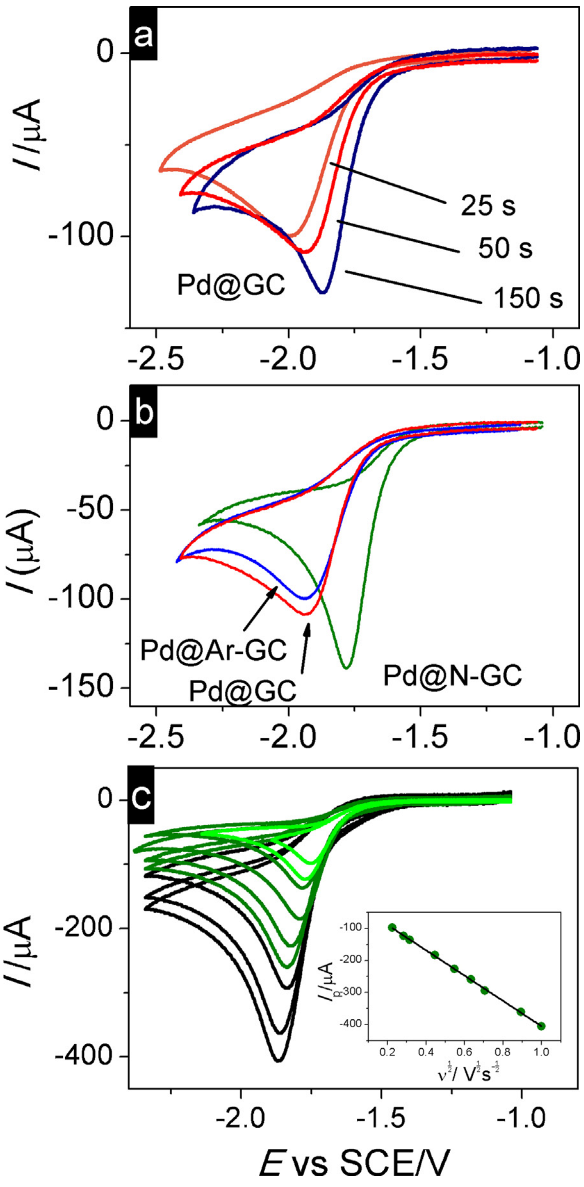

Fig. 8. Cyclic voltammetry of 2 mM benzyl chloride recorded in $CH_3CN + 0.1$ M $TBABF_4$ at different electrodes: (a) Pd@GC at different Pd loading; (b) Pd@N-GC, Pd@Ar-GC and Pd@GC; and (c) effect of the scan rate at Pd@N-GC.

The electrochemical behavior was tested also at Pd@N-GC ($t_{grow} = 50$ s) (Fig. 8b), and, this time, Pd@N-GC is more active in terms of overpotential, mass catalytic activity (peak current/grams of Pd) and specific catalytic activity (peak current/surface area) not only with respect to Pd@GC or Pd@Ar-GC, but also to bulk Pd (Table 2). The integrated current for the deposition process indicates that the Pd amount loaded on N-GC is comparable to that at Ar-GC; thus, the improved catalytic activity is not the result of different Pd loading or particle size on the three supports. This represents a clear example where the electrodic support exerts a synergistic action, promoting the catalytic activity of metal NPs toward a catalytic process. The nature of this increased catalytic activity derives from the interaction between nitrogen functional groups and Pd NPs during the reduction process since the Pd free N-GC was found to be not active by itself. Actually, both N-GC and Ar-GC supports result to be even less active than pristine GC by several mV. To verify that the increased catalytic activity is not the result of a different reduction mechanism, we have evaluated the dependence of the voltammetric peak from the scan rate (Fig. 8c). The linear dependence of I_p from the square root of the scan rate indicates a diffusion-controlled process, while values of $\alpha = 0.33$ assert a concerted reduction mechanism, as already observed at Pd@GC and bulk Pd. Furthermore, Pd@N-GC is active even after several days at open atmosphere, indicating an intrinsic chemical and mechanical stability. This was confirmed also by *post eventum* XPS measurements that assert the same content of Pd and N.

Compared with other catalysts reported in the literature well-known to possess high catalytic activity, such as Ag, Pd@N-GC shows comparable catalytic activity with respect to bulk Ag, that so far is considered the best catalyst for R—X activation in non-aqueous solution [12], while it is far more active (several hundred mV) than Ag NPs of similar size (20–30 nm) deposited on GC [39].

4. Conclusions

Morphologically and chemically stable Pd NPs deposited on N-GC have been prepared by a double potential-step deposition in $H_2O + 0.1$ M H_2SO_4 containing millimolar amounts of $PdSO_4$. The NPs are spherical in shape with average dimension of 20 nm and are uniformly distributed over the N-GC surface. The presence of nitrogen functional groups introduced into GC support seems to influence the nucleation and growth kinetics during Pd NPs deposition, which results in smaller catalyst particle sizes and higher particle dispersion. The most striking result is that the presence of nitrogen functionalities promotes the catalytic performance of Pd NPs toward activation of the C—Cl bond, so extensively that Pd@N-GC is more active not only than Pd NPs loaded on undoped GC, but even than bulk Pd.

Acknowledgments

The research leading to these results has received funding from the European Union's Seventh Framework Programme (FP7/2007-2012) for Fuel Cell and Hydrogen Joint Technology Initiative under grant agreement no. [303492] 10. MF thanks Fondazione Cariparo for a PhD fellowship. We acknowledge financial support from Ateneo Italo-Tedesco/Deutsch-Italienisches Hochschulzentrum within the Vigoni bilateral framework.

References

[1] A.A. Isse, C. Durante, A. Gennaro, Electrochemistry Communications 13 (2011) 810–813.
[2] V. Jouikov, J. Simonet, Electrochemistry Communications 12 (2010) 781–783.
[3] A.J.D. Magenau, N.C. Strandwitz, A. Gennaro, K. Matyjaszewski, Science 332 (2011) 81–84.
[4] N. Bortolamei, A.A. Isse, A.J.D. Magenau, A. Gennaro, K. Matyjaszewski, Angewandte Chemie International Edition 50 (2011) 11391–11394.
[5] A.A. Isse, B. Huang, C. Durante, A. Gennaro, Applied Catalysis B: Environmental 126 (2012) 347–354.
[6] C. Durante, B. Huang, A.A. Isse, A. Gennaro, Applied Catalysis B: Environmental 126 (2012) 355–362.
[7] B. Huang, A.A. Isse, C. Durante, C. Wei, A. Gennaro, Electrochimica Acta 70 (2012) 50–61.
[8] A.A. Isse, A. Gennaro, C.Y. Lin, J.L. Hodgson, M.L. Coote, T. Guliashvili, Journal of the American Chemical Society 133 (2011) 6254–6264.
[9] C. Costentin, M. Robert, J.-M. Savéant, Journal of the American Chemical Society 125 (2003) 10729–10739.
[10] Y.F. Huang, D.Y. Wu, A. Wang, B. Ren, S. Rondinini, Z.Q. Tian, C. Amatore, Journal of the American Chemical Society 132 (2010) 17199–171210.
[11] A. Wang, Y.F. Huang, U.K. Sur, D.Y. Wu, B. Ren, S. Rondinini, C. Amatore, Z.Q. Tian, Journal of the American Chemical Society 132 (2010) 9534–9536.
[12] A.A. Isse, S. Gottardello, C. Durante, A. Gennaro, Physical Chemistry Chemical Physics 10 (2008) 2409–2416.
[13] C. Durante, A.A. Isse, A. Gennaro, Journal of Applied Electrochemistry 43 (2013) 227–235.
[14] P. Poizot, J. Simonet, Electrochimica Acta 56 (2010) 15–36.
[15] V. Jouikov, J. Simonet, Electrochemistry Communications 12 (2010) 331–334.
[16] J. Simonet, Electrochemistry Communications 7 (2005) 74–80.
[17] G. Zhang, Y. Kuang, J. Liu, Y. Cui, J. Chen, H. Zhou, Electrochemistry Communications 12 (2010) 1233–1236.

[18] C. An, Y. Kuang, C. Fu, F. Zeng, W. Wang, H. Zhou, Electrochemistry Communications 13 (2011) 1413–1416.

[19] S. Pylypenko, A. Queen, T.S. Olson, A. Dameron, K. O'Neill, K.C. Neyerlin, B. Pivovar, H.N. Dinh, D.S. Ginley, T. Gennett, R. O'Hayre, Journal of Physical Chemistry C 115 (2011) 13667–13675.

[20] S. Pylypenko, A. Queen, T.S. Olson, A. Dameron, K. O'Neill, K.C. Neyerlin, B. Pivovar, H.N. Dinh, G.S. Ginley, T. Gennett, R. O'Hayre, Journal of Physical Chemistry C 115 (2011) 13676–13684.

[21] A. Minguzzi, O. Lugaresi, G. Aricci, S. Rondinini, A. Vertova, Electrochemistry Communications 22 (2012) 25–28.

[22] N.L. Pocard, D.C. Alsmeyer, R.L. McCreery, T.X. Neenan, M.R. Callstrom, Journal of Materials Chemistry 2 (1992) 771–784.

[23] T.X. Neenan, M.R. Callstrom, B.J. Bachman, R.L. McCreery, D.C. Alsmeyerb, British Polymer Journal 23 (1990) 171–177.

[24] A.A. Perić-Grujić, O.M. Nešković, M.V. Veljković, Z.V. Laušević, M.D. Laušević, Bulletin of Materials Science 30 (2007) 587–593.

[25] Y. Fang, S.R. Al-Abed, Applied Catalysis B: Environmental 80 (2008) 327–334.

[26] Z. Sun, X. Wei, X. Hu, K. Wang, H. Shen, Colloids and Surfaces A: Physicochemical and Engineering Aspects 414 (2012) 314–319.

[27] S. Chen, Z. Qin, X. Quan, Y. Zhang, H. Zhao, Chinese Science Bulletin 55 (2010) 358–364.

[28] M. Favaro, L. Perini, S. Agnoli, C. Durante, G. Granozzi, A. Gennaro, Electrochimica Acta 88 (2013) 477–487.

[29] V.C. Diculescu, A.M. Chiorcea-Paquim, O. Corduneanu, A.M. Oliveira-Brett, Journal of Solid State Electrochemistry 11 (2007) 887–898.

[30] S. Guerin, G.S. Attard, Electrochemistry Communications 3 (2001) 544–548.

[31] M. Favaro, L. Perini, S. Agnoli, C. Durante, A. Gennaro, G. Granozzi, Physical Chemistry Chemical Physics 15 (2013) 2923–2931.

[32] A.N. Correia, L.H. Mascara, S.A.S. Machado, L.A. Avaca, Electrochimica Acta 42 (1997) 493–495.

[33] L.L. Fang, Q. Tao, M.F. Li, L.W. Liao, D. Chen, Y.X. Chen, Chinese Journal of Chemical Physics 23 (2010) 543–548.

[34] Y. Zhou, R. Pasquarelli, T. Holme, J. Berry, D. Ginley, R. O'Hayre, Journal of Materials Chemistry 19 (2009) 7830–7838.

[35] Y. Zhou, T. Holme, J. Berry, T.R. Ohno, D. Ginley, R. O'Hayre, Journal of Physical Chemistry C 114 (2010) 506–515.

[36] Y. Zhou, K. Neyerlin, T.S. Olson, S. Pylypenko, J. Bult, H.N. Dinh, T. Gennett, Z. Shao, R. O'Hayre, Energy & Environmental Science 3 (2010) 1437–1446.

[37] A.J. Bard, L.R. Faulkner, Electrochemical Methods, 2nd ed., John Wiley & Sons, New York, 2001.

[38] A. Gennaro, A.A. Isse, C.L. Bianchi, P.R. Mussini, M. Rossi, Electrochemistry Communications 11 (2009) 1932–1935.

[39] A.A. Isse, S. Gottardello, C. Maccato, A. Gennaro, Electrochemistry Communications 8 (2006) 1707–1712.

Surface Science 646 (2016) 132–139

Contents lists available at ScienceDirect

Surface Science

journal homepage: www.elsevier.com/locate/susc

A synchrotron-based spectroscopic study of the electronic structure of N-doped HOPG and PdY/N-doped HOPG

M. Favaro [a,1], G.A. Rizzi [a], S. Nappini [b], E. Magnano [b], F. Bondino [b], S. Agnoli [a], G. Granozzi [a,*]

[a] *Department of Chemical Sciences, University of Padova, Via Marzolo 1, 35131 Padova, Italy*
[b] *IOM-CNR, Laboratorio TASC, Area Science Park Basovizza, s.s. 14 km 163, 5 Basovizza, 34149 Trieste, Italy*

ARTICLE INFO

Available online 21 August 2015

Keywords:
HOPG
N-doped HOPG
NP/support interaction
Ion implantation
Synchrotron radiation
HR-PES
ResPES
PdY nanoparticles

ABSTRACT

N-doped Highly Oriented Pyrolytic Graphite (HOPG) (obtained by ion implantation) was used as a model system for mimicking the effect of N-doping in sp^2 hybridized carbon based supports. The electronic structure of such system has been careful characterized by means of spectroscopic techniques adopting synchrotron radiation. We demonstrate that it is possible to tailor different functional groups simply by tuning the annealing temperature after ion implantation. On such chemical modified HOPG, PdY catalyst nanoparticles have been deposited under strictly controlled conditions in ultra-high-vacuum (UHV) and the nanoparticle/support interactions studied by photoemission. The formation of the Pd_3Y alloy is evidenced by core level shift in Y 3*d* and Pd 3*d* states due to charge transfer.

1. Introduction

The best way to reach the goal of stable, efficient and cost effective electrodic materials for fuel cells is to use a rational design of the metal catalyst/support assembly. In this respect, the approach based on studies of model electrodes can be of value and their outcomes can be capitalized to implement efficient real electrodes to be properly tested in real working conditions.

In particular, HOPG (Highly Oriented Pyrolytic Graphite) is a reliable sp^2-carbon model substrate that represents a simplified playground where the interaction between the catalyst nanoparticles (NPs) and the support can be easily studied.

HOPG is a carbon-based material made by high-temperature decomposition of gaseous hydrocarbons, often acetylene, followed by hot pressing at high pressure and temperature [1]. Pyrolytic carbon usually has a single cleavage plane because the single graphene sheets crystallize with an ordered stacking, as opposed to graphite that forms microscopic randomly-oriented zones. Because of this peculiar structure, pyrolytic carbon exhibits several unusual anisotropic properties [1].

Usually, a strong NP/support interaction is beneficial to reduce several degradation processes (e.g. agglomeration, detaching…) therefore increasing the electrode stability. A viable strategy to enhance the catalyst NPs/support interaction is associated with the introduction of substrate defects that can act as trapping sites for anchoring highly dispersed catalyst NPs. In general, morphological defects introduced by a carbon atom re-hybridization (sp^2 to sp^3) and amorphization of the substrate are beneficial to increase the NP/support interaction [2]. On the other hand, extended amorphization of the support is detrimental with respect to the substrate conductivity, so a trade-off is needed. One route to minimize the conductivity decrease while maximizing the NP/support interaction is to resort to extrinsic chemical defects (such as boron, nitrogen and sulfur) rather than to morphological defects. They can be introduced by means of doping, and specific interactions, possibly modulating the electronic charge of the catalyst NPs, can be produced. Therefore the modification of the support allows tailoring the electronic properties of the catalyst.

In the last few years, chemical doping of sp^2-carbon materials by nitrogen has been studied [3–6], and excellent stability and high performances over time of the NP/support assembly have been obtained [5,7]. Moreover, specific chemical interactions can trigger enhanced chemical reactivity so that even normally inert materials become highly reactive. Even more interestingly, it has been fully demonstrated that a properly doped support can become catalytically active itself [5,8].

In this study, N-doped HOPG (obtained by ion implantation, hereafter N-HOPG) was used as a model system for mimicking the effect of N-doping in sp^2 hybridized carbon based supports. The outcomes of this study can be also of relevance in the field of metal NPs/graphene composites for advanced energetics, since the special properties of these composite systems stem from very subtle electronic interactions (i.e. interfacial hybridisation), which very often involve specific defects of the sp^2 carbon lattice [9–11]. On such chemical modified HOPG, metal catalyst NPs have been deposited under strictly controlled

---

[*] Corresponding author.
E-mail address: gaetano.granozzi@unipd.it (G. Granozzi).
[1] Current address: Advanced Light Source (ALS), Joint Center for Artificial Photosynthesis (JCAP), Lawrence Berkeley National Laboratory, 1 Cyclotron Rd., M/S 6R2100 Berkeley, CA 94720, United States.

http://dx.doi.org/10.1016/j.susc.2015.08.012
0039-6028/© 2015 Elsevier B.V. All rights reserved.

conditions in ultra-high-vacuum (UHV) and the NP/support interactions studied by the premises of surface science. We have herein considered PdY NPs as a potentially innovative catalyst. Actually, large efforts are currently devoted to test Platinum Group metals (PGMs) alloys with Rare Earth (RE) metals in order to reduce the content of the PGM while maintaining a sufficient catalyst activity and durability [12].

We report herein a detailed study of the chemical and electronic properties of N-HOPG based on several synchrotron-based surface techniques, namely High Resolution Photoemission Spectroscopy (HR-PES), Resonance Photoemission Spectroscopy (Res-PES), Near Edge X-ray Absorption Fine structure Spectroscopy (NEXAFS) and Low Energy Electron Diffraction (LEED). This study fully confirms the observations already obtained in our previous works [13–15] on HOPG and N-HOPG based on standard photoemission, and provides new insights in the electronic properties of these modified systems, with a detailed study of the valence band (VB). Moreover, on such HOPG and N-HOPG substrates we have deposited in UHV ultrathin films of Pd and Y and prepared by thermal annealing Pd_3Y alloyed NPs, as demonstrated by the use of HR-PES.

2. Experimental

Concerning the morphology, pure HOPG shows microcracks with varied length and width [16]. The existence of these cracks in crystallites of polycrystalline graphite was proposed firstly by Mrozowski [17]; for this reason, these features are usually known as *Mrozowski cracks*. In situ observations show that these cracks tend to close up heating HOPG at high temperature. For this reason, in order to obtain a clean and flat sample surface, annealing in UHV has been performed after the peeling (by scotch tape) of HOPG (Mikromasch, ZYB) in air, according to the procedure depicted in Fig. 1.

The ion implantation by nitrogen has been performed at room temperature (r.t.) and with a pressure of the precursor gas equal to $2.2 \cdot 10^{-6}$ mbar. In order to obtain a short projected range of ions into the target (to have chemical defect localized close the surface, in the case of N-implantation) and, at the same time, to study the surface morphology and chemistry upon nitrogen implantation, the energy of the incident ions was set to 100 eV, as reported in our previous study [15].

Pd and Y were evaporated in situ by e-beam bombardment from a high purity Pd rod and Y flakes, respectively (the last mentioned were contained in a Mo crucible). The deposition rate were equal to 0.25 MLE/min for Pd and to 0.10 MLE/min for Y (1 MLE (monolayer equivalent) corresponds to 2.26 Å [18] and to 1.77 Å [19] for Pd and Y, and represents the interlayer spacing between (111) planes in ten pure metals, respectively).

The characterization of the prepared systems was performed in situ, using HR-PES, Res-PES, NEXAFS and LEED at the Bach beamline operating at the Elettra Synchrotron Facility. Photoemission data were collected at RT with a SCIENTA R3000 analyzer set in transmission mode, using a photon energy of 595 eV (with a total energy resolution of 100 meV). C 1s and N 1s peaks were separated into individual chemically shifted components (after *Shirley* background removal) using a *Doniach–Sunjic* shape for the sp^2 component and symmetrical Voigt functions for the fitting of the molecular-like C and N 1s components. The χ^2 minimization was ensured by the use of nonlinear least squares routine. NEXAFS measurements on C and N K-edges were performed in Total Electron Yield (TEY) mode.

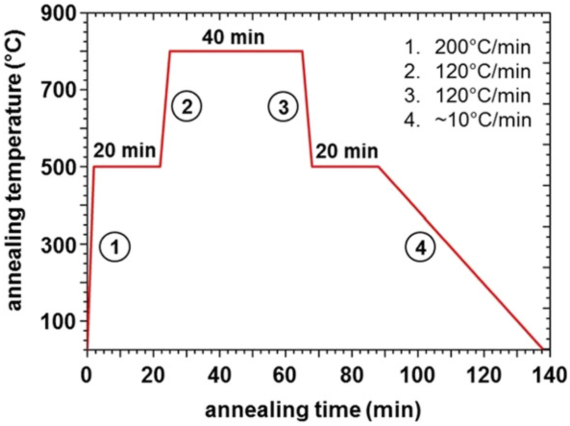

Fig. 1. Thermal annealing cycle carried out on the HOPG sample after the introduction in the UHV system.

3. Results and discussion

3.1. Characterization of N-doped HOPG

In this part, we will provide a detailed characterization of N-HOPG using synchrotron light-based techniques. Fig. 2 reports HR-PES data obtained on annealed HOPG, at Bach beamline. Fig. 2a reports the C 1s peak of HOPG, acquired with a photon energy of 595 eV. The peak shows a *Doniach–Sunjic* shape, with a FHWM of 0.35 eV. The high cleanliness of the surface and the low presence of defects is also highlighted by the survey scan reported in inset in Fig. 2a and by the NEXAFS measurements reported in Fig. 2b.

For the NEXAFS measurement acquired in p polarization mode (*out of plane*) it is possible to observe the typical 1s-π* sharp transition at 285.0 eV [20], whereas the 1s-σ* transitions (between 290 and 315 eV) can be measured in s polarization mode (*in plane*) [20].

The effect of the different implantation energies can be visualized by the LEED patterns reported in Fig. 3. The LEED pattern of the pure support (Fig. 3b) is a superposition of the diffraction patterns of the single orientational domains present in HOPG [21]; because ZYB grade HOPG has little distortion angles between adjacent mosaic tessellation (≈0.4°), the pattern is not characterized by single spots, but it assumes a circular geometry [16] due to the overlap of all the single domain diffraction spots (such as the *Debye–Scherrer* phenomenon that occurs in X-ray diffraction of powders, see Fig. 3a). Fig. 3c shows that the implantation at 100 eV leads to a weaker and more diffuse LEED pattern, because of partial surface amorphization with the consequent loss of crystalline order. On the other hand, ion implantation performed at higher energies (500 eV) generates a heavily amorphous surface [13,14], which eventually gives no diffraction. Thus, the surface does not show a LEED pattern, as shown in Fig. 3d.

In order to have a deeper physical insight into ion implantation procedure, Monte Carlo simulations of the N-implantation in HOPG have been carried out assuming the *Kinchin–Pease* modeling [22] of the ion-target atom interaction.

Under the experimental conditions of the N-implantation, performed by using common ion guns, the nitrogen plasma contains both N^+ and N_2^+ ionic species. By simulating the interaction of both the species with the carbon support and taking the average, Monte Carlo simulations give a *projected range*, R_p, and a *full width at half maximum* (FWHM) of the distribution, ΔR_p, equal to 7.9 Å and 10.3 Å for 100 eV implantation, and to 18.6 Å and 17.3 Å for implantation at 500 eV. Preliminary studies using standard photoemission and Monte Carlo simulations, demonstrated that it is possible to tune the projected range of the implanted atoms [13–15] and that no significant change occurs in the type or in the relative concentration of the chemical functionalities introduced by N implantation.

Fig. 4a and b reports the multipeak analysis of the C 1s and N 1s signals of the as-implanted N-HOPG, acquired in normal emission (NE) and grazing emission (GE) at Bach beamline (using a photon at 595 eV). The implantation was performed in situ at using 100 eV ions. In the case of C 1s, four components at binding energy (BE) of 283.7, 284.4, 285.5 and 286.5 eV, can be resolved. According to literature, they can be assigned to carbon vacancy (dangling bonds) [23,24], to sp^2 hybridized carbon forming the pure graphitic lattice, to sp^3

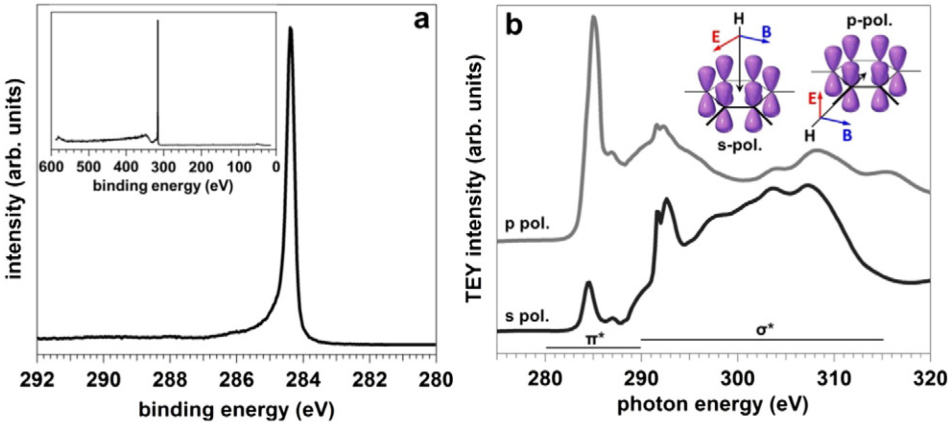

Fig. 2. a: C 1s HR-PES of annealed HOPG, acquired at 595 eV (the inset reports a wide survey scan); b: NEXAFS measurements of annealed HOPG acquired in s polarization (in plane) and p polarization (out of plane).

hybridized carbon from the partial surface amorphization induced by the ion implantation [25,26] and finally to C–N bonds [7,8,27], respectively. A fifth minor component, centered at about 288.1 eV can be associated with C bound to N and O (formally described as C–N(O)), due to low oxygen contamination of the preparation chamber or of the gas line providing the N_2 to the ion gun.

N-doping induces many different chemical defects in HOPG (the C–N signal counts for the 10.2% of the total C 1s photoemission line), whose characterization has been carried out by analyzing the N 1s HR-PE signal for the as-implanted HOPG, as reported in Fig. 4b. Five different components have been identified, whose FWHM and BE values are perfectly in agreement with literature data on related systems [4,5,8,13–15,30]. The components centered at 398.1 eV, 400.2 eV and 401.4 eV correspond to sp^2 C–N defects, which can be described as *pyridinic* [7,8,28,29], *pyrrolic* [7,8,15] and *N graphitic defects* [7,8,15,23], respectively. The component centered at 399.0 eV matches with –CN terminal groups [13,23,29]. Finally, the component centered at 402.8 eV can be attributed to a N^+ or N_2^+ ion species trapped into a carbon vacancy [20].

In order to observe the temperature evolution of these defects, C 1s and N 1s photoemission measurements at different annealing temperatures (at 500 °C and 750 °C) have been carried out. Every thermal cycle was 30 min long. The ratio of the area of each chemically shifted peak over the total core level signal area is shown in Fig. 5 and reported in Table 1. The most striking feature is the partial removal of the –CN groups as the annealing temperature increases (see also the change in the shape of the N 1s signal obtained after annealing at 500 °C and 750 °C, reported in Fig. 4d and f, which is due to the important decrease of the –CN related peak). This result is in agreement with previous works [30,31], where the authors report TPD measurements indicating that desorption of CN species (as HCN by H uptake from the residual H_2 in the UHV chamber) starts from 140 °C. It is important to highlight

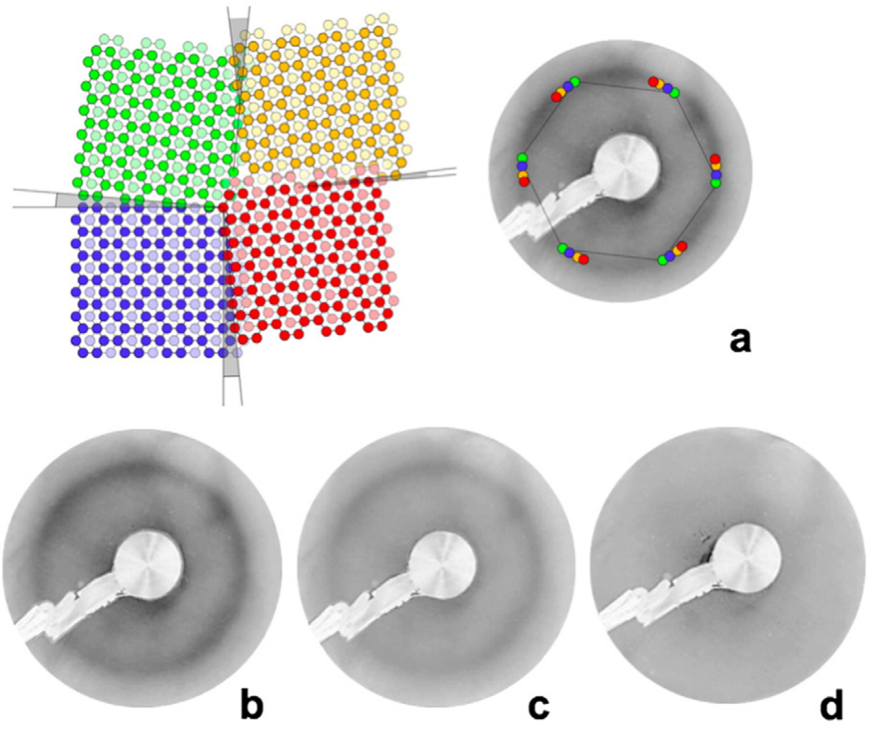

Fig. 3. a: Mechanism at the base of the formation of the “Debye–Scherrer” rings in the LEED pattern of HOPG. The shaded spheres indicate the second graphenic layer; b, c, and d: LEED patterns (acquired at 170 eV) of pristine HOPG and N-HOPG obtained by nitrogen implantation at 100 eV and 500 eV, respectively.

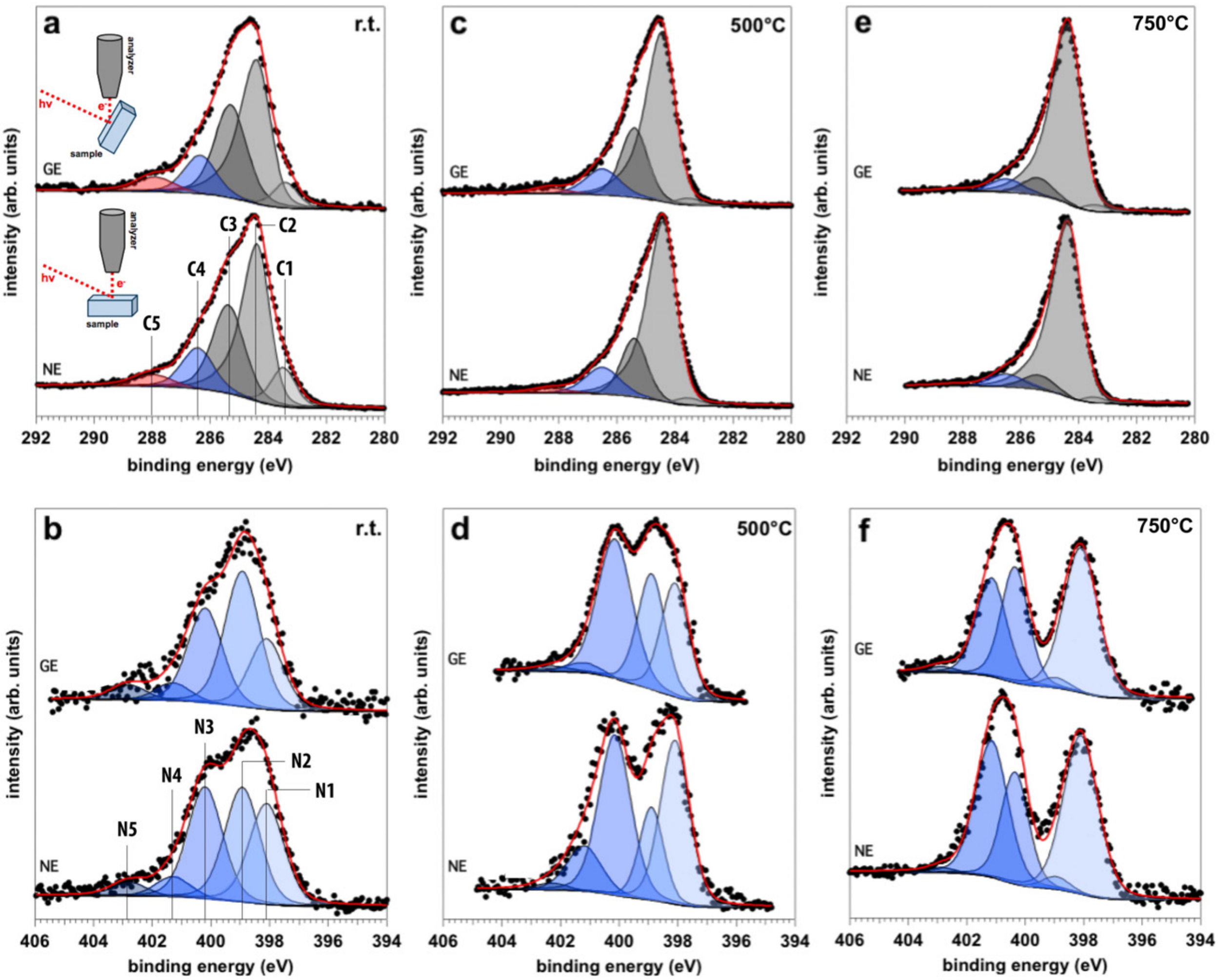

Fig. 4. Multipeak analysis of C 1s and N 1s core levels, for as-implanted N-HOPG (a, b) and annealed samples at 500 °C (c, d) and 750 °C (e, f).

that the removal of the –CN groups at 750 °C is not complete (even if the concentration undergoes to an important decrease). In fact, it is still possible to observe a weak –CN-related component in the N 1s photoemission line after the final annealing at high temperature. As reported in the following, we will discuss the influence of the –CN group presence on the electronic properties of the annealed N-HOPG. Another important consequence of the thermal annealing is the increase of the intensity of the *N substitutional* defects with the increase in the annealing temperature. This is in line with the higher thermodynamic stability exhibited by *graphitic* N compared to the other N-based configurations, thanks to the highest coordination of nitrogen with other C atoms. The same behavior has been observed in the case of the thermal treatment of N-doped graphene layers obtained by chemical vapor deposition [14].

As a general comment, it is interesting to highlight that the *pyrrolic* defects can be efficiently converted in *graphitic* defects upon thermal annealing at temperature higher than 500 °C [8,14]. As it possible to observe from Fig. 5 and Table 1, that the *pyridinic* defect concentration (together with the concentration of the other sp^2 C–N defects) undergoes an initial increase at 500 °C, as result of the general decrease in the overall N 1s signal due to the desorption of HCN and healing of the carbon vacancies with the consequent release of N_2. For temperature above 500 °C, the concentration of *graphitic* N increases since it is a product of the conversion of the *pyrrolic* defect, whose concentration undergoes an important decrease. Moreover, the thermal annealing cycles are accompanied by an important decrease in the surface amorphization (as evidenced by the decrease in the sp^3 C component), appreciable in particular at 750 °C. All these results consistently delineate a picture where HOPG modified surfaces can be used as model system where to investigate the impact of different C–N functional groups on specific electrochemical processes.

Another important observation can be discussed about the spatial localization of the N-based defects, from the angle resolved HR-PES measurements performed on the as-implanted and annealed N-HOPG. As it can be observed from Fig. 5 and Table 1, in the as-implanted sample the –CN defects are localized mainly in the first atomic layers constituting the HOPG surface, since the relative intensity of the –CN defect component is higher when the take-off angle approximates the GE condition (high surface sensitivity). On the other hand, with the exception of the *pyridinic* defect, whose concentration is higher close the R_p (Table 1), the other defects are homogeneously distributed in the sample. At high annealing temperature (i.e. 750 °C), Fig. 5 and Table 1 show that the *N-defects* distribution is quite uniform in the sample, with the exception of the *graphitic* N, whose concentration is higher closer to the topmost layer. Table 1 shows that the concentration trend of *pyrrolic* N is closely related to the one observed for the graphitic defect: for both NE and GE, the *pyrrolic* N concentration decreases about 18% by changing the annealing temperature from 500 °C to 750 °C, whereas the *graphitic* N concentration accordingly increases by the same amount.

To gain further insight into the site- and symmetry-specific electronic properties of the N-HOPG, NEXAFS measurements have been performed on as-prepared and annealed (at 750 °C) samples. It is well-known that NEXAFS can be successfully applied to explore the orientation and bond length of planar π-conjugated molecules adsorbed on a surface. Moreover, it was widely used to study the polarization

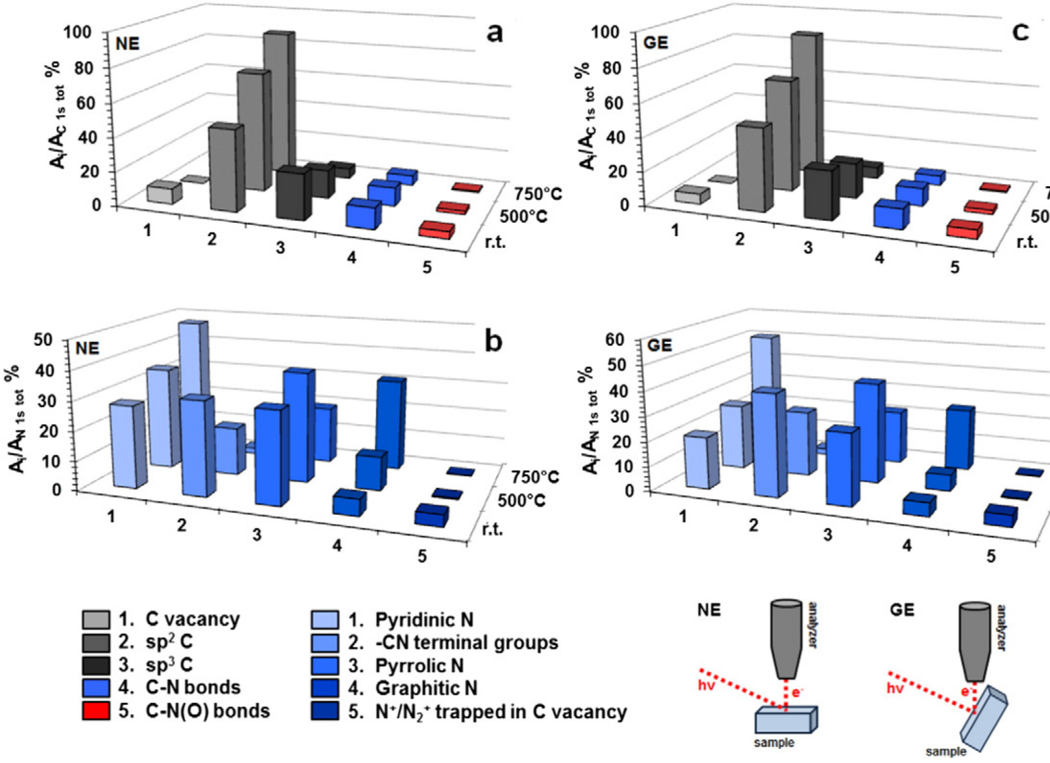

Fig. 5. Trend of the at.% of the single chemically shifted components for C 1s (a, c) and N 1s (b, d) photoemission peaks, as function of the annealing temperature. Subpanels a–b and c–d report the results obtained in case of normal emission (NE) and grazing emission (GE), respectively.

dependence of the π- and σ-resonances for graphene- and graphite-functionalized systems. Fig. 6 reports the polarization dependence of the NEXAFS spectra of C and N K edges. By the analysis of the N K edges, it is possible to observe a triplet centered between 399 eV and 402 eV, related to the N 1s-π* transition of different chemical states of N. The first feature, centered at 399.0 eV is associated with *pyridinic* N [15,32], while the third one (at 401.8 eV) represents *graphitic* N defects [15,26]. The second absorption peak is ascribed to the terminal –CN groups, as reported in literature [26], supporting the analysis discussed above. Interestingly, the *graphitic* N component intensity is strongly influenced by photon polarization, both for the as-implanted and annealed system, with the maximum value reached under *out of plane* conditions (thanks to the presence of the lone pair in a *sp* orbital hybridized with the π density). Differently, it is possible to observe that the –CN component intensity is only weakly influenced by the photon polarization, meaning that the –CN groups are characterized by a random orientation on the as-implanted surface. Moreover, although the C K edge spectra does not exhibit relevant differences before and after the thermal annealing cycle, the N K edge spectrum acquired in p polarization clearly show an enhancement of the *graphitic* N component after thermal annealing at 750 °C, in line with the HR-PES data reported above.

Table 1
Trend of the at.% of the single chemically shifted components for C 1s and N 1s photoemission peaks, as function of the annealing temperature and for the two normal (NE) and grazing emission (GE) geometries.

	r.t.		500 °C		750 °C	
	NE	GE	NE	GE	NE	GE
Carbon 1s						
C vacancy	9.04	5.96	0.40	0.35	0.21	0.16
sp^2	47.79	48.73	70.82	66.47	87.21	86.62
sp^3	26.71	28.43	16.16	20.40	5.95	6.69
C–N	12.33	11.74	10.73	10.40	5.89	5.76
C–N(O)	4.13	5.14	1.89	2.38	0.74	0.77
Nitrogen 1s						
Pyridinic	27.92	20.86	34.71	26.41	47.31	50.49
–CN terminal groups	31.77	40.86	16.17	26.23	2.00	2.36
Pyrrolic	30.97	28.47	37.32	40.41	19.36	21.65
Graphitic	5.51	5.33	11.37	6.56	31.10	25.18
N$^+$/N$_2^+$ trapped C vacancy	3.83	4.48	0.43	0.39	0.23	0.32

Finally, we also carried out VB-PES measurements using a photon at 190 eV, as reported in Fig. 7a. The spectrum of the pristine HOPG surface displays the typical graphite VB features, commonly described in terms of σ- and π-subbands [33a–d], as already introduced for the C K edge NEXAFS analysis. The σ-bands are formed from the intra-layer sp^2-hybridized 2s, 2p$_x$, and 2p$_y$ orbitals, while the π-bands arise from the overlapping 2p$_z$ orbitals which lie along the crystallographic axis *c*, normal to the layers (i.e. to the (0001) family planes). With respect to Fig. 7a, the features labelled as A and B centered at 2.7 eV and 4.0 eV below the Fermi level are attributed to the flat π-bands near the symmetry point Q, while the features C and D at 8.9 eV and 11.8 eV, respectively, are attributed to the flat σ-bands near the symmetry points Γ, along the Γ–Q and Γ–P directions within the graphite first Brillouin zone [33a–d]. Finally, the sharp peak at about 14.0 eV arises from the photoelectrons scattered into unoccupied states [33e].

On the other hand, the N-HOPG systems (both the as-prepared and the annealed surfaces) exhibits basically two different features: the first, centered at 4.0 eV below the Fermi level, corresponds to the B feature discussed above. The intensity of this feature increases accordingly to the increase of annealing temperature, due to the partial recovery of the surface amorphization caused by ion implantation [13,33a–c]. The second feature, centered at 7.0 eV below the Fermi level, is originated by the downward shift of the σ-bands at the Γ point, as a result of the local symmetry loss due to the replacement of C atoms with N atoms

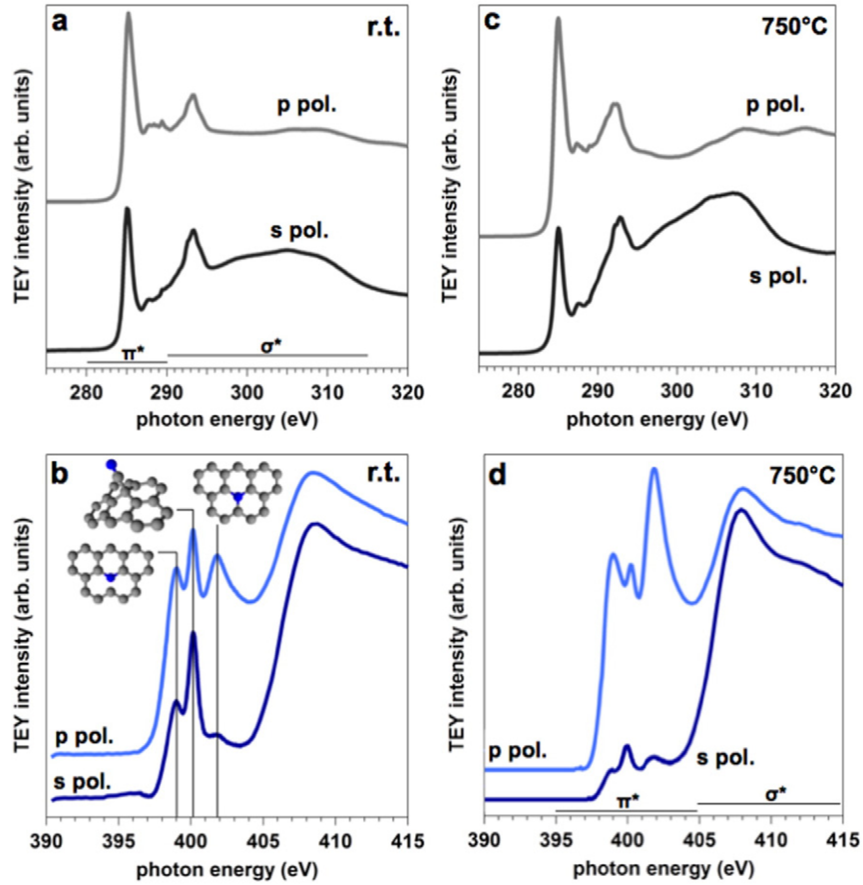

Fig. 6. NEXAFS measurements of C (a, c) and N K edges (b, d) on N-HOPG at different polarizations, for the as-implanted (a, b) and annealed (750 °C) system (c, d).

in the graphitic lattice. This assumption is confirmed by the fact that the intensity of this feature increases with the increase of the annealing temperature (i.e. with the increase of the N-*substitutional* defects as discussed above).

Finally, a new broad feature (centered between 18 and 20 eV) is introduced in the VB spectra upon N implantation. To identify the exact origin of this new peak (which undergoes to an upward shift by increasing the annealing temperature), we have acquired the VB on

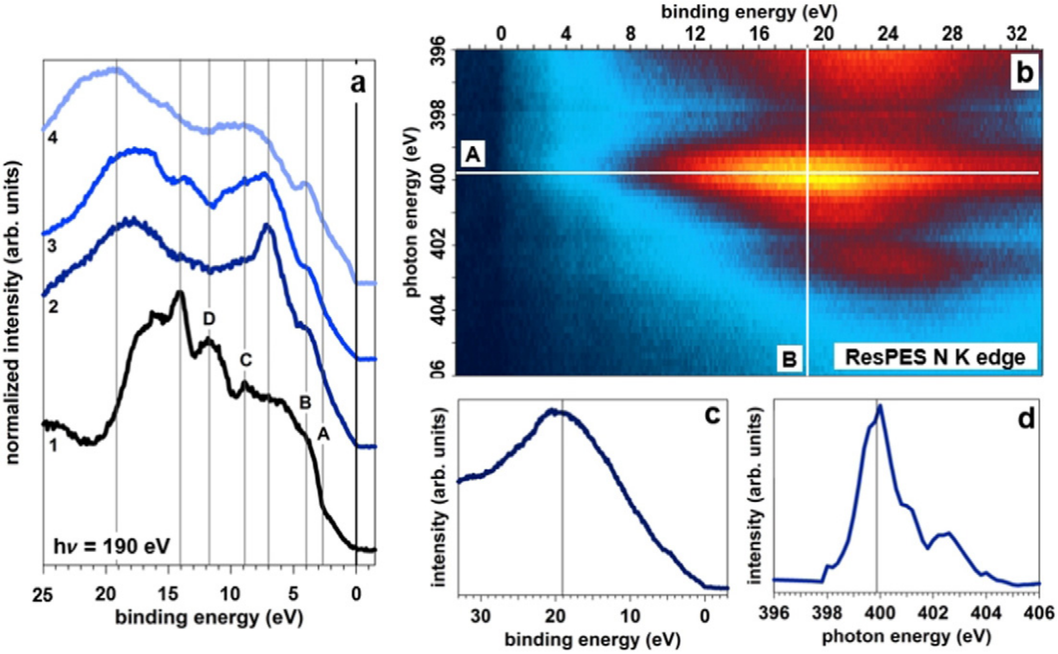

Fig. 7. a: Integrated area normalized-VB spectra acquired in normal emission mode using a photon energy of 190 eV (1: pristine HOPG; 2: as-implanted N-HOPG; 3: N-HOPG annealed at 500 °C; 4: N-HOPG annealed at 750 °C); b: ResPES measurements on the N K edge performed on the N-HOPG annealed at 750 °C; c: profile along the A line, showing the VB spectrum acquired on resonance, at about 400 eV; d: profile along the B line (across the resonance) as function of the photon energy.

the N-HOPG system (annealed at 750 °C) scanning over the photon energy on the same range of the N K edge. The result is reported in the 2D plot shown in Fig. 7b, which shows a strong resonance centered at 19 eV, excited by a photon energy of about 400 eV. A comparison between the spectra reported in Fig. 7a and in Fig. 7c (which reports the VB spectrum acquired at 400 eV), allows to observe a much higher intensity of the peak centered at 19 eV when the incoming photon is on resonance with the N K edge. Fig. 7d reports the resonant line profile obtained from the 2D plot as function of the photon energy: it fully resembles the NEXAFS spectra reported in Fig. 6d (since the N electron density of the *pyridinic* and *substitutional* defects is delocalized thanks to the hybridization with the π states of graphite, they are not affected by VB resonance phenomena). In particular, Fig. 7d shows the presence of the strong resonance peak centered at about 400 eV. By the comparison between these results and the N K edge NEXAFS measurements reported in Fig. 6, we can finally unambiguously point out that the observed resonance observed in the VB spectrum at 19 eV is due to residual presence of the –CN groups on the surface after the thermal annealing.

3.2. Characterization of a PdY nanoparticles deposited on pure and N-doped HOPG

Having in mind the goal described in Ref. [12], we then focused on the formation of PdY alloyed NPs, both on HOPG and N-HOPG. Pd and Y have been deposited in situ onto pure and N-HOPG during the beamtime at Elettra. The deposition of the two metals was performed sequentially, adding 0.25 MLE of Y to 0.75 MLE of Pd previously deposited on the substrate (pure or N-HOPG previously annealed at 750 °C) with a total coverage equal to 1.0 MLE. The deposition was performed while keeping the substrate at a constant temperature of 500 °C, followed by a final annealing at 750 °C for 10 min. The base pressure during the sample preparation and characterization was about $6 \cdot 10^{-9}$ mbar. From the HR-PE measurements, the Pd/Y ratio results to be about 2.9, very close to the stable alloy having a Pd_3Y stoichiometry [34].

As it is possible to observe from Fig. 8a, after the heat treatment, the Pd $3d_{5/2}$ peak of the stacked Y/Pd ultrathin films on pristine HOPG (dark blue curve in Fig. 8a) presents a downward shift with respect to the Pd ultrathin film case (gray curve in Fig. 8a), passing from 335.4 eV to about 335.1 eV, respectively. As it is already reported in literature, the spectral position of the Pd 3d level undergoes a slight downward shift when an alloy with a second transition metal (with lower electronegativity) is formed [35], due to a partial *d*–*d* band hybridization [36] which leads to a charge transfer from the less electronegative metal (in this case Y) to the more-electronegative Pd [36]. This is confirmed by the observation of a symmetrically opposite effect on the Y 3d photoemission line (Fig. 8b), whose $3d_{5/2}$ peak passes from 156.2 eV (in case of pure metal Y) to 156.5 eV (in the alloy). Such an evidence can be taken as a proof for the formation of the Pd_3Y alloy. It is important to outline that, according to our HR-PES data, the same phenomenology is observed both in the case of the deposition on the pristine HOPG and on the N-HOPG.

However, a major difference is observed when passing from the Pd_3Y/HOPG to the Pd_3Y/N-HOPG case: by the comparison between the Pd 3d spectral regions for the two (bright blue and gray curves in Fig. 8a), it is possible to observe a further Pd $3d_{5/2}$ component at higher BE (centered at 337.3 eV) on the N-modified support. This evidence is also confirmed when comparing the deposition of pure Pd NPs on both undoped and N-HOPG. Actually, a similar behavior was observed in a previous work on UHV deposited Pd NPs on N-HOPG using standard photoemission data [14]. We retain that the presence of surface nitrogen-based chemical defects triggers the formation of an additional component in the Pd 3d photoemission spectrum deriving from the coordination of Pd with highly electronegative N-groups, and it can be assigned to Pd^{4+} states localized at the interface between the metal NPs and the substrate surface rich in N-based centers. We demonstrate here that the same is true for Pd_3Y NPs on N-doped HOPG.

Interestingly, the detailed analysis of the Y 3d photoemission line reported in Fig. 8b shows the presence of oxide species (Y_2O_3) on both pure and N-HOPG (with a Y^{3+}/Y^0 ratio of 0.25 and 0.26, respectively). This is in line with previously reported data on RE/PGM alloyed NPs deposited by wet chemistry on a high surface area carbon support [37]. Interestingly, such an oxide component is observed also when operating in UHV, which demonstrates the extremely high affinity of Y toward oxygen, capable of scavanging the residual oxygen from the UHV chamber. This evidence suggests that the preparation of oxide-free RE/PGM alloyed NPs is extremely difficult, even with UHV techniques. However, the good news is that it has been demonstrated that this oxide component is not detrimental for the efficiency of the Y alloyed NPs as electrocatalyst for the oxygen reduction reaction [37].

Finally, we would like to comment on the morphology of the Pd_3Y NPs reported in this paper. Morphological characterization was not accessible during the experiments at the beamline. However, in previous papers we already studied by scanning tunneling microscopy the

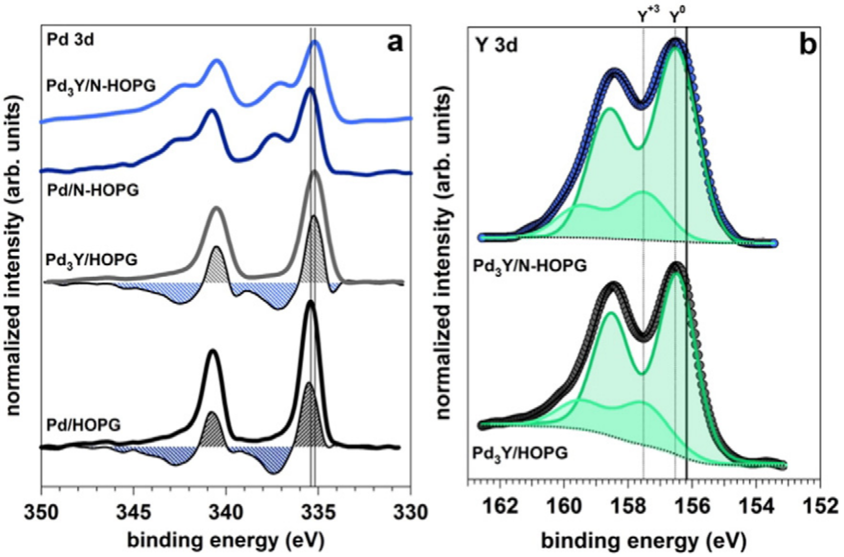

Fig. 8. Pd (a) and Y (b) 3d spectra (area normalized) acquired in normal emission mode for 1.0 MLE of Pd or stacked Y/Pd ultrathin films (after annealing at 750 °C) on HOPG and N-HOPG (using a photon energy of 595 eV). The reported difference spectra in (a) have been obtained by the subtraction of dark and bright blue curves from the black and gray curve, respectively.

growth morphology of Pd NPs grown in UHV on HOPG and N-HOPG, both at RT and at high temperature [14]. The Pd NP diameter was much lower on the N-HOPG support with respect to HOPG at RT, and a size difference is also maintained at 750 °C, indicating a drastic increase in the thermal stability of the Pd NPs against agglomeration when deposited onto N-HOPG. In the present experiments we needed to heat the Y/Pd ultrathin film at 750 °C in order to form alloyed Pd_3Y NPs. On the other hand, ex situ STM characterization was not possible because of the well-known easy oxidation of the Y component of the alloy into the corresponding oxide. Thence, the current electronic structure characterization of the Pd_3Y NPs cannot be easily associated with a specific morphology other than the one already reported for the Pd NPs on both HOPG and N-HOPG.

4. Conclusion

In this work we have performed a detailed analysis, based on synchrotron-related techniques, of the chemistry and electronic property modulation in HOPG upon nitrogen doping obtained by in-situ ion implantation. The advantage of this technique relies on the fact that it is possible to finely tune the doping dose, as well as the typology of the introduced chemical defects. We have demonstrated that it is possible to select different functional groups simply by adjusting the annealing temperature after the ion implantation.

The deposition of Pd_3Y alloy nanoparticles has been successfully obtained both on pure and on nitrogen-modified HOPG. We have demonstrated that, when the alloy is formed, a core level shift takes place, thanks to a partial *d*–*d* hybridization that leads to charge transfer between Y and Pd. The presence of this BE shift, supported by previous findings in literature, validates the heat-driven alloy formation from the Y/Pd ultrathin films.

Acknowledgments

MF acknowledges Fondazione Cariparo for financial support. We acknowledge also financial support from the Fuel Cell and Hydrogen Initiative-Joint Undertaking (FCH-JU) within the CathCat project under contract No. 303492.

References

[1] W.D. Callister, D.G. Rethiwisch, Materials science and engineering, Wiley & Co., 2010
[2] Y. Zhou, R. Pasquarelli, T. Holme, J. Berry, D. Ginley, R. O'Hayre, J. Mater. Chem. 19 (2009) 7830.
[3] X. Wang, X. Li, L. Zhang, Y. Yoon, P.K. Weber, H. Wang, J. Guo, H. Dai, Science 324 (2009) 768.
[4] L. Qu, Y. Liu, J.B. Baek, L. Dai, ACS Nano 4 (2010) 1321;
L. Feng, L. Yang, Z. Huang, J. Luo, M. Li, D. Wang, Y. Chen, Sci. Rep. 3 (2013) 3306.
[5] Z.H. Sheng, L. Shao, J.J. Chen, W.J. Bao, F.B. Wang, X.H. Xia, ACS Nano 5 (2011) 4350.
[6] Y. Shao, S. Zhang, M.H. Engelhard, G. Li, G. Shao, Y. Wang, J. Liu, I.A. Aksay, Y. Lin, J. Mater. Chem. 20 (2010) 7491.
[7] T. Kondo, T. Suzuki, J. Nakamura, J. Phys. Chem. Lett. 2 (2011) 577.
[8] M. Favaro, L. Ferrighi, G. Fazio, L. Colazzo, C. Di Valentin, C. Durante, F. Sedona, A. Gennaro, S. Agnoli, G. Granozzi, ACS Catal. 5 (2015) 129.
[9] S. Agnoli, G. Granozzi, Surf. Sci. 609 (2013) 1.
[10] C. Xu, X. Wand, J. Zu, J. Phys. Chem. C 112 (2008) 19841.
[11] Q. Li, N. Mahmood, J. Zhu, Y. Hou, S. Sun, Nano Toaday 9 (2014) 668.
[12] a. M. Escudero-Escribano, A. Verdaguer-Casadevall, P. Malacrida, U. Grønbjerg, B.P. Knudsen, A.K. Jepsen, J. Rossmeisl, I.E.L. Stephens, I. Chorkendorff, J. Am. Chem. Soc. 134 (2012) 16476;
b. I.E.L. Stephens, A.S. Bondarenko, U. Grønbjerg, J. Rossmeisl, I. Chorkendorff, Energy Environ. Sci. 5 (2012) 6744;
c. I.E.L. Stephens, I. Chorkendorff, Angew. Chem. Int. Ed. 50 (2011) 1476;
d. I.E.L. Stephens, A.S. Bondarenko, F.J. Pérez-Alonso, F. Calle-Vallejo, L. Bech, T.P. Johansson, A.K. Jepsen, R. Frydendal, B.P. Knudsen, J. Rossmeisl, I. Chorkendorff, J. Am. Chem. Soc. 133 (2011) 5485;
e. J. Greeley, I.E.L. Stephens, A.S. Bondarenko, T.P. Johansson, H.A. Hansen, T.F. Jaramillo, J. Rossmeisl, I. Chorkendorff, J.K. Nørskov, Nat. Chem. 1 (2009) 552.
[13] M. Favaro, L. Perini, S. Agnoli, C. Durante, G. Granozzi, A. Gennaro, Electrochim. Acta 88 (2013) 477.
[14] M. Favaro, S. Agnoli, L. Perini, C. Durante, A. Gennaro, G. Granozzi, Phys. Chem. Chem. Phys. 15 (2013) 2923.
[15] W. Ju, M. Favaro, C. Durante, S. Agnoli, O. Schneider, U. Stimming, G. Granozzi, Electrochim. Acta 141 (2014) 89.
[16] K. Wen, J. Marrow, B. Marsden, J. Nucl. Mater. 381 (2008) 199.
[17] S. Mrozowski, Phys. Rev. 85 (1952) 609.
[18] D.O. Demchenko, G.M. Sacha, M. Salmeron, L.-W. Wang, Surf. Sci. 602 (2008) 2552.
[19] F.H. Spedding, A.H. Daane, K.W. Herrmann, Acta Crystallogr. 9 (1956) 559.
[20] R.A. Rosenberg, P.J. Love, V. Rehn, Phys. Rev. B 33 (1986) 4034.
[21] A. Güttler, T. Zecho, J. Küppers, Chem. Phys. Lett. 395 (2004) 171.
[22] G.H. Kinchin, R.S. Pease, Rep. Prog. Phys. 18 (1995) 1.
[23] a. D.Q. Yang, E. Sacher, Surf. Sci. 531 (2003) 185;
b. D. Brete, D. Przyrembel, C. Eickhoff, R. Carley, W. Freyer, K. Reuter, C. Gahl, M. Weinelt, J. Phys. Condens. Matter 24 (2012) 394015.
[24] J.-A. Yan, M.Y. Chou, Phys. Rev. B 82 (2010) 125403.
[25] R.A.P. Smith, G.C. Smith, P. Weightman, J. Electron Spectrosc. Relat. Phenom. 152 (2006) 152.
[26] T.S. Wang, J.J. Ding, R. Cheng, H.B. Peng, X. Lu, Y.T. Zhao, Nucl. Inst. Methods Phys. Res. B 272 (2012) 15.
[27] C. Zhang, L. Fu, N. Liu, M. Liu, Y. Wang, Z. Liu, Adv. Mater. 23 (2011) 1020.
[28] D. Usachov, O. Vilkov, A. Grüneis, D. Haberer, A. Fedorov, V.K. Adamchuk, A.B. Preobrajenski, P. Dudin, A. Barinov, M. Oehzelt, C. Laubschat, D.V. Vyalikh, Nano Lett. 11 (2011) 5401.
[29] N. Hellgren, J. Guo, Y. Luo, C. Såthe, A. Agui, S. Kashtanov, J. Nordgren, H. Ågren, J.E. Sundgren, Thin Solid Films 471 (2005) 19.
[30] I. Kusunoki, M. Sakai, Y. Igari, S. Ishidzuka, T. Takami, T. Takaoka, M. Nishitani-Gamo, T. Ando, Surf. Sci. 492 (2001) 315.
[31] J.A. Taylor, G.M. Lancaster, J.W. Rabalais, J. Am. Chem. Soc. 100 (1978) 4441.
[32] X. Wang, Z. Hou, T. Ikeda, M. Oshima, M. Kakimoto, K. Terakura, J. Phys. Chem. A 117 (2013) 579.
[33] a. A. Mansour, P. Oelhafen, Appl. Phys. A 58 (1994) 437;
b. F.R. McFeely, S.P. Kowalczyk, L. Ley, R.G. Cavell, R.A. Pollak, D.A. Shirley, Phys. Rev. B 9 (1974) 5268;
c. A. Bianconi, S.B.M. Hagstrgm, R.Z. Bachrach, Phys. Rev. B 16 (1977) 5543;
d. R.F. Willis, B. Fitton, G.S. Painter, Phys. Rev. B 9 (1974) 1926;
e. R.F. Willis, B. Feuerbacher, B. Fitton, Phys. Lett. 34A (1971) 231.
[34] R.A. Alqasmi, S. Paasch, H.-J. Schaller, J. Alloys Comp. 283 (1999) 173.
[35] M.H. Seo, S.M. Choi, J.K. Seo, S.H. Noh, W.B. Kim, B. Han, Appl. Cat. B: Environ. 129 (2013) 163.
[36] M. Wakisaka, S. Mitsui, Y. Hirose, K. Kawashima, H. Uchida, M. Watanabe, J. Phys. Chem. B 110 (2006) 23489.
[37] Y. Luo, A. Habrioux, L. Calvillo, G. Granozzi, N. Alonso-Vante, Chem. Phys. Chem. 15 (2014) 2136.

ACS APPLIED MATERIALS & INTERFACES

Research Article

www.acsami.org

Metal–Support Interaction in Platinum and Palladium Nanoparticles Loaded on Nitrogen-Doped Mesoporous Carbon for Oxygen Reduction Reaction

Lorenzo Perini,[†] Christian Durante,*[,†] Marco Favaro,[†] Valentina Perazzolo,[†] Stefano Agnoli,[†] Oliver Schneider,[‡] Gaetano Granozzi,[†] and Armando Gennaro[†]

[†]Department of Chemical Sciences, University of Padua, Via Marzolo 1, 35131 Padova, Italy

[‡]Physik Department E 19, Institute of Informatics VI, Technische Universität München, Schleißheimerstr. 90a, 85748 Garching, Germany

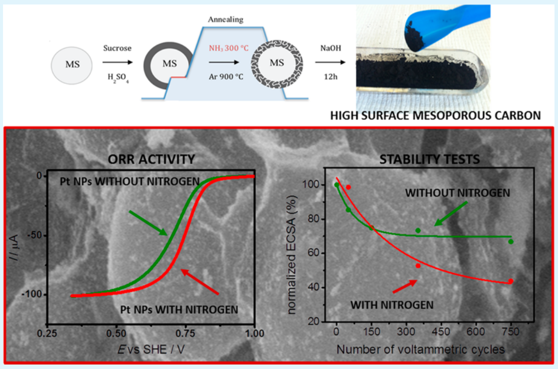

ABSTRACT: Mesoporous carbons are highly porous materials, which show large surface area, chemical inertness and electrochemical performances superior to traditional carbon material. In this study, we report the preparation of nitrogen-doped and undoped mesoporous carbons by an optimized hard template procedure employing silica as template, sucrose and ammonia as carbon and nitrogen source, respectively. Surface area measurements assert a value of 900 and 600 $m^2\ g^{-1}$ for the best doped and undoped samples, respectively. Such supports were then thoroughly characterized by surface science and electron microscopy tools. Afterward, they were decorated with Pt and Pd nanoparticles, and it was found that the presence of nitrogen defects plays a significant role in improving the metal particles dimension and dispersion. In fact, when doped supports are used, the resulting metal nanoparticles are smaller (2–4 nm) and less prone to aggregation. Photoemission measurements give evidence of a binding energy shift, which is consistent with the presence of an electronic interaction between nitrogen atoms and the metal nanoparticles, especially in the case of Pd. The catalytic properties of electrodes decorated with such catalyst/support systems were investigated by linear sweep voltammetry and by rotating disk electrode measurements, revealing excellent stability and good activity toward oxygen reduction reaction (ORR). In particular, although Pd nanoparticles always result in lower activity than Pt ones, both Pt and Pd electrodes based on the N-doped supports show an increased activity toward ORR with respect to the undoped ones. At the same mass loading, the Tafel slope and the stability test of the Pt@N-doped electrocatalysts indicate superior performances to that of a commercial Pt@C catalysts (30 wt % Pt on Vulcan XC-72, Johnson Matthey).

KEYWORDS: *mesoporous carbon, electrocatalysis, palladium, platinum, nitrogen doping, oxygen reduction reaction*

1. INTRODUCTION

Fuel cells and metal–air batteries are promising technologies, especially for automotive industries, due to their high energy densities, low operating temperature and environmental compatibility.[1,2] It is well-known that the slow kinetics of the oxygen reduction reaction (ORR) at the cathode limits the efficiency of fuel cells and metal–air batteries. So far, only platinum-based electrocatalysts have been found to be effective in final devices. However, Pt is expensive and its abundance in nature is not sufficient to sustain a widespread commercialization of fuel cells and metal–air batteries. Therefore, the synthesis of platinum-free electrocatalysts or the preparation of electrocatalysts with much lower content of the precious metal, preserving at least the same catalytic activity, is a current strategic issue. A viable way to reach the latter goal deals with the synthesis of new electrode support materials able to enhance the catalytic activity of the metal phase, while preserving the chemical and mechanical stability. In fact, the nature of the supports has a strong influence on some important properties of the catalyst, such as dispersion of the active phase, inhibition of sintering and loss of the catalyst during operation,[3,4] morphology of the metallic crystallites[5] and electrochemically active area.[6,7]

In recent years, there has been a growing interest in the synthesis of mesoporous carbon (MC) materials with well-controlled and well-defined morphologies and nanostructures.[8] MCs are promising materials because of their large surface area, tunable pore structure, uniform and adjustable pore size, mechanical stability, good conductivity and electrochemical performances superior to traditional carbon materials such as Acetylene Black, Vulcan XC-72R or Ketjen Black. Most of the known MCs have highly hydrophobic surfaces and a limited

Received: October 8, 2014
Accepted: December 19, 2014
Published: December 19, 2014

DOI: 10.1021/am506916y
ACS Appl. Mater. Interfaces 2015, 7, 1170–1179

number of specific active sites, which hinder their practical application as catalytic supports. It is well established in literature that the presence of a certain amount of surface oxygen groups can decrease the hydrophobicity of the carbon material, thus making its surface more accessible to the metal precursor during impregnation with aqueous solutions.[9,10] By doping with heteroatoms, the physical and chemical properties of carbon can be modified and new sites can even be created, which make the tailoring of the catalytic properties possible.[11] Among the various surface modification methods, nitrogen doping is currently in the spotlight because it is supposed that nitrogen induces a beneficial change on both the electronic and structural properties of the carbon supports. For example, changes in the surface polarity, electronic conductivity and electron-transfer tendency have been demonstrated to be beneficial to build improved electrode materials.[12] Furthermore, N-doped carbons resulted in some ORR catalytic activity even in the absence of metal loading, and even better performance and stability when mixed with Pt or non-Pt catalysts.[13−18]

In this work, we report the optimized synthesis of undoped and N-doped MCs (NMC) and their subsequent decoration with Pt or Pd nanoparticles (NPs). Sucrose and ammonia were used as sources of carbon and nitrogen, respectively, whereas Pd has been chosen as a possible substitute candidate for Pt as the active phase. The MC and NMC supports were thoroughly characterized by surface science and electron microscopy tools. The electrochemical activity toward ORR of the various materials, before and after Pd or Pt NPs decoration, was evaluated by linear sweep voltammetry using a rotating disk electrode setup. The effects of N-doping on the electrocatalytic activity are discussed.

2. EXPERIMENTAL SECTION

2.1. Chemicals. Mesoporous Silica (MS) (200 nm particle size, 4 nm pore size), sucrose (>99.5%), $PtCl_2$ (>99.9%), $PdSO_4$ (>98%), Nafion (5 wt % in EtOH) and $NaBH_4$ were purchased from Sigma-Aldrich and used as received without further purification.

2.2. Syntheses. MC samples were synthesized through impregnation of a P200 mesoporous silica template (1 g) with sucrose (1 g) and sulfuric acid (0.12 g), in water solution (5 mL). The mixture was dried in an oven at 100 °C for 6 h and then the temperature was increased to 160 °C overnight. During this pretreatment step, the carbonization starts and the color of the sample turned from white to brown. The powder was subsequently heated in a quartz tube to 900 °C for 5 h in Ar atmosphere to reach the complete carbonization of the sample. To optimize the synthesis, several heating rates from 2 to 20 $°C\ min^{-1}$ were tested.

The synthesis procedure for the NMCs is quite similar to the synthesis described above for the MCs. In this case, after the pretreatment, the temperature was not increased directly to 900 °C but a new step at 300 °C for 4 h under flow of pure ammonia was introduced. After the final heat treatment for both MC and NMC, the silica content was removed by dissolution with NaOH (1 M) solution in $EtOH/H_2O$ (50% v/v) for 24 h under vigorous stirring.

Pt or Pd NPs were loaded by reduction of the corresponding metal salts with $NaBH_4$ on MCs and NMCs. Initially, 5 mg of MC was dispersed in 2 mL of bidistilled water, then the metal salts solution (10 mg in 1 mL $EtOH/H_2O$ mixture 1/1 v/v) was added dropwise to the suspension under stirring). After 2 h at room temperature (r.t.), 1 mL of $NaBH_4$ was added and the solution was kept under stirring for 12 h to complete the reaction. The mixture was filtered on a nylon filter membrane (pore size 0.22 μm, Sigma-Aldrich), washed with bidistilled water and dried at 80 °C for 4 h.

2.3. Electrochemical Tests. The electrochemical activity measurements were carried out by cyclic voltammetry (CV) and rotating disk electrode (RDE) voltammetry, using an EG&G PAR Model 273/A potentiostat. A conventional three-electrode configuration consisting of a glassy carbon (GC) electrode with an area of 0.071 cm^2 as the working electrode, Pt as the counter electrode, and a satured calomel electrode (SCE) as the reference electrode, was used. The GC was polished to a mirror finish with silicon carbide papers of decreasing grain size (Struers, grit: 500, 1000, 2400, 4000) followed by diamond paste (3, 1, 0.25 μm particle size).

The catalyst inks were prepared by adding 2.5 mg of M@MC or M@NMC (M = Pd, Pt) in 2.5 mL of Nafion (5% in EtOH, Sigma-Aldrich) solution via ultrasonication for 10 min. Then 10 μL of suspension was carefully pipetted onto the clean GC electrode. After that, it was dried in air at room temperature for at least 8 h. For comparison, inks based on a commercial Pt catalyst (30 wt % Pt on Vulcan XC-72, Johnson Matthey) were used as a benchmark for both (N)MC-derived Pt and Pd catalysts.

The LSV and RDE study was carried out in 0.1 M H_2SO_4, and the solutions were purged with Ar before each measurement, whereas for the ORR test, the electrolyte was bubbled with high-purity O_2 gas for at least 30 min to ensure O_2 saturation. The determination of the number of transferred electrons was measured via the ring rotating (Pt) disk (GC) electrode (RRDE) technique (Metrohm Italiana Srl). The RRDE (disk diameter 5 mm), with a collection efficiency of 25%, was prepared by dropcasting 50 μL of the catalyst ink onto the surface of the GC disk with a Hamilton microliter syringe. The electrode was dried at ambient temperature for 12 h prior to immersion into the electrochemical cell for data acquisition.

2.4. Characterization. The specific surface areas of the samples were calculated by a multipoint Brunauer−Emmett−Teller (BET) analysis of the nitrogen adsorption/desorption isotherms, whereas the pore size distribution curves were derived from the Barret−Joyner−Halenda (BJH) method (for mesopores) and the Horvath−Kawazoe (HK) method (for micropores), by using the adsorption/desorption branches.

X-ray photoemission spectroscopy (XPS) measurements were performed in an UHV chamber (base pressure $< 5 \times 10^{-9}$ mbar), equipped with a double anode X-ray source (PSP), a hemispherical electronanalyzer (VG Scienta) at r.t., using nonmonochromatized Mg Kα radiation ($h\nu = 1253.6$ eV) and a pass energy of 50 and 20 eV for the survey and the single spectral windows, respectively. The calibration of the Binding Energy (BE) scale was carried out using Au 4f as reference (BE Au 4f = 84.0 eV).

For the characterization of the NMCs, the nitrogen amount was determined by normalizing the intensity of the N 1s XPS peak to the integrated area of the C 1s photoemission peak (both corrected for the differential cross section and inelastic mean free path of photoelectrons), obtaining a nitrogen concentration of 5.7 at% for the best sample (see below). The XPS peaks of carbon and nitrogen were separated into single chemical shifted components (after Shirley background removal), using symmetrical Voigt functions; the χ^2 was minimized by the use of a nonlinear least-squares routine.

To perform XPS measurements, 2.5 mg of the M@MC or M@NMC powders was dispersed in 50 μL of toluene and then gently sonicated (for 5 min) in order to efficiently disperse the powders; the solutions were then drop-casted onto electropolished polycrystalline copper or GC substrates (with a surface area of 1 cm^2). Thereafter, the samples were first dried overnight under nitrogen flux to obtain homogeneous films; then they were vacuum-dried for 2 h at about 10^{-6} mbar.

For the Raman characterization, we used a ThermoFisher DXR Raman spectrometer. All spectra were recorded using a laser with an excitation wavelength of 532 nm (1.5 mW), focused on the sample with a 50× objective (Olympus). Thermogravimetric analysis (TGA) was carried out with a Q5000IR TGA instrument (TA Waters). The samples were exposed to air and their mass was recorded while the temperature was raised from r.t. to 1000 °C. After the complete oxidation of the carbon structure to gaseous products, metal and silica residues were left.

Scanning electron microscopy (SEM) and transmission electron microscopy (TEM) images were obtained using a Zeiss Supra 35VP

Gemini scanning electron microscope operating at 5 kV and a FEI Tecnai G2 transmission electron microscope operating at 100 kV.

3. RESULTS AND DISCUSSION

3.1. Characterization of MCs and NMCs. The samples investigated in the present paper are reported in Table 1, where also the different experimental conditions to obtain them are specified together with the data obtained by BET and BJH. The nitrogen-adsorption isotherms of MC prepared with a temperature ramp of 2 °C min^{-1} (MC-2) are presented in Figure 1a: according to IUPAC classification, the isotherms are of type IV. The hysteresis is indicative of the presence of mesopores (2−50 nm diameter), whereas the pore size distribution can be calculated from the BJH adsorption isotherm reported in Figure 1b. The specific BET surface area, specific pore volume (V_p) and the pore diameters (D_p) of the MC-2 are summarized in Table. 1, along with the other MCs obtained in different experimental conditions. MC-2 exhibits 914 m^2 g^{-1} of ultrahigh specific BET surface area and 3.0 cm^3 g^{-1} of specific pore volume. The BJH method (Figure 1b) furnishes an average pore diameter of mesopores and micropores around 3 and 1 nm, respectively (Table 1). Figure 1c,d show the effect of the temperature scan rate on the surface area and pore size distribution. Although the specific surface area (Table 1) decreases from 914 to 765 m^2 g^{-1} (16.3%) with the increase of heating rate from 2 to 20 °C min^{-1}, the average pore diameter of mesopores and micropores is constant with a value around 3 and 1 nm, respectively (Figure 1d). This means that the number of pores is the parameter varying with the heating rate: at low heating rate the number of pores results to be higher than the one obtained under higher heating rates.

Table 1. BET Surface Area and Pore Structure Parameters of Different MCs and NMCs

sample[a]	BET surface area (m^2/g)	pore volume (cm^3/g)	BJH pore size (nm)	H−K pore size (nm)
MC-2	914	0.30	3.1	1.2
MC-5	857	0.31	3.1	0.9
MC-10	856	0.31	3.2	1.1
MC-20	765	0.27	3.1	1.0
NMC-2	608	0.29	3.0	0.9

[a] Numbers stand for the heating rate express in °C min^{-1}.

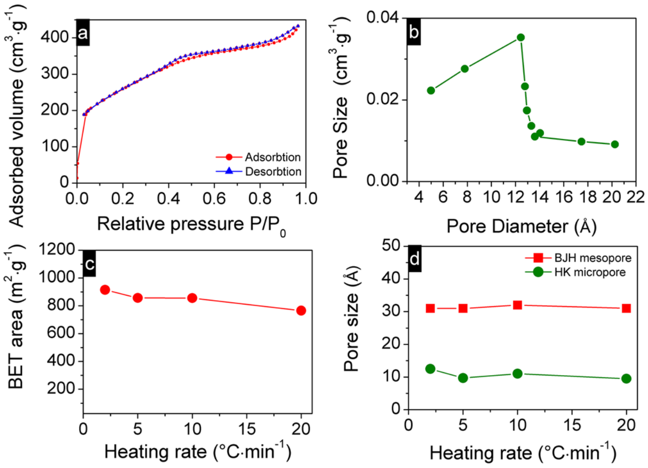

Figure 1. (a) Nitrogen adsorption/desorption isotherms of MC pyrolized at 2 °C min^{-1}; (b) BJH pore-size distribution in MC-2; (c) BET areas at different heating rates; (d) BJH and HK pore size distribution at different heating rates. The fitting error associated with the employed DFT model is less than 0.3%.

On the basis of these observations, N-doped mesoporous carbon (NMC-2) was prepared at a low heating rate in the very same experimental conditions as MC-2, but an additional step was inserted where ammonia was allowed to flow at 300 °C. NMC-2 exhibits an isotherm type IV (IUPAC), corresponding to a BET surface area of 608 m^2 g^{-1} and meso- and micropores of similar size as in MC-2 (Table 1). The NMC-2 surface area is only 2/3 of the one of MC-2; however, it is still much higher than that of the commercial standard Vulcan XC-72R (222 m^2 g^{-1}).[19] Because the pore structure parameters of NMC-2 and MC-2 are similar (Table 1), a possible explanation of this BET surface area reduction upon N-doping, could be referred to a partial collapse of the silica pores structure after ammonia reaction with silica. In fact, the collapse of the structure upon the template removal would end up in a general loss of the number of pores.

The SEM images of MC-2 and NMC-2 are presented in Figures 2a,b, respectively. Both samples consist of hollow spherical carbon particles, as good replica of the templating silica, along with other collapsed and fractured particles that give rise to a heterogeneous morphology. The average diameter of the spheres is about 300−400 nm. A more detailed structural study of NMC-2 was carried out with TEM measurements, which point out the presence of spherical carbon particles (Figures 2c,d). Pores are randomly located to construct the whole sphere, achieving a loosely packed nanostructure. In fact, several three-dimensionally interconnected bright spots can be observed on the sphere surfaces indicating the presence of mesopores, whereas the dark contrast that characterizes the edges confirms their hollow nature (Figure 2d).

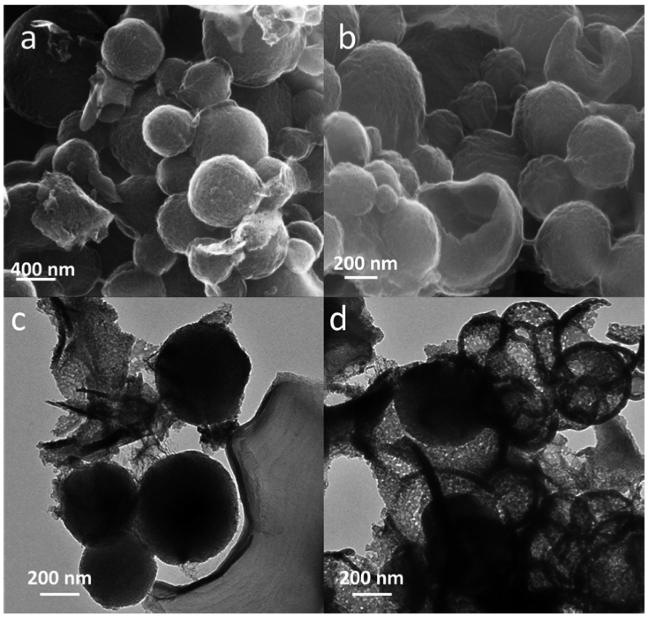

Figure 2. Representative SEM images for (a) MC-2 and (b) NMC-2. (c, d) TEM images of NMC-2.

To characterize the surface chemistry of the studied systems, we carried out an XPS investigation. Figures 3a,b report wide range measurements acquired for MC-2 and NMC-2 samples,

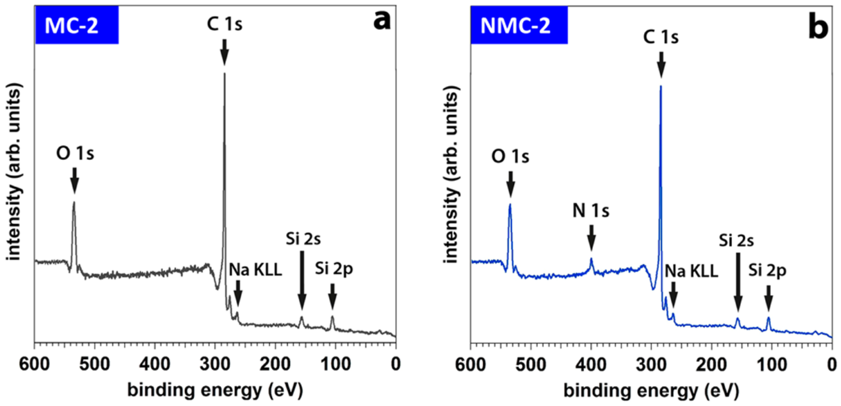

Figure 3. XPS survey spectra for (a) MC-2 and (b) NMC-2.

Table 2. Elemental Analysis Derived from XPS Measurements, for MC-2 and NMC-2

	Si (%$_{at}$)	Na (%$_{at}$)	C (%$_{at}$)	N (%$_{at}$)	O (%$_{at}$)
MC-2	4.1	0.8	80.3		14.8
NMC-2	3.7	0.8	75.8	5.7	14.0

respectively, and the corresponding elemental surface stoichiometries are reported in Table 3. Both survey spectra exhibit the photoionization peaks of C 1s (284.6 eV) and O 1s (533.7 eV) core levels, whereas only NMC-2 samples show the N 1s photoemission peak (399.4 eV). The nitrogen concentration in NMC-2 is 5.7 at. % (Table 2). Furthermore, XPS reveals traces of contamination from the templating silica and from the concentrated NaOH solution used to dissolve the templating agent. The trace of silica can be completely removed by a prolonged washing in EtOH/NaOH solution followed by the rinse with abundant bidistilled water.

To get a more precise description of the chemical identity of the functional groups present on MC-2 and on NMC-2, the C 1s and N 1s energy regions were acquired at high resolution and the corresponding peaks were fitted with Voigt functions, imposing a full width at half-maximum (FWHM) in the range of 1.0−1.4 eV. Figure 4 reports the multipeak analysis of the C 1s and N 1s signals for MC-2 and NMC-2, together with ball and stick models of the different chemical species identified. Concerning MC-2, we can distinguish five different components in the deconvolution of the C 1s photoemission spectrum: the main component (which constitutes 72% of the signal), centered at 284.5 eV, represents the sp^2-hybridized carbon (Csp^2) forming the graphitic lattice. The component centered at 285.5 eV is due to sp^3-hybridized carbon (Csp^3), which constitutes tetragonally coordinated carbon clusters and C—H bonds,[20,21] while the third and fourth components at 286.4 and 288.0 eV, respectively, are related to C—OH bonds and carbonyl (−C═O) groups. For a correct fitting procedure, it is also necessary to introduce a small component in the low-energy tail, which is related to C atoms around vacancy sites (BE = 283.7 eV).[22]

Interestingly, the C 1s spectrum of NMC-2 (Figure 4c) shows a significant increase of the Csp^3 component, which can be associated with the formation of amorphous carbon. In fact, this side reaction is promoted by the low temperature treatment in ammonia (4 h, 300 °C), performed on the MC precursor in order to obtain the N-doping. Concerning the component centered at 286.4 eV, it is not possible to distinguish the contribution of the C—OH groups from that of the C—N bonds, which are known to give a characteristic signal centered at 286.6 eV.[23] Moreover, the carbonyl component at 288.0 eV overlaps that of the −N—C—OH groups.[24] The new component at the high BE tail (BE = 289.0 eV) can be related to the presence of strong electron-withdrawing groups, such as formamide-like fragments (−N—C═O).[24] Table 3 summarizes the results and makes a comparison between the fits of the different C 1s spectra.

The nitrogen functional groups characterization was carried out by analyzing the N 1s XPS signals, as reported in Figure 4d. Seven different components were identified,[25] with the main peaks centered at 398.1, 399.0, 400.3 and 401.2 eV, which can be described as pyridinic groups,[24,26] amine groups,[22,24] pyrrolic groups[25] and graphitic N,[25] respectively. According to the literature, in order to fit a curve consistently with the experimental data, we added three components centered at 402.5, 403.7 and 404.8 eV, in the high-energy tail of the N 1s spectrum. These are associated with quaternary nitrogen groups (402.5 eV), N—C—OH[27] and N—C═OH[27] groups (403.7 eV), and highly oxidized nitrogen groups[27] (404.8 eV), such as NO$_x$ groups, even though in limited amount.

Figure 5 compares Raman spectra of MC-2 and NMC-2; the analysis of the peak positions and intensities gives information

Table 3. Results of the Fitting Procedure Performed on the C 1s Spectra Related to MC-2 (left) and NMC-2 (right)[a]

MC-2	A_i/A_{tot} (%)	NMC-2	A_i/A_{tot} (%)
C vacancy (BE = 283.7 eV, Δ = 1.3 eV)	6.6	C vacancy (BE = 283.7 eV, Δ = 1.3 eV)	6.8
Csp^2 (284.5 eV, Δ = 1.3 eV)	72.3	Csp^2 (BE = 284.5 eV, Δ = 1.3 eV)	57.3
C—H (Csp^3) (BE = 285.5 eV, Δ = 1.1 eV)	11.8	C—H (Csp^3) (BE = 285.5 eV, Δ = 1.2 eV)	16.4
C—OH (BE = 286.4 eV, Δ = 1.3 eV)	7.1	C—OH/C—N bonds (BE = 286.5 eV, Δ = 1.3 eV)	14.7
C═O (BE = 288.0 eV, Δ = 1.2 eV)	2.2	C═O/−N—C—OH (BE = 288.0 eV, Δ = 1.3 eV)	2.7
		−N—C═O (BE = 289.0 eV, Δ = 1.2 eV)	2.1

[a] The percentages of each single component are normalized to the total integrated area of the C 1s spectrum. Δ is the FWHM of each component.

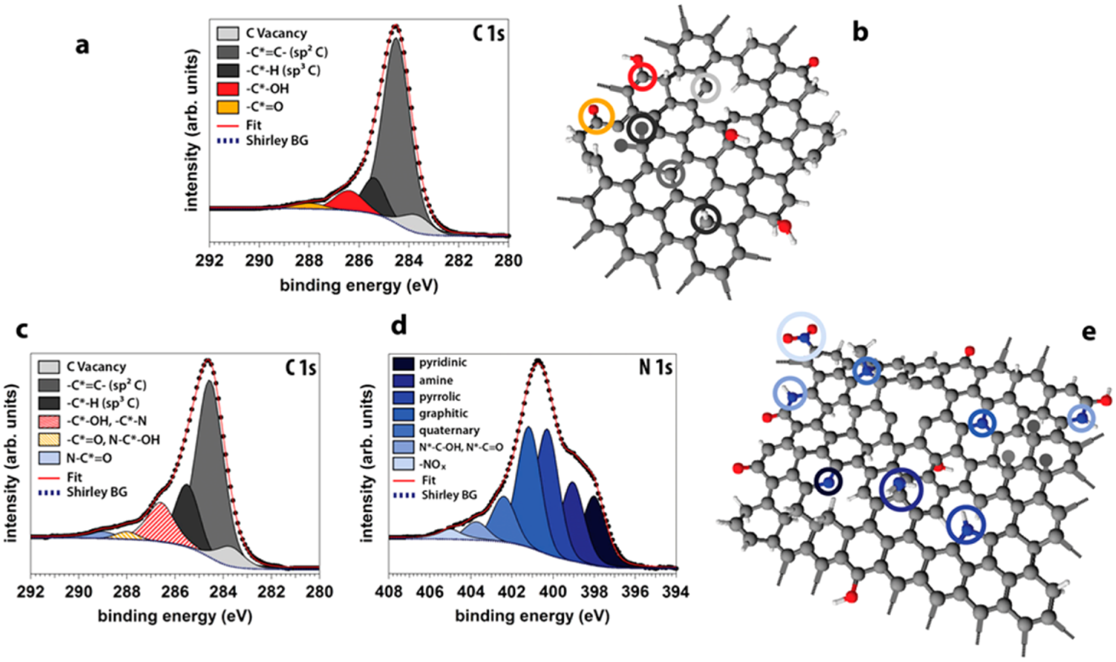

Figure 4. XPS detailed study of (a) MC-2 and (c, d) NMC-2. Modeling of the surface functional groups (b) MC and (e) NMC.

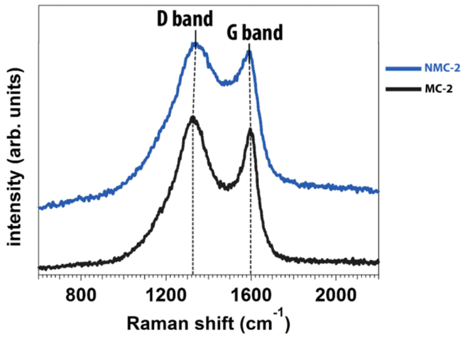

Figure 5. Raman spectra for MC-2 and NMC-2.

about the changes of the atomic structure of the samples. The two intense bands observed at 1600 and at 1325 cm^{-1} are the G band[28] (tangential vibration mode, E_{2g} symmetry group) and the D band,[28] also known as disorder vibration mode (belonging to the A_{1g} symmetry group), respectively. The latter is observable only in the presence of defects that lead to a local breakdown of the D_{6h} symmetry of the graphitic honeycomb lattice[28] (such as sp^3 carbon or dopant atoms). Compared to undoped MC, the NMC sample shows a significant increase in structural disorder, as evidenced by the increase and the broadening of the D band. This is in agreement with the previous XPS observations; in fact, the evolution of the D band with the doping is due to both the increase of the Csp^3 and the doping of the carbon structure. Moreover, it is found that in NMC-2 the G band shifts from 1593 to 1589 cm^{-1} and the D band moves from 1330 to 1321 cm^{-1} in comparison to those of the mesoporous carbon MC-2, which can be ascribed to the incorporation of nitrogen into the carbon matrix.[29]

3.2. Characterization of Metal Loaded-MC and NMC.

Nanoparticles from different metal salts ($PdSO_4$, $PtCl_2$) were loaded on undoped (Pd@MC-2, Pt@MC-2) and doped (Pd@NMC-2, Pt@NMC-2) samples by a simple chemical reduction method with sodium borohydride ($NaBH_4$) as the reducing agent. TEM images of Pt@MC-2 (Figure 6a) and Pt@NMC-2 (Figure 6c) clearly show that Pt NPs with high loading are uniformly dispersed throughout the samples. The corresponding particle size distribution histograms (Figures 6b,d) were obtained by calculating the size of more than 50 randomly selected particles in the magnified TEM images. For Pt@MC-2 and Pt@NMC-2 samples, the mean Pt particle size diameter is ca. 1.7 and 1.3 nm, respectively, and the NPs were well dispersed on the surface of pristine and doped MC. However, the formation of some Pt aggregates (>8 nm) can be clearly seen, especially in the case of Pt@MC-2, suggesting that the nitrogen surface doping is helpful to stabilize Pt NPs on Pt@NMC-2. Regarding Pd NPs supported on MC-2 (Figure 6e), the size distribution histogram (Figure 6f) shows an average diameter of ca. 5–6 nm. When Pd NPs nucleate and grow on NMC-2 (Figure 6g), the particle size diameter decreases to 2–3 nm (Figure 6h). In this case, Pd agglomerates are still present though to a lesser extent than in Pd@MC-2. It is evident that the presence of homogeneously distributed nitrogen functional groups can provide nucleation sites and thus promote a higher dispersion of metal NPs. Furthermore, nitrogen doping results in an improvement of hydrophilicity and wettability of NMC-2. The enhanced access of solvated and charged metal precursor ions to the NMC-2 surface can be associated with the superior dispersion of metal NPs and it effectively prevents agglomeration.[30] It is also known that nitrogen functional groups can increase the interaction between metal NPs and the substrate, immobilizing Pt or Pd NPs.[18,31] This has been confirmed also for Pt and Pd NPs deposited on N-doped HOPG[4,32,33] CNTs[30] and N-doped GC.[5] Figure 7 reports the XPS Pd 3d and Pt 4f spectral regions of samples deposited on MC-2 and NMC-2. As can be observed, the photoemission spectra of the metals show significant peak broadening when they are deposited on NMC-2. This can be explained by the formation of oxidized metal species over the nitrogen sites. Moreover, a BE shift of the signals takes place after the deposition on NMC-2 and this is particularly evident in the case of Pd@NMC-2 (Figure 7a). For

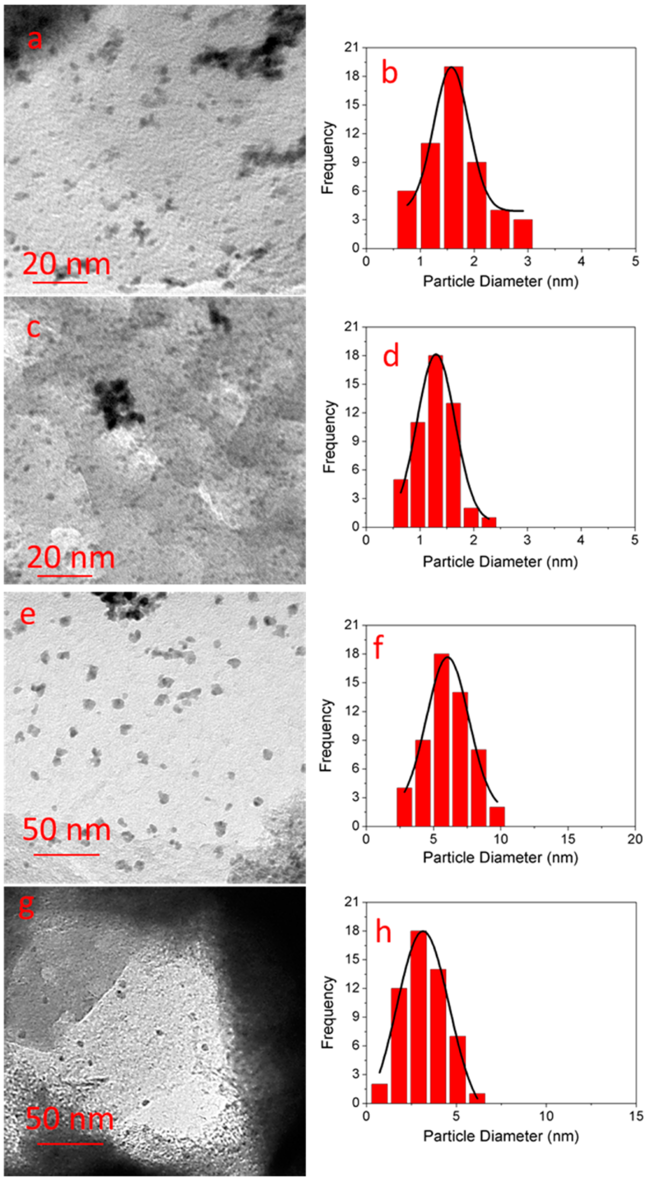

Figure 6. TEM images and size distribution of Pt@MC-2 (a and b), Pt@NMC-2 (c and d), Pd@MC-2 (e and f) and Pd@NMC-2 (g and h).

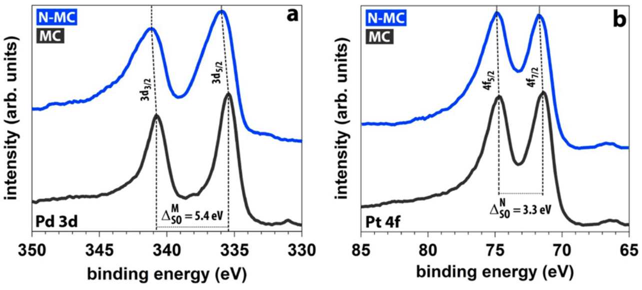

Figure 7. Pd 3d (a) and Pt 4f (b) XPS regions of M@MC and M@NMC (M= Pd, Pt).

Pt, it was reported that the addition of nitrogen to the support induces a BE shift that is proportional to the number and proximity of nitrogen atoms to the carbon−platinum bond and that it is a result of the destabilization induced by nitrogen atoms on the delocalized double bond present in the undoped structure.[31,34] Table 4 summarizes the values of BEs and FWHMs of the photoemission peaks recorded for Pt and Pd deposited on both MC-2 and NMC-2. The metal loading was evaluated by XPS analysis to be ca. 30 wt % for each sample; this result was confirmed also by thermogravimetric analysis (TGA).

Table 4. BE and FWHM of XPS signals of Pd and Pt deposited on MC-2 and NMC-2

	MC-2		NMC-2	
	BE (eV)	FWHM (eV)	BE (eV)	FWHM (eV)
Pd $3d_{5/2}$	335.4	1.7	336.0	2.9
Pt $4f_{7/2}$	71.3	1.4	71.6	1.7

3.3. Electrochemical Analyses. The electrochemical properties of pure MC-2 and NMC-2 were examined by cyclic voltammetry (CV) in Ar purged 0.1 M H_2SO_4 solution at a scan rate of 200 mV s^{-1} (Figures 8a,b). NMC-2 shows an increased capacitance with respect to MC-2; it is commonly known that nitrogen doping improves the capacitive behavior of carbon materials and this is generally attributed to the electron donor capability of nitrogen atoms.[35,36] Specifically, the strong electron donor nature of nitrogen atoms promotes reinforcement in π bonding, enhancing wettability of the material at the electrode/electrolyte interface. Therefore, the presence of nitrogen functional groups induces a pseudocapacitive effect,[37] caused by the increased adsorption of proton and electrolyte ions in the electrical double layer.[38]

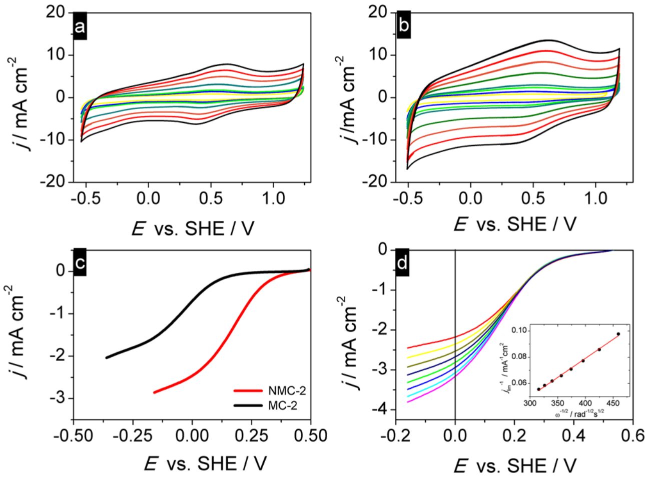

Figure 8. Cyclic voltammetry at different scan rates in 0.1 M H_2SO_4 on (a) MC-2 and (b) NMC-2. (c) RDE linear sweep voltammetry curves on MC-2 and NMC-2 modified GC electrode in O_2-saturated 0.1 M H_2SO_4 solution. Scan rate 10 mV s^{-1}. (d) RDE linear sweep voltammetry curves on NMC-2 at different rotation rates in the range 1000−3100 rpm/s in O_2-saturated 0.1 M H_2SO_4 solution at scan rate of 10 mV s^{-1}. The inset reports the corresponding Koutecky−Levich plot at 0.0 V vs SHE.

A well-defined quasi-reversible redox peak couple was observed on both MC-2 and NMC-2 in the potential range of 0.75 and 0.25 V vs SHE. The presence of these peaks may be ascribed to redox active surface oxygen functional groups such as hydroquinone/quinone, which usually undergo proton coupled electron transfer. This type of surface electrochemistry behavior can be found in other type of mesoporous carbon and carbon nanotubes modified electrodes.[39,40]

The linear sweep voltammetry (LSV) with a rotating disk electrode (RDE) was undertaken at different rotating rates from 1000 to 3100 rpm in an O_2-saturated 0.1 M H_2SO_4 solution, at a scan rate of 5 mV s^{-1} in order to ensure a steady-state condition (Figure 8c). Both MC-2 and NMC-2 show mixed kinetic and mass transport control, but the influence of mass transport becomes visible at much lower potentials for MC, in a region where thermodynamically other reactions like hydrogen evolution could take place. An ideal plateau was not fully reached in these experiments but clearly approached at all rotation rates for NMC-2 (Figure 8d). NMC-2 approached the plateau of diffusion-limiting currents below −0.1 V vs SHE, and showed an onset reduction potential for O_2 at 0.33 V vs SHE almost 300 mV more positive than that of MC-2. Such a difference in the onset potential between the two materials highlights a pronounced electrocatalytic activity of NMC-2 for oxygen reduction with respect to the undoped MC-2. The improved catalytic activity of nitrogen doped carbon based electrodes toward ORR is a well-established effect although the actual mechanisms involved in the reaction are not well understood to date.[41] The effect is generally ascribed to the n-type dopant character of nitrogen, which allows a faster adsorption of oxygen molecules on carbon atoms that are next neighbors to the nitrogen doping atoms, in particular those placed in a substitutional, pyridinic or pyrrolic position.[42−46] To investigate the mechanism of the electron transfer process, we used the Koutecky−Levich (K-L) plot (Figure 8d inset), which was obtained from the polarization curves at various rotation rates (Figure 8d).

$$\frac{1}{j}=\frac{1}{j_k}+\frac{1}{j_d}=\frac{1}{nFkC_{O_2}}+\frac{1}{0.62nF(D_{O_2})^{2/3}\nu^{-1/6}C_{O_2}\omega^{1/2}} \quad (1)$$

In the K-L equation j is the measured current density, j_k and j_d are the kinetic and diffusion-limited current densities, respectively, n is the number of electrons transferred per O_2 molecule, k is the rate constant for O_2 reduction, F is the Faraday constant (96 485 C mol^{-1}), ω is the rotation rate, C_{O_2} is the concentration of oxygen in the bulk (1.1×10^{-6} mol cm^{-3}),[47] D_{O_2} is the diffusion coefficient of oxygen (1.4×10^{-5} cm^2 s^{-1})[48] and ν is the kinematic viscosity of the solution (0.01 cm^2 s^{-1}).[48] The geometric surface area (0.0706 cm^2) was considered in the calculation. The slope of the straight line (Figure 8d inset) allows us to assess the number of electrons involved in the ORR. The experimentally determined number of electrons is 3.47 at 0.0 V vs SHE for NMC-2, which indicates that the four-electron process leading directly to water is the favored reduction mechanism.

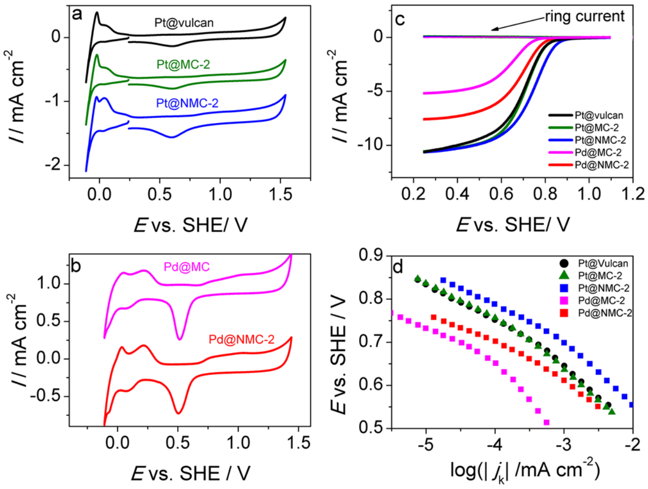

Figure 9. (a,b) Cyclic voltammetry of the electrocatalysts in an oxygen-free 0.1 M H_2SO_4, scan rate 100 mV s^{-1}. (c) RRDE linear sweep voltammetry curves on Pt@vulcan, M@MC-2 and M@NMC-2 (M = Pt, Pd) in O_2-saturated 0.1 M H_2SO_4 solution. Scan rate 10 mV s^{-1}, rotation rate 1600 rpm. (d) Mass transfer corrected Tafel plots extracted from the data of the RDE linear sweeps; the current density is normalized to the geometric surface area of the electrode.

Table 5. Electrochemical Data Obtained from Cyclic and Linear Sweep Voltammetry

catalyst	E_p[ac] (V)	E_{onset}[bc] (V)	$E_{1/2}$[bc] (V)	$\Delta E_{1/2}$[bd] (mV)	n[e]	EAS[a] (m^2/g)
Pt@vulcan	0.687	0.804	0.707	0	3.93	43
Pt@MC-2	0.687	0.804	0.707	0	3.98	46
Pt@NMC-2	0.701	0.842	0.748	41	3.89	67
Pd@MC-2	0.660	0.734	0.646	−61	3.98	26
Pd@NMC-2	0.668	0.753	0.682	−25	3.86	32

[a] Data obtained from cyclic voltammetery. [b] Data obtained from RDE voltammetry. [c] All potentials are referred to SHE. [d] $\Delta E_{1/2} = E_{1/2}^{catalyst} - E_{1/2}^{Pt@vulcan}$. [e] Number of transferred electrons calculated from RRDE measurements

The electrochemical investigation was extended also to Pt@NMC-2 and Pd@NMC-2, and the results were compared with Pt@MC-2, Pd@MC-2 and with the commercial standard Johnson Matthey 30 wt % Pt on Vulcan XC72R (hereafter denoted as Pt@vulcan). The electrochemical properties of Pt and Pd NPs deposited on MC-2 and NMC-2 were first examined by cyclic voltammetry, as shown in Figure 9a,b. For both types of NPs, there are three distinct potential regions in the voltammograms: the hydrogen adsorption/desorption region between 0.0 and 0.25 V, the double-layer region between 0.25 and 0.50 V and the surface oxide formation/reduction region (>0.50 V). The Coulombic charge for hydrogen adsorption/desorption (Q_H) can be used to calculate the electrochemical active Pt and Pd surface area of the electrodes.[49,50] The value of Q_H (mC cm^{-2}) was calculated as the mean value between the amounts of charge exchanged during the electroadsorption and desorption of H_2 on Pt or Pd sites, with the correction of the capacitive current contribution. The electrochemical active surface area can therefore be calculated according to the formula:

$$\mathrm{EAS} = \frac{Q_H}{[M]\cdot q} \quad (2)$$

where [M] is the metal loading in the electrode and represents the M/C wt % determined by XPS and TGA measurements, which in the present case is 42.5 μg cm^{-2}. The factor q = 0.21 represents the charge required to oxidize a monolayer of H_2 on smooth Pt and Q_H (μC cm^{-2}) is the charge for hydrogen adsorption/desorption. Table 5 summarizes the results for the catalysts tested. The results point out that Pt@MC-2 and Pt@vulcan have similar EAS, whereas Pt@NMC-2 sample shows the higher EAS. The increase in EAS indicates that a larger fraction of the Pt surface is exposed. This in agreement with the consideration expressed in section 3.2 where it was observed that on nitrogen doped mesoporous carbon, there is a better nucleation and dispersion of Pt NPs, and less agglomeration. It is worth noting that the EAS decreases sensitively when passing from Pt to Pd NPs loaded on MC-2. This effect can be associated with the NPs dimension that in the case of Pd@MC-2 results to be 3−4 times greater than for Pt NPs, causing a decrease of the NPs surface area. However, when Pd NPs are loaded on NMC-2, it is possible to observe again an increase of the EAS, in accordance with the fact that Pd@NMC-2 shows smaller catalyst particles.

The electrocatalytic performances for the whole batch of electrocatalysts toward ORR were tested by both cyclic voltammetry and linear sweep voltammetry at RDE and RRDE. The reduction peak potentials (E_p) for the irreversible reduction of O_2 in silent condition at all the investigated surfaces are reported in Table 5. Figure 9c presents the ORR polarization curves at RRDE (1600 rpm, 10 mVs^{-1}) for Pt and Pd catalysts with different carbon supports. From the disk current response, it should be noted that the onset and the half-wave potential of Pt@MC-2 are in good agreement with the values of Pt@vulcan. Therefore, it appears that the mere increase of the carbon support surface area does not improve the mass specific catalytic activity. It is interesting to observe that Pt@NMC-2 is characterized by better performances (in terms of onset potential and E_p, Table 5) than the commercial standard Pt@vulcan; in fact the diffusion limiting current density of Pt@NMC-2 reaches that of Pt@vulcan and a positive shift of about 40 mV exists in the half-wave potential of Pt@NMC-2 as compared to Pt@vulcan (Table 5). Also in the case of Pd based catalyst, an increased catalytic activity is observed when the Pd NPs are supported on NMC-2. However, the catalytic performance is significantly worse than Pt@vulcan, especially in term of half wave potential.

The K-L plots (not shown), resulting from the polarization curves for the ORR at different rotation rates, are linear for all the investigated catalysts. This indicates a first-order dependence of the kinetics for the ORR on the Pt and Pd surface. Figure 9c reports also the ring current recorded at RRDE for all the investigated electrodes in an oxygen saturated 0.1 M H_2SO_4 solution. The ring currents were at least 2 orders of magnitude lower than the disk currents, indicating the production of minimal amounts of H_2O_2. The electron number calculated from the formula:

$$n = \frac{4I_d}{(I_d + I_r/N)}$$

where I_d is the limiting disk current, I_r is the limiting ring current, and N is the collection efficiency (0.25), shows that $n \approx 3.8{-}3.9$ within the range of 0.3 to 0.5 V for the commercial Pt/C as well as for the new catalysts (Table 5).

The mass transfer corrected Tafel plots for ORR activity of these samples are shown in Figure 9d. The kinetic current density of the different catalysts at various potentials can be determined according to the equation:

$$j_k = \frac{j_{\mathrm{lim}} \cdot j}{j_{\mathrm{lim}} - j} \qquad (3)$$

In all five observed cases, double slope Tafel plots are evident, which is known to be dependent on the formation of metal oxide on the NPs surface.[51] The higher current density is observed in the case of Pt@NMC-2 catalyst, which indicates that the O_2 reduction rate is faster on Pt NPs loaded on a nitrogen-doped support. The same observation can be made in the case of Pd NPs loaded on doped MC. As it was seen above for the NMC, the presence of nitrogen defects on MC improves the catalytic performance of Pt and Pd NPs toward ORR. In terms of onset and peak potentials, the ORR activity increases as follows: Pd@MC-2 < Pd@NMC-2 < Pt@vulcan ≈ Pt@MC < Pt@NMC-2, as particularly evidenced by the $E_{1/2}$ potentials of these samples (Table 5).

3.3. Stability Tests of Pt NPs on Doped and Undoped Mesoporous Carbon.

The active surface area of Pt NPs, which is determined from the hydrogen adsorption/desorption region,[49] is used in order to compare the loss rate of Pt and Pd quantitatively. In Figure 10a, the initial active area is fixed as 100%, and the residual active area after potential cycles is normalized to the initial area in percentage. The residual active area versus the number of potential cycles is fitted to the exponential decay function shown as the solid lines. In Figure 10b is reported, as an example, the electrochemical behavior of Pt@NMC-2 recorded after zero, 150 and 350 potential cycles. After 750 voltammetric cycles performed between 0.25 and 1.45 V vs SHE at 50 mV s^{-1} in 0.1 M H_2SO_4 at 25 °C, a Pt@vulcan 25% of Pt active area remains, whereas the Pt@NMC-2 and Pt@MC-2 keep 44% and 67%, respectively, of initial Pt active area. In the case of Pd NPs, the active surface area decreases to the 20% of the initial value after 50 and 150 cycles for NMC-2 and MC-2, respectively. This indicates that the Pt and Pd NPs supported on doped MC have a lower stability as compared with the undoped MC, but in the case of Pt NPs, they show higher stability with respect to the commercial standard Pt@vulcan. These results may be indicative of an increased stabilization provided by the mesoporous carbon with respect to the vulcan as an electrode support. A possible rationalization of the higher stability of Pt NPs on mesoporous carbon may be done by considering the particle dimension with respect to the pore size of the supporting matrix. Pt NPs are very small (1−2 nm) and therefore, besides dissolution, Pt NPs can be subjected to Ostwald ripening.[52] This effect is less pronounced when mesoporous carbon is adopted due to a beneficial confinement effect inside the mesoporous structure. In the case of N doped MC the confinement effect could be limited on the bases of a lower number of available mesopores with respect the undoped MC, as already observed from the BET analysis.

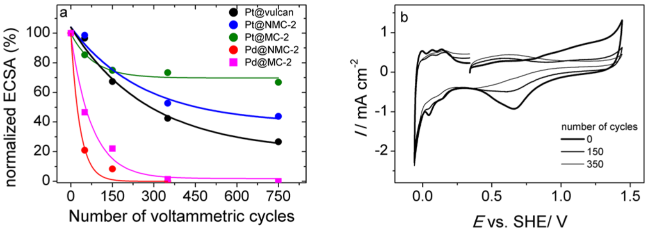

Figure 10. (a) Degeneration of the Pt and Pd active area of supported Pt particles in the stability measurements, (b) cyclic voltammograms recorded in 0.1 M H_2SO_4 solution on Pt@NMC-2 at 0, 150 and 350 voltammetric cycles, scan rate 50 mV s^{-1}.

Even though the increased stabilization expected for the interaction between Pt NPs with the nitrogen functional groups was not observed, these represent very promising and interesting results since they allow to better define the parameters influencing the catalyst activity and stability and therefore to design with a clear view carbon supports able to outclass standard commercial material both in term of activity and chemical and mechanical stability.

4. CONCLUSIONS

N-doped mesoporous carbon with high surface area and enhanced catalytic activity toward ORR was prepared by an optimized hard template approach, employing NH_3 as the doping agent. Pd and Pt NPs were deposited by wet impregnation on both doped and undoped samples, showing that the presence of nitrogen functional groups drives the dimension and the dispersion of metal NPs. The shift of Pt and Pd binding energy reveals the presence of a chemical interaction between metal NPs and nitrogen defects, especially in the case of Pd. All the catalysts were characterized by electrochemical techniques, showing the general superiority of metal NPs loaded on doped MC, with respect to the same amount and type of metal deposited on undoped MC-2. In particular, Pt nanoparticles supported on N-doped supports showed high activities for the ORR in acidic solutions, with better performances than those of commercial Pt@vulcan (30 wt % Pt on Vulcan XC-72). Furthermore, Pt NPs loaded on mesoporous carbon seems to possess higher stability with respect to the standard Pt@vulcan. This was rationalized in term of a better confinement effect inside the mesoporous structure. In conclusion, the doped mesoporous carbon supports prepared in this work represent a viable tool for the preparation of new electrocatalysts characterized by good activities, a key factor in future fuel cell technology.

■ AUTHOR INFORMATION

Corresponding Author

*C. Durante. Tel.: +39 049 8275112. Fax: +39 049 8275829. E-mail: christian.durante@unipd.it.

Notes

The authors declare no competing financial interest.

■ ACKNOWLEDGMENTS

The research leading to these results has received funding from the University of Padova (PRAT CPDA139814/13) and the Fuel Cells and Hydrogen Joint Undertaking (FCH-JU) within the CathCat project under contract No. 303492. M.F. thanks Fondazione Cariparo for a Ph.D. fellowship.

■ REFERENCES

(1) Mayrhofer, K. J. J.; Arenz, M. Improvements to the Efficiency and Lifetime of Polymer Electrolyte Membrane Fuel Cells Can Be Realized by Finding More Active and Stable Electrocatalytic Cathode Materials. A Computational Search Has Found Two Such Alloys and Confirmed Their Enhanced Properties Experimentally. *Nat. Chem.* **2009**, *1*, 518–519.

(2) Jung, H. G.; Hassoun, J.; Park, J. B.; Sun, Y. K.; Scrosati, B. An Improved High-Performance Lithium-Air Battery. *Nat. Chem.* **2012**, *4*, 579–585.

(3) Liu, C. W.; Wei, Y. C.; Wang, K. W. Surface Condition Manipulation and Oxygen Reduction Enhancement of PtAu/C Catalysts Synergistically Modified by CeO_2 Addition and N_2 Treatment. *J. Phys. Chem. C* **2011**, *115*, 8702–8708.

(4) Favaro, M.; Perini, L.; Agnoli, S.; Durante, C.; Gennaro, A.; Granozzi, G. Palladium Nanoparticles Supported on Nitrogen-Doped HOPG: A Surface Science and Electrochemical Study. *Phys. Chem. Chem. Phys.* **2013**, *15*, 2923–2931.

(5) Perini, L.; Durante, C.; Favaro, M.; Agnoli, S.; Granozzi, G.; Gennaro, A. Electrocatalysis at Palladium Nanoparticles: Effect of The Support Nitrogen Doping on the Catalytic Activation of Carbon-Halogen Bond. *Appl. Catal., B* **2014**, *144*, 300–307.

(6) Leiva, E.; Iwasita, T.; Herrero, E.; Feliu, J. M. Effect of Adatoms in the Electrocatalysis of HCOOH Oxidation. A Theoretical Model. *Langmuir* **1997**, *13*, 6287–6293.

(7) Smith, S. P. E.; Abruña, H. D. Structural Effects on the Oxidation of HCOOH by Bismuth Modified Pt(111) Electrodes with (110) Monatomic Steps. *J. Electroanal. Chem.* **1999**, *467*, 43–49.

(8) Wei, J.; Zhou, D.; Sun, Z.; Deng, Y.; Xia, Y.; Zhao, D. A Controllable Synthesis of Rich Nitrogen-Doped Ordered Mesoporous Carbon for CO_2 Capture and Supercapacitors. *Adv. Funct. Mater.* **2013**, *23*, 2322–2328.

(9) Alegre, C.; Gálvez, M. E.; Baquedano, E.; Moliner, R.; Pastor, E.; Lázaro, M. J. Oxygen-Functionalized Highly Mesoporous Carbon Xerogel based Catalysts for Direct Methanol Fuel Cell Anodes. *J. Phys. Chem. C* **2013**, *117*, 13045–13058.

(10) Lin, M. L.; Lo, M. Y.; Mou, C. Y. PtRu Nanoparticles Supported on Ozone-Treated Mesoporous Carbon Thin Film as Highly Active Anode Materials for Direct Methanol Fuel Cells. *J. Phys. Chem. C* **2009**, *113*, 16158–16168.

(11) Favaro, M.; Agnoli, S.; Ferrighi, L.; Colazzo, L.; Di Valentin, C.; Durante, C.; Sedona, F.; Sambi, M.; Gennaro, A.; Granozzi, G. Single and Multiple Doping in Graphene Quantum Dots: Unraveling the Origin of Selectivity in the Oxygen Reduction Reaction. *ACS Catal.* **2015**, *5*, 129–144.

(12) Zhang, J.; Kong, L. B.; Cai, J. J.; Luo, Y. C.; Kang, L. Nano-Composite of Polypyrrole/Modified Mesoporous Carbon for Electrochemical Capacitor Application. *Electrochim. Acta* **2010**, *55*, 8067–8073.

(13) Maldonado, S.; Stevenson, K. J. Influence of Nitrogen Doping on Oxygen Reduction Electrocatalysis at Carbon Nanofiber Electrodes. *J. Phys. Chem. B* **2005**, *109*, 4707–4716.

(14) Wu, J.; Yang, Z.; Li, V.; Sun, Q.; Jin, C.; Strasserd, P.; Yang, R. Phosphorus-Doped Porous Carbons as Efficient Electrocatalysts for Oxygen Reduction. *J. Mater. Chem. A* **2013**, *1*, 9889–9896.

(15) Qu, L.; Liu, Y.; Baek, J. B.; Dai, L. Nitrogen-Doped Graphene as Efficient Metal-Free Electrocatalyst for Oxygen Reduction in Fuel Cells. *ACS Nano* **2010**, *4*, 1321–1326.

(16) Liang, H. W.; Wei, W.; Wu, Z. S.; Feng, X.; Müllen, K. Communication Mesoporous Metal–Nitrogen-Doped Carbon Electrocatalysts for Highly Efficient Oxygen Reduction Reaction. *J. Am. Chem. Soc.* **2013**, *135*, 16002–16005.

(17) Sheng, Z. H.; Shao, L.; Chen, J. J.; Bao, W. J.; Wang, F. B.; Xia, X. H. Catalyst-Free Synthesis of Nitrogen-Doped Graphene via Thermal Annealing Graphite Oxide with Melamine and Its Excellent Electrocatalysis. *ACS Nano* **2011**, *5*, 4350–4358.

(18) Zhou, Y.; Pasquarelli, R.; Holme, T.; Berry, J.; Ginley, D.; O'Hayre, R. Improving PEM Fuel Cell Catalyst Activity and Durability Using Nitrogen-Doped Carbon Supports: Observations from Model Pt/HOPG Systems. *J. Mater. Chem.* **2009**, *19*, 7830–7838.

(19) Kumar, S. M. S.; Herrero, J. S.; Irusta, S.; Scott, K. The Effect of Pretreatment of Vulcan XC-72R Carbon on Morphology and Electrochemical Oxygen Reduction Kinetics of Supported Pd Nano-Particle in Acidic Electrolyte. *J. Electroanal. Chem.* **2010**, *647*, 211–221.

(20) Wei, D.; Liu, Y.; Wang, Y.; Zhang, H.; Huang, L.; Yu, G. Synthesis of N-Doped Graphene by Chemical Vapor Deposition and Its Electrical Properties. *Nano Lett.* **2009**, *9*, 1752–1758.

(21) Wang, T. S.; Ding, J. J.; Cheng, R.; Peng, H. B.; Lu, X.; Zhao, Y. T. Diamond-like Carbon Produced by Highly Charged Ions Impact on Highly Oriented Pyrolytic Graphite. *Nucl. Instrum. Methods Phys. Res., Sect. B* **2012**, *272*, 15–17.

(22) Barinov, A.; Malcioglu, O. B.; Fabris, S.; Sun, T.; Gregoratti, L.; Dalmiglio, M.; Kiskinova, M. Initial Stages of Oxidation on Graphitic Surfaces: Photoemission Study and Density Functional Theory Calculations. *J. Phys. Chem. C* **2009**, *113*, 9009–9013.

(23) Zhang, C.; Fu, L.; Liu, N.; Liu, M.; Wang, Y.; Liu, Z. Synthesis of Nitrogen-Doped Graphene Using Embedded Carbon and Nitrogen Sources. *Adv. Mater.* **2011**, *23*, 1020–1024.

(24) Usachov, D.; Vilkov, O.; Grüneis, A.; Haberer, D.; Fedorov, A.; Adamchuk, V. K.; Preobrajenski, A. B.; Dudin, P.; Barinov, A.; Oehzelt,

M.; Laubschat, C.; Vyalikh, D. V. Nitrogen-Doped Graphene: Efficient Growth, Structure, and Electronic Properties. *Nano Lett.* **2011**, *11*, 5401−5407.

(25) Favaro, M.; Perini, L.; Agnoli, S.; Durante, C.; Granozzi, G.; Gennaro, A. Electrochemical Behavior of N and Ar Implanted Highly Oriented Pyrolytic Graphite Substrates and Activity Toward Oxygen Reduction Reaction. *Electrochim. Acta* **2013**, *88*, 477−487.

(26) Hellgren, N.; Guo, J.; Luo, Y.; Såthe, C.; Agui, A.; Kashtanov, S.; Nordgren, J.; Ågren, H.; Sundgren, J. E. Electronic Structure of Carbon Nitride Thin Films Studied by X-ray Spectroscopy Techniques. *Thin Solid Films* **2005**, *471*, 19−34.

(27) Pylypenko, S.; Queen, A.; Olson, T. S.; Dameron, A.; O-Neill, K.; Neyerlin, K. C.; Pivovar, B.; Dinh, H. N.; Ginley, D. S.; Gennet, T.; O-Hayre, R. Tuning Carbon-based Fuel Cell Catalyst Support Structures via Nitrogen Functionalization. I. Investigation of Structural and Compositional Modification of Highly Oriented Pyrolytic Graphite Model Catalyst Supports as a Function of Nitrogen Implantation Dose. *J. Phys. Chem. C* **2011**, *115*, 13667−13675.

(28) Dresselhaus, M. S.; Jorio, A.; Saito, R. Characterizing Graphene, Graphite, and Carbon Nanotubes by Raman Spectroscopy. *Annu. Rev. Condens. Matter Phys.* **2010**, *1*, 89−108.

(29) Zhao, Z.; Dai, Y.; Lin, J.; Wang, G. Highly-Ordered Mesoporous Carbon Nitride with Ultrahigh Surface Area and Pore Volume as a Superior Dehydrogenation Catalyst. *Chem. Mater.* **2014**, *26*, 3151−3161.

(30) Chen, Y.; Wang, J.; Liu, H.; Banis, M. N.; Li, R.; Sun, X.; Sham, T. K.; Ye, S.; Knights, S. Nitrogen Doping Effects on Carbon Nanotubes and the Origin of the Enhanced Electrocatalytic Activity of Supported Pt for Proton-Exchange Membrane Fuel Cells. *J. Phys. Chem. C* **2011**, *115*, 3769−3776.

(31) Jua, W.; Favaro, M.; Durante, C.; Perini, L.; Agnoli, S.; Schneider, O.; Stimming, U.; Granozzi, G. Pd Nanoparticles Deposited on Nitrogen-Doped HOPG: New Insights into the Pd-Catalyzed Oxygen Reduction Reaction. *Electrochim. Acta* **2014**, *141*, 89−101.

(32) Zhou, Y.; Holme, T.; Berry, J.; Ohno, T. R.; Ginley, D.; O'Hayre, R. Dopant-Induced Electronic Structure Modification of HOPG Surfaces: Implications for High Activity Fuel Cell Catalysts. *J. Phys. Chem. C* **2010**, *114*, 506−515.

(33) Zhou, Y.; Neyerlin, K.; Olson, T. S.; Pylypenko, S.; Bult, J.; Dinh, H. N.; Gennett, T.; Shao, Z.; O'Hayre, R. Enhancement of Pt and Pt-Alloy Fuel Cell Catalyst Activity and Durability via Nitrogen-Modified Carbon Supports. *Energy Environ. Sci.* **2010**, *3*, 1437−1446.

(34) Groves, M. N.; Chan, A. S. W.; Malardier-Jugroot, C.; Jugroot, M. Improving Platinum Catalyst Binding Energy to Graphene through Nitrogen Doping. *Chem. Phys. Lett.* **2009**, *481*, 214−219.

(35) Kim, N. D.; Kim, W.; Joo, J. B.; Oha, S.; Kim, P.; Kim, Y.; Yi, J. Electrochemical Capacitor Performance of N-Doped Mesoporous Carbons Prepared by Ammoxidation. *J. Power Sources* **2008**, *180*, 671−675.

(36) Hulicova, D.; Yamashita, J.; Soneda, Y.; Hatori, H.; Kodama, M. Supercapacitors Prepared from Melamine-based Carbon. *Chem. Mater.* **2005**, *17*, 1241−1247.

(37) Ania, C. O.; Khomenko, V.; Raymundo-Piñero, E.; Parra, J. B.; Béguin, F. The Large Electrochemical Capacitance of Microporous Doped Carbon Obtained by Using a Zeolite Template. *Adv. Funct. Mater.* **2007**, *17*, 1828−1828.

(38) Lota, G.; Lota, K.; Frackowiak, E. Nanotubes based Composites Rich in Nitrogen for Supercapacitor Application. *Electrochem. Commun.* **2007**, *9*, 1828−1823.

(39) Jia, N.; Wang, Z.; Yang, G.; Shen, H.; Zhu, L. Electrochemical Properties of Ordered Mesoporous Carbon and Its Electroanalytical Application for Selective Determination of Dopamine. *Electrochem. Commun.* **2007**, *9*, 233−238.

(40) Musameh, M.; Wang, J.; Merkoci, A.; Lin, Y. Low-Potential Stable NADH Detection at Carbon-Nanotube-Modified Glassy Carbon Electrodes. *Electrochem. Commun.* **2002**, *4*, 743−746.

(41) Ikeda, T.; Boero, M.; Huang, S. F.; Terakura, K.; Oshima, M.; Ozaki, J. Carbon Alloy Catalysts: Active Sites for Oxygen Reduction Reaction. *J. Phys. Chem. C* **2008**, *112*, 14706−14709.

(42) Wong, W. Y.; Daud, W. R. W.; Mohamad, A. B.; Kadhum, A. A. H.; Loh, K. S.; Majlan, E. H. Recent Progress in Nitrogen-Doped Carbon and Its Composites as Electrocatalysts For Fuel Cell Applications. *Int. J. Hydrogen Energy* **2013**, *38*, 9370−9386.

(43) Wang, D. W.; Su, D. Heterogeneous Nanocarbon Materials for Oxygen Reduction Reaction. *Energy Environ. Sci.* **2014**, *7*, 576−591.

(44) Yang, Z.; Nie, H.; Chen, X.; Chen, X.; Huang, S. Recent Progress in Doped Carbon Nanomaterials as Effective Cathode Catalysts for Fuel Cell Oxygen Reduction Reaction. *J. Power Sources* **2013**, *236*, 238−249.

(45) Lai, L.; Potts, J. R.; Zhan, D.; Wang, L.; Poh, C. K.; Tang, C.; Gong, H.; Shen, Z.; Lin, J.; Ruoff, R. S. Exploration of the Active Center Structure of Nitrogen-Doped Graphene-based Catalysts for Oxygen Reduction Reaction. *Energy Environ. Sci.* **2012**, *5*, 7936−7942.

(46) Xing, T.; Zheng, Y.; Li, L. H.; Cowie, B. C. C.; Gunzelmann, D.; Qiao, S. Z.; Huang, S.; Chen, Y. Observation of Active Sites for Oxygen Reduction Reaction on Nitrogen-Doped Multilayer Graphene. *ACS Nano* **2014**, *8*, 6856−6862.

(47) Gottesfeld, S.; Raistrick, I. D.; Srinivasan, S. Oxygen Reduction Kinetics on a Platinum RDE Coated with a Recast Nafion Film. *J. Electrochem. Soc.* **1987**, *134*, 1455−1462.

(48) Song, C.; Zhang, J. In *PEM Fuel Cell Electrocatalyst and Catalyst Layers Fundamentals and Applications*; Zhang, J., Ed.; Springer-Verlag, London, 2008.

(49) Schmidt, J.; Gasteiger, H. A.; Stab, G. D.; Urban, P. M.; Kolb, D. M.; Behm, R. J. Characterization of High-Surface-Area Electrocatalysts Using a Rotating Disk Electrode Configuration. *J. Electrochem. Soc.* **1998**, *145*, 2354−2358.

(50) Pozio, A.; De Francesco, M.; Cemmi, A.; Cardellini, F.; Giorgi, L. Comparison of High Surface Pt/C Catalysts by Cyclic Voltammetry. *J. Power Sources* **2002**, *105*, 13−19.

(51) Zecevic, S. K.; Wainright, J. S.; Litt, M. H.; Gojkovic, S. L.; Savinell, R. F. Kinetics of O_2 Reduction on a Pt Electrode Covered with a Thin Film of Solid Polymer Electrolyte. *J. Electrochem. Soc.* **1997**, *144*, 2973−2982.

(52) Ferreira, P. J.; la O', G. J.; Shao-Horn, Y.; Morgan, D.; Makharia, R.; Kocha, S.; Gasteiger, H. A. Instability of Pt/C Electrocatalysts in Proton Exchange Membrane Fuel Cells. *J. Electrochem. Soc.* **2005**, *152*, A2256−A2271.